

COMMON REFLECTION POINT STACKING

A MACRO MODEL DRIVEN APPROACH TO DIP MOVEOUT

PROEFSCHRIFT

ter verkrijging van de graad van doctor
aan de Technische Universiteit Delft,
op gezag van de Rector Magnificus,
prof.dr.s. P.A. Schenck,
in het openbaar te verdedigen
ten overstaan van een commissie,
aangewezen door het College van Dekanen
op dinsdag 17 oktober 1989 te 16.00 uur door

ADRIAAN VAN DER SCHOOT

geboren te Dordrecht
natuurkundig ingenieur



Gebotekst Zoetermeer / 1989

TR diss
1757

Dit proefschrift is goedgekeurd door de promotor

prof.dr.ir. A.J. Berkhout

Copyright © 1989, by Delft Geophysical, Delft, The Netherlands.

All rights reserved. No part of this publication may be reproduced, stored in a retrieval system or transmitted in any form or by any means, electronic, mechanical, photocopying, recording or otherwise, without the prior written permission of Delft Geophysical b.v., P.O. Box 148, 2600 AC Delft, The Netherlands.

CIP-DATA KONINKLIJKE BIBLIOTHEEK, DEN HAAG

Schoot, Ad van der

Common reflection point stacking/ Ad van der Schoot

[S.l. : s.n.] (Zoetermeer : Gebotekst). – III.

Thesis Delft. – With ref. – With summary in Dutch

ISBN 90-9003020-4

SISO 567.2 UDC 550.34 (043.3)

Subject headings: seismology, dip moveout, stacking

printed in The Netherlands by: N.K.B. Offset bv, Bleiswijk

aan Sofieke

PREFACE

Initially the research presented in this thesis was carried out at Delft Geophysical.

When in 1986 the TRITON research project started at the group of Seismics and Acoustics of the Delft University it became clear that my research project would fit in the TRITON project. Therefore from March 1986 onwards it became an integrated part of TRITON.

The research described in this thesis could only be carried out with the help and support of others.

First of all I would like to express my sincere gratitude to Dr. N. de Voogd, managing director of Delft Geophysical, for the opportunity he gave me to carry out this research. Initially it coincided quite well with my responsibilities as research geophysicist within the company. However, when these responsibilities changed and it became more difficult to combine them with this research activity, he kept his promise to give me the possibility of finalizing this project.

It is my sincere wish that the results of the research will be of value to Delft Geophysical, which I think they will.

I also would like to thank my promotor Prof. Dr. A.J. Berkhout, for his critical, stimulating and constructive attention.

I especially express my gratitude to Dr. Kees Wapenaar who managed to guide me in my day to day research activity. Without his scientific creativity and erudition — and his patience with me — it is hard to imagine how this thesis would have been finished. Also my colleagues Dr. Adri Duijndam and Remco Romijn were of invaluable help to me. I very much appreciate the many fruitful discussions we had and all the computer experiments, *including the real data processing, they carried out.*

I thank Terry Davies not only for careful reading of the manuscript but also for looking after all my responsibilities when I was working on this thesis. He carried out an enormous amount of work for me.

Dr. L. Ongkiehong of Delft Geophysical is acknowledged for many stimulating discussions.

I would like to thank Walter Rietveld for carrying out the experiments in chapter VI and N.A.M., Assen for the permission to use their seismic data.

Sander Oosterhof prepared all the drawing. I would like to express my appreciation for the professional work he delivered and the valuable advice he gave me.

Also I would like to thank Corina van der Heide for all the work — including typing the manuscript — the writing of a thesis bring with it. Her kindness and helpfulness are greatly appreciated.

Gerda Boone of Gebotekst prepared the final version of the manuscript.

I appreciated the interest and support of my parents and parents in law.

Last but not least I would like to thank Sofieke for her encouragement, patience and support over the years.

Delft, September 1989

Ad van der Schoot

CONTENTS

I	INTRODUCTION	1
I	A COMPARATIVE OVERVIEW OF CMP, CRP AND CDP PROCESSING	
I.1	Introduction	9
I.2	Wave-theoretical description of CMP, CRP and CDP processing	13
I.2.1	The double square root equation	13
I.2.2	The DSR operator and CMP processing	26
I.2.3	The DSR operator and CRP processing	32
I.2.4	Summary of main results	37
II	CRP PROCESSING BY CONSTANT VELOCITY DMO	
II.1	Introduction	41
II.2	Claims for DMO	42
II.3	Kinematic aspects of the DMO impulse response	50
II.4	Implementation aspects of DMO operators	54
II.4.1	Integral type formulation	55
II.4.2	Mapping method	55
II.4.3	Poststack DMO	59
II.4.4	Finite-difference method	63
II.5	Amplitude and phase characteristics in DMO	65
II.5.1	Wave-theoretical approach	65
II.5.2	Heuristic approach	67
II.5.3	Simple amplitude tapering	75
II.5.4	Summary	78
III	CRP STACKING IN CONSTANT VELOCITY MEDIA	
III.1	Introduction	81
III.2	A kinematic derivation of CRP stacking	82
III.3	Amplitude and phase characteristics of CRP stacking	91
III.4	Prestack migration by CRP processing	91
III.5	Examples of the application of CRP processing in constant velocity media	92
III.6	Summary and conclusions	105

IV	CRP STACKING IN INHOMOGENEOUS MEDIA	
IV.1	Introduction	109
IV.2	The need for generalization of CRP stacking	110
IV.3	Previous attempts to generalize CRP processing to inhomogeneous media	114
IV.3.1	CRP processing in depth-variable media	117
IV.3.2	CRP stacking in the midpoint-time-velocity space	117
IV.3.3	CRP stacking according to French	118
IV.4	A CRP stacking scheme for inhomogeneous media	122
IV.4.1	Mapping to zero-offset by CRP stacking	122
IV.4.2	CRP prestack migration	126
IV.4.3	Summary of methods and description of the computational flow diagram	126
IV.5	A synthetic data example of CRP stacking in an inhomogeneous medium	128
V	REAL DATA EXAMPLE OF CMP, CRP AND CDP PROCESSING	
V.1	Introduction	139
V.2	Real data example	139
V.3	Conclusions	156
VI	CRP STACKING IN 3-D MEDIA	
VI.1	Introduction	157
VI.2	CRP stacking in 3-D media	157
Appendix A	The half differential filter in DMO operators	163
Appendix B	Derivation of DMO formula	169
Appendix C	The relation between spatial and dip angle sampling	171
Appendix D	Depth point smear in inhomogeneous media	173
REFERENCES	185
SUMMARY	189
SAMENVATTING	190
CURRICULUM VITAE	192

INTRODUCTION

GEOPHYSICS IN THE SEARCH FOR OIL AND GAS

Geophysics is the science that studies the physics of the earth and its surrounding atmosphere. Applied geophysics in search for minerals, oil and gas — also called exploration geophysics — can be divided into a number of general exploration methods (see Telford et al., 1976). Some methods deal with surface measurements, such as

seismic

magnetic

gravity

radioactivity

electromagnetic

and electrical measurements.

Other methods deal with subsurface measurements or in situ measurements, such as well logging and miscellaneous chemical and thermal methods.

All methods can be characterized by two basic properties:

1. the physical parameter of interest
2. the nature of this parameter and the way it is measured.

Rapid lateral variations, for instance, require a dense spatial sampling. The temporal sampling density is determined by the frequency contents of the measured quantity. This may range from low frequent (gravity, apart from tidal corrections) to high-frequent quantities (transient waves in seismics).

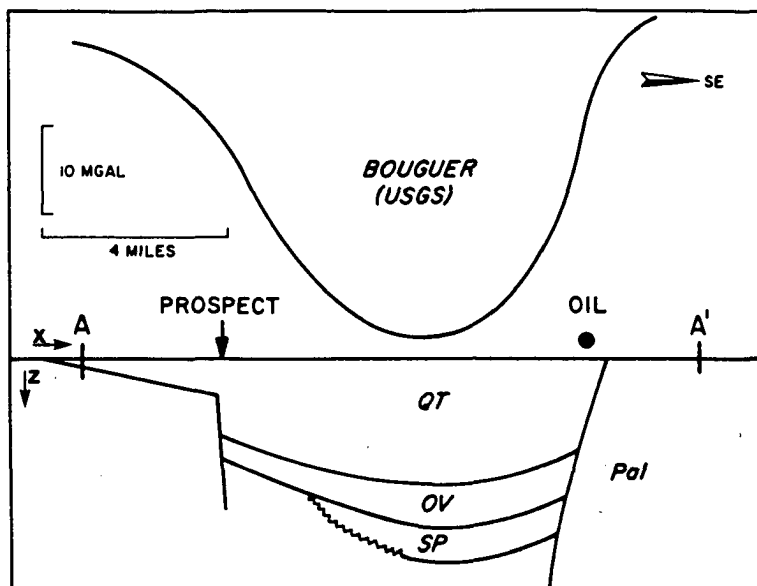


Figure 1 Reconnaissance gravity profile of the U.S. Geological Survey (USGS) through the Railroad Valley Nevada. The Sheep Pass formation (SP) and Oligocene ignimbrites (OV) are the reservoir rocks. The Tertiary to Quaternary fill (QT) forms a seal and has a low density (after Healey, 1975, quoted by Guion, 1981). Note that the trapping fault on the east side of the valley is apparent in the gravity data. Also the major bounding fault at the left side is detectable.

Within the physical limit of the specific method, the sampling density also determines the maximum resolution that may be obtained.

An example of a geophysical method is the gravity profile shown in figure 1 (after Healey 1975, quoted by Guion et al., 1981). The gravity method detects lateral variations in rock densities. The gravity data result from time-invariant integral measurements. The latter means that at each surface location the measured gravity value is the total response of the subsurface. The method will therefore be a global one. In general only trend information is obtained. Gravity may be used to identify prospects, thus significantly reducing the amount of seismic data needed to evaluate the prospect.

This suggests that different geophysical measurements can be combined in order to arrive at a better description of the subsurface. This is indeed the case. It especially applies to the combination of well log data and seismic data, which can be used to arrive at more detailed reflectivity information of the subsurface than can be obtained from seismic data only. An example of this is given in figure 2. A seismic section is shown, together with a reflectivity

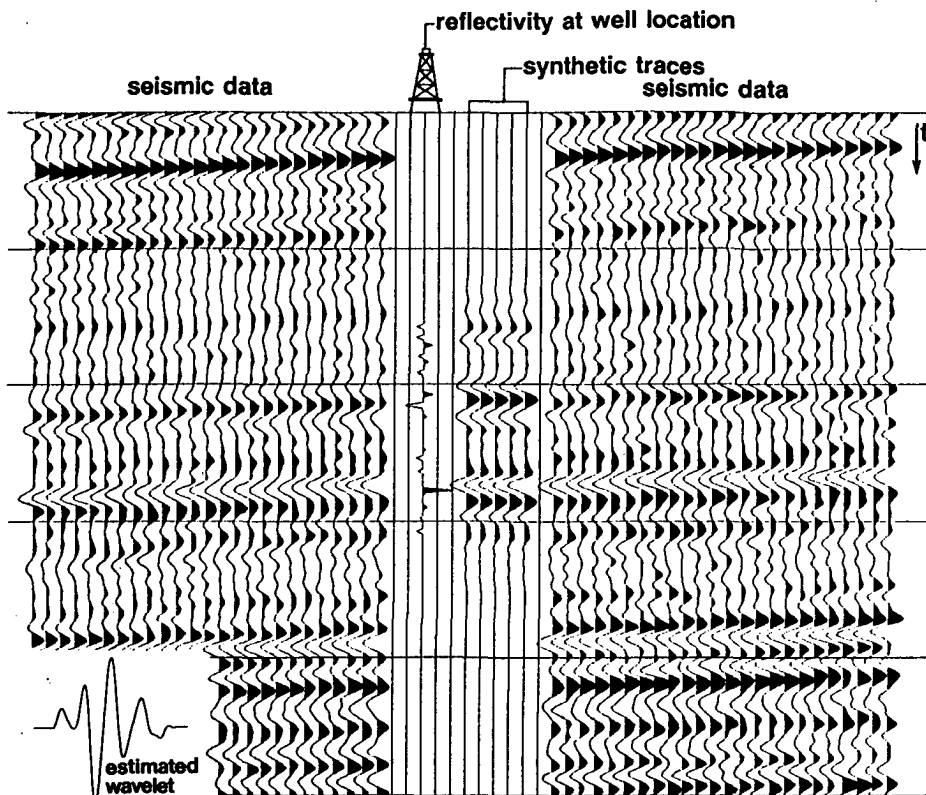


Figure 2 CMP stack related with a reflectivity sequence derived from well log information. From the reflectivity sequence and some seismic traces around the well a wavelet is determined. The wavelet and the reflectivity are then used to calculate some synthetic seismic traces.

sequence derived from a well at the center of the section. Using the well log and the seismic data, a wavelet can be determined.

The wavelet can then be used to deconvolve the seismic section, or to compute a synthetic seismic section, using the reflectivity information. The synthetic traces are also shown. We see that they match the seismic data around the well fairly well.

Seismic exploration is by far the most important geophysical exploration technique in terms of expenditures and number of geophysicists involved worldwide. The predominance of the seismic method over other geophysical methods is due to various factors, the most important of which are the high accuracy, high resolution and large penetration of which the method is capable (Telford et al., 1976).

SEISMIC DATA PROCESSING

Seismic data processing is defined as the analysis of measured seismic data with the help of computers. In the history of seismic data processing we can distinguish specific time periods of significant progress, related to the invention and introduction of new concepts (Berkhout, 1984).

In the early 1950s, the common midpoint concept was introduced in seismic data acquisition and processing. This meant a drastic improvement in the quality of seismic data with respect to signal-to-noise ratio.

Through the 1960s emphasis was put on time series analysis and statistical filtering. Also digital processing was introduced.

In the early 1970s the first imaging methods based on the wave equation were developed.

Finally, in the early 1980s important new developments in computer hardware made properly formulated wave theory solutions feasible.

However, practical seismic data acquisition and processing techniques are still greatly governed by the common midpoint principle and time series methods. This also applies to the more recently developed three dimensional (3-D) techniques, which are often a straight forward extension of the two dimensional (2-D) ones. While many well known procedures and processes have been very well refined, it should be remembered that most of the underlying basic principles are largely untouched (Berkhout, 1984). These include:

- data gathering around a common midpoint (CMP);
- velocity analysis on CMP gathers;
- normal moveout (NMO) correction and CMP stacking;
- deconvolution;
- time migration.

Time oriented processing — although it may be appropriate for processing of 90% of the acquired data — will not suffice in the search and evaluation of geologically complicated hydrocarbon accumulations.

Therefore there is nowadays an increasing awareness that the emphasis in seismic data processing should be redirected from a time-oriented approach to a depth-oriented approach.

The aim of seismic data acquisition and processing (and interpretation) can therefore be defined as:

“To obtain a detailed, high resolution subsurface image in terms of a correctly positioned, true amplitude reflectivity. The reflectivity information can then be used to arrive at the rock and pore parameters”.

The laboratory of seismic and acoustics of the Delft University of Technology has played a leading role in reformulation of seismic data processing in terms of depth technology. It was in fact the main goal behind the organizing of their Triton consortium (Triton research proposal, 1985). More precisely, the Triton project aimed at the development of a new depth-oriented technology for the processing of seismic data in two and three dimensions. These developments have led to the formulation of three methods, that all transform prestack data into zero-offset data. The methods are depicted in figure 3. They will be discussed in the following chapters. The CMP stacking scheme is the conventional route.

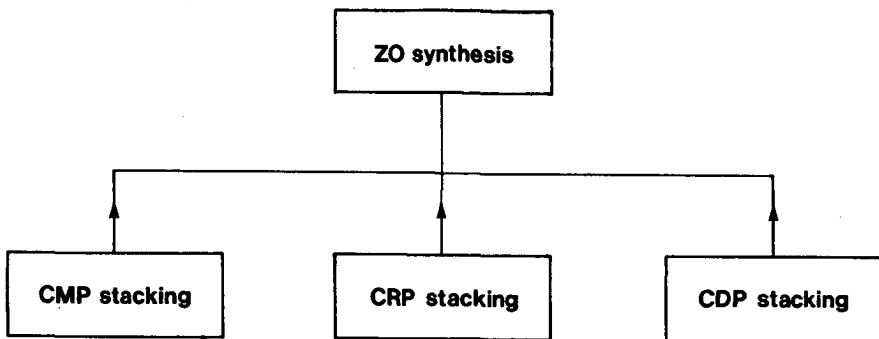


Figure 3 Three processing schemes that transform multi-offset measurements into zero-offset (ZO) data.

In the Triton research project CRP and CDP stacking in both 2-D and 3-D have been studied. The main characteristics of CRP and CDP stacking can be summarized as follows:

- stacking velocity distributions are replaced by geologically oriented macro interval velocity models;
- single-dip normal moveout (NMO) correction is replaced by multi-dip NMO correction combined with compensation for reflecton point smear (CRP) or, even better, downward extrapolation (CDP);
- common midpoint (CMP) stacking is replaced by common reflection point (CRP) stacking or, even better, true common depth point (CDP) stacking.

A problem — in particular with 3-D data — is that 3-D shot record migration followed by genuine CDP stacking is very elaborate. Even for the fastest current computer systems, application of full multi-offset depth processing schemes in 3-D is not yet realistic. However, instead of turning to simplified algorithms, a target-oriented processing approach was proposed for the Triton project. By limiting the output of multi-offset depth processing to a detailed reflectivity of the target zone only, the method becomes feasible (Kinneging, 1989). Target-oriented processing consists of three basic steps (see figure 4):

– Redatuming:

Non-recursive extrapolation of the downgoing source wave field and the upgoing reflected wave field from the acquisition surface to the upper boundary of the target zone;

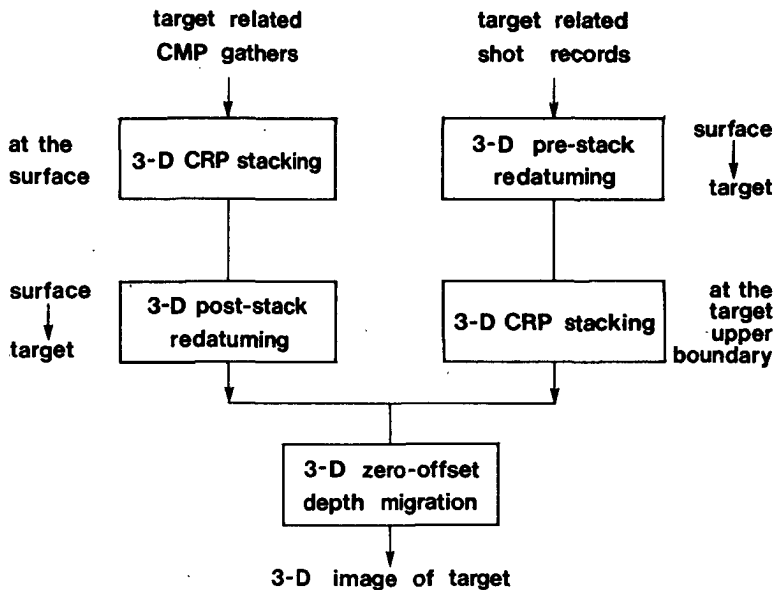


Figure 4 Target oriented processing.

– CRP (or CMP) stacking at the target upper boundary:

After extrapolation new shot records are constructed, followed by CRP (or CMP) stacking for the synthesis of zero-offset data;

– Zero-offset migration:

After stacking full 3-D zero offset depth migration within the target zone.

In case of less complicated media an alternative route may be followed. This route — also depicted in figure 4 — contains common reflection point stacking at the surface, followed by 3-D poststack redatuming and finally full zero-offset depth migration.

The latter procedure is less general than the prestack redatuming procedure, but on the other hand computationally far less intensive. Macro model based common reflection point stacking is the subject of this thesis.

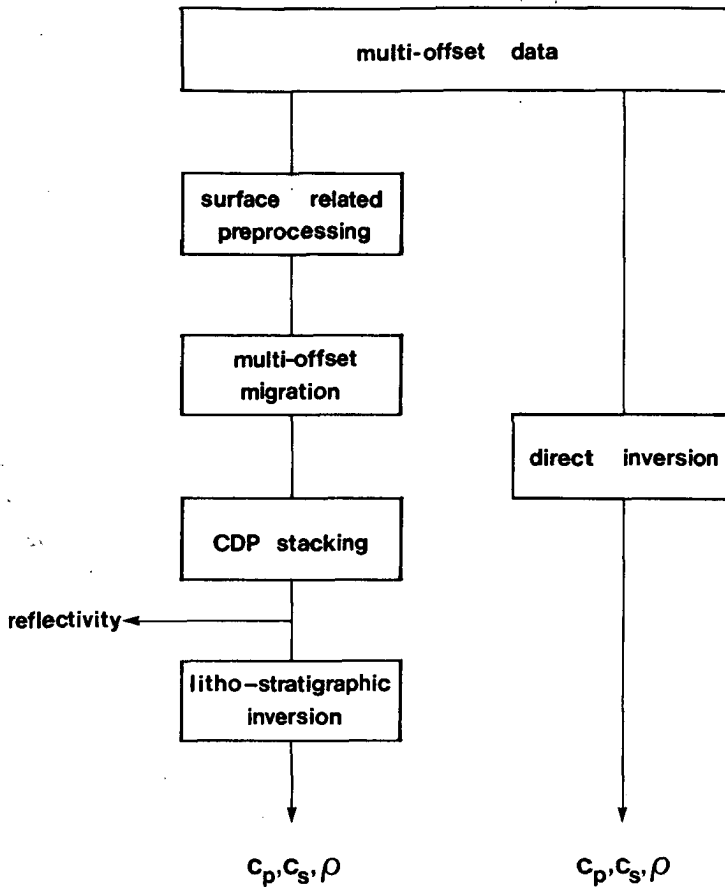


Figure 5 Two approaches to determine elastic subsurface parameters.

A macro model is defined as an interval-velocity versus depth model of the subsurface which contains the information necessary to describe the propagation effects of waves travelling through the subsurface. Details which describe the reflectivity properties are not included in the macro model description. These details are obtained by applying a depth migration scheme to the data, using the macro model.

An entirely different solution to the problems of seismic data processing is the inverse scattering approach. In its most general formulation this approach attempts to estimate directly the elastic subsurface parameters (Tarantola, 1986). Schemes for this approach are not yet commercially available.

Summarizing, we may distinguish two approaches, see figure 5. The first approach, which has been introduced by the Triton and Delphi consortia (Delphi research proposal, 1988), is a four-step procedure. First surface related preprocessing is applied. Secondly the multi-offset data is migrated and — thirdly — subsequently stacked to arrive at a definition of the angle-dependent reflectivity of the subsurface. Fourthly the data is inverted to end up with the detailed p- and s-wave velocity and density.

The other approach is the inverse scattering approach.

A discussion of the inverse scattering approach in general and the differences between the two approaches presented in figure 5 is beyond the scope of this dissertation. The interested reader is referred to the literature (Tarantola, 1986; Duijndam, 1987; Berkhout, 1984)

THE OUTLINE OF THIS THESIS

In chapter I, a general introduction to seismic data processing is given. The three main techniques currently available and applied will be discussed from a theoretical point of view. The aim is to relate the CRP technique to the alternative CMP and CDP techniques.

In chapter II, an introduction to CRP stacking in constant velocity media — which is also known as dip moveout (DMO) — is given, based on the literature on DMO. Several proposed DMO schemes will be discussed.

Chapter III gives an alternative description of CRP stacking in constant velocity media. This description leads to chapter IV, which deals with CRP stacking in inhomogeneous media. Chapter IV forms the heart of this thesis. First the theory is given. Next ample attention is paid to synthetic data examples. Those examples will show the characteristics of CRP processing, and give comparisons with the CMP and CDP techniques. In chapter V a real data example is used to compare the CMP, CRP and CDP techniques. In chapter VI some ideas about CRP stacking in three dimensions are presented.

A COMPARATIVE OVERVIEW OF CMP, CRP AND CDP PROCESSING

I.1 INTRODUCTION

As mentioned in the introduction chapter, in today's seismic data processing three main approaches are available and feasible. Those approaches — depicted in figure I.1 — may function as different branches in a processing scheme, which starts with preprocessing of the seismic data and leads to a bandlimited reflectivity image of the subsurface, either in time or in depth.

Conventional preprocessing may contain — but is not restricted to — demultiplexing, time-variant single trace filtering, velocity filtering in the shot- and receiver domain, static correction, wavelet and/or statistical deconvolution. Depending on the specific branch to be followed spherical divergence correction, compensation of inelastic losses and CMP sorting could also be included.

The CMP method includes the conventional processing of single-dip NMO followed by common midpoint stacking. The method is robust but dip-selective and the reflection point is smeared, see figure I.2. However, as can be observed the travelttime compensation before stack is correct for the selected dip.

The CRP technique — for homogeneous media also called the DMO method — is, for one CMP gather, visualized in figure I.2e. In the CRP method the main disadvantages of the CMP technique (dip-selectivity and the reflection point smearing) are addressed. As can be

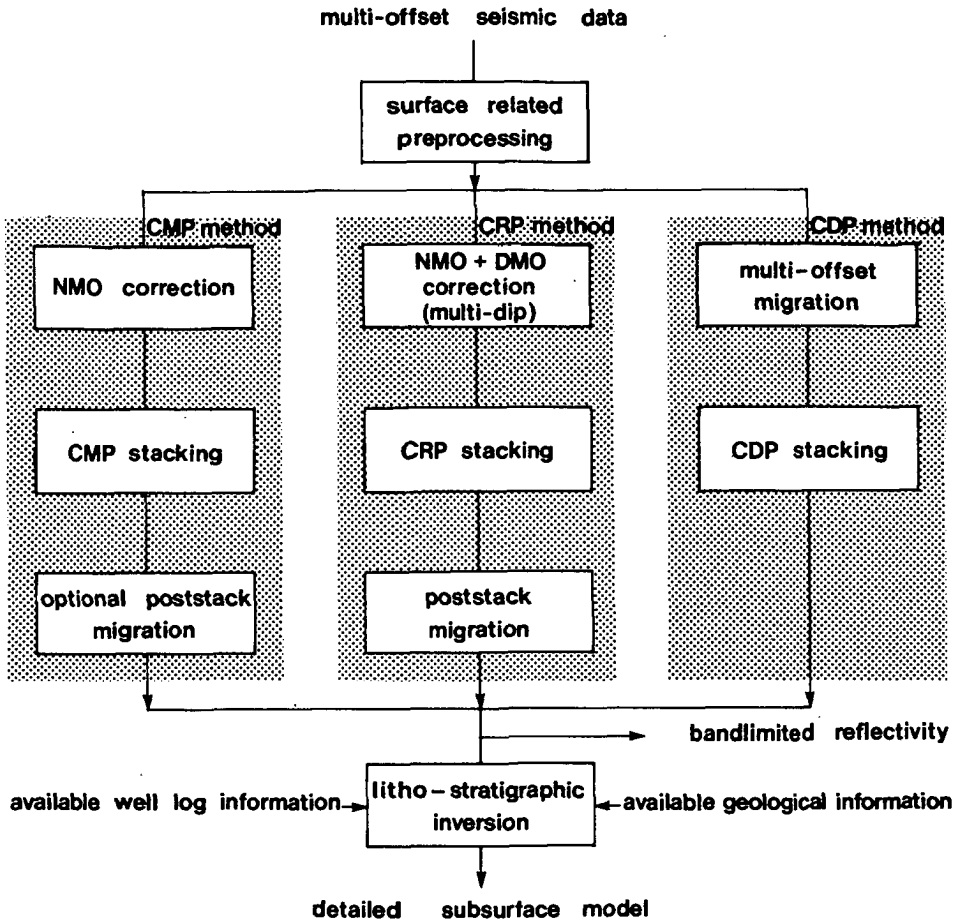


Figure I.1 Seismic data processing aims at transforming multi-offset data into a bandlimited reflectivity image of the subsurface, optionally followed by inversion (Berkhout, 1985).

seen in figure I.2e, the reflection events from both the dipping and the horizontal reflector have now been corrected properly.

The CDP method is the full prestack migration — i.e. — accomplished by single shot record migration. The CDP method is the only applicable technique when the hyperbolic moveout assumption is not valid (i.e. when media become arbitrarily complicated). An example from one shot record before and after migration is shown in figure I.3.

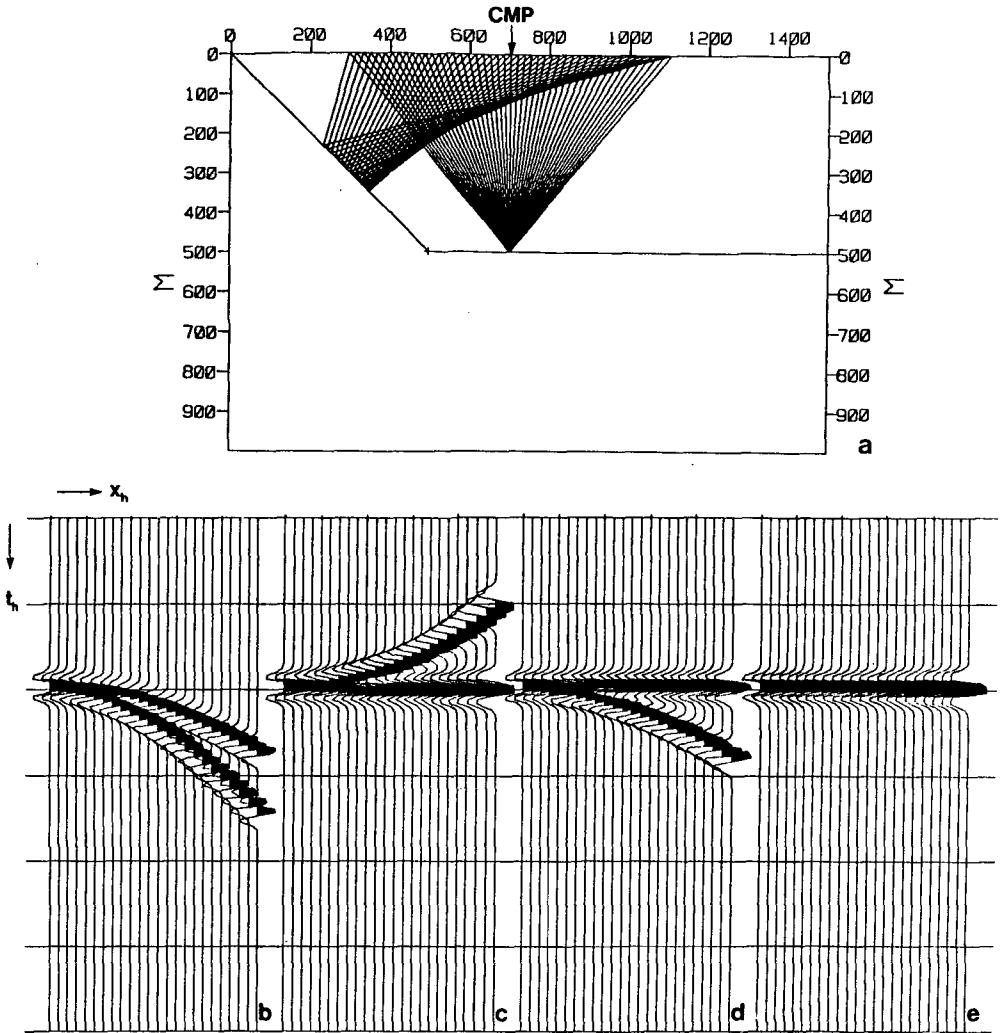


Figure I.2 Simple subsurface geometry, showing raypaths and data acquired for one CMP gather. The velocity of the overburden is homogeneous. Note that no diffraction energy has been modelled.

- a. geometry and raypaths.
- b. CMP gather, uncorrected traveltimes.
- c. CMP gather, NMO correction for horizontal reflector.
- d. CMP gather, NMO correction for dipping reflector.
- e. CRP processing, one gather of zero-offset traces related to the same surface point is shown.

Note that x_h refers to the original offset; note also that figure e shows two superimposed CRP gathers.

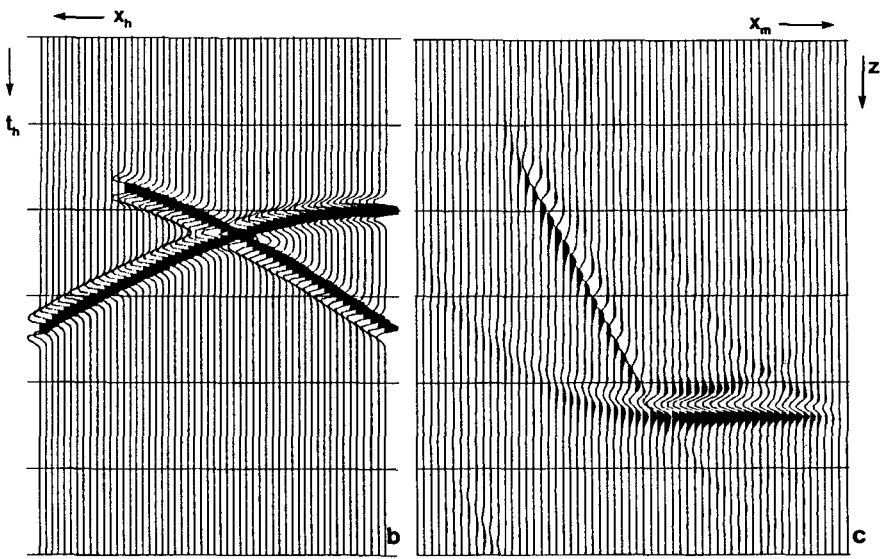
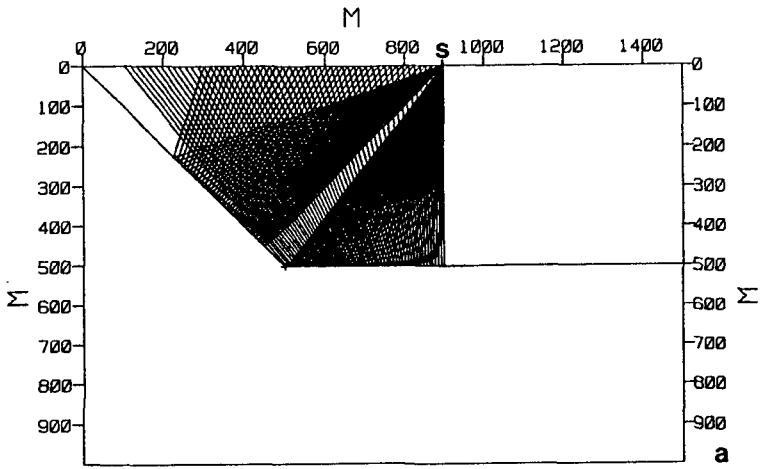


Figure 1.3 The same subsurface geometry as depicted in figure 1.2. No diffraction energy has been modelled.

- a. geometry and raypaths for one shot record.
- b. shot record, unmigrated.
- c. shot record, migrated.

Note, that going from left to right in figure I.1, the methods become more sophisticated and are based on fewer assumptions and/or approximations. However, the methods also become less robust, more complicated and computationally more intensive.

In the course of this dissertation the typical properties of these three methods will be made clear.

In this chapter we will study the relation between CMP, CRP and CDP processing. The double square root (DSR) equation — that is the one-way wave equation for constant velocity media, formulated in the double Fourier domain — will be used as a starting point. CMP and CRP processing schemes will be described in terms of different approximations to the DSR equation.

The theory presented here is partly a summary of the existing literature. Several authors, Yilmaz (1979), Deregowski (1981), Hale (1983) and Berkhout (1984) a.o. have published about the DSR equation.

I.2 WAVE THEORETICAL DESCRIPTION OF CMP, CRP AND CDP PROCESSING

I.2.1 The double square root equation

In this section we present a wave theoretical description of CMP, CRP and CDP processing. We will use a vector notation to represent a monochromatic shot record, following Berkhout (1984). If $P_i^-(x_n, z_0, \omega_m)$ represents the monochromatic response (in terms of one complex-valued number) at detector position (x_n, z_0) due to the i th source position — see figure I.4 —, then the monochromatic seismic data vector $\vec{P}_i^-(z_0)$ is defined as

$$\vec{P}_i^-(z_0) = \begin{pmatrix} P_i^-(x_0, z_0, \omega_m) \\ P_i^-(x_1, z_0, \omega_m) \\ \vdots \\ P_i^-(x_N, z_0, \omega_m) \end{pmatrix}, \quad (I.1)$$

where $z = z_0$ represents the data acquisition plane. By combining all seismic data vectors in a matrix,

$$P^-(z_0) = \left(\vec{P}_1^-(z_0), \vec{P}_2^-(z_0), \dots, \vec{P}_I^-(z_0) \right), \quad (I.2)$$

the i th column containing the elements of the i th shot record, then the monochromatic seismic data matrix is obtained for frequency component ω_m .

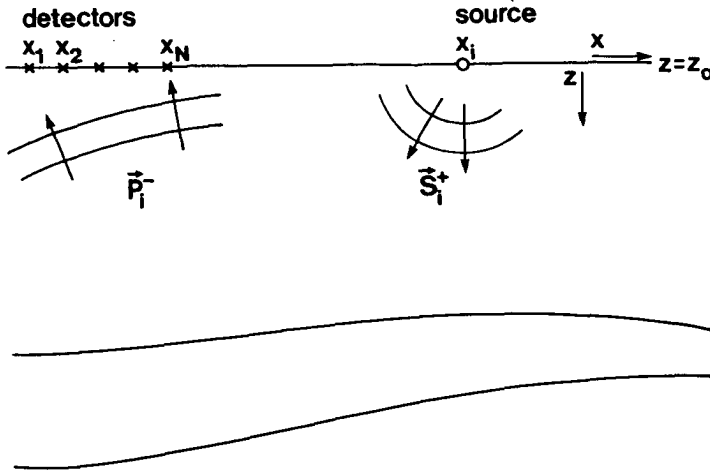


Figure I.4 Seismic experiment. Indicated is a seismic source vector \vec{S}_i^+ and a reflected wavefield \vec{P}_i^- being detected by detectors at x_0, x_1, \dots, x_N .

Within the data matrix different data gathers can be indicated (see also figure I.5):

- one column : one common source point gather, or shot record
- one row : one common receiver point gather
- the main diagonal : zero offset gather
- one sub diagonal : one common offset gather
- one anti diagonal : one common midpoint gather

Note, that if sources and receivers have the same directivity property then, according to the principle of reciprocity,

$$\mathbf{P}^-(z_0) = \left[\mathbf{P}^-(z_0) \right]^T, \tag{I.3}$$

“T” meaning that rows and columns should be interchanged. Note, that in practice the data matrix is never completely filled. The usefulness of the matrix notation will easily be appreciated if we understand the relation between matrix multiplication and convolution. The convolution process is frequently applied in different stages of seismic data processing. If a convolution process is applied to an input data series then each input sample is replaced by a weighted sum applied to this input sample and its neighbours, the weighting factors being determined by the convolution operator. For example, using the convolutional model, a seismic data trace can be described by

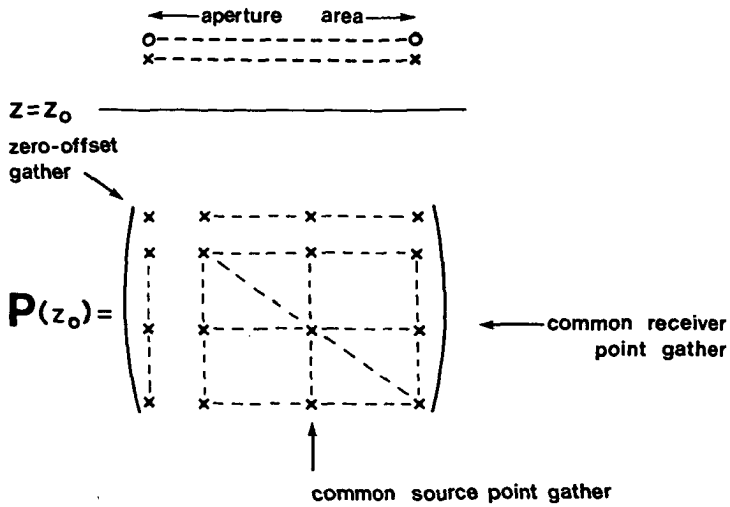


Figure I.5 Monochromatic data matrix.

$$s(t_n) = \sum_m w(t_n - m\Delta\tau) r(m\Delta\tau) \quad , \quad (I.4)$$

where $t_n = n\Delta t$.

As convolution defines a weighted sum per output sample the matrix notation is preeminently suited to describe the convolution process. Taking $M = N$ and $\Delta t = \Delta\tau$:

$$\begin{pmatrix} s(0) \\ s(\Delta t) \\ \cdot \\ \cdot \\ s(N\Delta t) \end{pmatrix} = \begin{pmatrix} x & \dots & x \\ x & \dots & \dots & x \\ \cdot & & & \\ \cdot & & & \\ x & \dots & \dots & x \\ x & \dots & x \end{pmatrix} \begin{pmatrix} r(0) \\ r(\Delta t) \\ \cdot \\ \cdot \\ r(N\Delta t) \end{pmatrix} \quad , \quad (I.5)$$

or, symbolically,

$$\vec{s} = \mathbf{W} \vec{r} \quad , \quad (I.6)$$

where the n th row of \mathbf{W} contains the samples of operator $w(t_n - m\Delta\tau)$ for all m , and the m th column of \mathbf{W} contains the samples of wavelet $w(n\Delta t - \tau_m)$ for all n . Note that the m th column may be considered as the impulse response due to $\delta(t - \tau_m)$. For a time invariant convolution operator the impulse response is independent of m , which means that the

elements on one diagonal of \mathbf{W} are all equal. On the other hand, for a time variant convolution operator the elements on one diagonal of \mathbf{W} will not be equal.

Using the matrix notation explained above, an elegant expression can be obtained for the discrete measurements of one seismic experiment, that is the data of one shot record. As pointed out already, the formulation is a monochromatic one (the circular frequency ω is a parameter).

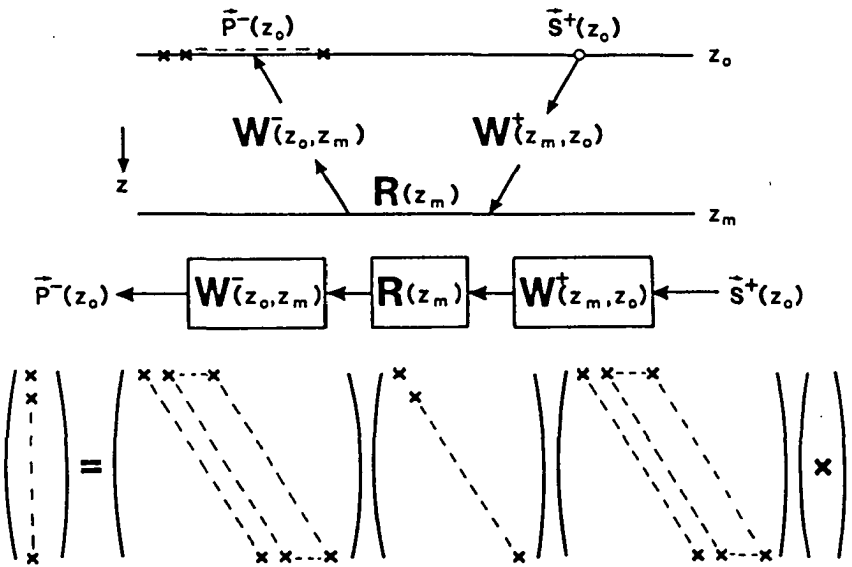


Figure I.6 Basic model for the seismic response from depth level $z = z_m$ (no field patterns, homogeneous surface).

The basic model is depicted in figure I.6. Reflection from only one interface is considered. The figure gives a schematic illustration of the acoustic forward (that is modelling) process which appeals well to physical intuition and contains the essentials of any echo technique:

1. illumination with a source field given by vector \vec{S}_1^+ ;
2. downward propagation given by matrix \mathbf{W}^+
3. reflection given by matrix \mathbf{R}
4. upward propagation given by matrix \mathbf{W}^-
5. detection of a wave field given by vector \vec{P}_1^- .

In figure I.6 only one source position is indicated, giving one shot record. Extending this shot record model to a multi-record data set can easily be done by extending the vectors \vec{S}_i^+ and \vec{P}_i^- to matrices $S^+(z_0)$ and $P^-(z_0)$ respectively.

Summarizing, for one shot record the model depicted in figure I.6 reads as follows (we consider one depth level only):

$$\vec{P}_i^-(z_0) = W^-(z_0, z_m) R(z_m) W^+(z_m, z_0) \vec{S}_i^+(z_0) \quad , \quad (I.7)$$

whereas for a multi-record data set the model reads

$$P^-(z_0) = W^-(z_0, z_m) R(z_m) W^+(z_m, z_0) S^+(z_0) \quad . \quad (I.8)$$

If we assume no lateral velocity variations, then the matrix description can be replaced by a convolution along the source coordinate followed by a convolution along the receiver coordinate (compare expressions (I.4) and (I.6)). We also assume for the sake of simplicity the source matrix to be equal to the unity matrix. Rewriting (I.8) in terms of convolutions leads then to

$$P_i^-(x_s, x_d, z_0, \omega) = W_d^-(x_d, \Delta z, \omega) *_{d} R(x_s, x_d, z_m, \omega) *_{s} W_s^+(x_s, \Delta z, \omega) \quad . \quad (I.9)$$

The symbols “*_s” and “*_d” denote a spatial convolution over the source and detector coordinate respectively, and Δz is equal to $|z_0 - z_m|$.

In the wavenumber-frequency domain expression (I.9) reads

$$\tilde{P}_i^-(k_s, k_d, z_0, \omega) = \tilde{W}_d^-(k_d, \Delta z, \omega) \tilde{R}(k_s, k_d, z_m, \omega) \tilde{W}_s^+(k_s, \Delta z, \omega) \quad . \quad (I.10)$$

The transformation to the wavenumber-frequency domain assumes the velocity laterally constant. Note also, that we still consider the response from one depth level only.

From expression (I.10) it can be seen that determination of $\tilde{R}(k_s, k_d, z_m, \omega)$, that is the reflectivity at depth level $z_0 + \Delta z$, is obtained by inverting for the propagation operators \tilde{W} :

$$\langle \tilde{R}(k_s, k_d, z_m, \omega) \rangle = \left[\tilde{W}_d^-(k_d, \Delta z, \omega) \right]^{-1} \tilde{P}_i^-(k_s, k_d, z_0, \omega) \left[\tilde{W}_s^+(k_s, \Delta z, \omega) \right]^{-1} \quad , \quad (I.11)$$

(when $\langle \tilde{R}(k_s, k_d, z_m, \omega) \rangle$ still contains reflectivity information from other depth levels — which is always the case in practice — the reflectivity information for the current depth level z_m can be obtained by integrating over all frequencies. This is called the imaging principle).

If we define the inverse operators as $\tilde{F}_d^-(k_d, \Delta z, \omega)$ and $\tilde{F}_s^+(k_s, \Delta z, \omega)$ respectively we arrive at expression

$$\langle \tilde{R}(k_s, k_d, z_m, \omega) \rangle = \tilde{F}_d^-(k_d, \Delta z, \omega) \tilde{P}_i^-(k_s, k_d, z_0, \omega) \tilde{F}_s^+(k_s, \Delta z, \omega) \quad . \quad (I.12)$$

The derivation of the extrapolation operators \tilde{F} can be accomplished using the scalar wave equation.

The scalar wave equation, which describes the propagation of a compressional wavefield $p(x,z,t)$ in a medium with velocity $c(x,z)$ and a constant material density, is given by

$$\left[\frac{\partial^2}{\partial x^2} + \frac{\partial^2}{\partial z^2} - \frac{1}{c^2} \frac{\partial^2}{\partial t^2} \right] p(x,z,t) = 0 \quad , \quad (I.13)$$

where x denotes the horizontal spatial coordinate and z denotes the depth.

Before we proceed we first define the forward and inverse Fourier transforms for temporal and spatial transients.

For a temporal coordinate the Fourier transform pair is defined as

$$P(x,z,\omega) = \int_{-\infty}^{+\infty} p(x,z,t) e^{-j\omega t} dt \quad (I.14a)$$

and

$$p(x,z,t) = \frac{1}{2\pi} \int_{-\infty}^{+\infty} P(x,z,\omega) e^{+j\omega t} d\omega \quad . \quad (I.14b)$$

For a spatial coordinate the Fourier transform pair reads

$$\tilde{P}(k_x,z,\omega) = \int_{-\infty}^{+\infty} P(x,z,\omega) e^{+jk_x x} dx \quad (I.14c)$$

and

$$P(x,z,\omega) = \frac{1}{2\pi} \int_{-\infty}^{+\infty} \tilde{P}(k_x,z,\omega) e^{-jk_x x} dk_x \quad . \quad (I.14d)$$

We now assume that the medium velocity can only vary as a function of depth z :

$$c = c(z) \quad . \quad (I.15)$$

Using expressions (I.15) and (I.14a–d), the wave equation (I.13) can be transformed to the following expression:

$$\frac{\partial^2}{\partial z^2} \tilde{P}(k_x,z,\omega) + \left(\frac{\omega^2}{c(z)^2} - k_x^2 \right) \tilde{P}(k_x,z,\omega) = 0 \quad . \quad (I.16)$$

For $c = \text{constant}$ the downgoing (or forward travelling) wave solution to (I.16) is given by

$$\tilde{P}^+(k_x, z, \omega) = \tilde{P}^+(k_x, 0, \omega) \exp \left[-j \left(\frac{\omega^2}{c^2} - k_x^2 \right)^{1/2} z \right]. \quad (I.17)$$

This is also the solution to the one-way wave equation (Berkhout, 1984)

$$\frac{\partial}{\partial z} \tilde{P}^+(k_x, z, \omega) = -j \left(\frac{\omega^2}{c^2} - k_x^2 \right)^{1/2} \tilde{P}^+(k_x, z, \omega). \quad (I.18)$$

Expression (I.17) can be rewritten as

$$\tilde{P}^+(k_x, z, \omega) = \tilde{W}^+(k_x, z, \omega) \tilde{P}^+(k_x, 0, \omega) \quad (I.19a)$$

with

$$\tilde{W}^+(k_x, z, \omega) = \exp \left[-j \left(k^2 - k_x^2 \right)^{1/2} z \right] \quad (I.19b)$$

and

$$k = \frac{\omega}{c}. \quad (I.20)$$

\tilde{W}^+ is the forward extrapolation operator.

From this result we conclude that the forward extrapolation operators in expression (I.10) — which describes the seismic experiment in the wavenumber-frequency domain — should be defined as follows

$$\tilde{W}_d^-(k_d, \Delta z, \omega) = \exp \left[-jk \sqrt{1 - \left(\frac{k_d}{k} \right)^2} \Delta z \right], \quad k_d^2 \leq k^2 \quad (I.21a)$$

$$\tilde{W}_d^-(k_d, \Delta z, \omega) = \exp \left[-k \sqrt{\left(\frac{k_d}{k} \right)^2 - 1} \Delta z \right], \quad k_d^2 > k^2 \quad (I.21b)$$

$$\tilde{W}_s^+(k_s, \Delta z, \omega) = \exp \left[-jk \sqrt{1 - \left(\frac{k_s}{k} \right)^2} \Delta z \right], \quad k_s^2 \leq k^2 \quad (I.21c)$$

and

$$\tilde{W}_s^+(k_s, \Delta z, \omega) = \exp \left[-k \sqrt{\left(\frac{k_s}{k} \right)^2 - 1} \Delta z \right], \quad k_s^2 > k^2. \quad (I.21d)$$

The wavenumbers $k_d^2 > k^2$ and $k_s^2 > k^2$ define the so called evanescent field. Evanescent waves will not be considered here. Note that the total propagation effect (extrapolation) is described by two square root operators (I.21a) and (I.21c). These operators can be combined to form one operator:

$$\tilde{W}_d^-(k_d, \Delta z, \omega) \tilde{W}_s^+(k_s, \Delta z, \omega) = \exp \left[-jk \left(\sqrt{1 - \left(\frac{k_d}{k}\right)^2} + \sqrt{1 - \left(\frac{k_s}{k}\right)^2} \right) \Delta z \right] \quad (I.22)$$

Equation (I.22) describes the modelling or forward extrapolation.

Inverse extrapolation operators can be defined — in accordance with (I.11) and (I.12) — as the inverse of the forward extrapolation operators (I.21a–d):

$$\tilde{F}_d^-(k_d, \Delta z, \omega) = 1 / \tilde{W}_d^-(k_d, \Delta z, \omega) \quad (I.23a)$$

and

$$\tilde{F}_s^+(k_s, \Delta z, \omega) = 1 / \tilde{W}_s^+(k_s, \Delta z, \omega) \quad (I.23b)$$

Since these operators are not stable — due to exponential increase — for $k_d^2 > k^2$ or $k_s^2 > k^2$, we choose \tilde{F} to be the matched filter of \tilde{W} :

$$\tilde{F}_d^-(k_d, \Delta z, \omega) = \left[\tilde{W}_d^-(k_d, \Delta z, \omega) \right]^* \quad (I.24a)$$

and

$$\tilde{F}_s^+(k_s, \Delta z, \omega) = \left[\tilde{W}_s^+(k_s, \Delta z, \omega) \right]^* \quad (I.24b)$$

The asterisk indicates the complex conjugate.

For details about the choice for a matched filter approach, the reader is referred to Berkhout (1984).

In other words, \tilde{F} is now defined as follows:

$$\tilde{F}_d^-(k_d, \Delta z, \omega) = \exp \left[+jk \sqrt{1 - \left(\frac{k_d}{k}\right)^2} \Delta z \right], \quad k_d^2 \leq k^2 \quad (I.25a)$$

$$\tilde{F}_d^-(k_d, \Delta z, \omega) = \exp \left[-k \sqrt{\left(\frac{k_d}{k}\right)^2 - 1} \Delta z \right], \quad k_d^2 > k^2 \quad (I.25b)$$

and

$$\tilde{F}_s^+(k_s, \Delta z, \omega) = \exp \left[+jk \sqrt{1 - \left(\frac{k_s}{k}\right)^2} \Delta z \right], \quad k_s^2 \leq k^2 \quad (I.25c)$$

$$\tilde{F}_s^+(k_s, \Delta z, \omega) = \exp \left[-k \sqrt{\left(\frac{k_s}{k}\right)^2 - 1} \Delta z \right], \quad k_s^2 > k^2 \quad (I.25d)$$

Let us again restrict ourselves to travelling waves only. Then, the inverse extrapolation operator, which describes the full prestack migration process in the shot-receiver wavenumber and frequency domain, can be described as

$$\tilde{F}(k_s, k_d, \Delta z, \omega) = \left[\tilde{W}_d^-(k_d, \Delta z, \omega) \tilde{W}_s^+(k_s, \Delta z, \omega) \right]^* \quad (I.26a)$$

$$= \left[\tilde{W}_d^-(k_d, \Delta z, \omega) \right]^* \left[\tilde{W}_s^+(k_s, \Delta z, \omega) \right]^* \quad (I.26b)$$

Summarizing the results obtained sofar, we recognize two basic steps in the inverse extrapolation or downward continuation of a multi-record data set, defined in the shot-receiver domain:

1. Inverse wavefield extrapolation for the upward propagating wavefield;
2. Inverse wavefield extrapolation for the downward propagating wavefield.

We have three alternative descriptions of the downward continuation procedure, which read as follows:

1. A multiplication in the (k_s, k_d, ω) -domain according to

$$\tilde{F}_d^-(k_d, \Delta z, \omega) \tilde{P}^-(k_s, k_d, z_0, \omega) \tilde{F}_s^+(k_s, \Delta z, \omega) \quad ,$$

see figure I.8.

2. A double convolution operation in the (x_s, x_d, ω) -domain, see figure I.8 according to a lateral deconvolution of shot records

$$F_d^-(x_d, \Delta z, \omega) *_{d} P^-(x_s, x_d, z_0, \omega)$$

followed by a lateral deconvolution of detector gathers

$$\left[F_d^-(x_d, \Delta z, \omega) *_{d} P^-(x_s, x_d, z_0, \omega) \right] *_{s} F_s^+(x_s, \Delta z, \omega) \quad ,$$

see figures I.7 and I.8.

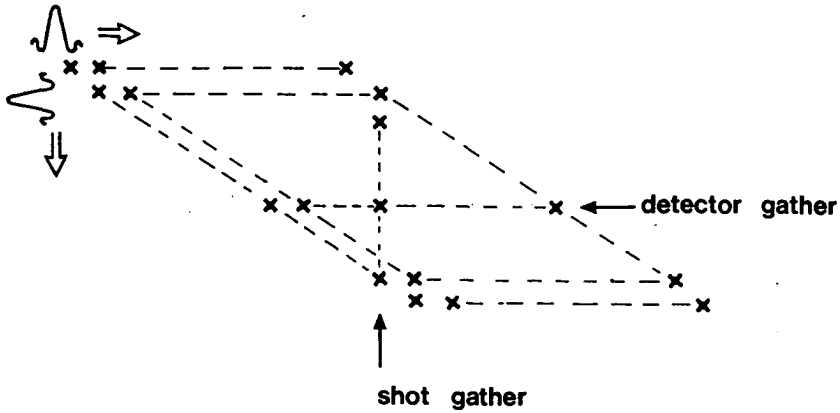


Figure I.7 Full prestack extrapolation can be carried out as a set of independent convolutions in the source-detector space.

3. A matrix multiplication in the (x_s, x_d, ω) -domain yielding

$$\mathbf{F}^-(z_m, z_0) \mathbf{P}^-(z_0) \mathbf{F}^+(z_0, z_m) \quad ,$$

where again $\Delta z = |z_m - z_0|$.

Prestack migration consists of two basic steps, viz. downward continuation of the wavefields, followed by imaging. Imaging at the depth level of downward continuation implies selection of the zero offset data at time zero at this depth level.

A CDP processing scheme for prestack migration in the shot-receiver spatial and wavenumber domain is illustrated by a flow diagram in figure I.8.

Combining equation (I.26a,b) with (I.22) results in

$$\tilde{\mathbf{F}}^-(k_s, k_d, \Delta z, \omega) = \exp \left\{ +jk \left[\sqrt{1 - \left(\frac{k_d}{k}\right)^2} + \sqrt{1 - \left(\frac{k_s}{k}\right)^2} \right] \Delta z \right\} \quad . \quad (\text{I.27a})$$

This operator is known in the literature (e.g. Yilmaz, 1979) as the Double Square Root (DSR) operator. The DSR operator is the solution to the DSR equation, that is the one way wave equation in the shot-geophone space. This equation reads

$$\frac{\partial}{\partial z} \tilde{\mathbf{P}}^-(k_s, k_d, z, \omega) = \left\{ +jkz \left[\sqrt{1 - \left(\frac{k_d}{k}\right)^2} + \sqrt{1 - \left(\frac{k_s}{k}\right)^2} \right] \right\} \tilde{\mathbf{P}}^-(k_s, k_d, z, \omega) \quad . \quad (\text{I.27b})$$

The DSR operator downward continues the shots and receivers into the earth, thus transforming the data as if it were measured at another depth level inside the earth.

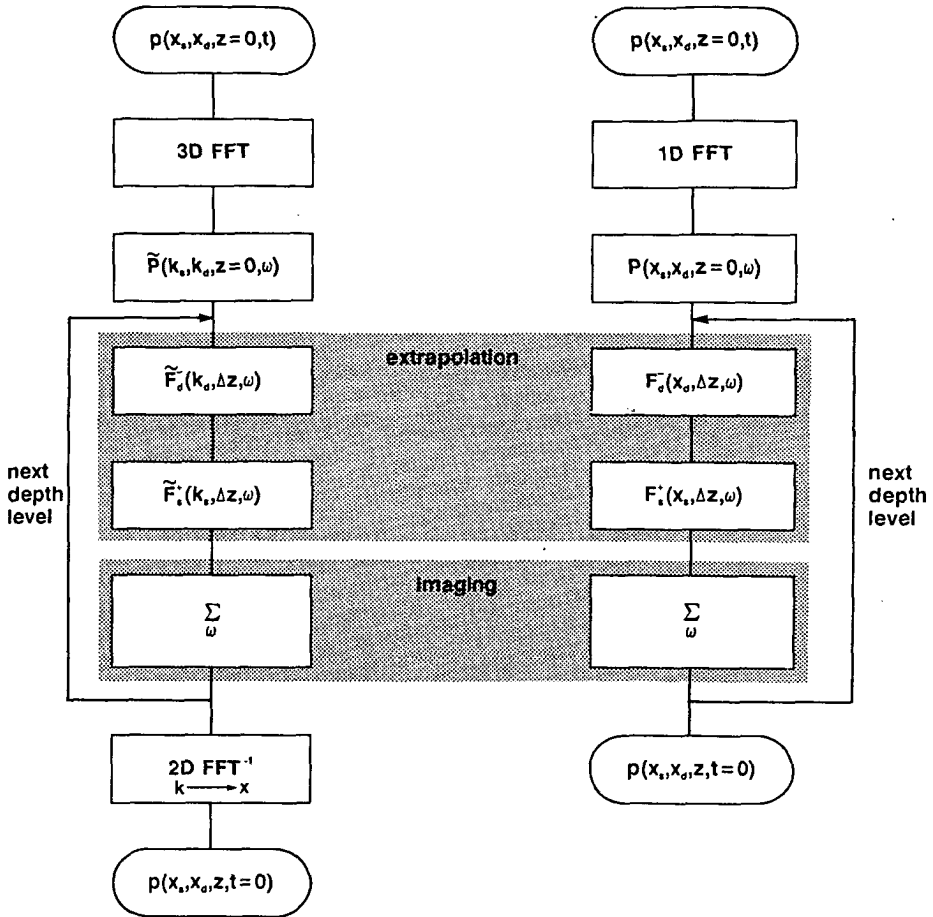


Figure I.8 CDP processing scheme in the shot and receiver wavenumber (figure a) and spatial (figure b) domain respectively.

Let us now consider the midpoint-offset coordinate system (see figure I.9).

We introduce midpoint x_m and half-offset x_h coordinates according to

$$x_m = \frac{1}{2}(x_d + x_s) \tag{I.28a}$$

$$x_h = \frac{1}{2}(x_d - x_s) \tag{I.28b}$$

Since wavefields do not change under a coordinate transformation, we can write

$$p(x_s, x_d, z, t) = p'(x_m, x_h, z, t) \quad , \quad (I.29)$$

where z and t are invariant under the coordinate transformation. Bearing in mind that ∂_x transforms to $-jk_x$ in the wavenumber domain, we use expressions (I.28a,b) and (I.29) to arrive at a relation between shot-geophone wavenumbers and midpoint-offset wavenumbers.

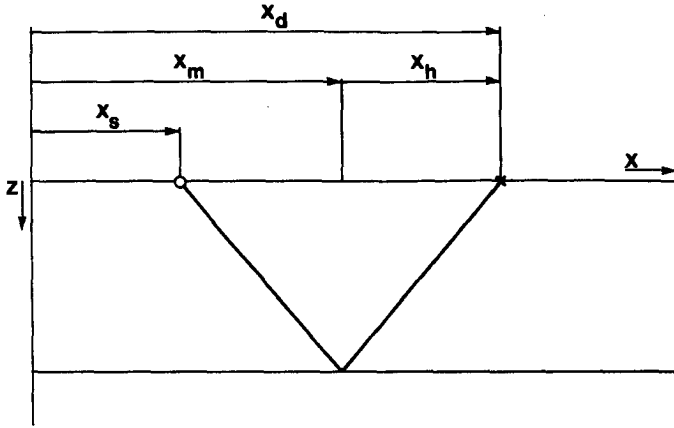


Figure I.9 Definition of shot-geophone (or source-detector) coordinates and midpoint-offset coordinates.

Applying the chain rule for differentiation to equation (I.29) yields

$$\frac{\partial p}{\partial x_s} = \frac{\partial p'}{\partial x_m} \frac{\partial x_m}{\partial x_s} + \frac{\partial p'}{\partial x_h} \frac{\partial x_h}{\partial x_s} \quad (I.30a)$$

and

$$\frac{\partial p}{\partial x_d} = \frac{\partial p'}{\partial x_m} \frac{\partial x_m}{\partial x_d} + \frac{\partial p'}{\partial x_h} \frac{\partial x_h}{\partial x_d} \quad (I.30b)$$

Using expressions (I.28a,b) we see that

$$\frac{\partial x_m}{\partial x_s} = \frac{1}{2} ; \quad \frac{\partial x_m}{\partial x_d} = \frac{1}{2} \quad (I.31a,b)$$

$$\frac{\partial x_h}{\partial x_s} = -\frac{1}{2} ; \quad \frac{\partial x_h}{\partial x_d} = \frac{1}{2} \quad (I.31c,d)$$

Substitution of expressions (I.31a-d) into (I.30a,b), Fourier transforming both sides of the resulting expression and finally using (I.29) to cancel $p=p'$, leads to the midpoint-offset wavenumbers in terms of shot-receiver wavenumbers:

$$k_d = \frac{1}{2} (k_m + k_h) \tag{I.32a}$$

$$k_s = \frac{1}{2} (k_m - k_h) \tag{I.32b}$$

The wavenumbers k_d , k_s , k_m and k_h are related to the spatial coordinates x_d , x_s , x_m and x_h respectively.

The latter result means, that expression (I.27a) can be rewritten:

$$\tilde{F}(k_m, k_h, \Delta z, \omega) = \exp \left\{ +jk \left[\sqrt{1 - \left(\frac{k_m + k_h}{2k} \right)^2} + \sqrt{1 - \left(\frac{k_m - k_h}{2k} \right)^2} \right] \Delta z \right\} \tag{I.33}$$

Note, that in this expression both square roots are dependent on the midpoint and offset wavenumbers. In other words:

$$\tilde{F}(k_m, k_h, \Delta z, \omega) \neq \tilde{F}(k_m, k_h = 0, \Delta z, \omega) \tilde{F}(k_m = 0, k_h, \Delta z, \omega) \tag{I.34}$$

for all k_m and k_h values not equal to zero.

We conclude that full 2-D prestack extrapolation can not be carried out by two independent one-dimensional convolutions along the midpoint and offset coordinates, see figure I.10.

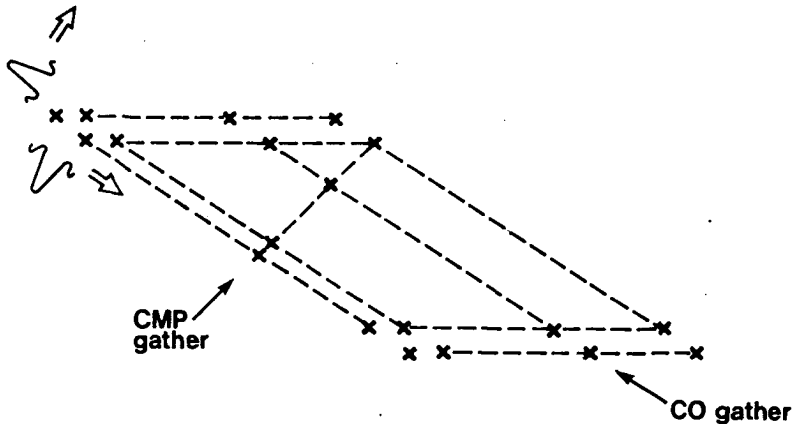


Figure I.10 Full prestack extrapolation by a set of independent convolutions in the midpoint-offset space necessarily involves approximations.

For small wavenumbers (e.g. small dips both in midpoint and offset space), relation (I.33) can be approximated by:

$$\tilde{F}(k_m, k_h, \Delta z, \omega) \approx \exp \left\{ +jk \left[\sqrt{1 - \frac{1}{2} \left(\frac{k_m}{k} \right)^2} + \sqrt{1 - \frac{1}{2} \left(\frac{k_h}{k} \right)^2} \right] \Delta z \right\} \quad (\text{I.35a})$$

$$= \tilde{F}_m(k_m, \Delta z, \omega) \tilde{F}_h(k_h, \Delta z, \omega) \quad , \quad (\text{I.35b})$$

with \tilde{F}_m defined by

$$\tilde{F}_m(k_m, \Delta z, \omega) = \exp \left\{ +jk \sqrt{1 - \frac{1}{2} \left(\frac{k_m}{k} \right)^2} \Delta z \right\} \quad (\text{I.35c})$$

and \tilde{F}_h defined by

$$\tilde{F}_h(k_h, \Delta z, \omega) = \exp \left\{ +jk \sqrt{1 - \frac{1}{2} \left(\frac{k_h}{k} \right)^2} \Delta z \right\} \quad . \quad (\text{I.35d})$$

Relations (I.35c) and (I.35d) can be verified by expanding the square roots in (I.33).

Relation (I.33) provides the basis for migration of CMP slant stacks, as proposed by Ottolini and Claerbout (1984). Ottolini suggests that the coupling between the square roots in the midpoint and offset wavenumber can be evaded by transforming the data to the (τ, p) -domain and applying the downward continuation to data which is sorted into constant ray parameter sections. The method is only valid for 1-D media. A discussion of this approach is beyond the scope of this thesis.

Summarizing, we have derived two expressions of the DSR operator, one in the shot-receiver wavenumber domain and one in the midpoint-offset wavenumber domain. The expression of the DSR operator in the midpoint-offset wavenumber domain is the most suitable for linking the CMP, CRP and CDP methods.

I.2.2 The DSR operator and CMP processing

We will now make an analysis of conventional CMP processing, to see how it can be developed from the theory of the DSR operator. We will assume constant velocity.

We repeat the DSR operator (I.33) for non-recursive application, assuming $z_0 = 0$:

$$\tilde{F}(k_m, k_h, z, \omega) = \exp \left\{ +jk \left[\sqrt{1 - \left(\frac{k_m + k_h}{2k} \right)^2} + \sqrt{1 - \left(\frac{k_m - k_h}{2k} \right)^2} \right] z \right\} \quad . \quad (\text{I.36})$$

This equation describes the — theoretically correct — process of downward extrapolation of shots and detectors in the midpoint-offset domain. Followed by the imaging principle, it implies full prestack migration.

In CMP processing the whole process of downward continuation followed by imaging has been replaced by an approximate process, consisting of two distinct steps:

1. Normal moveout correction and stacking in the offset domain;
2. Poststack migration in the midpoint domain.

The assumptions underlying this two-step process are respectively:

1. Zero-dip assumption.

The conventional NMO correction formula is based on a stratified earth (or zero-dip) assumption.

2. Zero-offset assumption.

Assuming zero-offset means that we deal with a CMP stack in conventional processing.

Let us now apply these assumptions to the DSR equation (I.36) and see if we can extract the processes that describe CMP processing viz. NMO correction, stacking and poststack migration.

The zero-dip assumption implies that in the midpoint wavenumber domain all energy is concentrated around the midpoint wavenumber $k_m = 0$. Setting k_m to zero in (I.36) means that we arrive at the following expression:

$$\tilde{F}\left(k_m=0, k_h, \frac{ct_0}{2}, \omega\right) = \exp\left\{+j2k \sqrt{1 - \left(\frac{k_h}{2k}\right)^2} \frac{ct_0}{2}\right\}, \quad (\text{I.37})$$

where $\frac{ct_0}{2}$ equals z .

We can make the following remarks:

1. Expression (I.37) — a special case of (I.36)! — obeys the wave equation (I.16).
2. If we define

$$k' = 2k \quad (\text{I.38a})$$

$$= \frac{\omega}{c/2}, \quad (\text{I.38b})$$

then (I.37) can be rewritten as:

$$\tilde{F}\left(k_m=0, k_h, \frac{ct_0}{2}, \omega\right) = \exp\left\{+j\sqrt{k^2 - k_h^2} \frac{ct_0}{2}\right\}. \quad (\text{I.39})$$

Compare this result with formula (I.19b), that is the forward extrapolation operator.

Expression (I.39) can be interpreted as an inverse wavefield extrapolation operator in the offset wavenumber-frequency domain, also called the phase shift operator.

The space-time domain expression corresponding to the phase shift operator is the Kirchhoff summation operator. Using the far field approximation ($2\pi r \gg \lambda_{\max}$, r is the distance, λ_{\max} is the maximum wavelength) the 2-D version of this operator can be written as

$$f\left(k_m=0, x_h, \frac{ct_0}{2}, t_h\right) = \frac{\cos \phi}{\sqrt{2\pi r}} d_{-1/2}\left(\frac{c}{2} t_h\right) * \delta\left(t_h - \frac{2r}{c}\right), \quad (\text{I.40})$$

where

'*' denotes a convolution along the spatial axis x_h and the time axis t_h ,

$\cos \phi$ is defined by $\frac{(ct_0/2)}{r}$,

$$r = \sqrt{\left(\frac{ct_0}{2}\right)^2 + x_h^2}, \quad (\text{I.41})$$

c is the medium velocity,

δ is the delta function

and $d_{-1/2}(t)$ is a half differentiator, whose Fourier transform is given by

$$d_{-1/2}(t) \xrightarrow{\text{F.T.}} \sqrt{-jk} \quad \text{for } \omega_{\min} < |\omega| < \omega_{\max}. \quad (\text{I.42})$$

Application of $f(k_m=0, x_h, \frac{ct_0}{2}, t_h)$ involves collection of data from neighbouring offset traces at larger traveltimes, defined by the hyperbola

$$t_h = 2r/c \quad (\text{I.43a})$$

$$= \sqrt{t_0^2 + \left(\frac{x_h}{c/2}\right)^2}. \quad (\text{I.43b})$$

Since t_h is the offset traveltime and t_0 denotes in fact the two-way vertical traveltime, formula (I.43b) — used in combination with the imaging condition — represents the well known hyperbolic moveout equation.

Figure.I.11 shows what in fact happens:

1. Mapping of data along a hyperbolic trajectory ("focussing effect") implying
 - NMO correction
 - Stacking
2. Decrease of time delays, implying an application of a phase shift equal to $\exp(+j\omega t_0)$. Imaging implies that the data at time zero is placed in the output data domain at time equal to t_0 .

We may conclude that operator (I.37) indeed represents NMO correction plus stacking, when used in combination with an imaging step.

Therefore (I.37) is rewritten as

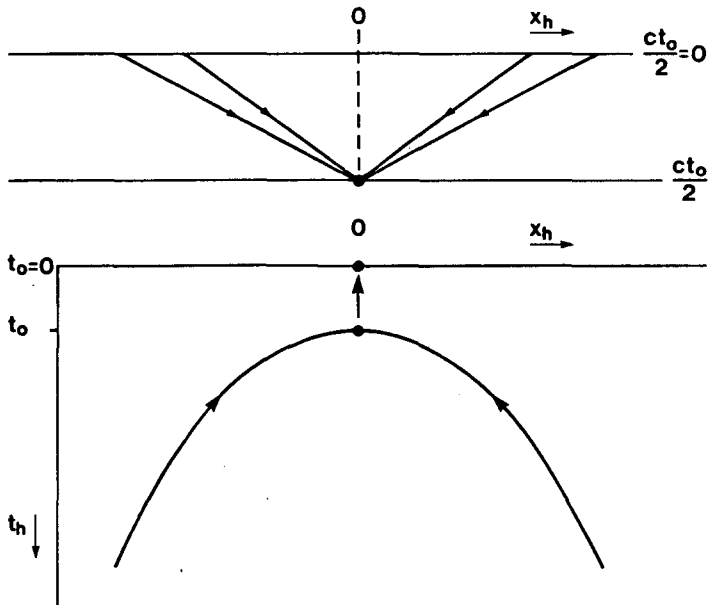


Figure I.11 The inverse extrapolation result at $t_0 = 0$ is obtained by integration along the hyperbola

$$t_0 + \frac{r}{c/2} \text{ where } r = \sqrt{\left(\frac{ct_0}{2}\right)^2 + x_h^2} .$$

$$\tilde{F}_{st}(k_h, t_0, \omega) = \exp \left\{ +j\omega \sqrt{1 - \left(\frac{k_h}{2k}\right)^2} t_0 \right\} . \tag{I.44}$$

A synthetic data example of NMO correction and stacking by means of (I.37) and (I.44) is shown in figure I.12.

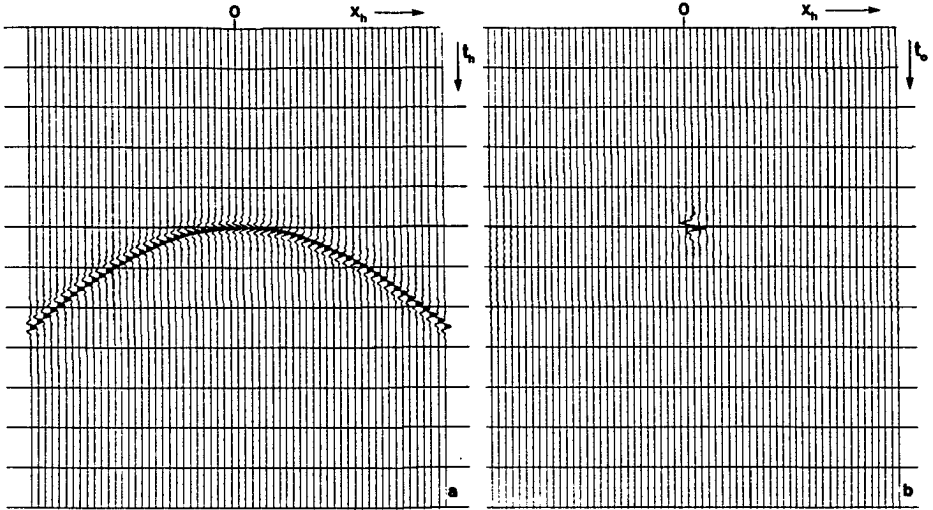


Figure I.12 A synthetic data example of NMO correction and stacking by means of migration with a phase shift operator.

a. Uncorrected CMP gather.

b. Migrated CMP gather. The migrated CMP gather for $x_h = 0$ forms the so called CMP stack.

Assuming zero offset means that we deal with a CMP stack in conventional processing. In an NMO corrected unstacked CMP gather all energy in the offset wavenumber-frequency domain is concentrated at $k_h = 0$; that is zero spatial frequency. So setting $k_h = 0$ in DSR operator (I.36) (written as a recursive expression) results in

$$\tilde{F}_{ex}(k_m, \Delta z, \omega) = \exp \left\{ +j2k \sqrt{1 - \left(\frac{k_m}{2k} \right)^2} \Delta z \right\} \quad (I.45)$$

Expression (I.45) is the well known zero-offset exploding reflector extrapolation operator. Note that the multiplication of k by a factor of 2 accounts for the half of the medium velocity, this is typical for exploding reflector models.

In practice the zero-dip assumption will never be completely fulfilled. Therefore the mapping to zero-offset by normal moveout correction and stacking will imply an approximation. By the same token it is more appropriate to apply \tilde{F}_{st} in the (k_m, k_h, ω) -domain for all values of k_m instead of $k_m = 0$ only.

A realistic CMP processing scheme based on application of operators \tilde{F}_{st} and \tilde{F}_{ex} is depicted in figure I.13.

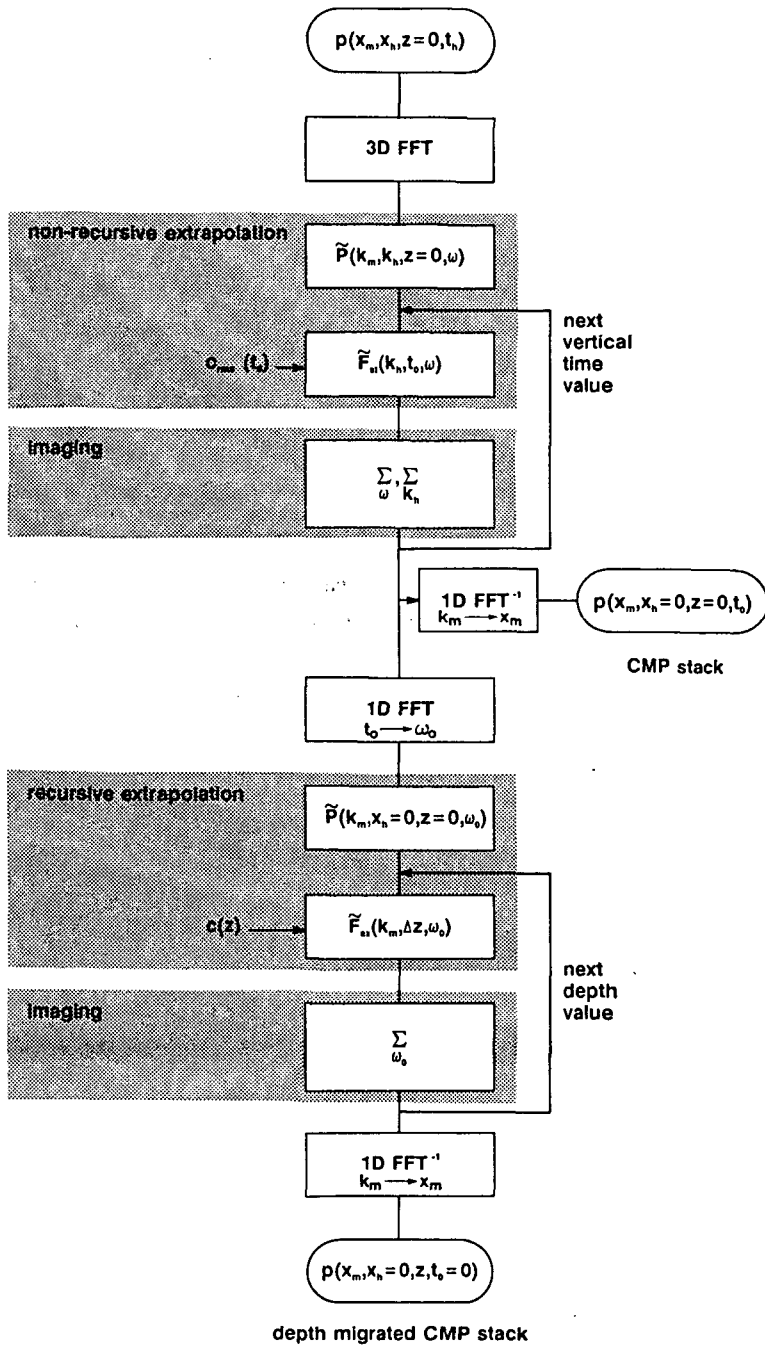


Figure I.13 Flow diagram, showing conventional CMP processing by means of application of the non-recursive operator \tilde{F}_{st} and the recursive operator \tilde{F}_{ex} .

Note, that for a stratified medium (as opposed to a homogeneous medium), the medium velocity c is replaced by the stacking velocity c_{stack} .

We conclude that CMP processing is based on a two-pass migration procedure; CMP stacking by means of non-recursive extrapolation and imaging according to expression (I.44) followed by zero-offset migration by means of recursive extrapolation and imaging according to expression (I.45).

I.2.3 The DRS equation and CRP processing

An interesting improvement over CMP processing can be obtained if we use the relation (Levin, 1971):

$$c_{\text{stack}} = c / \cos \alpha_0 \quad , \quad (\text{I.46})$$

where c_{stack} is the stacking velocity, c is the medium velocity and α_0 is a specific (apparent) dip angle.

We will again assume the medium velocity to be constant.

Application of relation (I.46) to the conventional hyperbolic moveout equation implies the correct traveltime correction for reflection data from dipping events. The NMO equation can thus be rewritten as

$$t_h^2 = t_0^2 + \frac{4 x_h^2}{c_{\text{stack}}^2} \quad , \quad (\text{I.47a})$$

$$= t_0^2 + \frac{4 x_h^2}{c^2} \cos^2 \alpha_0 \quad , \quad (\text{I.47b})$$

$$= t_0^2 + \frac{4 x_h^2}{c^2} - \frac{4 x_h^2}{c^2} \sin^2 \alpha_0 \quad . \quad (\text{I.47c})$$

The extra term $-\frac{4 x_h^2}{c^2} \sin^2 \alpha_0$ is called the Dip Moveout (DMO) term (Deregowski, 1981, Hale, 1984). Application of this term ensures the correct traveltime correction for one particular dip. Since CMP processing is only valid for horizontally layered media, the application of the extra DMO term implies a considerable improvement over CMP processing. CMP processing with DMO included is called common reflection point (CRP) processing, because DMO corrects data according to their true common reflection point. This will be explained in great detail in chapter III.

We will now derive a stacking operator $\widetilde{F}_{\text{st}}^{\text{CRP}}$ which includes the DMO term.

In conventional CMP processing — where stacking operator $\widetilde{F}_{\text{st}}$ (I.44) is applied — the wavenumber k is defined by (I.20).

$$k = \frac{\omega}{c} \quad . \quad (I.48)$$

Here we assume a constant velocity medium.

In CRP processing we replace c (and k accordingly) as follows

$$c \rightarrow c / \cos \alpha_0 \quad , \quad (I.49a)$$

$$k \rightarrow k \cos \alpha_0 \quad . \quad (I.49b)$$

Substitution of this result into the CMP stacking operator (I.44)

$$\tilde{F}_{st}(k_h, t_0, \omega) = \exp \left\{ +j\omega \sqrt{1 - \left(\frac{k_h}{2k}\right)^2} t_0 \right\} \quad (I.50)$$

yields the non-recursive stacking operator defined by

$$\tilde{F}_{st}^{crp}(\alpha_0, k_h, t_0, \omega) = \exp \left\{ +j\omega \sqrt{1 - \left(\frac{k_h}{2k \cos \alpha_0}\right)^2} t_0 \right\} \quad , \quad (I.51)$$

where t_0 is the zero-offset time.

The operator \tilde{F}_{st}^{crp} applied to surface related data $\tilde{P}(k_m, k_h, z=0, \omega)$ yields

$$\tilde{P}_1(\alpha_0, k_m, k_h, t_0, \omega) = \tilde{F}_{st}^{crp}(\alpha_0, k_h, t_0, \omega) \tilde{P}(k_m, k_h, z=0, \omega) \quad . \quad (I.52)$$

The output data \tilde{P}_1 will be properly NMO corrected for dip α_0 and time t_0 and also stacked on the plane $x_h = 0$. Selection of this plane is accomplished by integration over the offset wavenumbers k_h , yielding

$$\tilde{P}_2(\alpha_0, k_m, t_0, \omega) = \int \tilde{F}_{st}^{crp}(\alpha_0, k_h, t_0, \omega) \tilde{P}(k_m, k_h, z_0=0, \omega) dk_h \quad . \quad (I.53)$$

The data \tilde{P}_2 , however, will in general also contain data corresponding to dips unequal to α_0 . The data that correspond to dip α_0 must, for $x_h = 0$, lie on the plane described by

$$k_m = 2k_0 \sin \alpha_0 \quad , \quad (I.54a)$$

with

$$k_0 = \frac{\omega_0}{c} \quad . \quad (I.54b)$$

The frequency ω_0 corresponds to the NMO corrected zero-offset time t_0 . To a good approximation relation (I.54a) also holds for t in the vicinity of t_0 . This means that the data

lies on a plane described by

$$k_m = 2k \sin \alpha_0 \quad , \quad (I.55)$$

the approximation lies in the fact that for t larger or smaller than t_0 the data is respectively under- and over corrected for NMO.

The data corresponding to dips unequal to α_0 can now be filtered out by using a dipfilter based on relation (I.55), which reads

$$\tilde{D}(\alpha_0) = \delta \left(\alpha_0 - \arcsin \left(\frac{k_m}{2k} \right) \right) \quad . \quad (I.56)$$

The actual dip filtering is described by

$$\begin{aligned} \tilde{P}_3(\alpha_0, k_m, t_0, \omega) &= \int \tilde{D}(\alpha'_0) \tilde{P}_2(\alpha'_0, k_m, t_0, \omega) d\alpha'_0 \quad , \\ &= \iint \delta \left(\alpha'_0 - \arcsin \left(\frac{k_m}{2k} \right) \right) \tilde{F}_{st}^{crp}(\alpha'_0, k_h, t_0, \omega) \tilde{P}(k_m, k_h, z=0, \omega) dk_h d\alpha'_0 \quad , \\ &= \int \exp \left[+j\omega \sqrt{1 - \left(\frac{k_h^2}{4k^2 - k_m^2} \right)} t_0 \right] \tilde{P}(k_m, k_h, z=0, \omega) dk_h \quad . \quad (I.57) \end{aligned}$$

Note, that the four-dimensional data volume \tilde{P}_3 will only contain non-zero data on the plane described by (I.54a). The operator \tilde{F}_{st}^{crp} can be written as

$$\tilde{F}_{st, \alpha_0}^{crp}(k_m, k_h, t_0, k) = \begin{cases} \exp \left[+j\omega \sqrt{1 - \left(\frac{k_h^2}{4k^2 - k_m^2} \right)} t_0 \right] & \text{for } k_m = 2k \sin \alpha_0 \\ 0 & \text{otherwise} \end{cases} \quad (I.58)$$

The last step is imaging by selecting the plane $t = 0$, or equivalently, by summing or integrating over ω , yielding

$$\begin{aligned} \tilde{P}_4(\alpha_0, k_m, t_0) &= \int \tilde{P}_3(\alpha_0, k_m, t_0, \omega) d\omega \\ &= \iint \tilde{P}(k_m, k_h, z=0, \omega) \tilde{F}_{st, \alpha_0}^{crp}(k_m, k_h, t_0, \omega) d\omega dk_h \quad . \quad (I.59) \end{aligned}$$

\tilde{P}_4 contains only data that is properly corrected for a specific dip α_0 . In complete CRP processing of course all dips should be taken into account. This is simply done by integration over α_0 , yielding

$$\begin{aligned} \tilde{P}_5(k_m, t_0) &= \int \tilde{P}_4(\alpha_0, k_m, t_0) d\alpha_0 , \\ &= \int \int \int \tilde{P}(k_m, k_h, z=0, \omega) \tilde{F}_{st, \alpha_0}^{crp}(k_m, k_h, t_0, \omega) d\omega dk_h d\alpha_0 , \end{aligned} \quad (I.60)$$

where the final CRP operator \tilde{F}_{st}^{crp} can easily be shown to be

$$\begin{aligned} \tilde{F}_{st}^{crp}(k_m, k_h, t_0, \omega) &= \int \tilde{F}_{st, \alpha_0}^{crp}(k_m, k_h, t_0, \omega) d\alpha_0 , \\ &= \begin{cases} \exp \left[+j\omega \sqrt{1 - \left(\frac{k_h^2}{4k^2 - k_m^2} \right)} t_0 \right] & \text{for } k_m^2 < 4k^2 \\ 0 & \text{otherwise} \end{cases} . \end{aligned} \quad (I.61)$$

CRP processing as described by (I.61) is depicted in a flowchart in figure I.14.

The performance of the CRP stacking operator (I.61) will now be shown, using two synthetic data examples.

The input data of the first example is a band limited impulse, shown in figure I.15a. The offset is 500 m. Application of NMO correction for zero-dip followed by DMO will yield the conventional DMO impulse response which will be discussed in detail in the next chapter.

In figure I.15b the impulse response of a conventional DMO integral implementation is shown.

Applying the CRP stacking operator \tilde{F}_{st}^{crp} to the input data should yield a similar impulse response. Since we are only looking after kinematic aspects, we will not compare the amplitudes.

First we apply \tilde{F}_{st}^{crp} with k_m set to zero. In this case \tilde{F}_{st}^{crp} reduces to a conventional NMO and stacking operator. The result is shown in figure I.15c. Note, that indeed an NMO correction — the stacking has no effect for one offset only — has been applied. Note also, the typical phase change inherent to the application of the phase shift operator. Next the \tilde{F}_{st}^{crp} operator is applied for all k_m values, according to expression (I.61). The result is shown in figure I.15d. We see that we get an impulse response very similar to the conventional DMO impulse response.

In a second example, we use again a band limited impulse, but now having an offset of 1500 m. The corresponding conventional DMO impulse response is shown in figure I.16a.

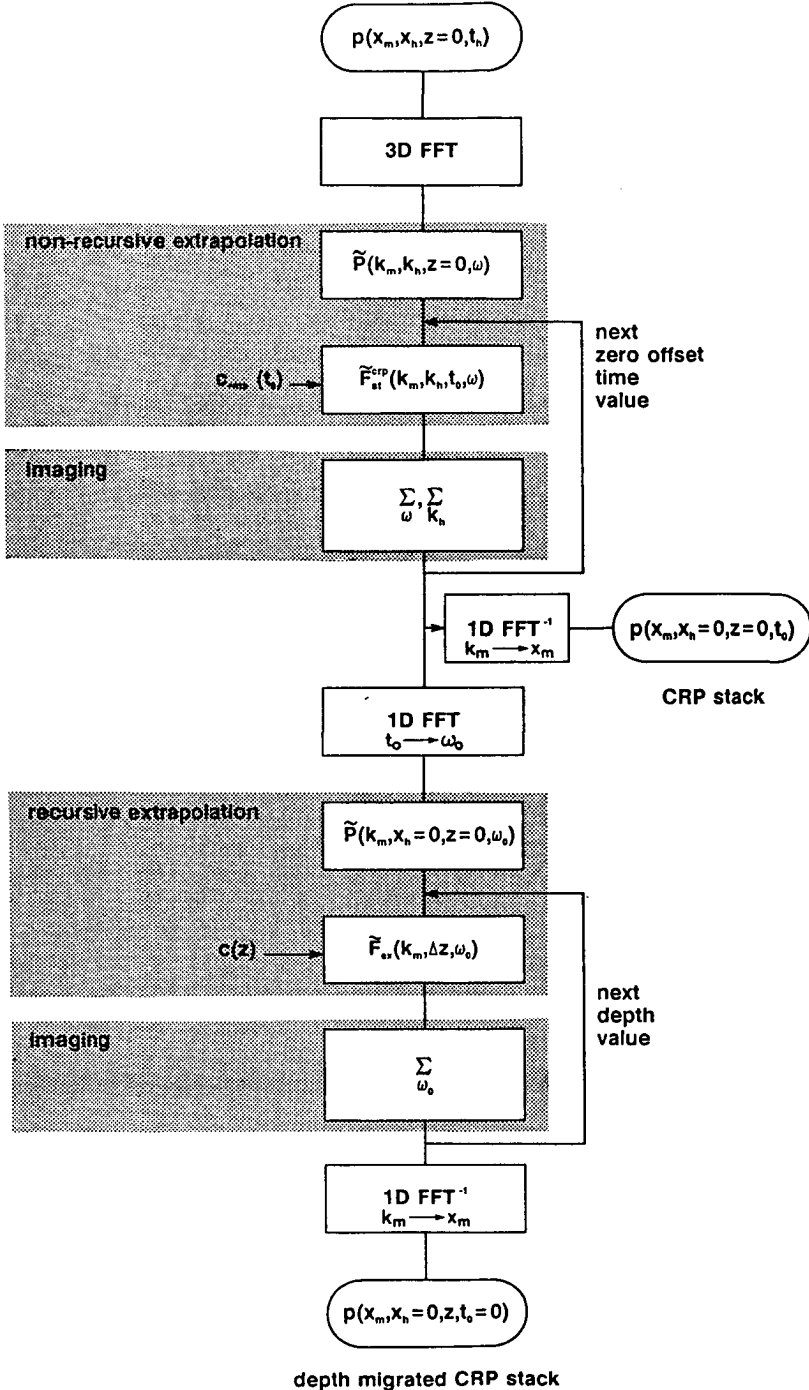


Figure I.14 Flow diagram, showing a CRP processing approach based on Fourier domain operators derived from the DSR operator.

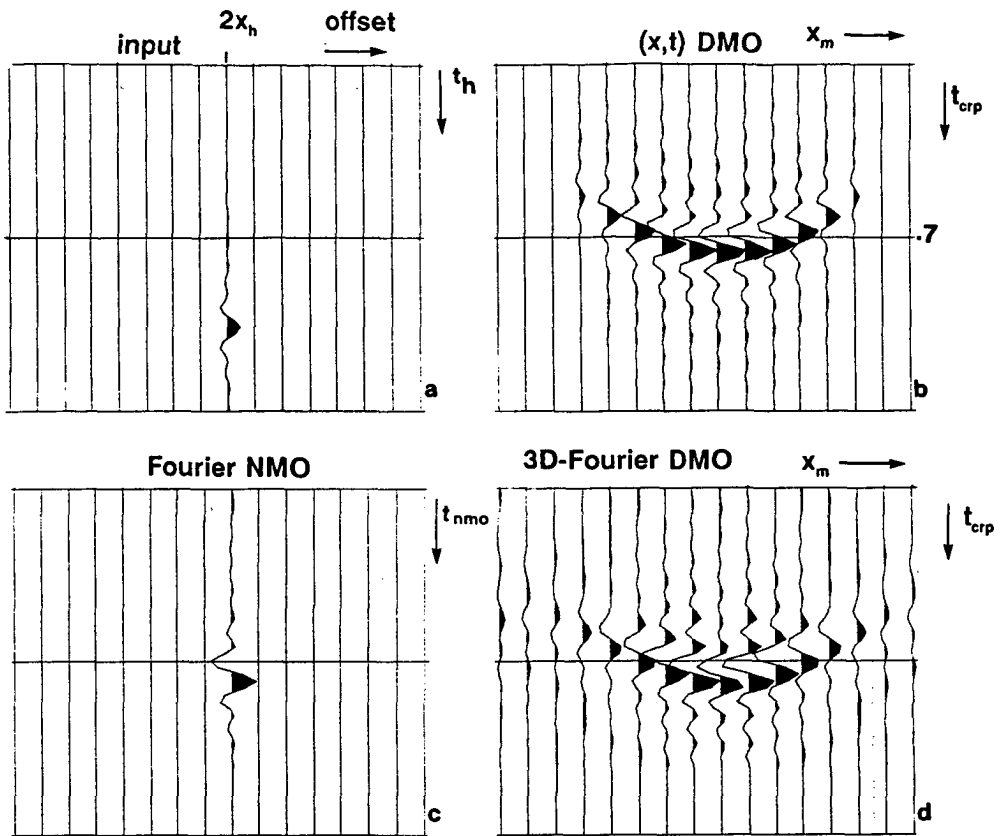


Figure I.15 The impulse responses of the conventional integral type DMO (b) and the Fourier DMO by means of \tilde{F}_{st}^{crp} according to (I.61) (see d) are identical with respect to traveltimes. The bandlimited zero-phase input impulse is shown in figure a. Figure c shows the result of zero-dip NMO (and “stack”) by means of application of \tilde{F}_{st}^{crp} . Note the phase change of the wavelet.
The offset is 500 m.

Application of the CRP stacking operator yields the result depicted in figure I.16b. We again see a DMO impulse response, similar to the one depicted in figure I.16a.

I.2.4 Summary of main results

Assuming a constant velocity medium, we started with the double square root operator, — which is the solution to the one way wave equation — and derived monochromatic expressions for CDP, CRP and CMP processing.

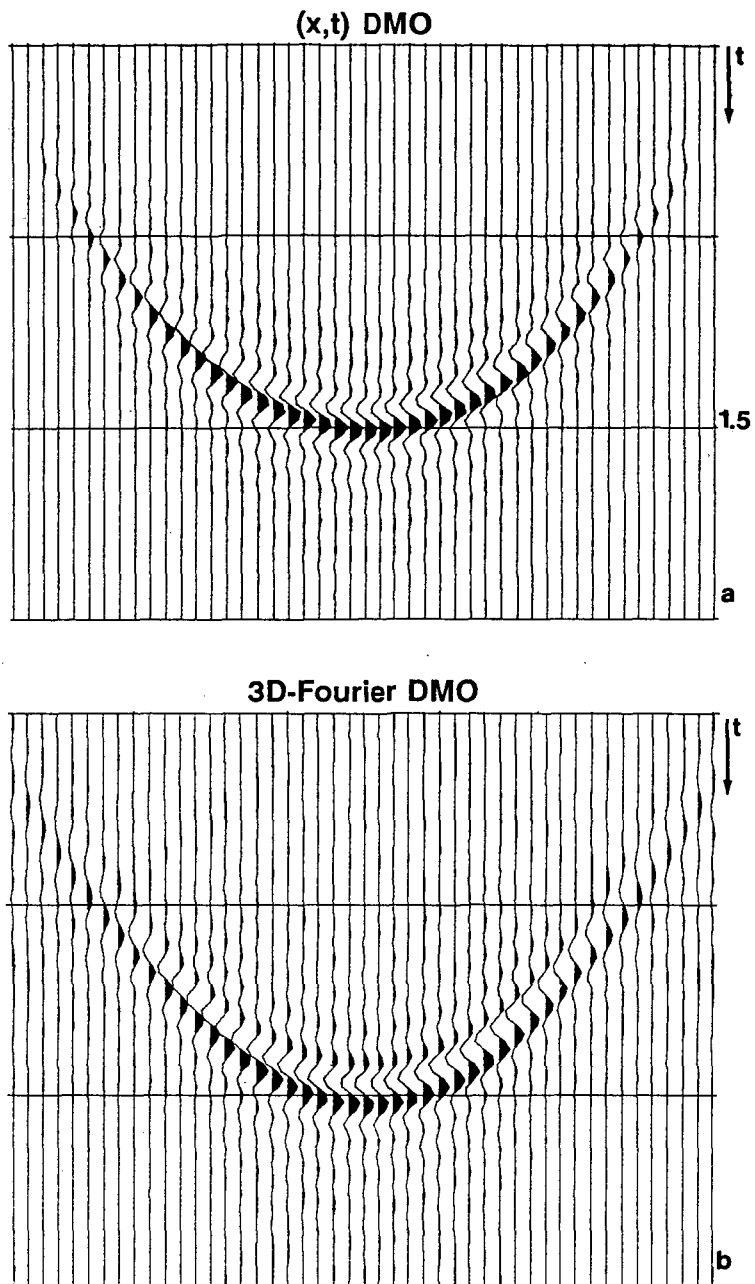


Figure I.16 Conventional (a) and Fourier domain DMO impulse response (b). The offset is 1500 m.

In CDP processing the DSR operator is applied without any approximation. The operator is by nature a split one in the shot-receiver domain, hence monochromatic CDP processing is described by:

1. A 1-D convolution along the shot coordinate
2. A 1-D convolution along the receiver coordinate
3. Imaging
4. Repeat 1. to 3. for all depth levels.

In CMP processing, the DSR operator has been simplified to a two-step process. Used are the zero-dip assumption for prestack data and the zero-offset assumption for stacked data. Hence, the CMP processing is accomplished by an operator that is naturally a two pass procedure in the midpoint-offset domain. Monochromatic CMP processing in the midpoint-offset domain is described by:

1. A 1-D convolution along the offset coordinate
2. Imaging
3. Repeat 1. and 2. for all depth levels
4. A 1-D convolution along the midpoint coordinate
5. Imaging
6. Repeat 4. and 5. for all depth levels.

Finally, CRP processing can be described as a natural extension to CMP processing. The operator is again a two-pass procedure in the midpoint-offset domain. CRP processing is described by

1. A 2-D convolution along the midpoint and offset coordinate
2. Imaging
3. Repeat 1. and 2. for all depth levels
4. A 1-D convolution along the midpoint coordinate
5. Imaging
6. Repeat 4. and 5. for all depth levels.

II

CRP PROCESSING BY CONSTANT VELOCITY DMO

II.1 INTRODUCTION

The subject of this thesis is CRP stacking in terms of macro-model driven DMO. This means that our main interest is directed to CRP stacking in inhomogeneous media.

However, there are several reasons why we should start with the investigation of CRP stacking in constant velocity media:

1. CRP stacking in constant velocity media — the better known name Dip Moveout or DMO will be used in this chapter only — has been well described in the literature. A proper understanding of DMO helps in the appreciation of its shortcomings and the generalization to CRP stacking in inhomogeneous media.
2. DMO has been approached theoretically from different standpoints. These various approaches will be summarized and a concise comparative analysis will be given in this chapter.
3. Nearly all published DMO methods have been derived as multi dip processing per constant offset. We start therefore to describe the phenomenon of DMO in the constant offset domain. In chapter III we will present our approach, which describes DMO as a natural extension of conventional processing, i.e. multi offset processing for a range of dips.

4. Finally, as has already been shown in chapter I, in CRP processing an approximation to the wave equation is used. The definition of a proper weighting of the amplitude characteristics of CRP and DMO operators is therefore a serious problem. This is a fortiori true for CRP operators in inhomogeneous media.

In section 2 we will start with an overview of the benefits of DMO. In section 3 we continue with a general description of the DMO operator impulse response for constant offset sections. We will then concentrate on the traveltimes aspects.

In practice the amplitude and phase characteristics of the DMO impulse response very much depend on the type of implementation. We will therefore first give an overview of several implementations in section 4 and will mention some amplitude and phase characteristics. In section 5 we will discuss the amplitude and phase behaviour of the different types of DMO operators.

II.2 CLAIMS FOR DMO

The process of DMO can be defined in several ways. The most elegant one is to define DMO as the process which — in combination with NMO correction for zero-dip (see next section) — corrects each event on an offset trace according to the traveltimes along the normal incidence ray to the corresponding reflection point and the surface location of this ray.

This implies that the DMO processing in constant velocity media — at least with respect to traveltimes — produces a stack which is very similar to a real zero-offset section.

It has already been shown in figure I.2 that a CMP stack does not necessarily produce a proper zero-offset section because of the reflection point smearing for dipping events.

In chapter I we mentioned two major claims for DMO when included in the conventional CMP processing stream.

A rather complete list of the claims for DMO is given by Deregowski (1986). According to that paper a perfect DMO operator would achieve the following:

1. Each trace is migrated to zero-offset so that each common offset section becomes a zero offset section.
2. This implies that after DMO, but before stacking, CMP gathers contain reflections from common depth points as defined by normal incidence rays. That is, reflector point dispersal for non-zero offset traces is removed, see figure II.1.
3. Stacking velocities become independent of dip, so that correct stacking of simultaneous events with conflicting dips is made possible, see figure II.2. Also fault plane reflections will be better imaged, see figure II.3.

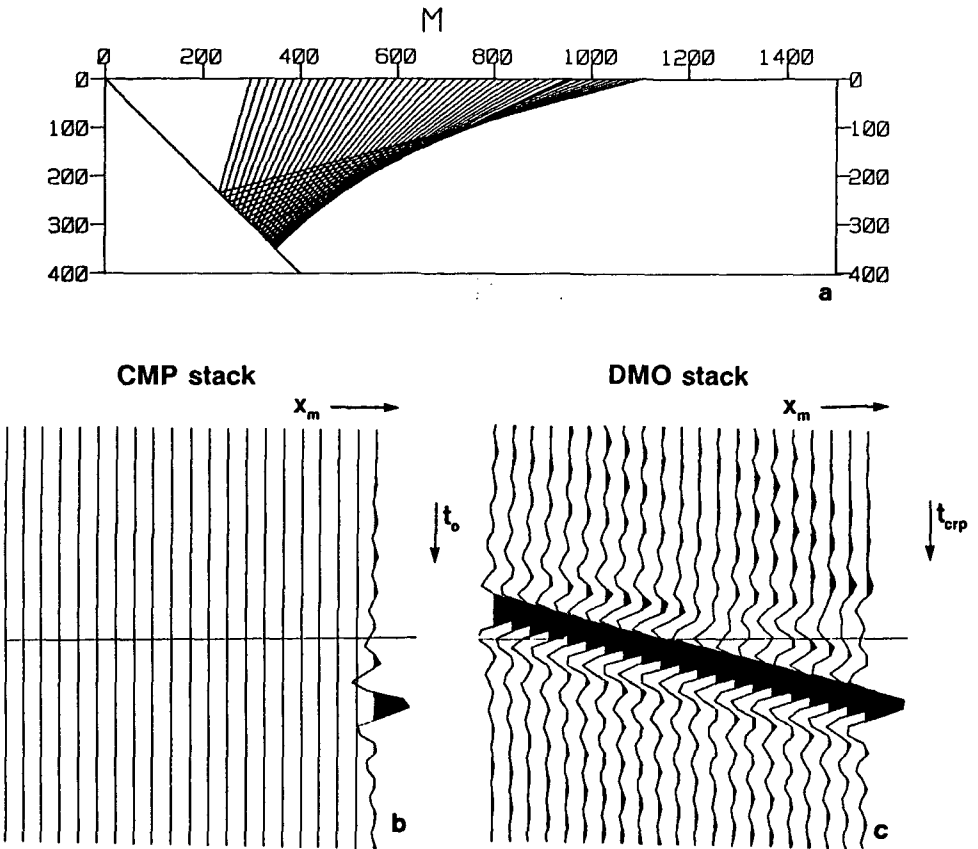


Figure II.1 Consider a reflector dip in a constant velocity medium and one CMP gather. The raypaths for the different offsets are shown in a. Note the smearing of the reflection points. In CMP processing all data related to the same input CMP gather will contribute to one stacked trace (b). In CRP processing each individual trace of the single CMP gather is corrected according to its own specific reflection point, implying that the input data of one CMP gather will be spread over several traces in the output space (c).

4. Velocity analysis is improved, and provides velocities which are more appropriate for migration as well as stacking, see figure II.2.
5. Coherent noise with inconsistent steep dip is removed, without the artificial alignments often associated with dip filters, and at the same time steeply dipping fault planes are better imaged alongside horizons with smaller dips, see figure II.4.
6. The signal-to-noise ratio is improved, especially at large offsets, see figure II.4.

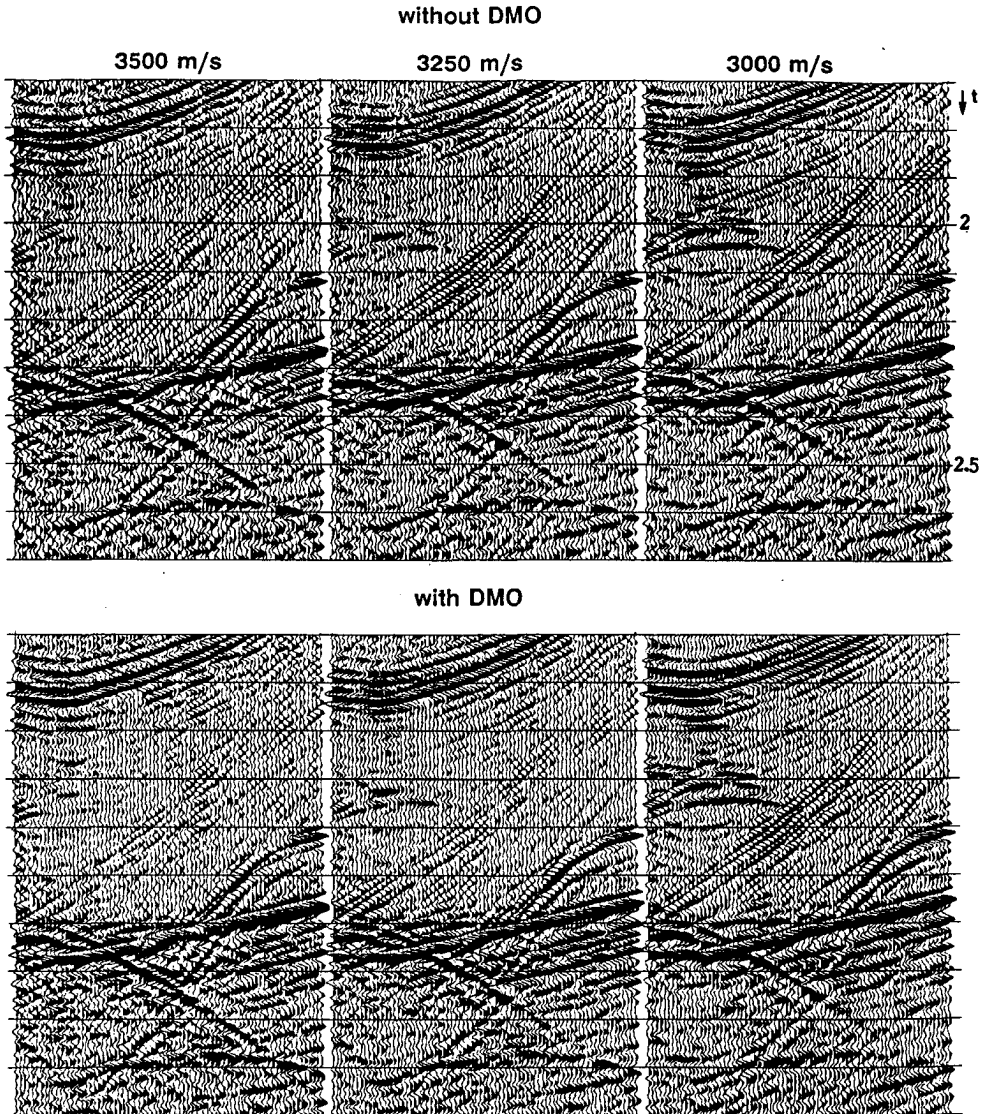


Figure II.2 After application of DMO (and removal of the preceding NMO correction) the stacking velocities become independent of dip. This can clearly be seen for the events between 2.0 and 2.1 s.

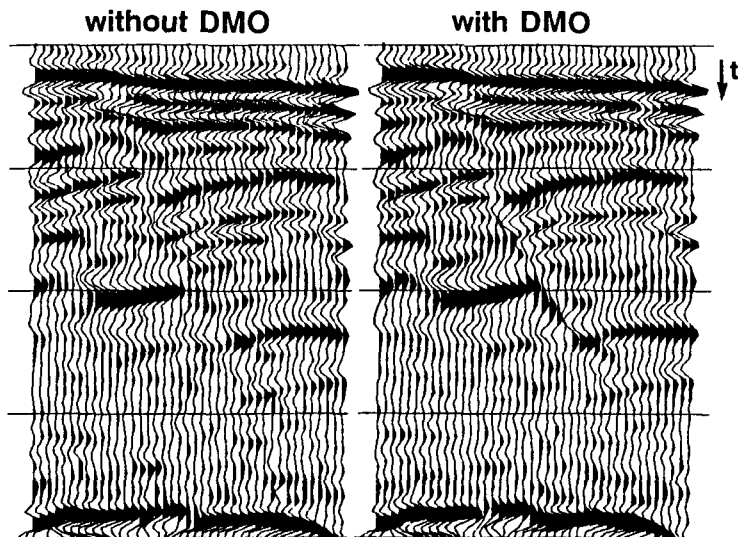


Figure II.3 Steeply dipping fault planes are better imaged by application of DMO.

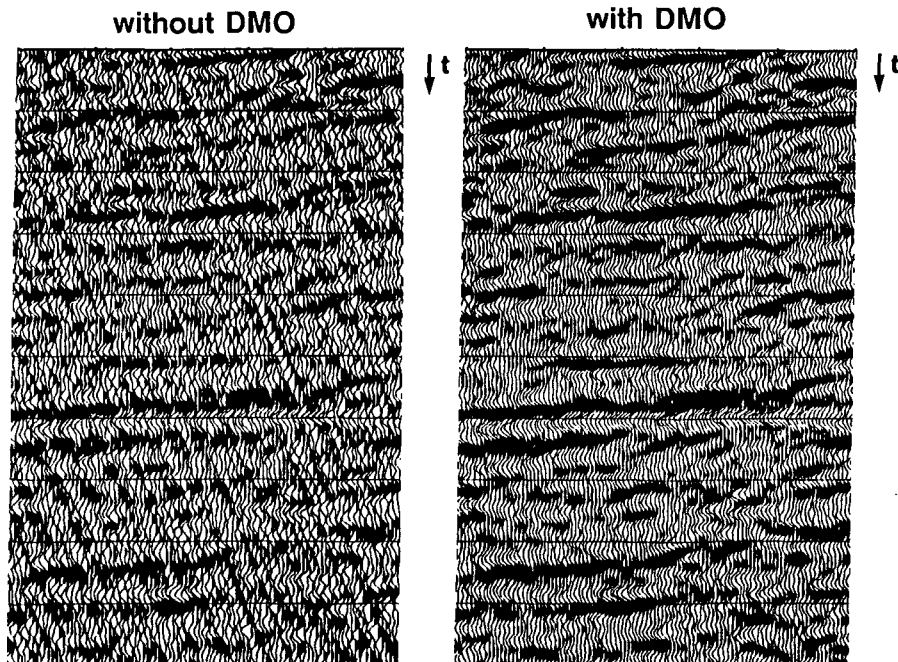


Figure II.4 Coherent noise with inconsistent steep dip is removed by application of DMO.

- 7. Cross-line ties are improved because a zero-offset trace is the same regardless of the direction of the offsets from which it is derived.
- 8. Dead traces are interpolated according to local time dips without those dips having to be estimated by a separate operation, see figure II.5.
- 9. Diffractions are preserved through the stacking process so as to give improved definition of discontinuities after poststack migration, see figure II.6.
- 10. Poststack time migration becomes equivalent to prestack time migration, but at considerably less expense.

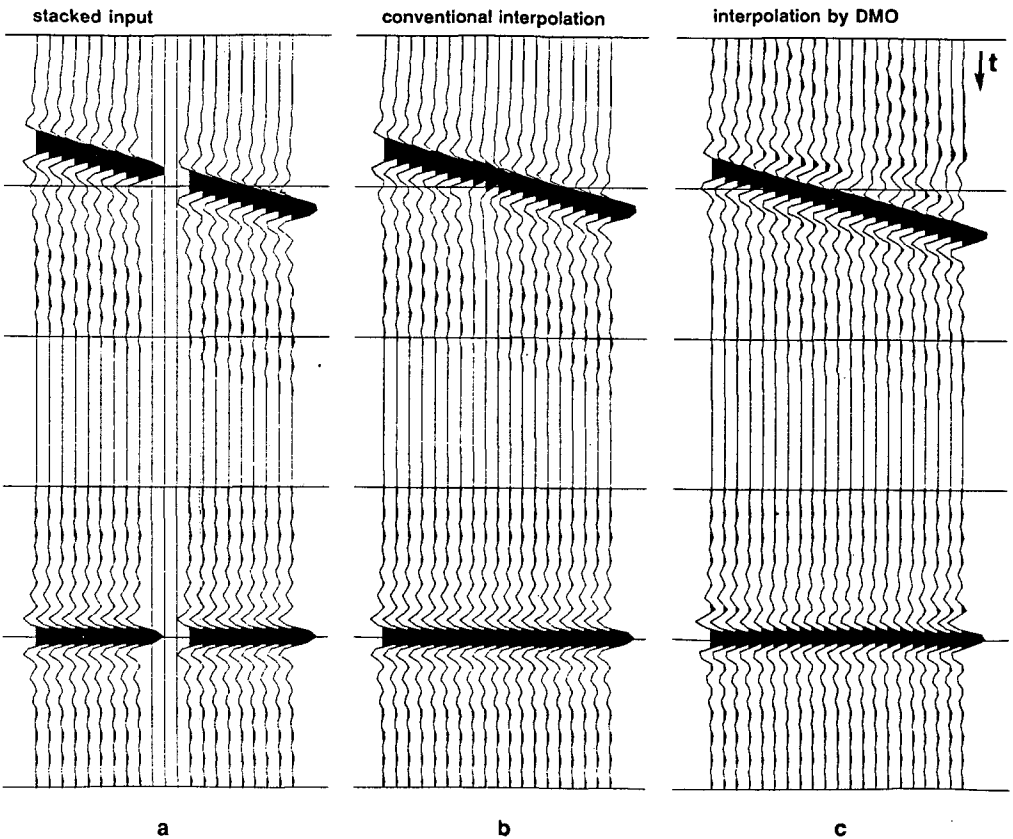
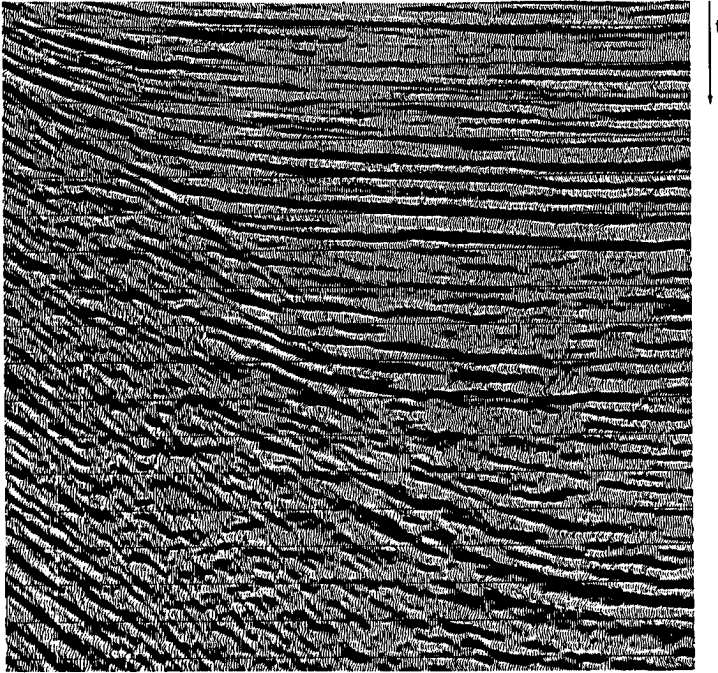


Figure II.5 Dead traces are interpolated according to local time dip by DMO. a: input after stack; b: interpolation by trace averaging; c: interpolation by DMO.

Stack without DMO



Stack with DMO

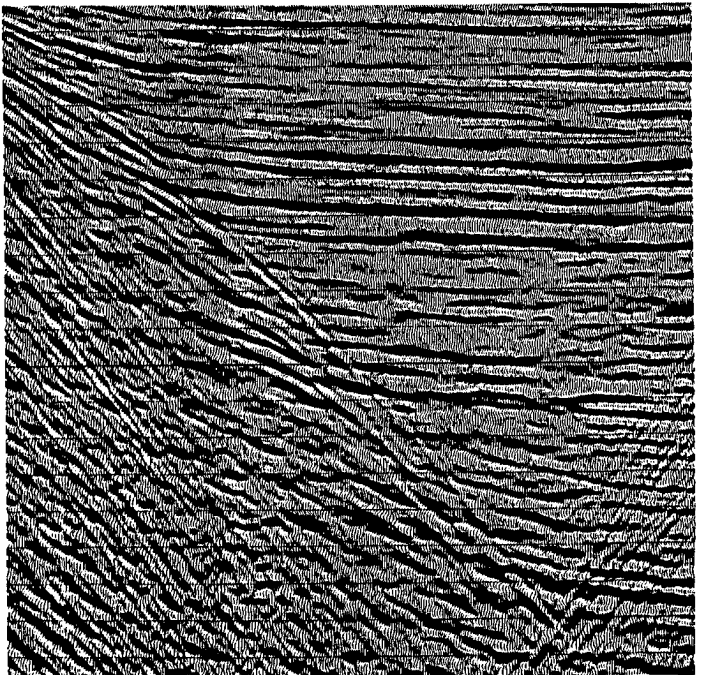


Figure II.6 Diffractions are preserved through the stacking process by application of DMO.

So far Deregowski; in addition the following claims are also valid:

11. Since — as will be shown later — the reflection point smear is compensated via the midpoint smear, DMO — partly — addresses the binning problem in conventional CMP processing.
12. (Related to item 5). Aliased energy in the stack and migrated sections is reduced, provided that the DMO processed traces are mapped on a finer output trace spacing, see figure II.7.

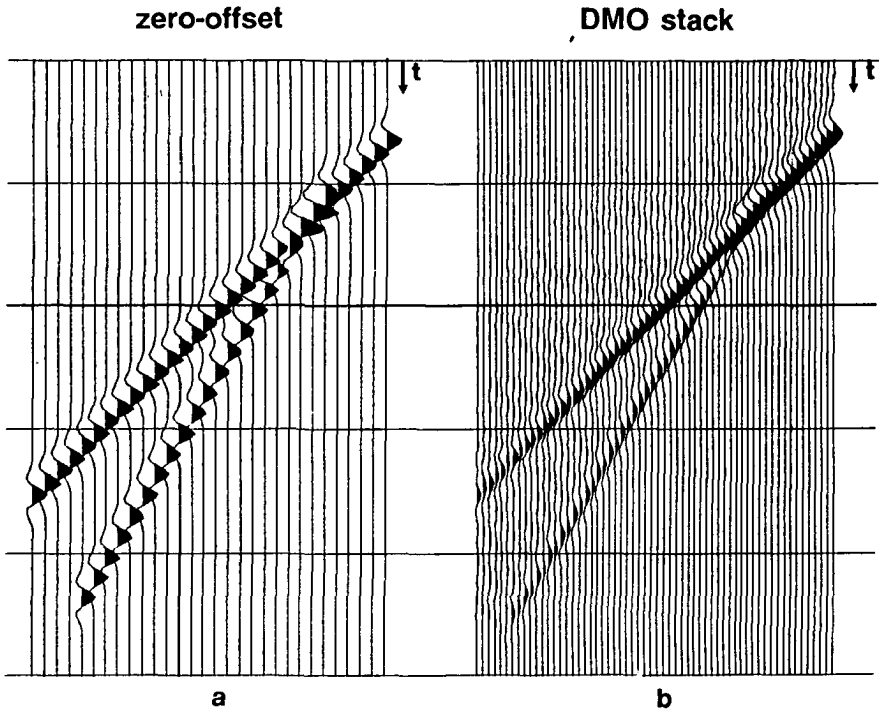


Figure II.7 Aliased energy is reduced in the stack, provided that DMO processed traces are mapped on a finer output grid. Note that the steeply dipping event in figure a. is aliased, whereas it is not aliased in figure b.

We see that some of the advantages have to do with a better definition of parameters such as prestack migration velocity analysis. The main advantage of application of DMO, however, is the better result we get from the poststack depth migration. Since the DMO stack is a better approximation to the zero-offset section and conflicting dips and diffractions have been preserved, the poststack depth migration will show superior results with respect to structural definition as well as resolution.

Since the DMO concept — developed in this chapter and currently used in the industry in production processing — is based on a constant velocity assumption, all the claims for DMO will only partly be fulfilled in practice. Practical experience has taught that a constant velocity DMO stack can even be worse than a CMP stack. The theoretical evidence for this statement will be given later in this dissertation. DMO is therefore — although more sophisticated — less robust than CMP processing.

Note, that — although different strategies should in the end lead to the same result — the first claim in the list suggests that the DMO process is a process applied on constant offsets. As has been pointed out in the introduction to this chapter the DMO process is indeed normally described in such a way.

We will therefore have a closer look at the DMO impulse response in the constant offset domain.

II.3 KINEMATIC ASPECTS OF THE DMO IMPULSE RESPONSE

In order to determine the impulse response of a DMO operator we assume one constant offset gather with a single impulsive event — all other constant offset gathers are zero — and determine the geometrical structure which would give rise to such an observation. It can be shown (Deregowski et al., 1981) that this geometrical structure is an elliptical reflector in the subsurface with the source and receiver placed in the focal points of the ellipse, see figure II.8a.

Figure II.8b shows the prestack dataset acquired from this elliptical reflector. After zero-dip NMO correction (and stacking) (figure II.8c) and poststack migration we obtain a semi-circle (figure II.8d) which is obviously not the elliptical subsurface reflector.

Application of DMO to this conventional CMP sequence should yield a DMO stack which in this homogeneous velocity case should be equal to the zero-offset section.

Therefore we first determine the zero-offset section corresponding to the elliptical reflector.

Figure II.9a shows the zero-offset raytraces and figure II.9b shows the corresponding zero-offset section.

The poststack depth migration result is shown in figure II.9c. This result does indeed show the elliptical reflector.

Let us now compare the zero-dip NMO corrected dataset which is shown in figure II.8c and the zero-offset section shown in figure II.9b. Since DMO is defined as a migration process which maps multi-offset data-NMO corrected for zero-dip- into zero-offset data, which can be subsequently stacked, we can conclude that the zero-offset section shown in figure II.9b must be the DMO impulse response for a certain offset. The offset is determined by the distance between the focal points of the ellipse.

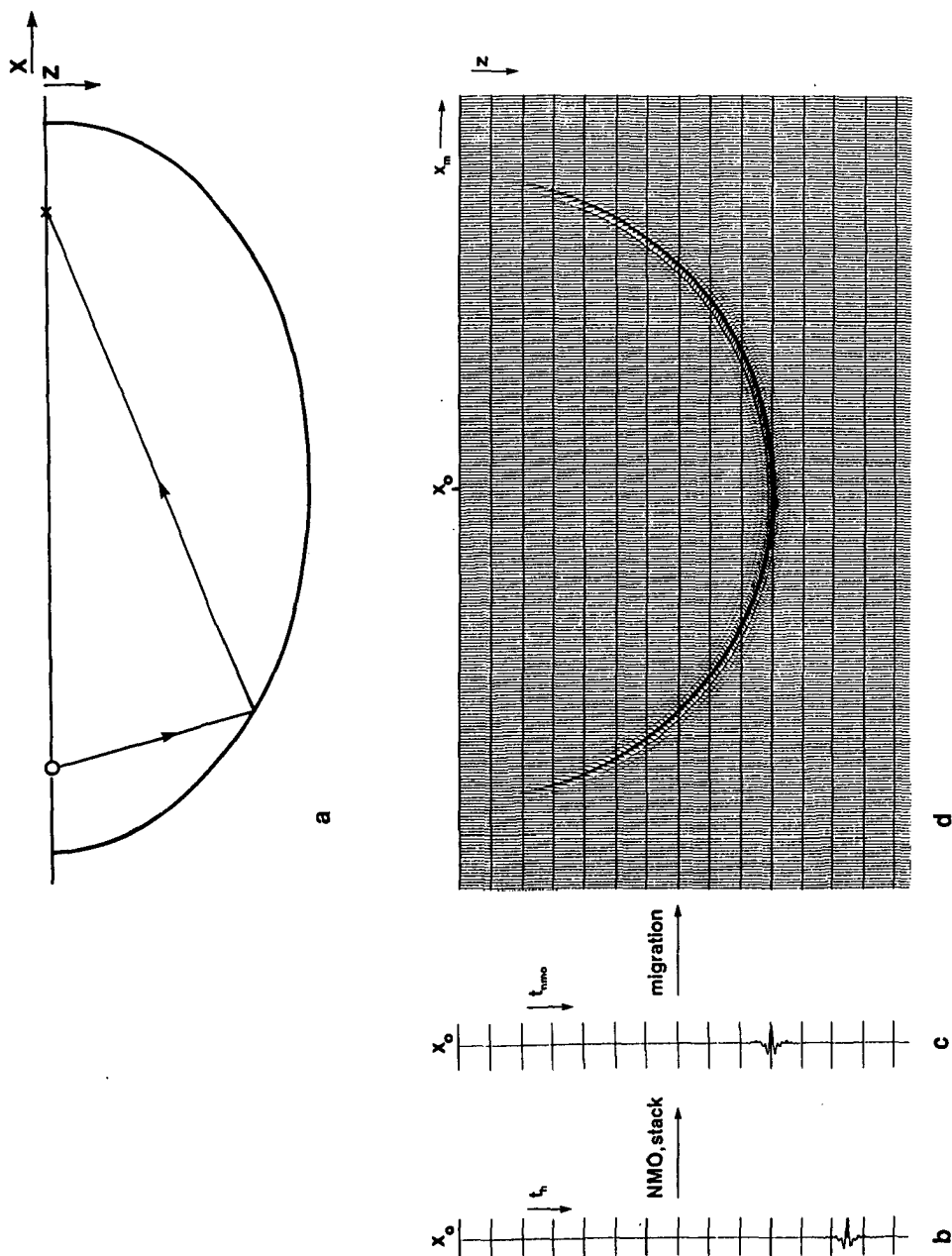


Figure II.8 In a, an elliptical reflector in the subsurface with the source and receiver placed in the focal points of the ellipse is shown. The resulting data set consists of one impulsive event, shown in b. Figure c. shows the same event after NMO correction (and stacking). By application of a poststack migration we obtain a semi-circle (d).

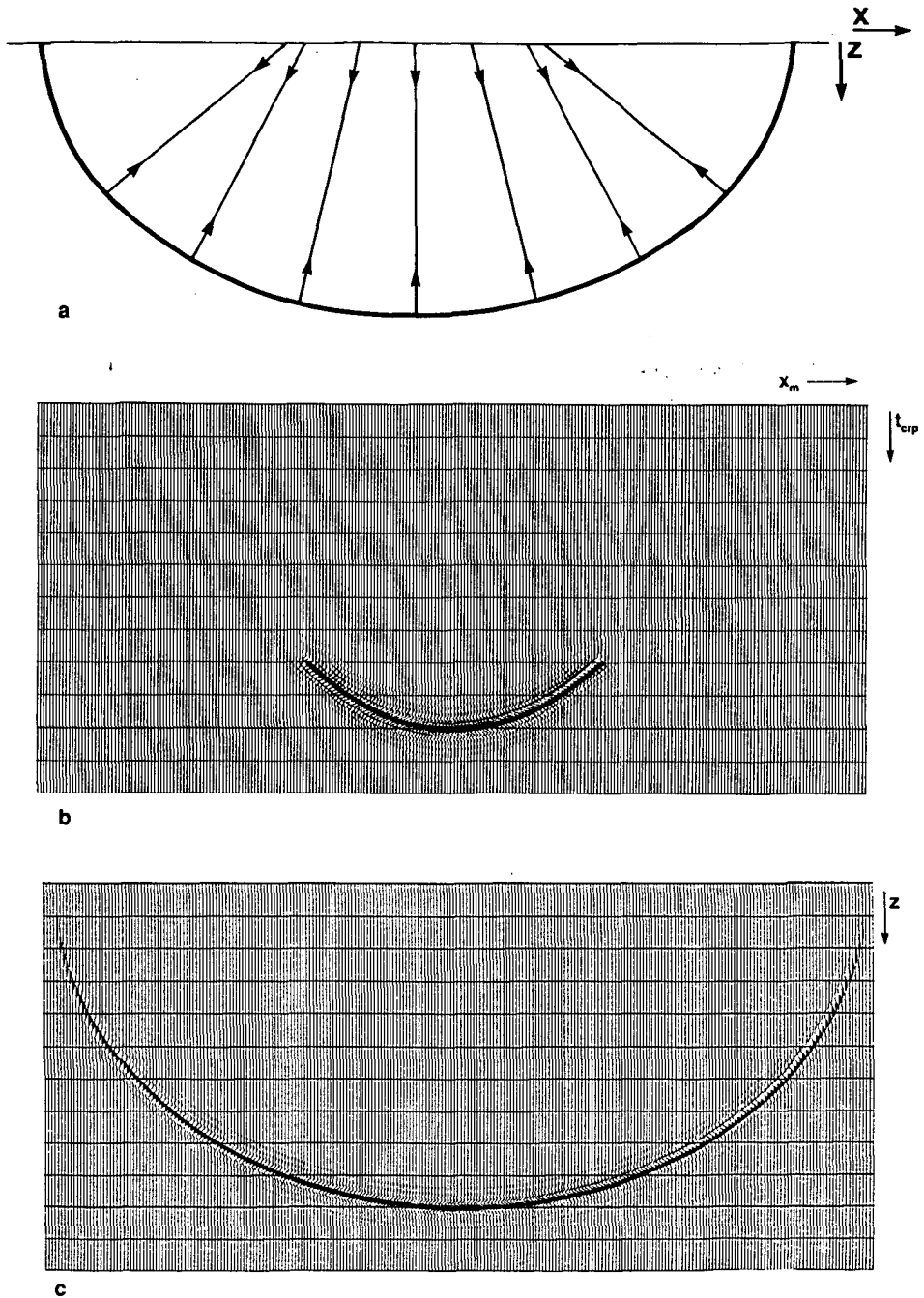


Figure II.9 a. zero-offset raytracing experiment on an elliptical reflector.
b. resulting zero-offset section.
c. poststack depth migration result.

The formula which describes the zero-offset section corresponding to the ellipse should therefore be the same formula which describes the DMO mapping process. Deregowski (1981) has shown that this formula reads

$$t_{\text{crp}}(x_m) = t_{\text{NMO}} \sqrt{1 - \frac{(x_m - x_0)^2}{x_h^2}}, \quad (\text{II.1})$$

where — see also figure II.10 — x_0 denotes the midpoint of the input trace, $x_m - x_0$ denotes the spatial distance and x_h is the half offset. The zero-offset traveltime after DMO correction is called $t_{\text{crp}}(x_m)$.

The maximum value to which x_m is bounded is

$$x_{\text{max}} = \frac{2 x_h^2}{c_{\text{DMO}} t_h}, \quad \text{with } x_{\text{max}} \leq x_h, \quad (\text{II.2})$$

where c_{DMO} is a cut-off velocity which can be chosen equal or larger than the medium

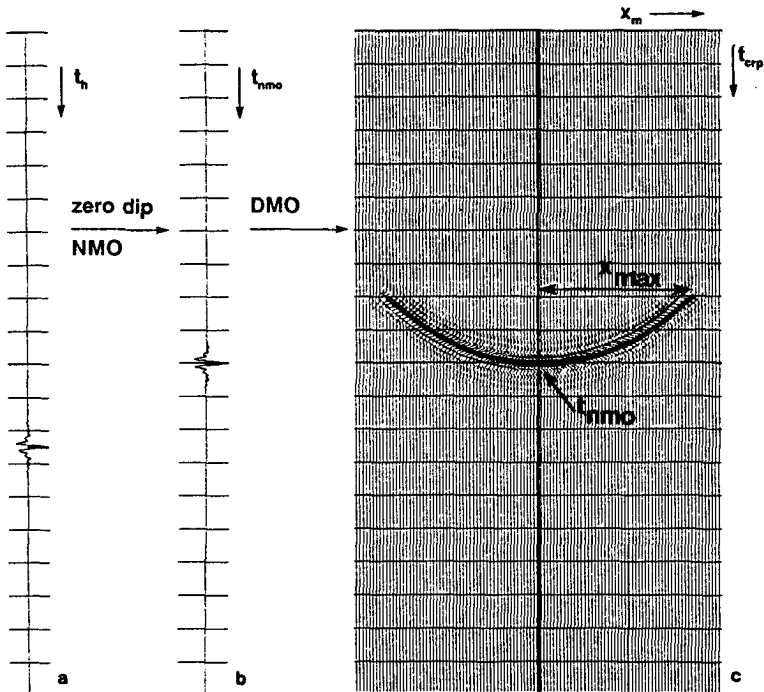


Figure II.10 Visualization of the application of DMO. First an input trace (a) is zero-dip NMO corrected (b). Then a constant velocity DMO is applied (c).

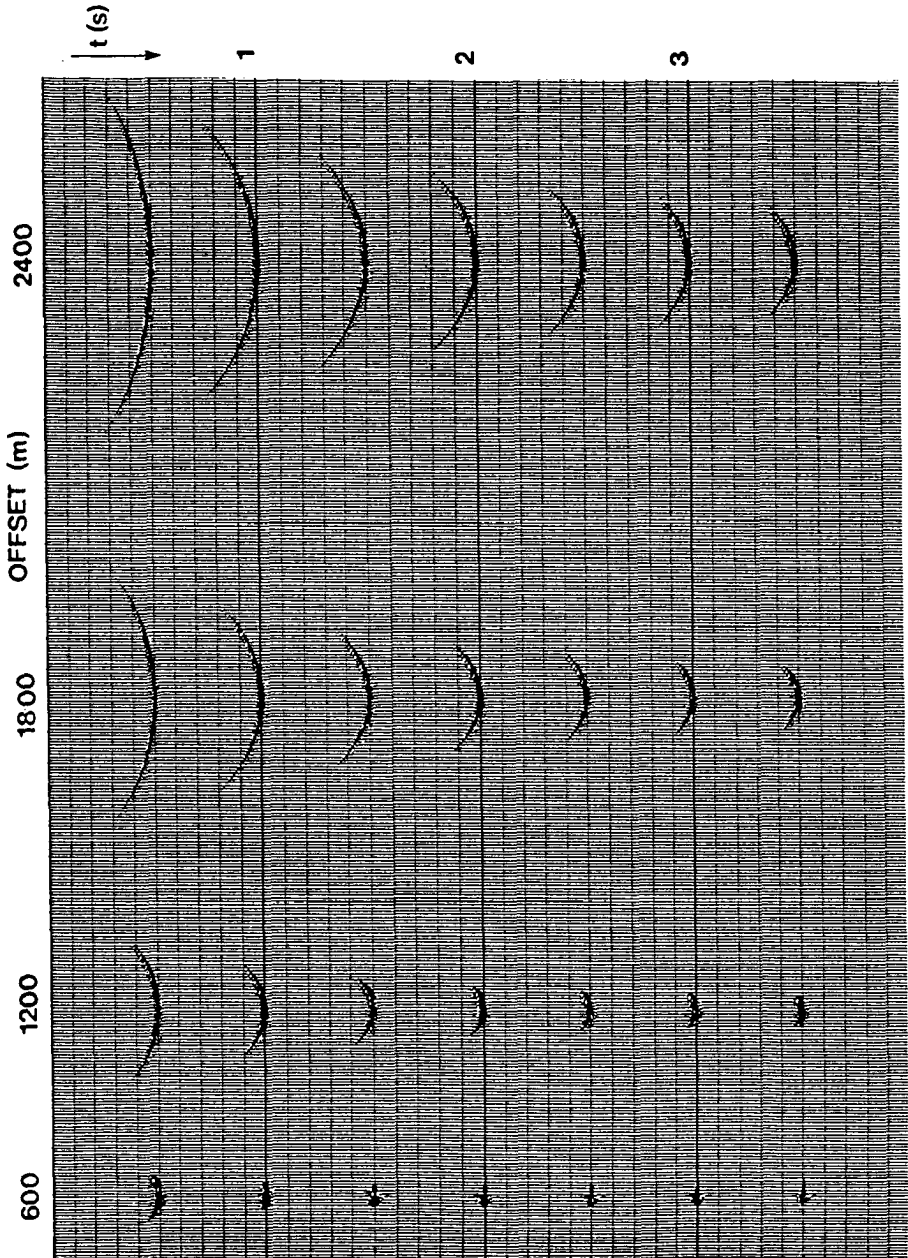


Figure II.11 DMO operators for different times and offsets.

velocity. A larger value of c_{DMO} may be used to avoid aliasing. In an entirely different way to that followed by Deregowski (1981) formulae (II.1, 2) will be derived in chapter III and appendix B. Note, that the cut-off velocity simply specifies the maximum time-dip in the output data. With respect to the maximum time dip, Deregowski (1986) makes the important remark that applying DMO does not increase the time dip, since the output is still unmigrated time.

Another important property of the DMO operator is that its shape only depends on the shot-receiver direction. That means that the 3D DMO impulse response is identical to the 2D response but with the horizontal axis in the azimuth of the shot-receiver offset. Outside this plane the 3D DMO operator is zero.

Finally figure II.11 shows a number of DMO operators for different offsets and times, revealing their dependency on these parameters.

II.4 IMPLEMENTATION ASPECTS OF DMO OPERATORS

CRP processing can be implemented in several ways. Since a DMO operator can be described as a kind of migration operator, it is plausible that the type of implementations used for migration algorithms are also applicable for DMO algorithms.

For migration, we can distinguish the following implementation schemes:

- | | |
|-----------------------------|--|
| 1. Integral method | (Kirchhoff summation migration) |
| 2. Phase shift method | (phase shift migration) |
| 3. Mapping method | (KF-migration) |
| 4. Finite-difference method | (finite-difference migration in (x,f) of (x,t)) |

These methods have indeed been used for DMO applications. All methods, except the phase shift method, are used in production processing environments. A phase shift formulation of DMO has been pioneered by Yilmaz (1979).

In this section we will discuss the other three schemes in general, using flow diagrams. It should be realized that for ideal (error-free) operators the form of an impulse response within the output space is independent of the type of DMO algorithm that generated the impulse response.

This statement may be true for the kinematic aspects. However, because no closed relations can be formulated for the amplitude characteristics, different implementation schemes will lead to different amplitudes. Therefore we first review the main types of DMO algorithms, before we discuss the amplitude and phase behaviour of DMO operators.

Since DMO is a linear procedure, the DMO impulse response contains all the information required to understand the properties of the DMO operator.

II.4.1 Integral type formulation

DMO is normally thought of as being applied in the constant offset domain. However, if we choose an integral type of implementation, DMO can also be applied in the CMP domain or the shot domain. The CMP domain has the advantage that the data already has been sorted into CMP gathers for application of NMO correction.

First the data is NMO corrected for zero-dip. Then each individual input trace, characterized by a (half-)offset x_h and CMP position x_0 is mapped to a number of traces in the output space, according to formulae (II.1) and (II.2):

$$p(x_0, x_h, t_{NMO}) \xrightarrow{DMO} p(x_m, x_h, t_{CRP}), \quad x_0 - x_{max} \leq x_m \leq x_0 + x_{max} \quad , \quad (II.3)$$

where t_{NMO} denotes zero-dip NMO corrected time for zero-dip and x_{max} is the maximum absolute value of $x_m - x_0$. Note, that an integral implementation has an important advantage that it makes the operator independent of the input or output grid of the data. However, care should be taken with respect to aliasing problems. A flow diagram of the integral implementation is shown in figure II.12.

II.4.2 Mapping method

DMO became well known when Hale (1983) published a Fourier representation of dip moveout.

The derivation is simple and elegant. It starts with (I.47c):

$$t_h^2 = t_0^2 + \frac{4 x_h^2}{c^2} - \frac{4 x_h^2}{c^2} \sin^2 \alpha \quad , \quad (II.4)$$

where α is the apparent dip angle in the zero-offset domain and t_0 is the zero-offset time. In chapter I it was explained that the term $\frac{4 x_h^2}{c^2}$ represents the NMO correction for zero-dip while the term $-\frac{4 x_h^2}{c^2} \sin^2 \alpha$ represents the DMO correction. For a single dip α the DMO zero-offset time is therefore denoted by t_0 . For a multi-dip expression the DMO zero-offset time is denoted by t_{CRP} , see figure II.13a. The reason for the difference in notation is the fact that for a single dip compensation for the reflection point smearing is superfluous and the zero-offset time t_0 does not need to be corrected for smaller zero-offset times from updip reflection points corresponding to larger offsets. For a multi-dip problem the compensation for reflection point smear needs to be done and the actual zero-offset time t_{CRP} along the normal incidence ray to the surface is used. This phenomenon will also be discussed in section II.4.3.

Consider the subsurface structure depicted in figure II.13a.

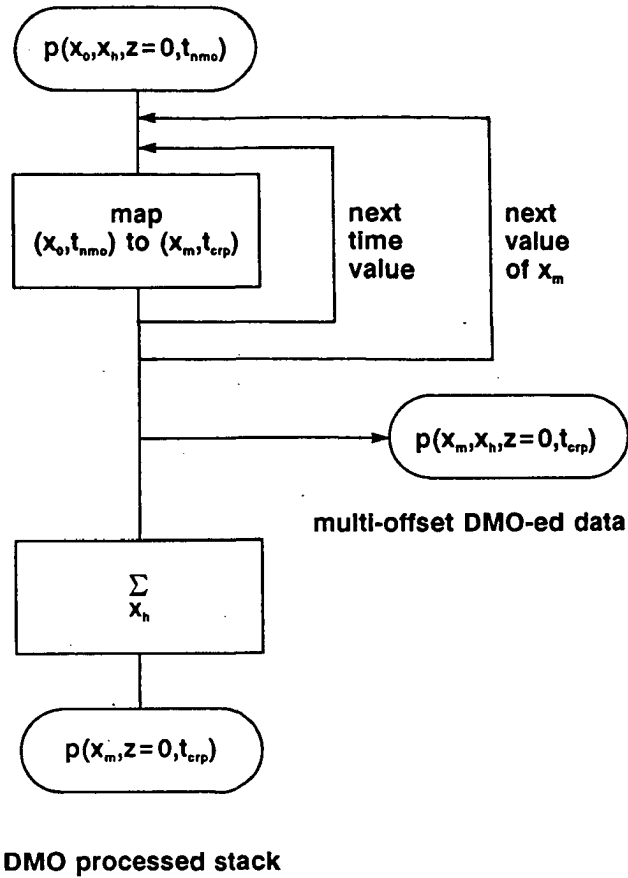


Figure II.12 Flow diagram of the integral implementation of DMO.

Expression (II.4) describes the hyperbolic travelt ime trajectory for a dipping reflector. The hyperbolic moveout curve for the flat reflector, having the same offset travelt ime t_h for offset $2x_h$ reads:

$$t_h^2 = t_{\text{NMO}}^2 + \frac{4x_h^2}{c^2}, \quad (\text{II.5})$$

where t_{NMO} denotes the zero-offset travelt ime for a flat event.

Note the difference in travelt ime trajectories in figure II.13b.

Since the offset travelt imes are equal for offset $2x_h$, we may combine (II.4) and (II.5), yielding

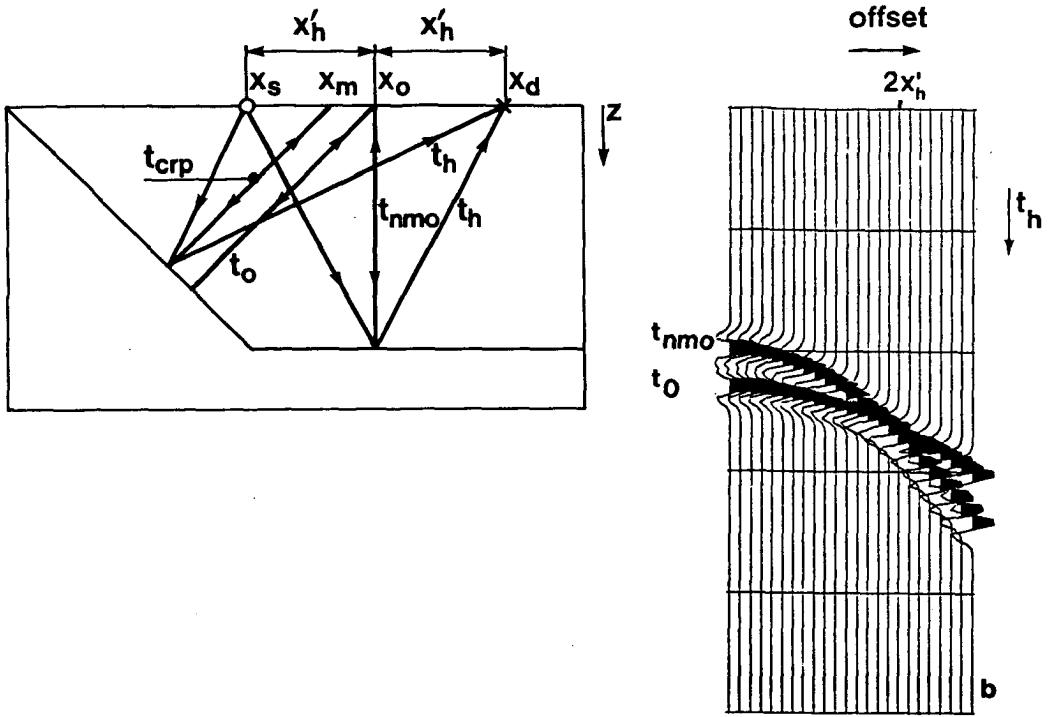


Figure II.13 Subsurface structure denoting several traveltimes (a) and corresponding traveltimes in the CMP gather at x_o (b). For the flat reflector DMO does not alter the traveltimes, so $t_{NMO} = t_{crp}$. For the dipping reflector the zero-offset ray from the CMP midpoint x_o has a traveltime t_o , while the zero-offset ray from the reflection point has the traveltime t_{crp} . In this geometry the configuration has been chosen such that for offset $2x'_h$ the offset traveltimes from the dipping and flat reflector are equal.

$$t_{NMO}^2 = t_o^2 - \frac{4x_h^2}{c^2} \sin^2 \alpha \quad \text{for } x_h = x'_h \quad (II.6)$$

Equations (II.4), (II.5) and (II.6) imply that dip-corrected NMO may be applied in two steps:

1. NMO correction by mapping from t_h to t_{NMO} :

$$t_{NMO} = \sqrt{t_h^2 - \frac{4x_h^2}{c^2}} \quad (II.7)$$

2. DMO correction by mapping from t_{NMO} to t_0 :

$$t_0 = \sqrt{t_{\text{NMO}}^2 + \frac{4 x_h^2 \sin^2 \alpha}{c^2}} \quad (\text{II.8})$$

The DMO correction should be repeated for all possible dips α . Note, that the slope of a reflector in the zero-offset domain reads

$$\frac{dt_0}{dx_m} = \frac{\sin \alpha}{c/2}, \quad (\text{II.9a})$$

$$= \frac{k_m}{\omega_0} \quad (\text{II.9b})$$

This means that the double Fourier domain (k_m, ω_0) is particularly useful for performing DMO, since all events having a particular slope in (x_m, t_0) transform to a single radial line $k_m/\omega_0 = \text{constant}$ in the (k_m, ω_0) domain.

The DMO correction expressed in (II.8) can be transformed to the following multi-dip expression in the Fourier domain (see Hale, 1983):

$$\tilde{P}(k_m, x_h, \omega_{\text{crp}}) = \iint p(x_m, x_h, t_{\text{NMO}}) \frac{1}{A} \exp[-j\omega_{\text{crp}} t_{\text{NMO}} A + jk_m x_m] dt_{\text{NMO}} dx_m, \quad (\text{II.10})$$

where $p(x_m, x_h, t_{\text{NMO}})$ is the NMO corrected for (zero-dip) input data and A reads

$$A = \frac{dt_{\text{NMO}}}{dt_{\text{crp}}}, \quad (\text{II.11a})$$

$$= \left[1 + \left(\frac{\partial t_{\text{crp}}}{\partial x_m} \right)^2 \frac{x_h^2}{t_{\text{NMO}}^2} \right]^{1/2}, \quad (\text{II.11b})$$

$$= \left[1 + \frac{k_m^2 x_h^2}{\omega_{\text{crp}}^2 t_{\text{NMO}}^2} \right]^{1/2} \quad (\text{II.11c})$$

Note that DMO is really done by the term $-\omega_{\text{crp}} t_{\text{NMO}} A$ in the exponent. The amplitude scaling is done by the Jacobian of the transformation

$$\frac{dt_{\text{crp}}}{dt_{\text{NMO}}}$$

Hale's algorithm is, however, not really used in the industry since this implementation makes DMO computationally as intensive as full prestack migration. The reason for the

inefficient implementation is clear if we realize that (II.10) is an integral transformation in which the integral over t_{NMO} cannot be expressed as a Fourier transform and therefore has to be evaluated numerically.

A flow diagram of DMO processing in the Fourier domain is shown in figure II.14. Figure II.15 shows some typical impulse responses.

II.4.3 Poststack DMO

A very interesting alternative to the DMO process in the Fourier domain has been proposed by Jakubowicz (1985). Jakubowicz noticed that if we consider only one dip in the data, the integral transformation (II.10) reduces to a simple Fourier domain expression of the data, NMO corrected for the specific dip angle, according to (II.4). Note, that this means that DMO reduces to a single trace process when the input data contains only one dip.

This all implies that the Fourier domain can be abandoned altogether.

Since seismic data always contains multi dips (a reflectivity variation along a reflector already implies multi-dip data), the data should be KF filtered, to remove all energy not related to the specific dip angle. Note, that it is the KF-filter which compensates for the reflection point smearing. This can be witnessed in figure II.16 which shows two examples of a poststack DMO constant offset operator. It is clearly seen how the DMO impulse response is built up for a number of dip ranges.

Summarizing, a practical poststack DMO processing scheme would look as follows:

1. Produce a CMP stack using a dip-dependent moveout correction for a certain dip (range).
2. Remove all other dips ranges by KF-filtering.
3. Repeat step 1, 2 for different dips.
4. Stack all results.

The width of a dip range to be passed by the KF-filter and the number of dip ranges should be determined in practice. Since a limited number will be needed in practice the method will be much faster than Hale's scheme.

A flow diagram of the method is shown in figure II.17.

We see that poststack DMO really produces a DMO impulse response.

Without KF-filtering the DMO stack would reduce to a wide angle CMP stack.

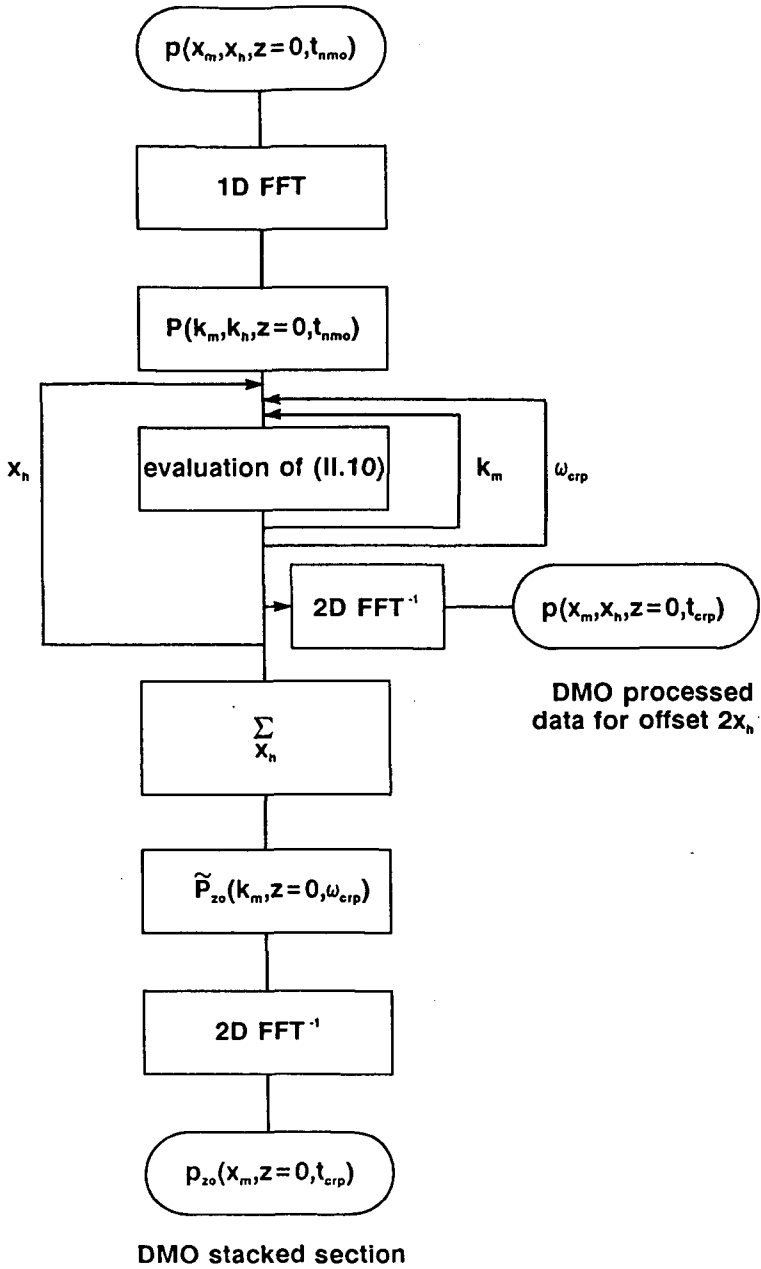


Figure II.14 Flow diagram of DMO processing in the Fourier domain.

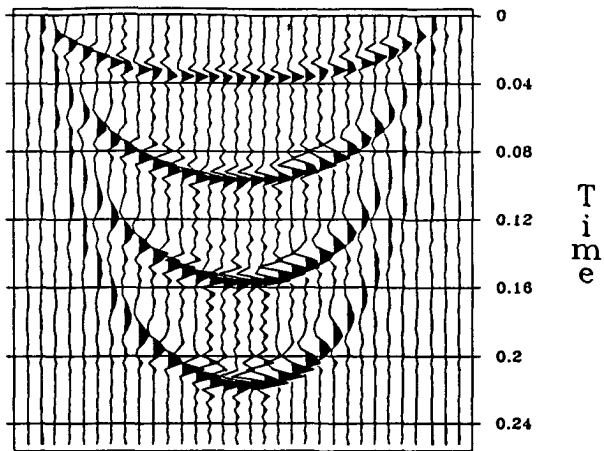


Figure II.15 Typical Fourier domain DMO operators as proposed by Hale (after Liner, 1988). The offset is 800 m. The trace spacing is 25 m.

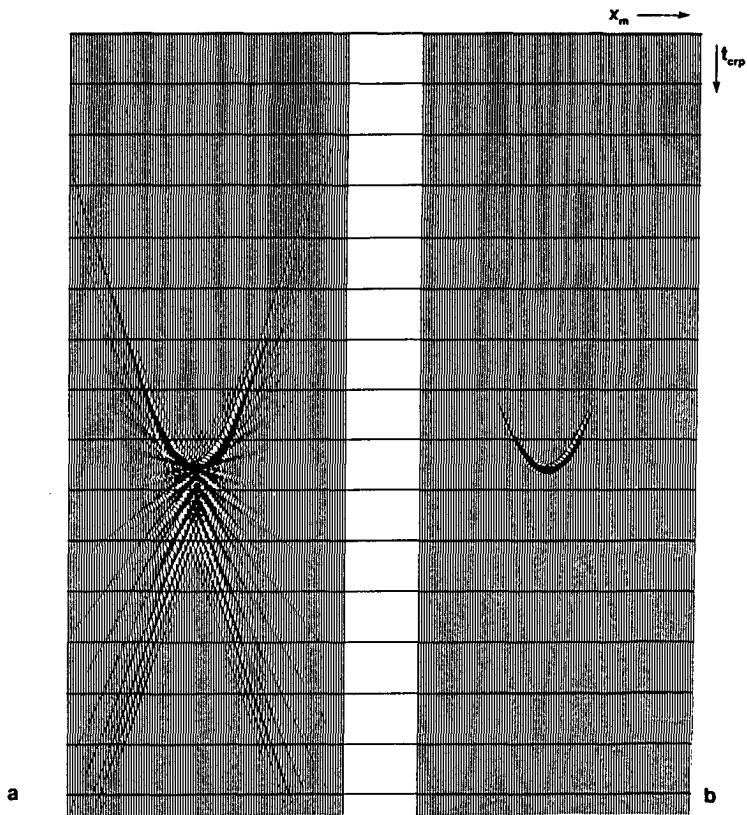


Figure II.16 Example of a poststack DMO operator (a), the offset is 1500 m and the dip filter increment is 10 degrees. b. shows the corresponding integral DMO operator.

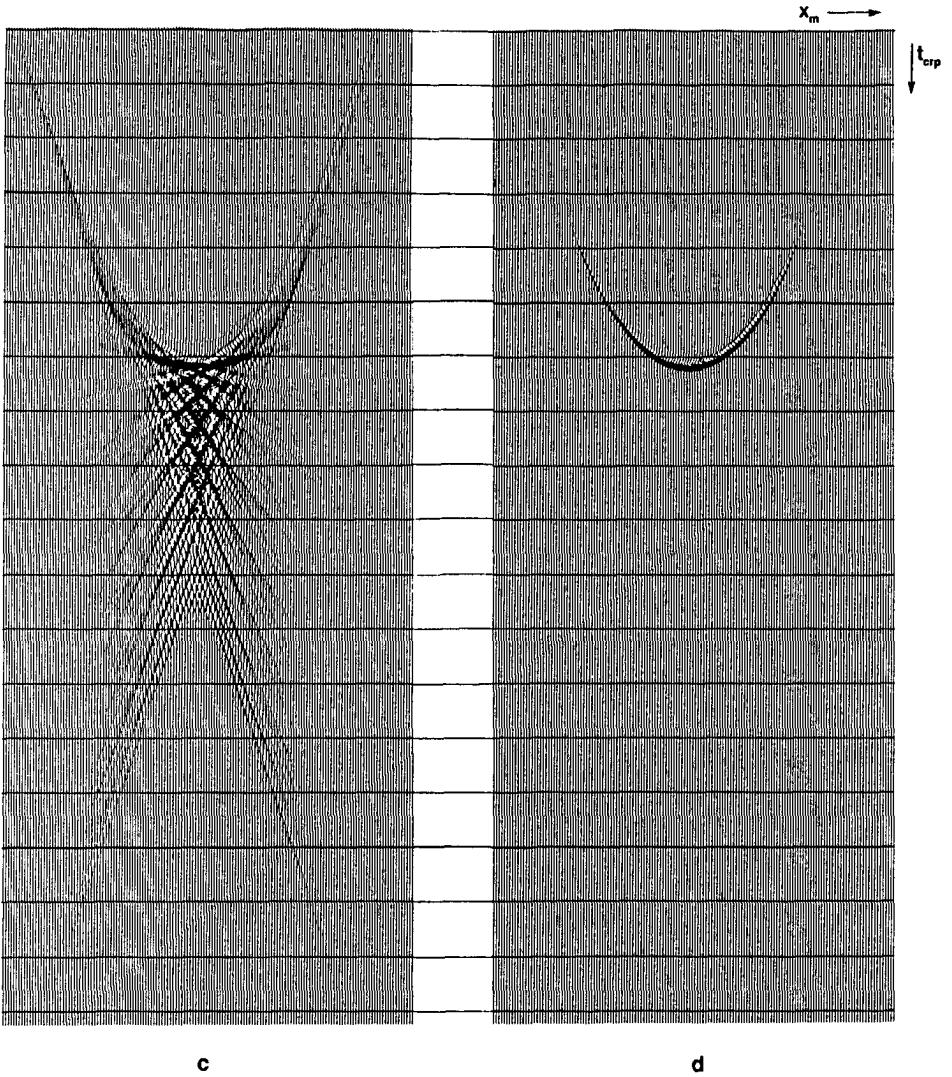


Figure II.16 (continued); Offset: 200 m; dip increment: 10 degrees. Note that the crosspoints of the different dip filters indicate the zero-offset time after NMO correction for the corresponding dip.

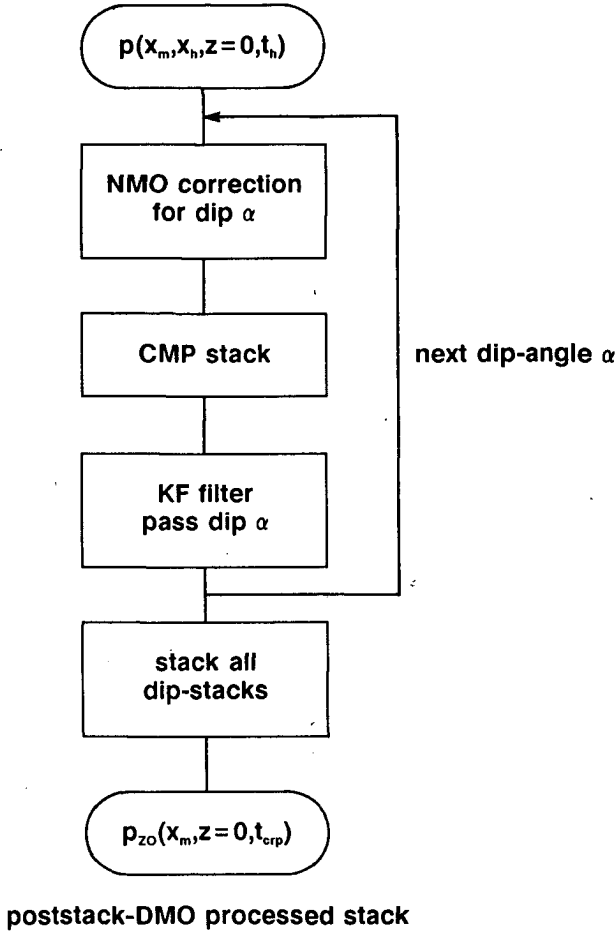


Figure II.17 Flow diagram of poststack DMO.

II.4.4 Finite-difference method

Bolondi et al. (1982) proposed a finite-difference implementation of a partial differential equation which approximates the DMO ellipse for a limited dip range. For high dip angles the solution to this equation will deviate from the DMO operator. The DMO implementations discussed sofar, are non-recursive implementations. They directly map the offset data into the zero-offset data plane.

However, the finite difference scheme is by nature recursive in all dimensions. This means that not only the time and CMP space axis need to be regular — which is normal practice — but also the offset distribution.

An advantage of recursive DMO is that each offset plane does not need to be converted to a zero-offset plane. Starting with the maximum offset, this constant offset section will be mapped to the nearest smaller offset section- and successively stacked. Then the mapping starts over again with the new constant offset plane being mapped to the following nearest smaller offset, and so on till the complete multi-offset data set has been mapped to zero-offset.

Because the DMO operator is applied recursively, it is also called "offset continuation". A flow diagram of a finite-difference scheme in the space-time domain is shown in figure II.18.

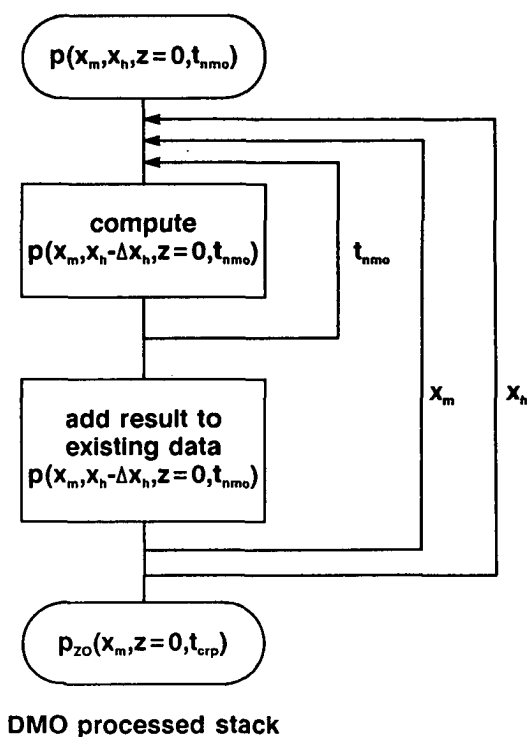


Figure II.18 Flow diagram of a finite-difference implementation of DMO.

A typical DMO operator, generated with a finite-difference scheme is shown in figure II.19.

Points of concern for finite difference implementations are the instability and the inaccuracy for larger dips (dispersion).

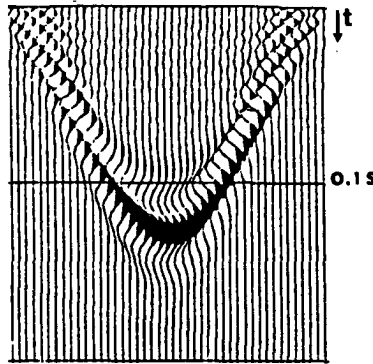


Figure II.19 Example of a typical finite-difference DMO operator. The offset is 1250 m (after Ristow (1988)). The number of continuation steps used is 200 ($\Delta h = 12.5$).

II.5 AMPLITUDE AND PHASE CHARACTERISTICS IN DMO

It has already been pointed out that DMO cannot be derived from the wave equation without approximations. While the traveltime characteristics of DMO are correct for constant velocity, the amplitudes will only be approximated.

In this section three descriptions of DMO amplitude weighting will be discussed. They can be considered as more or less representative of different types of approaches used to arrive at a proper amplitude and phase definition for DMO operators.

II.5.1 Wave-theoretical approach

Hale has made the most distinct attempt to put the ray-theoretical DMO process on a stronger wave-theoretical foundation. According to Hale, theoretically correct downward extrapolation and subsurface imaging can be described as follows.

1. Let $\tilde{P}(k_m, k_h, z=0, \omega)$ be the recorded wavefield at the surface, expressed in the wavenumber-frequency domain.
2. Apply the double square root downward continuation operator \tilde{F} (I.33), to the wavefield \tilde{P} :

$$\tilde{P}(k_m, k_h, \Delta z, \omega) = \tilde{F}(k_m, k_h, \Delta z, \omega) \tilde{P}(k_m, k_h, z=0, \omega) \quad . \quad (II.12)$$

3. Apply the imaging condition

$$p(x_m, x_h=0, z, t=0) = \frac{1}{(2\pi)^3} \int \int \int \tilde{P}(k_m, k_h, \Delta z, \omega) \exp[-jk_m x_m] dk_m dk_h d\omega \quad . \quad (II.13)$$

The DMO algorithm can now be derived by showing that each step in the conventional CMP processing sequence is precisely represented in equations (II.12) and II.13). The process remaining after successively eliminating the NMO correction, stacking and poststack migration processes from (II.12) and (II.13) must then represent the difference between conventional CMP processing and prestack migration. This leftover process is defined as DMO. In other words, DMO added to conventional CMP processing yields exactly the same subsurface image as prestack migration via equations (II.12) and (II.13). Notice that this only holds for constant velocity media.

The dissection of prestack migration as a cascade of CMP processes is quite lengthy and will not be given here. It turns out that no closed expression for DMO can be given. Only when we apply a high frequency approximation do we arrive at an expression for DMO which confirms the integral transformation (II.10), apart from an extra constant phase shift $\pi/4$ and an entirely different amplitude term.

It can be shown that the latter amplitude term for flat data — where DMO should do nothing — simplifies to

$$S\sqrt{\omega_{\text{crp}}} \quad , \quad (\text{II.14})$$

where S is a constant, absorbing all frequency-independent parameters.

Note, that for flat data the amplitude term $1/A$ in (II.10) will become equal to one. So, the $1/A$ term is at least correct for flat data.

Expression (II.14) is apparently wrong, since it implies that DMO amounts to an amplitude boost of 3 dB per octave on flat data.

The reason why the wave-equation based amplitude term is incorrect may be found in the way Hale has derived DMO from the wave equation. For instance, one problem that remains is that Hale does not account for a spherical divergence correction while on the other hand he applies an amplitude scaling in the NMO correction. A further investigation of this problem is beyond the scope of this dissertation.

It is remarkable that — although entirely based on ray-theory — DMO performed by (II.10), including the amplitude term, has widely been accepted as a reference for other DMO algorithms. This applies to kinematic as well as amplitude aspects.

Because the amplitude term $1/A$ is still an expression in the wavenumber-frequency domain, it is convenient to derive the corresponding space-time domain expression. This enables us to compare this weighting with other ones. Liner (1988) and Berg (1984) both determined this amplitude weighting in the space-time domain and arrived at

$$\sqrt{\frac{t_{crp}}{2\pi}} \frac{1}{x_h \left(1 - \frac{(x_m - x_0)^2}{x_h^2} \right)} \quad (II.15)$$

Deregowski (1985) showed that, in addition to the amplitude term (II.15), a windowed half-differential reversed time filter should be applied. This window ensures that the phase along the DMO operator changes in a time variant manner from 45 degrees at high offsets to zero at very small offset. This time variance is dictated by wave-theory (Deregowski (1985). Details are given in appendix A.

A clear comparative overview of the amplitude characteristics of several existing constant velocity DMO schemes is given by Liner (1988). He uses the DMO scheme of Hale (expressions (II.10,11)) as a reference for the other schemes. However, Liner does not come up with an amplitude weighting which is based on the wave theory.

II.5.2 Heuristic approach

An amplitude weighting for DMO operators which is based on heuristic arguments and appeals very well to physical intuition is given by Beasley (1988). We will pay ample attention to his method, because it gives a clear insight into the proper amplitude behaviour of DMO operators. An important aspect of the weighting proposed by Beasley is that not only the amplitude within a single DMO operator is balanced for different dips, but also that DMO operators for different offsets and times are mutually balanced. Balanced means that amplitudes are related on basis of certain (heuristic) arguments. The derivation of Beasley's weighting scheme is as follows.

Consider the DMO procedure proposed by Jakubowicz and described earlier. Provided that enough dips are used, this procedure should be equivalent to Hale's kinematic DMO scheme. According to Jakubowicz (and Hale) the DMO corrected wavefield, which we will denote by p_{DMO} , can be approximated by a sum over a number of wavefields

$$p_{DMO} = \sum_i p_{D(i)} \Delta D(i) \quad (II.16)$$

where $p_{D(i)}$ is the input wavefield, NMO corrected for a single dip $D(i)$ and $\Delta D(i)$ is the dip range surrounding $D(i)$.

From equation (II.16) a proper balancing of the amplitudes within a DMO operator can be derived. This is done by choosing $\Delta D(i)$ such that each trace in the DMO impulse response can be identified with a single term in equation (II.16). The determination of $\Delta D(i)$ goes as follows.

If t_{crp} is the DMO corrected zero-offset time, the dip D along the DMO ellipse reads

$$D = \frac{\partial t_{\text{crp}}}{\partial x_m} \quad (\text{II.17})$$

For ΔD it follows that, using expression (II.1),

$$\begin{aligned} \Delta D &= \frac{\partial D}{\partial x_m} \Delta x_m, \\ &= \frac{\partial^2 t_{\text{crp}}}{\partial x_m^2} \Delta x_m, \\ &= \frac{-t_{\text{NMO}}}{x_h^2 \left(1 - \left(\frac{x_m}{x_h}\right)^2\right)^{3/2}} \Delta x_m. \end{aligned} \quad (\text{II.18})$$

A proper weighting — for one DMO operator with offset $2x_h$ and time t_{NMO} —, balanced to unity at the center of the operator (that is for flat events) is thus approximately

$$W_I(x_m(i), x_h, t_{\text{NMO}}) = \frac{\Delta D(i)}{\Delta D(1)}, \quad (\text{II.19})$$

where $x_m(i)$ denotes the midpoint coordinate or trace position corresponding to dip $D(i)$ in the DMO operator. $\Delta D(1)$ corresponds to the center of the operator (where the dip angle and therefore x_m equals zero in expression (II.18)):

$$\Delta D(1) = -\frac{t_{\text{NMO}}}{x_h^2} \Delta x_m. \quad (\text{II.20})$$

Hence

$$\begin{aligned} W_I(x_m(i), x_h, t_{\text{NMO}}) &= \frac{\Delta D(i)}{\Delta D(1)}, \\ &= \frac{1}{\left(1 - \left(\frac{x_m}{x_h}\right)^2\right)^{3/2}}. \end{aligned} \quad (\text{II.21})$$

Expression (II.21) ensures that, for a given offset $2x_h$ and time t_{NMO} , dipping events are

balanced in relation to flat events (within one operator).

An additional weighting has to be applied to balance DMO operators for different offsets and traveltimes mutually.

A valid criterion for balancing operators for all offsets $2x_h$ and traveltimes t_{NMO} is that flat events in the stack should pass the DMO processing unaltered.

Therefore we compute the first Fresnel zone associated with the dominant frequency f_d in the data.

Consider a DMO operator depicted in figure II.20. For the dominant frequency f_d in the data, the width of the first Fresnel zone is defined by $1/2 t_d = 1/2 1/f_d$ and x_f (see figure II.20 for the symbols used).

Within $\pm x_f$ and $\Delta t_{crp} < 1/2 t_d$ all energy adds constructively. Recalling expression (II.1), setting x_0 to zero:

$$t_{crp}(x_m) = t_{NMO} \sqrt{1 - \left(\frac{x_m}{x_h}\right)^2} \quad , \quad (II.22)$$

we can write

$$\Delta t_{crp} < \frac{1}{2} t_d \quad , \quad (II.23a)$$

$$\rightarrow \left(1 - \sqrt{1 - \left(\frac{x_m}{x_h}\right)^2}\right) t_{NMO} < \frac{1}{2} t_d \quad , \quad (II.23b)$$

$$\rightarrow \sqrt{1 - \left(\frac{x_m}{x_h}\right)^2} > 1 - \frac{1}{2f_d t_{NMO}} \quad . \quad (II.23c)$$

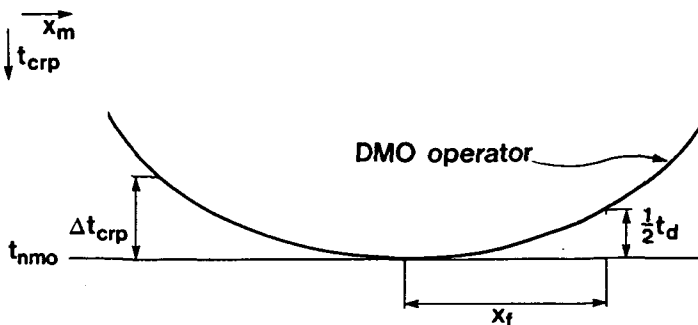


Figure II.20 Determination of the width of the first Fresnel zone for a DMO operator.

If we define $s = (2f_d t_{\text{NMO}})^{-1}$, then (I.23c) can be expressed as

$$\left(1 - \left(\frac{x_m}{x_h}\right)^2\right) > (1 - s)^2, \quad (\text{II.24a})$$

$$\rightarrow x_m < x_h \sqrt{2s - s^2}. \quad (\text{II.24b})$$

The number of traces N_x that add constructively within the first Fresnel zone is therefore

$$N_x = 2 \text{Int} \left(\frac{x_h \sqrt{2s - s^2}}{\Delta x_m} \right) + 1, \quad (\text{II.25})$$

where Int is the real to integer conversion function and Δx_m is the trace spacing.

Therefore normalizing the operators is done by multiplying the operators by

$$W_{\text{II}}(x_m, x_h, t_{\text{NMO}}) = \frac{1}{\text{Real}(N_x)} = \frac{\Delta x_m}{\left(\Delta x_m + 2x_h \sqrt{2s - s^2}\right)}, \quad (\text{II.26})$$

where Real is the integer to real conversion function.

The total weighting, as proposed by Beasley, therefore reads

$$W(x_m, x_h, t_{\text{NMO}}) = W_{\text{I}}(x_m, x_h, t_{\text{NMO}}) W_{\text{II}}(x_m, x_h, t_{\text{NMO}}), \quad (\text{II.27a})$$

$$= \frac{1}{\left(1 - \left(\frac{x_m}{x_h}\right)^2\right)^{3/2}} \frac{\Delta x_m}{\left(\Delta x_m + 2x_h \sqrt{2s - s^2}\right)}. \quad (\text{II.27b})$$

For realistic values of the different parameters, the following relation holds with good approximation

$$2s \gg s^2. \quad (\text{II.28})$$

This means that the second part of W can be rewritten as

$$W_{\text{II}}(x_m, x_h, t_{\text{NMO}}) \approx \frac{\Delta x_m}{\left(\Delta x_m + 2x_h \sqrt{2s}\right)}. \quad (\text{II.29})$$

The Δx_m in the denominator acts as a stabilization of the denominator. For realistic parameter values the second term in the denominator will be larger than Δx_m :

$$2x_h \sqrt{2s} \gg \Delta x_m. \quad (\text{II.30})$$

This means that W_{II} can be rewritten as

$$W_{II}(x_m, x_h, t_{NMO}) \approx \frac{\Delta x_m}{2x_h \sqrt{2s}} \quad , \quad (II.31a)$$

$$= \frac{\sqrt{t_{NMO}}}{2x_h} \Delta x_m \sqrt{f_d} \quad . \quad (II.31b)$$

Using these approximations, W can be rewritten as

$$W(x_m, x_h, t_{NMO}) = \frac{\sqrt{t_{NMO}}}{2x_h} \Delta x_m \sqrt{f_d} \frac{1}{\left(1 - \left(\frac{x_m}{x_h}\right)^2\right)^{3/2}} \quad . \quad (II.32)$$

Apart from the exponent 3/2 and some constants this weighting is quite similar to the weighting proposed by Hale, and given by (II.15). We may therefore expect a good agreement between both algorithms in practice.

The weighting defined by expressions (II.27) and (II.32) is one based on a constant trace increment Δx_m . So far we followed Beasley (1988).

A similar kind of weighting could be derived for a constant dip or dip angle increment.

The easiest way to arrive at such a weighting is to start with expression (II.27b) and transform that expression into one for constant dip or angle increment.

The relations between these increments are given by

$$\Delta x_m = \frac{\partial x_m}{\partial D} \Delta D \quad , \quad (II.33a)$$

$$= \frac{\partial x_m}{\partial D} \frac{\partial D}{\partial \alpha} \Delta \alpha \quad , \quad (II.33b)$$

where α denotes the dip angle.

Since

$$\frac{\partial x_m}{\partial D} = \left(\frac{\partial^2 t_{crp}}{\partial x_m^2} \right)^{-1} \quad , \quad (II.34)$$

(see also II.18)), it follows that

$$\frac{\partial x_m}{\partial D} = \frac{-x_h^2 \left(1 - \left(\frac{x_m}{x_h} \right)^2 \right)^{3/2}}{t_{NMO}} \quad (II.35)$$

Multiplying this Jacobian with the weighting (II.27) leads to the following expression

$$W(D, x_h, t_{NMO}) = \frac{-x_h^2}{t_{NMO}} \frac{\Delta x_m}{\left(\Delta x_m + 2x_h \sqrt{2s - s^2} \right)} \quad (II.36)$$

Note, that although the dip increment does not explicitly appear in (II.36), the weighting holds for a constant dip increment. The increment is just defined by the trace spacing of the output grid of the data.

Going to angle increments implies incorporating

$$\frac{\partial D}{\partial \alpha} = \frac{\partial}{\partial \alpha} \left(\frac{\partial t_{crp}}{\partial x_m} \right), \quad (II.37a)$$

$$= \frac{\partial}{\partial \alpha} \left(\frac{2 \sin \alpha}{c} \right), \quad (II.37b)$$

$$= \frac{-2 \cos \alpha}{c} \quad (II.37c)$$

The absolute value of this Jacobian should be taken, for reason of symmetry for positive and negative dip.

The weighting factor now becomes

$$W(\alpha_m, x_h, t_{NMO}) = \frac{x_h^2}{t_{NMO}} \frac{2 \cos \alpha}{c} \frac{\Delta x_m}{\left(\Delta x_m + 2x_h \sqrt{2s - s^2} \right)} \quad (II.38)$$

Note that results (II.36) and (II.38) could also have been derived directly following a similar strategy as was used in the derivation of expression (II.27).

Expression (II.38) can be approximated by again using assumption (II.28), that is $2s \gg s^2$. Together with the (realistic) assumption

$$\Delta x_m \ll 2x_h \sqrt{2s - s^2}$$

the weighting factor becomes

$$W(\alpha, x_h, t_{NMO}) = \frac{x_h}{\sqrt{t_{NMO}}} \frac{\cos \alpha}{c} \Delta x_m \sqrt{f_d} \quad (II.40)$$

SUMMARY OF MAIN RESULTS

The following weighting factors have now been derived:

Constant trace increment

$$W(x_m, x_h, t_{NMO}) = \frac{1}{\left(1 - \left(\frac{x_m}{x_h}\right)^2\right)^{3/2}} \frac{\Delta x_m}{\left(\Delta x_m + 2x_h \sqrt{2s - s^2}\right)}, \quad (II.41a)$$

$$\approx \left(\frac{1/2 \sqrt{f_d} \Delta x_m}{\left(1 - \left(\frac{x_m}{x_h}\right)^2\right)^{3/2}} \right) \frac{\sqrt{t_{NMO}}}{x_h} \quad (II.41b)$$

Constant angle increment

$$W(\alpha, x_h, t_{NMO}) = \frac{x_h^2}{t_{NMO}} \frac{2 \cos \alpha}{c} \frac{\Delta x_m}{\left(\Delta x_m + 2x_h \sqrt{2s - s^2}\right)}, \quad (II.42a)$$

$$\approx \left(\frac{\sqrt{f_d} \Delta x_m \cos \alpha}{c} \right) \frac{x_h}{\sqrt{t_{NMO}}} \quad (II.42b)$$

A closer look at the weighting factor (II.41a) reveals the following properties:

- For an offset going to zero the weighting becomes one, assuming $x_m \ll x_h$. In other words, the weighting leaves zero-offset traces unaltered.
- For large times, x_m as well as s will go to zero. This means that the weighting again goes to one.
- Note, that the Δx in the denominator acts as a kind of stabilization factor for $x_h = 0$.
- The weighting will increase for higher dips.

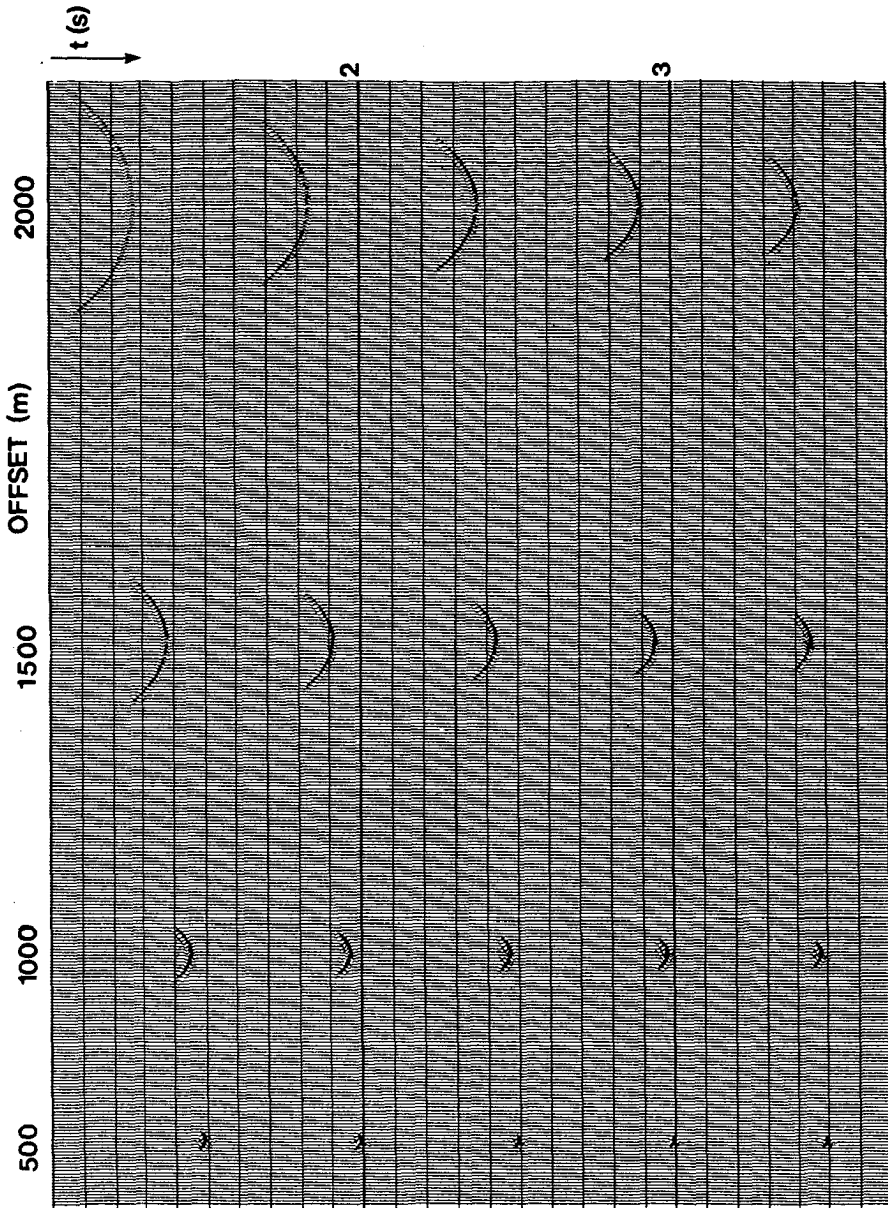


Figure II.21 Set of DMO operators with weighting scheme (II.42a) implemented. Note that the operators are well balanced.

Comparing weighting (II.41a,b) to (II.42a,b) leads to the following conclusions:

- The major part in expression (II.42b) $x_h/\sqrt{t_{NMO}}$ is exactly the reverse of the corresponding term in (II.41b). This can be explained by considering that for smaller offsets energy for all dip angles is mapped to a decreasing number of traces. In the limit all energy is mapped to one trace. Therefore the weighting for smaller offsets should be smaller than for larger offsets. Conversely, in the expression for constant trace increment, a summation of energy over different traces is accomplished. For larger x_h , the width of the operator is bigger, so the weighting should decrease for larger offset.
- The same argument also holds for larger traveltimes, since the energy for many dip angles is then mapped on fewer traces.

In chapter III, section 2 we will relate the density of the dip angle sampling to the density of the spatial increment sampling.

Weighting scheme II.42a has been used in generating the DMO impulse responses depicted in figure II.21. We see that the DMO operators are well balanced, mutually as well as individually. Figure II.22 shows a close up of one of the operators, for offset 1500 m.

We see that the amplitude along the operator is well balanced. It can also be seen that at the steep dip part of the operator the response has a lower frequency contents, due to anti-alias protection. The anti-alias protection has been applied per dip angle and per temporal frequency.

For any dip, given the spatial Nyquist frequency, the aliasing temporal frequency is easily computed using the DMO expression (II.22) in combination with the normal definition of dip in the zero-offset domain in terms of wavenumber.

The importance of anti-alias filtering will be shown with synthetic data examples.

II.5.3 Simple amplitude tapering

An entirely different weighting has been proposed by Deregowski (1985). He suggests that the DMO operator should simply be weighted according to the requirement that the amplitude goes to zero at the maximum time slope of the operator:

$$W(x_m, x_h, t_h) = \frac{1}{\sqrt{x_{max}}} \left(1 - \frac{x_m^2}{x_{max}^2} \right), \tag{II.43a}$$

with

$$x_{max} = \frac{2x_h^2}{c_{DMO}t_h}, \tag{II.43b}$$

already defined in (II.2).

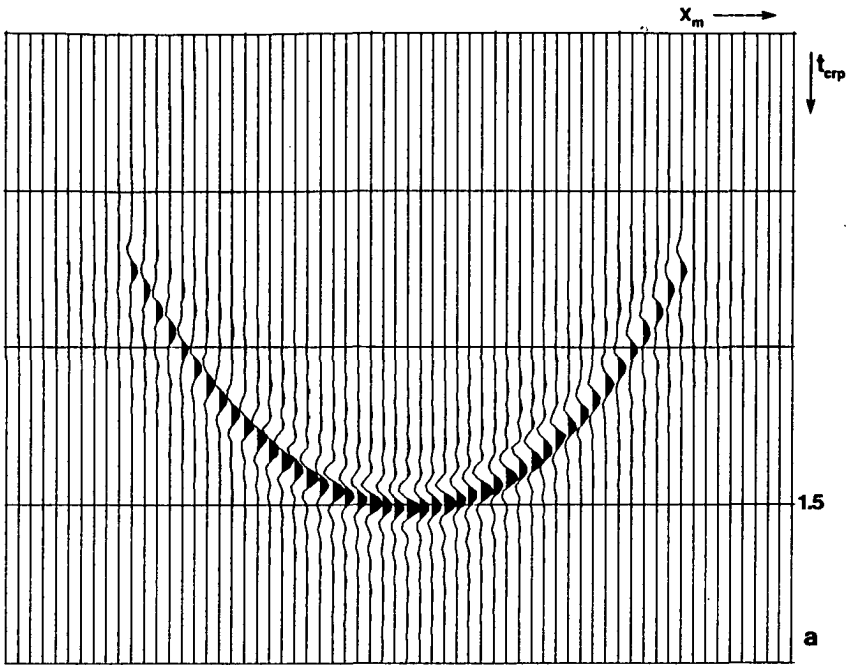


Figure II.22a DMO operator (offset 1500 m), with weighting (II.42a) applied. No anti-alias protection has been implemented. This can be seen in figure II.22c.

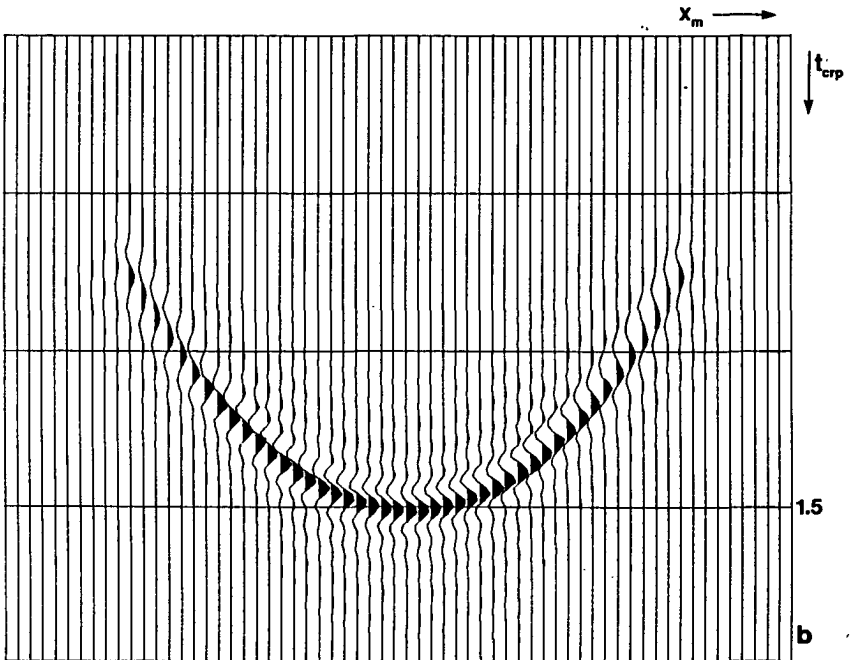


Figure II.22b As a., but with an anti-alias protection, see d.

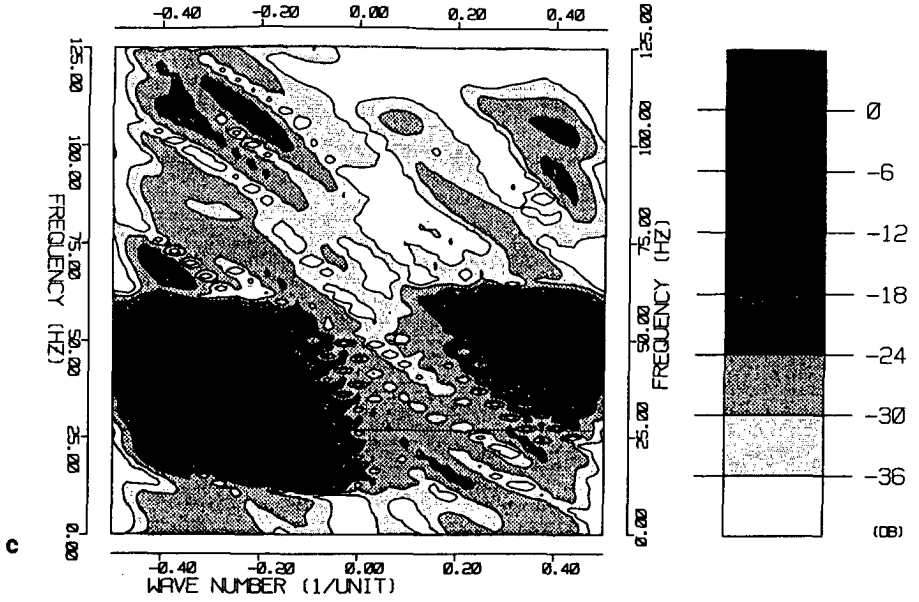


Figure II.22c KF-spectrum of the left part of the operator of figure II.22a. Note the aliasing energy at the right side.

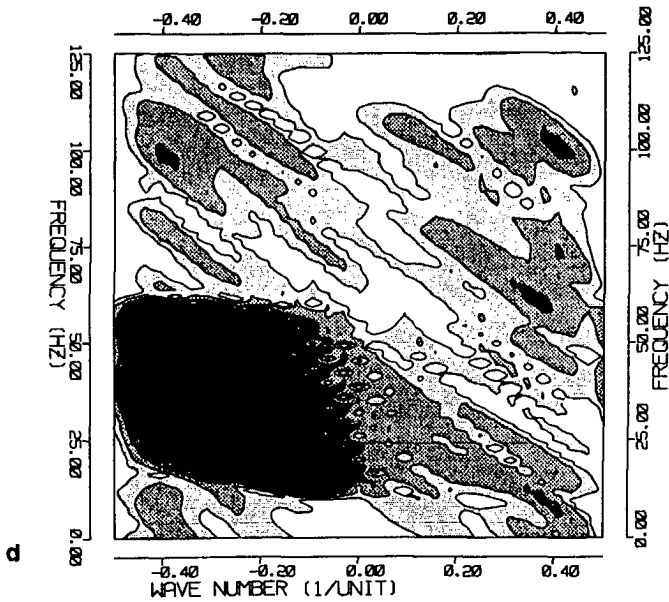


Figure II.22d KF-spectrum of the left part of the operator in figure II.22b. Note that no aliasing energy is present.

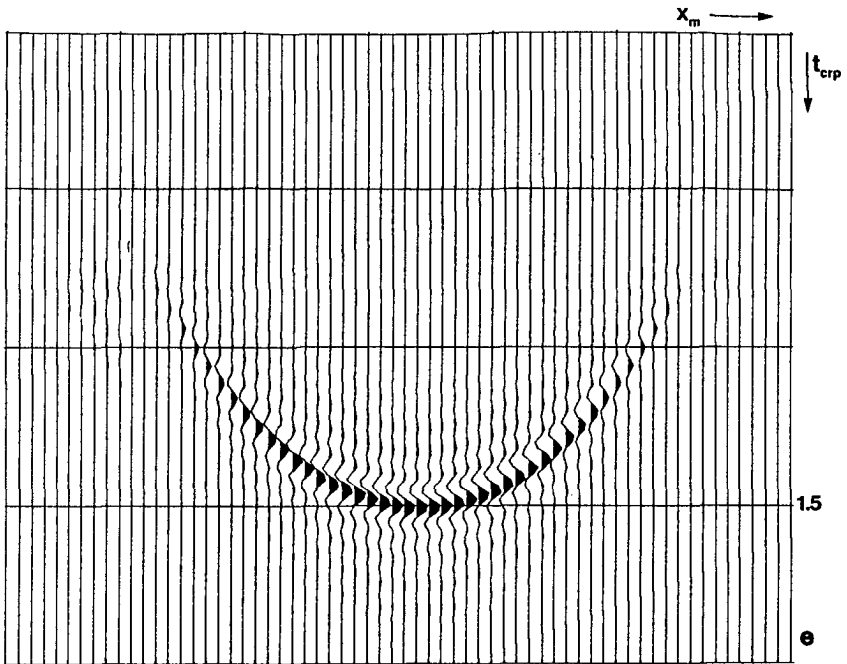


Figure II.22e For comparison, a DMO operator with the weighting (II.15), proposed by Deregowski, has been implemented. Note that the steep dips are relatively suppressed.

An example of this weighting is shown in figure II.22e.

The only argument for using this weighting is to avoid truncation effects along the operator.

II.5.4 Summary

A proper choice for an amplitude weighting is difficult, since a correct wave equation based balancing (if possible) has not yet been derived.

The question of how important a proper weighting scheme is, is difficult to assess. This especially holds for real data, where the approximations made when we use a constant velocity scheme are probably a magnitude of order larger than the approximations made in the different amplitude weighting schemes.

On the other hand, however, many spurious events can be generated by a wrongly balanced DMO operator. We could think for instance of aliasing noise, insufficient cancellation of energy, checker board effects etc. These events are often seen on real data especially in the shallow parts.

A proper weighting of amplitudes is also essential for amplitude versus offset analyses. This also holds for migration velocity analyses on DMO processed multi-offset data. We have chosen — and adapted to a constant dip increment — the weighting proposed by Beasley, because this weighting is based — albeit heuristically — on clear amplitude balancing considerations.

III

CRP STACKING IN CONSTANT VELOCITY MEDIA

III.1 INTRODUCTION

In the previous chapter it was shown that the DMO concept is derived on constant offset sections.

Such a derivation such does of course not imply that the DMO algorithms are necessarily applied on constant offset sections.

In a DMO algorithm we can recognize two essential parameters:

1. the apparent dip angle;
2. the offset.

If DMO is applied per constant offset, it means that for a chosen offset the dip angle is varied.

In this chapter we will again derive a DMO algorithm for constant velocity media. But now the underlying concept is that for a chosen dip angle the offset is varied. For constant velocity media this seems to be a superfluous exercise, since interchanging the offset loop and dip angle loop in a DMO algorithm will not alter the output. For inhomogeneous media, however, the description of DMO in terms of an operator per dip angle for varying offset will be of fundamental importance.

To stress the difference — even for constant velocity media — between the role of dip and offset, we will from now on only use the name Common Reflection Point (CRP) stacking if multi-offset operators are used. The name DMO will only be used to indicate the constant offset algorithms for constant velocity models derived in the previous chapter.

This chapter starts with a derivation of CRP stacking for constant velocity media based on kinematic arguments. The reflection point smearing formula derived by Levin (1971) is the starting point. Having described CRP stacking, the relationship with the DMO formulation presented in chapter II will be shown. In section 3 attention will be paid to the amplitude characteristics of CRP stacking. In section 4 the possibility of prestack migration by CRP processing is discussed and illustrated with a synthetic data example. In section 5 examples will be shown, to illustrate the concepts. Finally, in section 6, a summary together with the main conclusions will be given.

III.2 A KINEMATIC DERIVATION OF CRP STACKING

In section 2 of chapter II, it was stated that after DMO processing, CMP gathers contain reflections from common depth points as defined by normal incidence rays. That is, reflection point dispersal for non-zero offset traces is removed.

This claim will now be the starting point for an alternative look at DMO.

We therefore consider a dipping reflector in a constant velocity medium, see figure III.1.

In this figure a zero-offset and a non-zero offset travelpath, belonging to the same CMP gather, are depicted. Conventional CMP processing would involve a travelttime correction of offset travelttime t_h to the zero offset time t_0 followed by stacking. This means that the reflection point smearing l is included in the process.

The reflection point smearing can only be removed by a travelttime correction of offset travelttime t_h according to the zero offset time t_{crp} along the normal incidence ray to the reflection point. This implies that the corresponding surface midpoint position is “smeared” over a distance $x_m - x_0$, from midpoint x_0 to the new midpoint x_m . In other words, in CRP processing the data from one CMP gather is mapped to other CMP gathers.

This has been visualized in figure III.2.

A more quantitative analysis of the reflection point smear versus the midpoint “smear” will now be given.

According to Levin (1971), the distribution of reflection points along a reflector is defined by

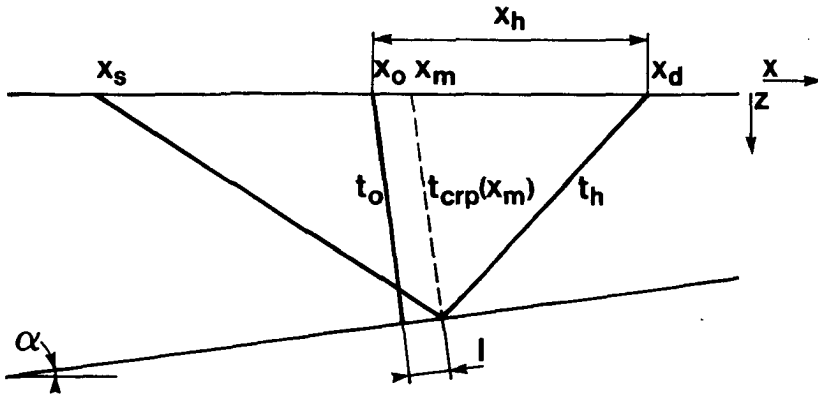


Figure III.1 Dipping reflector in a constant velocity medium.

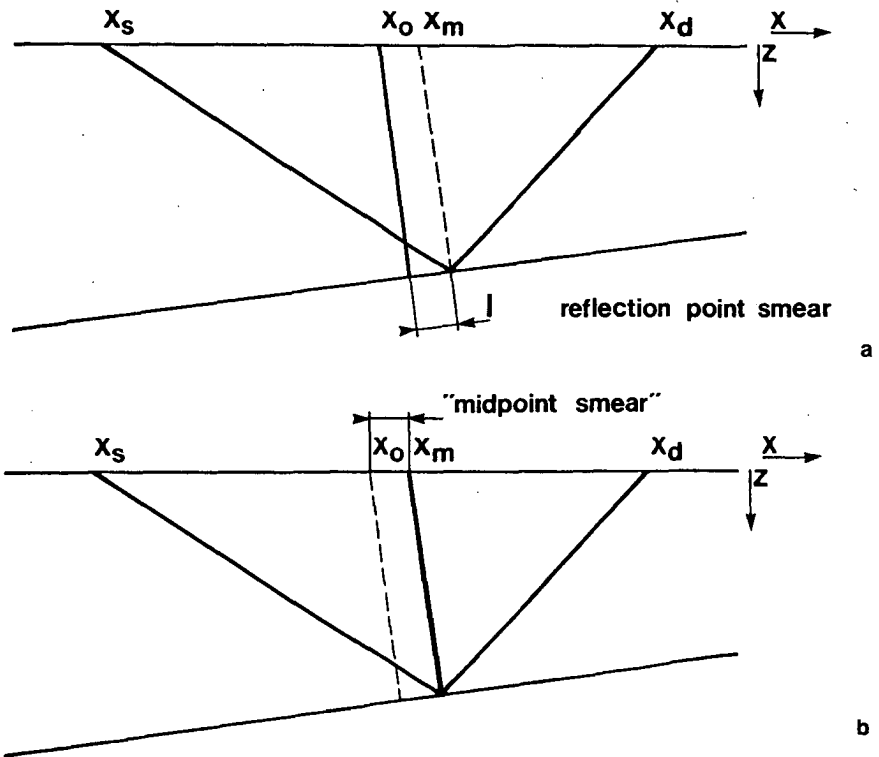


Figure III.2 In CMP processing the data from one common midpoint is corrected and stacked, thus causing the reflection point to be smeared (a). In CRP processing the data from one CMP gather is mapped to other CMP gathers, thus causing the midpoint to be "smeared" (b).

$$l = \frac{x_h^2}{\frac{c}{2} t_0} \sin \alpha \cos \alpha \quad (\text{III.1})$$

or

$$x_m - x_0 = \frac{x_h^2}{\frac{c}{2} t_0} \sin \alpha \quad , \quad (\text{III.2})$$

where

- l = reflection point smear
 x_m = surface midpoint of normal incidence ray to reflection point
 x_0 = CMP midpoint
 x_h = half offset
 c = medium velocity
 t_0 = zero offset traveltime
 α = dip angle of reflector

Furthermore the offset traveltime t_h is related to the zero-offset travel t_0 by the well known hyperbolic moveout equation

$$t_h^2 = t_0^2 + \frac{4x_h^2}{c^2} \cos^2 \alpha \quad . \quad (\text{III.3})$$

Finally, from the geometry in figure III.1 it can be determined that the relation between t_0 and t_{crp} (the latter being the zero-offset time along the normal incidence ray to the reflection point) is given by

$$t_{\text{crp}}(x_m) = t_0 - \frac{\sin \alpha}{\frac{c}{2}} (x_m - x_0) \quad . \quad (\text{III.4})$$

Using these formulae CRP processing can be described as follows:

1. Choose a dip angle α .
2. Apply a α -dependent moveout correction to the CMP data.
3. Apply for each offset $2x_h$ a lateral shift according to (III.2) followed by a temporal shift according to (III.4).
4. Repeat the process for the next dip angle.

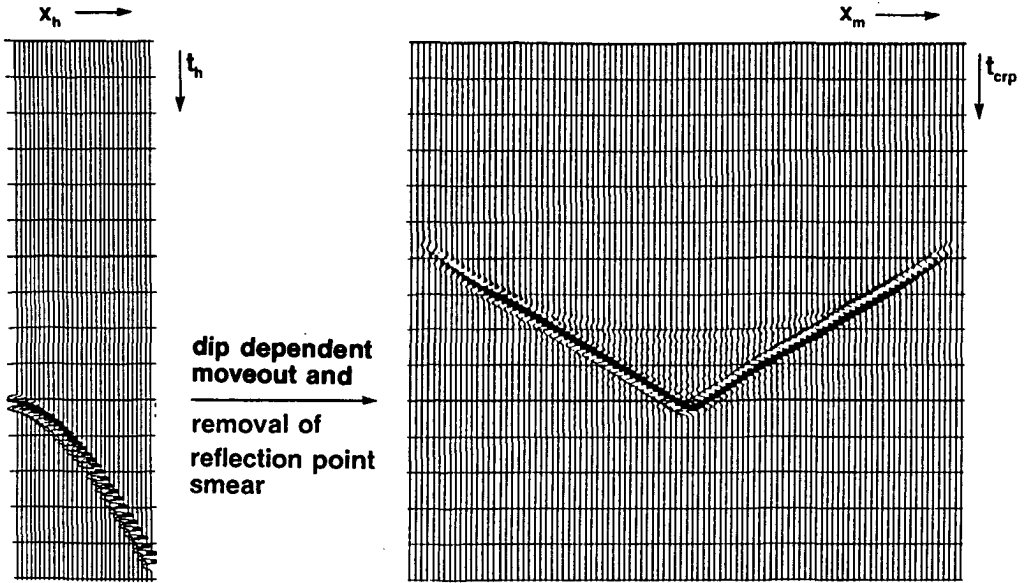


Figure III.3 CRP processing applied on one CMP gather. a: input CMP gather; b: CRP V-pattern.

This procedure is visualized in figure III.3 for one dip angle.

For a single CMP gather we cannot discriminate between positive and negative dip, as can be witnessed in expression (III.3).

If we process such an isolated CMP gather — with one hyperbolic event — for a single dip plus or minus α , the CRP processing transforms the CMP gather into a kind of V-pattern in the zero-offset domain, figure III.3b. The branches of the V-pattern correspond to the negative and positive α dip respectively.

The slopes of the branches of the V-pattern in the zero-offset domain can be determined using formula (III.4) and read

$$\frac{dt_{crp}}{dx_m} = \frac{-\sin \alpha}{c/2} \quad (III.5)$$

Since the dip of a single reflector in the zero-offset domain is described by

$$\frac{dt_0}{dx} = \pm \frac{\sin \alpha}{c/2} \quad (III.6)$$

(the sign also depends on the convention used in the dip definition), we see that one branch of the V-pattern has a slope identical to the slope of the zero-offset reflector. This is not surprising, since CRP processing as presented here performs a traveltme correction and

lateral shift according to the normal incidence ray paths to the reflector surface. The same normal incidence raypaths also constitute the zero-offset traveltimes of the reflector.

The other branch has a slope in the opposite direction. A synthetic data example is shown in figure III.4a. In a constant velocity medium the reflectivity data from one reflector, for one CMP gather has been CRP stacked, showing a V-pattern. Figure III.4b shows a sparse set of CRP stacked CMP gathers.

In figure III.4c all traces have been CRP stacked. Note that nearly all energy of the branches opposite to the reflector dip has been cancelled.

The question remains how the CRP stacking process described here, can be related to the constant offset DMO operator described in chapter II by expressions (II.1) and (II.2).

In order to answer this question we imagine the following experiment.

Suppose we have a constant velocity medium with one reflecting interface. The dip angle of the normal incidence ray to the reflector is unknown. Now we acquire a dataset containing one offset trace — with offset $2x_h$ — for a certain CMP gather at position x_0 . The offset trace will contain only one impulsive event at time t_h .

According to the same arguments used in section II.4.2, we can define the relation between the zero-dip zero-offset time t_{NMO} and dip dependent zero-offset time t_0 , both corresponding to a fixed value of t_h . The relation reads:

$$t_{NMO}^2 = t_0^2 - \frac{4x_h^2}{c^2} \sin^2 \alpha \quad (III.7)$$

Using this relation in combination with expressions (III.2) and (III.4) yields (see appendix B):

$$t_{crp}(x_m) = t_{NMO} \sqrt{1 - \frac{(x_m - x_0)^2}{x_h^2}} \quad (III.8)$$

With the maximum value of $x_m - x_0$ equal to

$$x_{max} = \frac{2x_h^2}{ct_h} \quad (III.9)$$

Expressions (III.8) and (III.9) are identical to the integral representation of the constant offset DMO algorithm, given by expressions (II.1) and (II.2).

This confirms that — for constant velocity media — both methods will yield identical results. Deregowski (1982) also showed — using an alternative approach — that the application of the integral DMO operator (III.8) just compensates the reflection point smear.

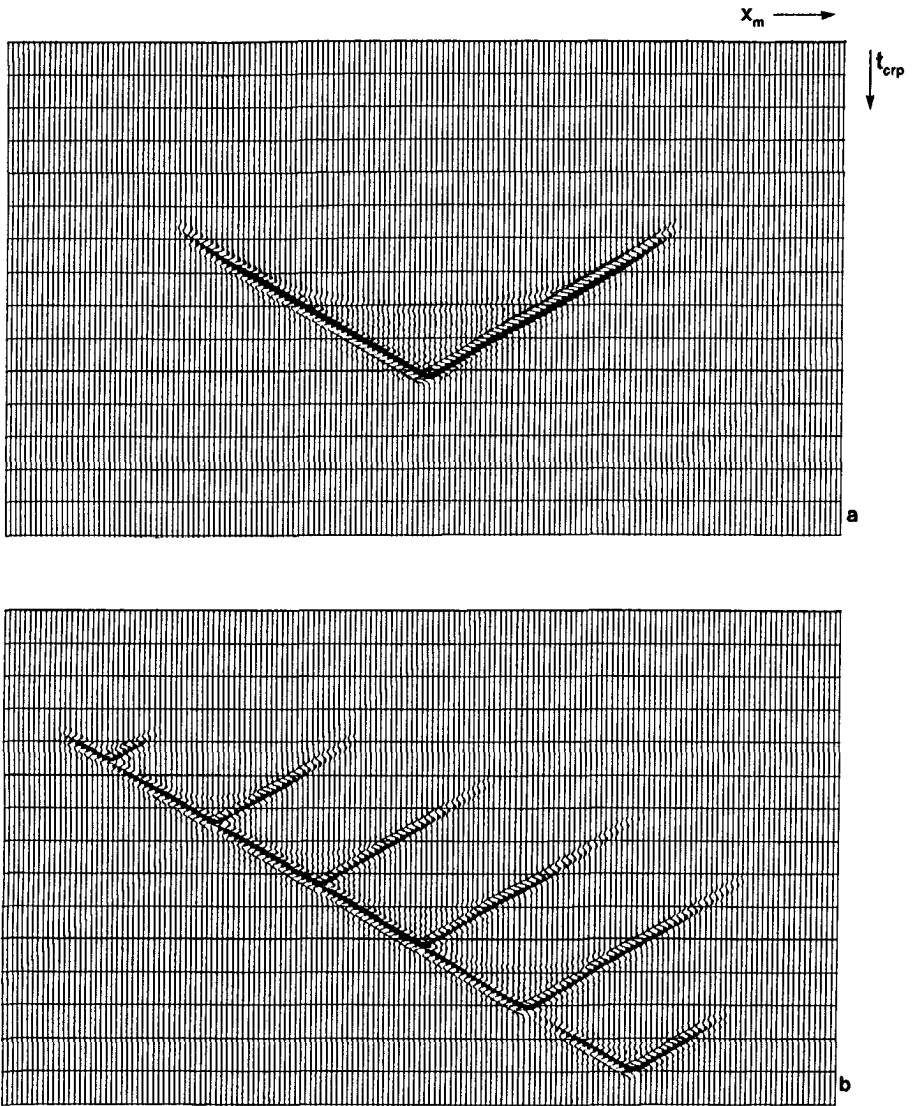


Figure III.4 CRP processing of reflectivity data obtained from one dipping reflector in a constant velocity medium. (The corresponding macro model is shown in figure IV.1, chapter IV).

a. Data corresponding to one CMP gather after CRP processing

b. A sparse set of CRP processed CMP gathers.

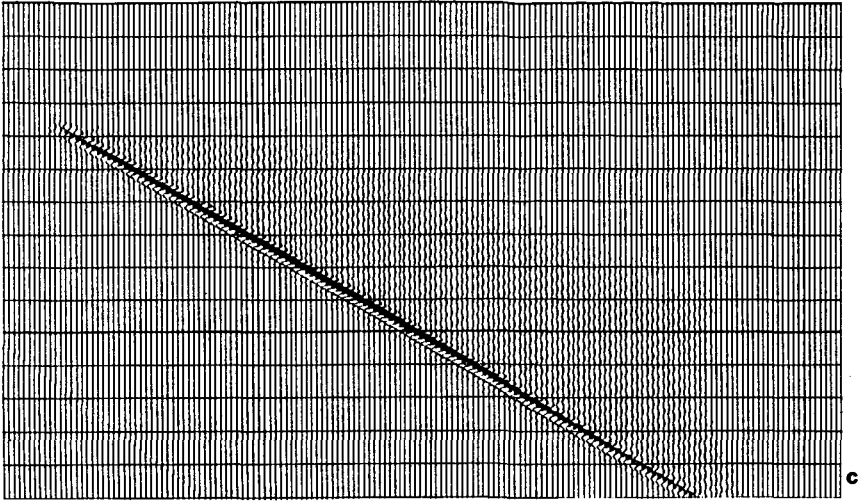


Figure III.4c All CMP gathers CRP processed. Note that all V-pattern branches with opposite slope to the reflector have been cancelled.

Apart from the mathematical confirmation of the compatibility of the different approaches to CRP processing, we can also evaluate both approaches geometrically.

The geometrical link is easy to understand if we realize that the dataset we started with (that is one impulsive event on one offset trace in only one CMP gather) is the one we would acquire from a semi-elliptical subsurface structure. This was explained in section II.3.

It follows then that the single reflector with an unknown dip angle α is just the tangent at any point on the (hypothetical) elliptical structure. The geometrical relation is shown in figure III.5.

It follows that in the zero-offset domain the dipping reflector is also tangential to the reflection event corresponding to the elliptical reflector. Since the latter is the DMO impulse response, it is clear that for a given reflector dip α the DMO operator should be tangential to the dipping reflector. This can be shown as follows.

Starting with the description of the DMO impulse response given by (III.8), the time-dip in the zero-offset domain is given by

$$\frac{\partial t_{\text{crp}}}{\partial x_m} = \frac{-(x_m - x_0) t_{\text{NMO}}}{x_h^2 \sqrt{1 - \frac{(x_m - x_0)^2}{x_h^2}}} \quad (III.10)$$

Substituting (III.2) and (III.7) we arrive at the expression

$$\frac{\partial t_{crp}}{\partial x_m} = -\frac{\sin \alpha}{c/2} \quad (III.11)$$

which is identical to the reflector dip (III.5).

The remaining question is how the DMO impulse response builds the V-pattern shown in figure III.4a.

Let us therefore consider a CMP gather with a sparse set of traces, acquired from the dipping reflector geometry shown in figure III.6. Then zero-dip NMO plus DMO involves smearing along a set of DMO operators — corresponding to the different offsets — which are all tangential to the reflector in the zero-offset domain.

The tangent points will be distributed in agreement with the reflection point smearing depicted in figure III.6; see figure III.7.

If we consider all traces in the CMP gather we end up with the envelope of the sum of all DMO operators, that is the V-pattern depicted in figure III.4a. See also Bolondi and Rocca (1984).

An item that needs some consideration is the density of dip sampling versus the density of lateral sampling used to build a DMO (or a CRP) operator. This relation is worked out in appendix C. It turns out that, especially for small zero-offset traveltimes, large offsets and small dip angles, the spatial increment corresponding to a constant dip angle increment may become too large. This means that in this situation a finer dip angle sampling should be chosen, to avoid empty traces in the operator.

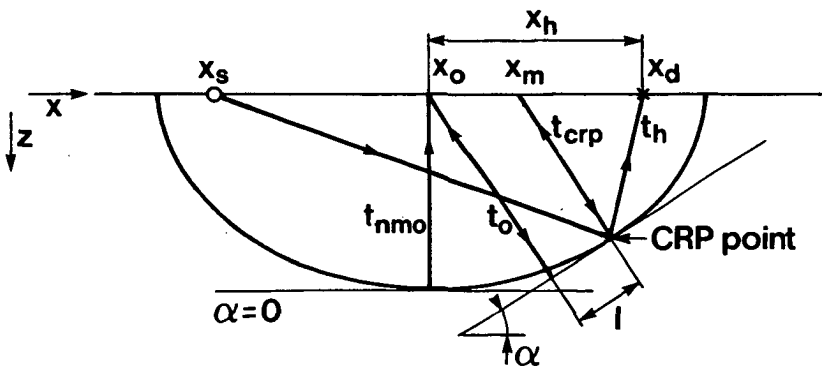


Figure III.5 Geometry and relevant traveltime parameters of an elliptical and dipping reflector.

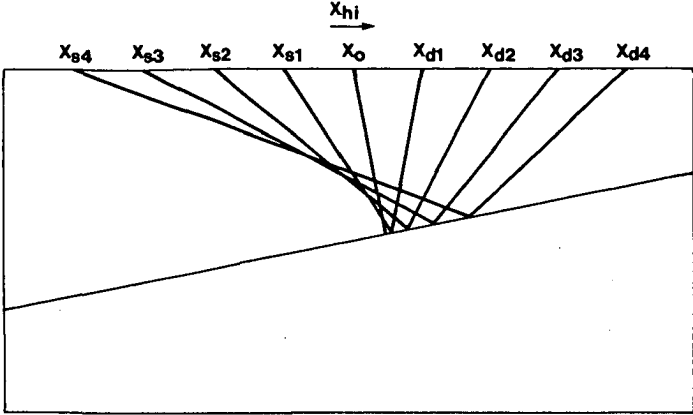


Figure III.6 Sparse set of travelpaths in a single CMP gather.

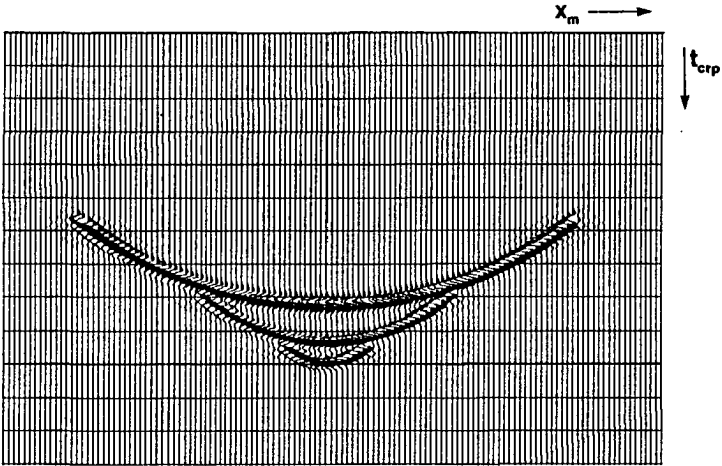


Figure III.7 Superposition of a sparse set of (three) DMO operators corresponding to different offsets ($2x_h = 740, 1340, 2340$ m respectively).

Because CRP processing ensures proper multi-dip correction, diffraction energy will be handled correctly. This can easily be deduced from the theory developed so far. Consider for instance figure III.5. Let the CRP point be a diffractor. For the specific shot-receiver pair in this figure and the travelttime t_h , the diffractor lies on the ellipse and has an apparent

dip angle α . Therefore mapping from t_h to $t_{\text{crp}}(x_m)$ will properly correct the diffraction energy. For any other shot-receiver pair — with respect to position as well as offset — and corresponding travel time t_h a similar ellipse can be imagined, going through the diffractor and leading to a proper correction. We conclude that CRP processing guarantees a correct treatment of diffraction energy. This will also be shown in section III.4 by means of a synthetic data example.

III.3 AMPLITUDE AND PHASE CHARACTERISTICS OF CRP STACKING

The same conclusions derived for DMO operators for constant offset sections hold for the CRP stacking scheme discussed in this chapter.

Therefore it is sufficient to apply the different amplitude weightings (and phase characteristics) directly to the V-patterns of the CRP stacking impulse response.

III.4 PRESTACK MIGRATION BY CRP PROCESSING

The derivation of CRP stacking presented so far in this chapter, reveals an important property of the depth oriented approach, not shared by the time-oriented DMO approach. Namely, the underlying Levin formula (III.1) that contains all ingredients necessary to carry out a direct mapping of multi-offset data to their correct lateral and vertical position in depth. This can be seen as follows. Consider a constant velocity macro model and a normal incidence ray to a (hypothetical) reflector. If the ray has an emergence angle α , to the surface at position x_0 and the medium velocity c and the zero-offset traveltime t_0 are known, then the endpoint of the ray on the reflector is completely determined. Now Levin's formula (III.1) dictates the amount and direction of the reflection point smear for all offsets in the CMP gather at x_0 . So this formula indeed can be used to carry out a prestack migration, which we will call CRP prestack migration.

Note that CRP prestack migration will also migrate diffraction energy properly. An example of this will be shown in figure III.9.

An example of the migration properties of the CRP algorithm is given in figure III.8. This figure shows the CRP prestack migration result of the input data and model depicted in figure I.3. Note, that the output grid is more finely spaced than the input grid.

This reveals the very important property of CRP processing that it is in fact a repositioning process. Data is repositioned according to its real reflection point in depth (CRP prestack migration) or to its real normal incidence ray with respect to traveltime as well as surface

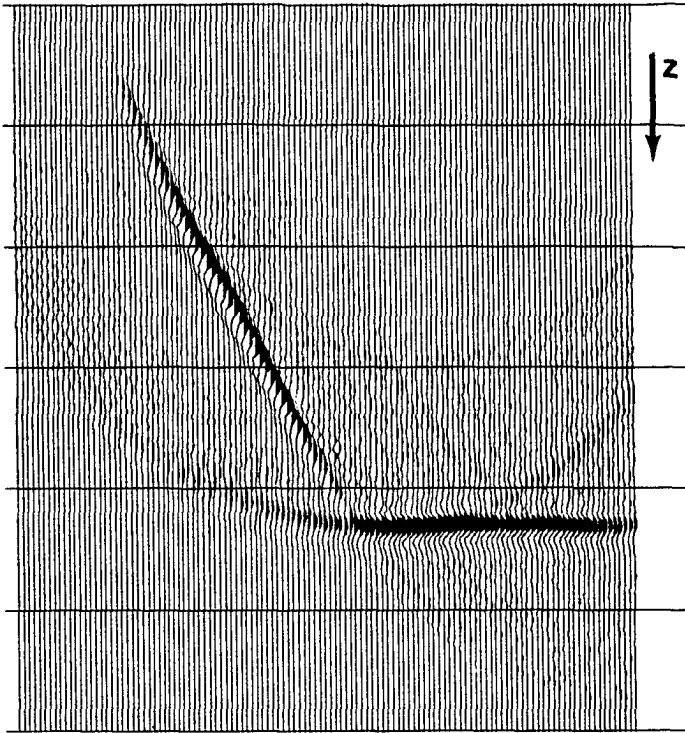


Figure III.8 CRP prestack migrated shot record. The input record is shown in figure I.3b. Compare this result with the result of wave-equation based shot record migration, figure I.3c.

position (CRP stacking). This repositioning need not necessarily be done on the same grid (trace spacing) as the CMP stack. It should be done on a much finer grid, thus acknowledging the dense subsurface sampling accomplished by multi-offset data (see also Bolondi (1982)).

III.5 EXAMPLES OF THE APPLICATION OF CRP PROCESSING IN CONSTANT VELOCITY MEDIA

Although the DMO schemes described so far are based on a constant velocity assumption, they are widely used in the industry, with more or less success. A number of examples have already been shown in section II.2 .

In this section we discuss two examples of CRP processing of data from a constant velocity medium.

The first example contains data from a single diffractor, see figure III.9a. Figure III.9b shows a sparse set of CMP gathers. Selection of one constant offset from all CMP gathers yields the common offset section depicted in figure III.9c. CRP processing of this common offset section results in the zero-offset diffractor response depicted in figure III.9d. Note, that two other phenomena can be observed. Due to the finite length of the diffraction tails in figure III.9c we get some edge effects at the apex of the diffraction. The second phenomenon is the aliasing energy remnant in the CRP zero-offset result. Since the CRP operator has a built-in aliasing protection the aliasing energy stems from the input data . Figure III.9f shows the result of CRP prestack migration of the common offset input section. Note, that very good focusing has been accomplished. Finally the sparse set of input CMP gathers — shown in figure III.9b — has been CRP processed. We see, see figure III.9e, that the well known V-patterns appear together building the shape of the zero-offset response. Note, that the branches of the V-pattern do not form straight lines, but instead follow the slope of the diffraction tails. The branches opposite to these tails will cancel when all CMP gathers are processed. We may conclude that diffraction energy is correctly processed by CRP processing schemes.

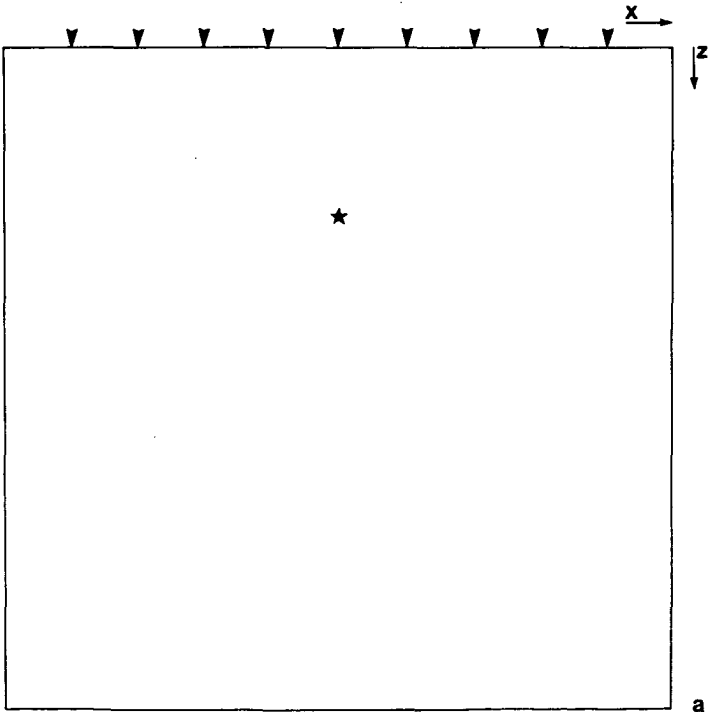


Figure III.9a Diffractor model, showing 9 CMP locations.

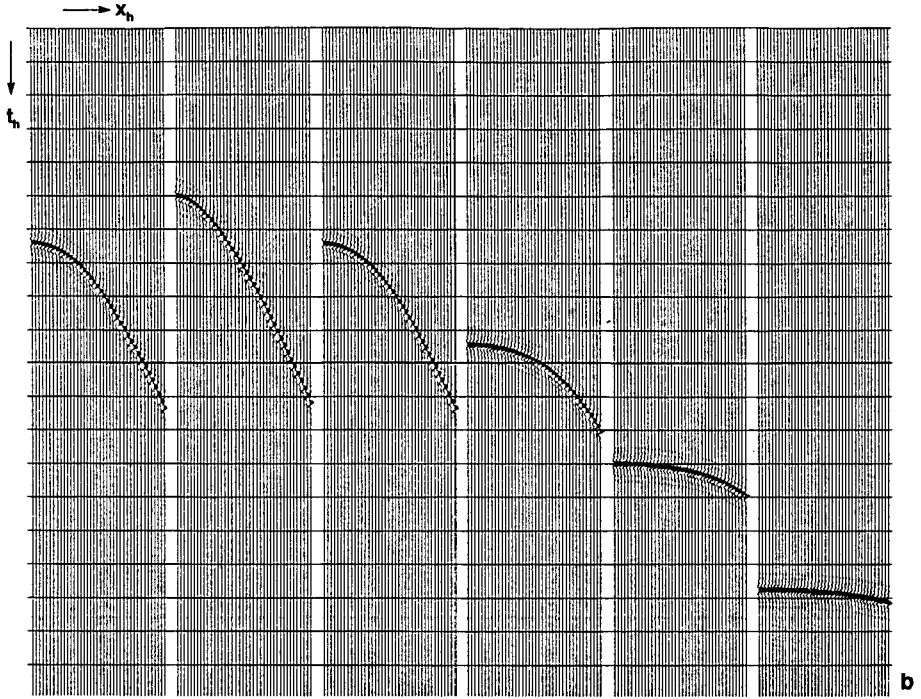


Figure III.9b Sparse set of CMP gathers containing diffraction energy. Four CMP gathers at the left side are not shown.

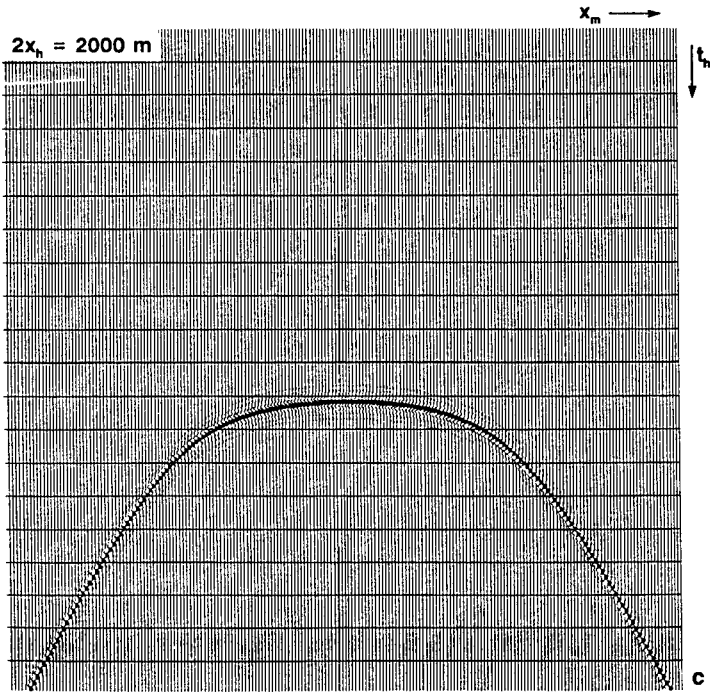


Figure III.9c Constant offset response of diffractor.

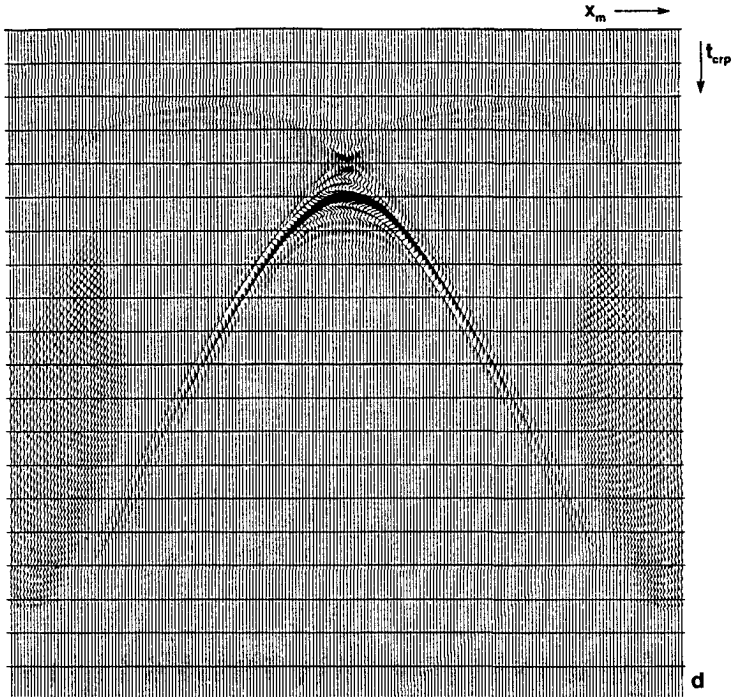


Figure III.9d Zero-offset section resulting from CRP processing of the constant offset section.

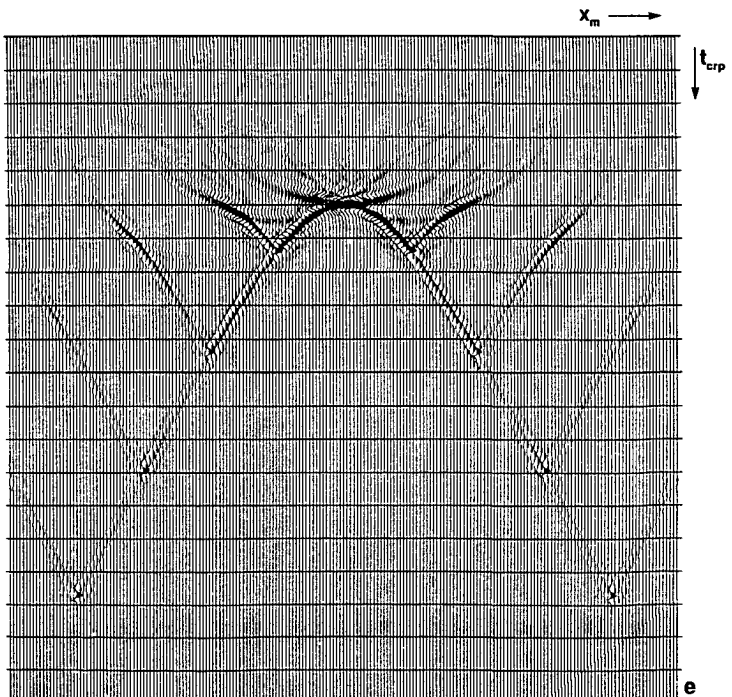


Figure III.9e Zero-offset section after CRP processing of a sparse set of CMP gathers.

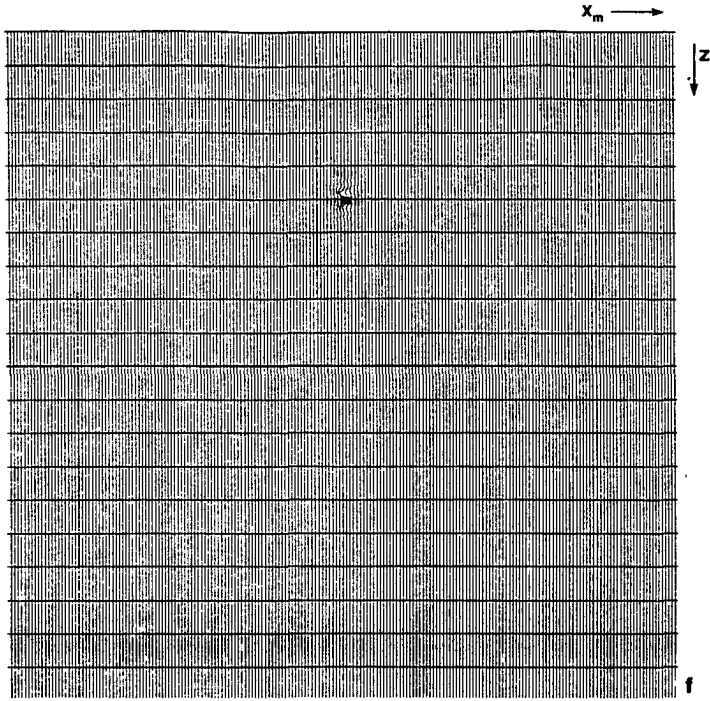


Figure III.9f CRP prestack migration result of input data shown in figure 9c (that is the constant offset section).

The second example contains (multi-offset) reflection data from the subsurface geometry depicted in figure III.10a. Note that no diffraction energy has been modelled. The geometry is meant to resemble one reflecting interface which contains a (reflecting) fault plane. The dominant frequency contents of the modelled data is chosen such that in the zero-offset section, shown in figure III.10b, the fault plane reflection is aliased for this frequency whereas the interface reflection is not. This can be seen in the KF-spectrum of the zero-offset section, shown in figure III.10c. The aliasing is also very visible in the depth migrated zero-offset section, see figure III.10d. Note, that the zero-offset section as such will never be available in a real world situation, since in each single channel recording in the field a field pattern is used. The summation over individual receiver groups will to first order approximation act as an anti-alias filter.

In conventional CMP processing, the stacking velocity applied, will be correct for the dipping interface reflection. For the fault plane reflections the stacking velocity will then be too low, resulting in an overcorrection of NMO and a misstacking (and smoothing) of the fault plane reflection. As a result the aliasing of the fault plane reflection will be less,

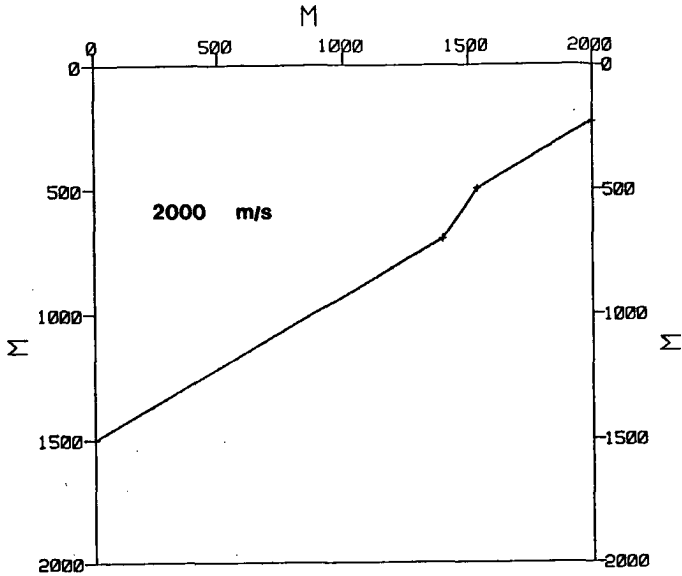


Figure III.10a Subsurface geometry with homogeneous overburden. The velocity of the overburden is 2000 m/s.

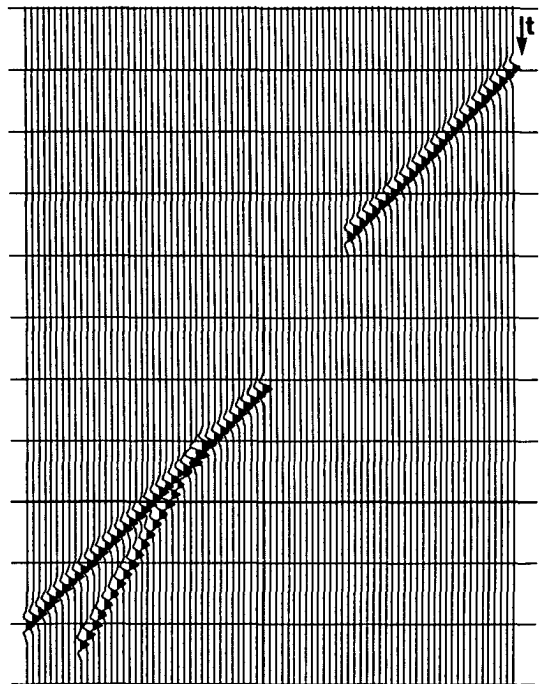


Figure III.10b Zero-offset section. Note that no diffractions have been modelled.

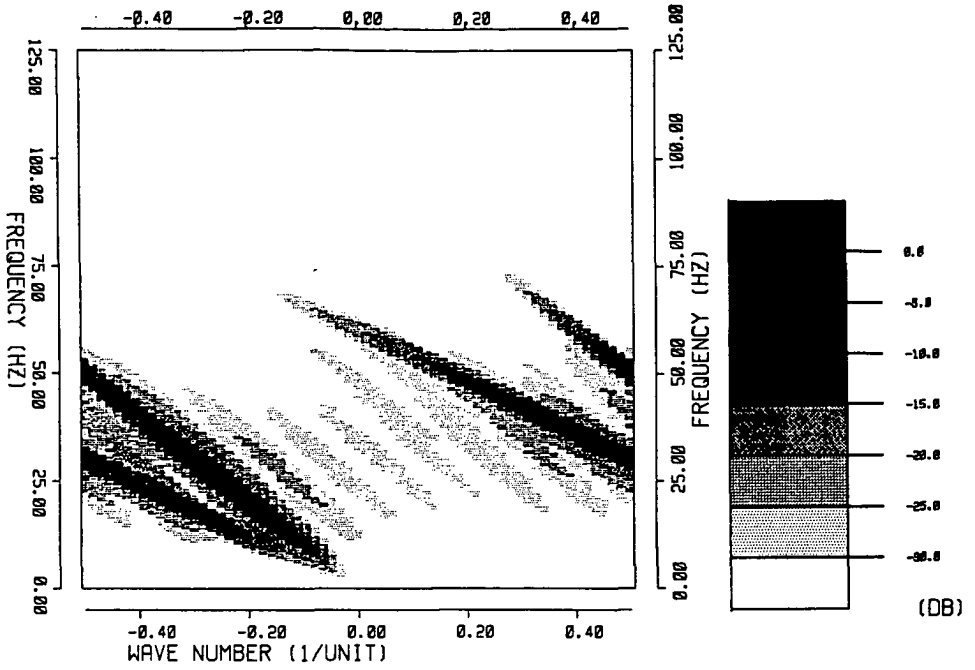


Figure III.10c KF-spectrum of zero-offset section.

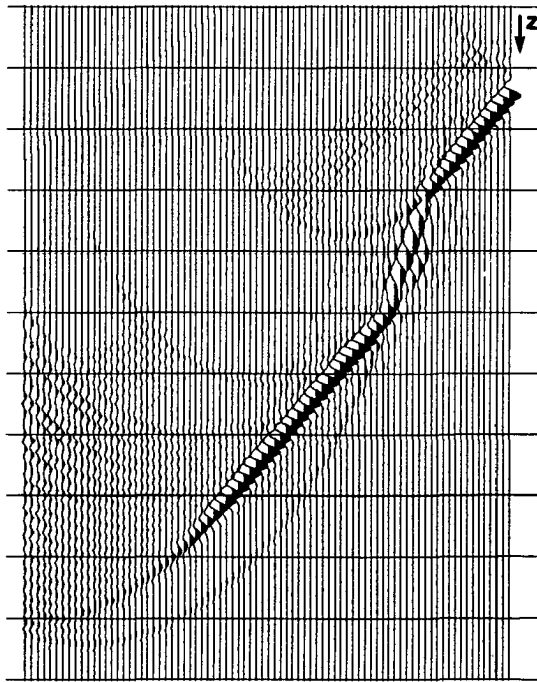


Figure III.10d Poststack depth migrated zero-offset section.

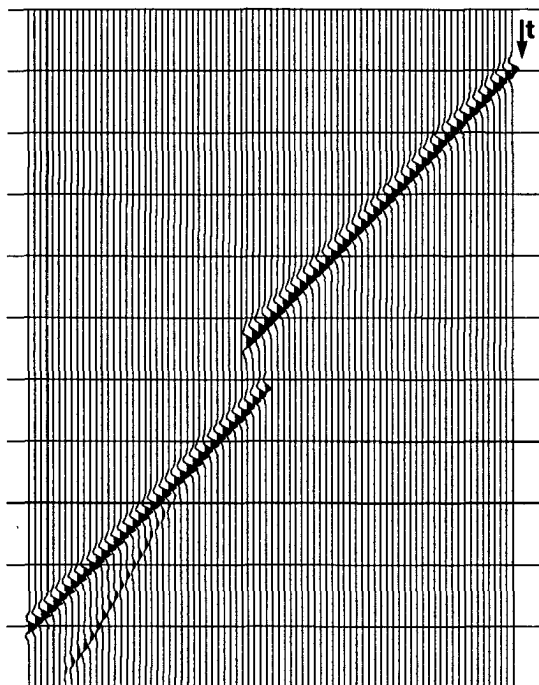


Figure III.10e CMP stack.

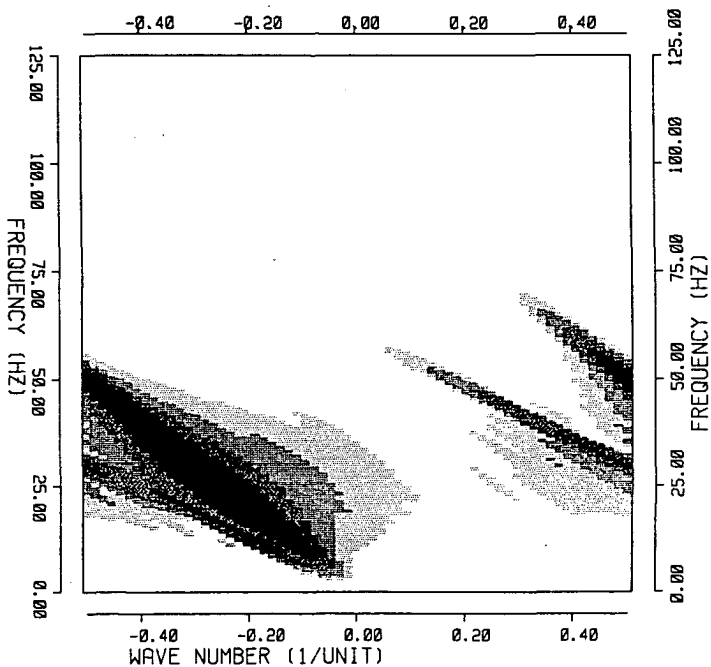


Figure III.10f KF-spectrum of CMP stack.

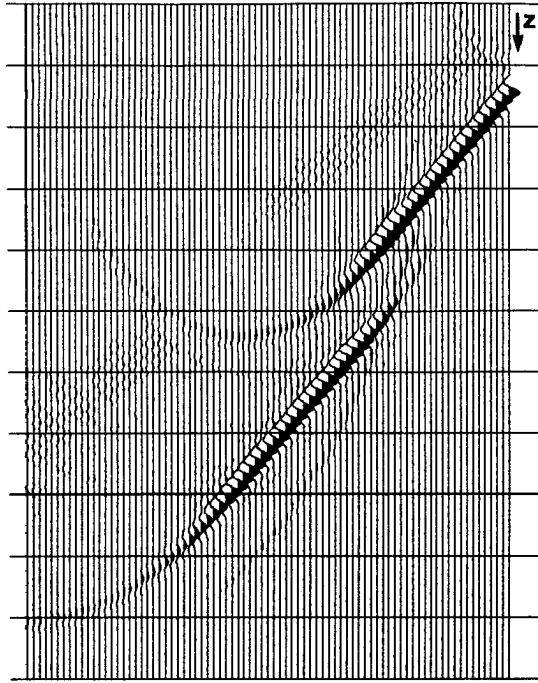


Figure III.10g Poststack depth migrated CMP stack.

relative to the total energy in the section. The conventional CMP stack is shown in figure III.10e. The corresponding KF-spectrum and the migrated CMP result are depicted in figures III.10f,g. The aliasing energy has indeed been reduced. If we now apply CRP processing we may expect that the CRP stack will again be aliased, due to correct travelttime compensation of both the interface reflection and the fault plane reflection. Figure III.10h shows a CRP stack (and KF-filter) obtained by application of an anti-alias protected CRP operator (see also figure II.22b). Figure III.10i shows the result when no anti-alias protection has been implemented in the CRP operator (see figure II.22a). Note that without anti-alias protection the CRP stack indeed contains more aliased energy than the CMP stack. This is due to the fact that the CRP process does not smear the data and therefore does not apply a sort of spatial low pass filtering. However, instead of mapping the data to an output grid equal to the input grid, we could map the data to a finer output grid. This means that we acknowledge the fact that reflection point smear is a dense subsurface sampling, which can be exploited by a CRP algorithm.

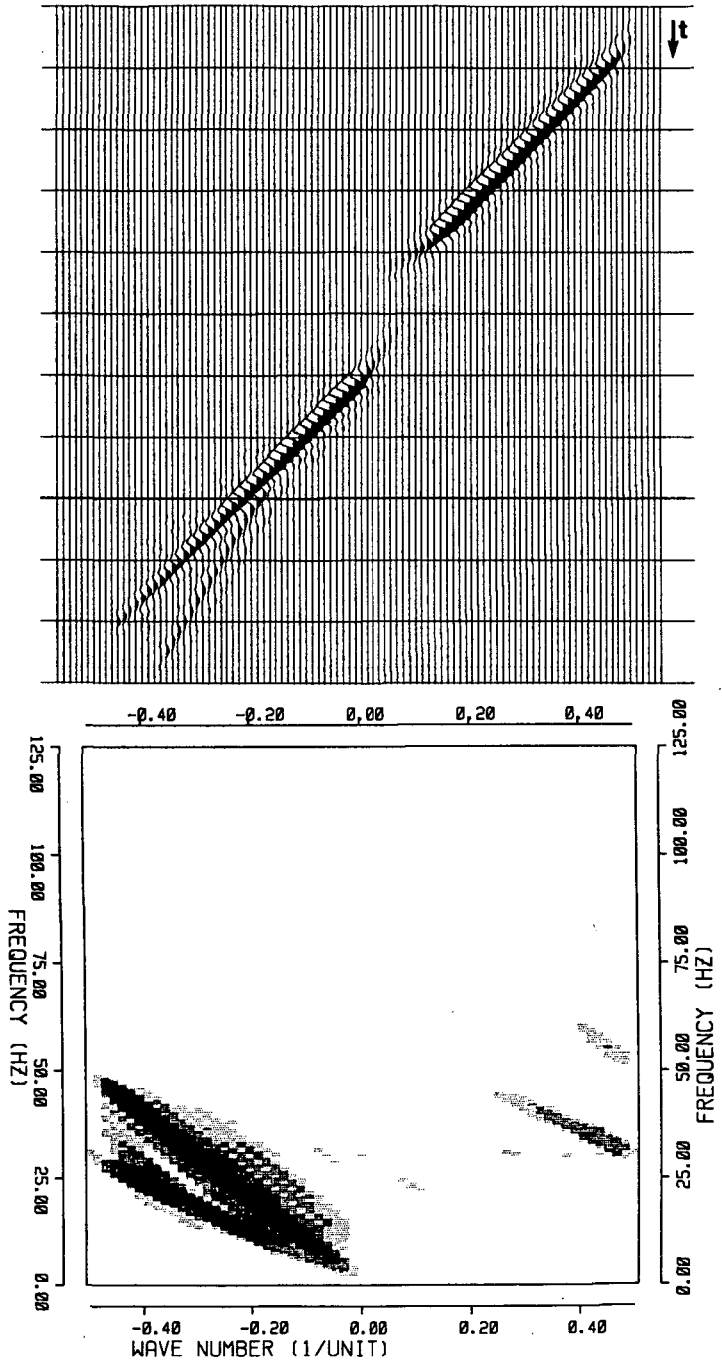


Figure III.10h Top: CRP stack with anti-alias protected operator.
Bottom: corresponding KF-spectrum.

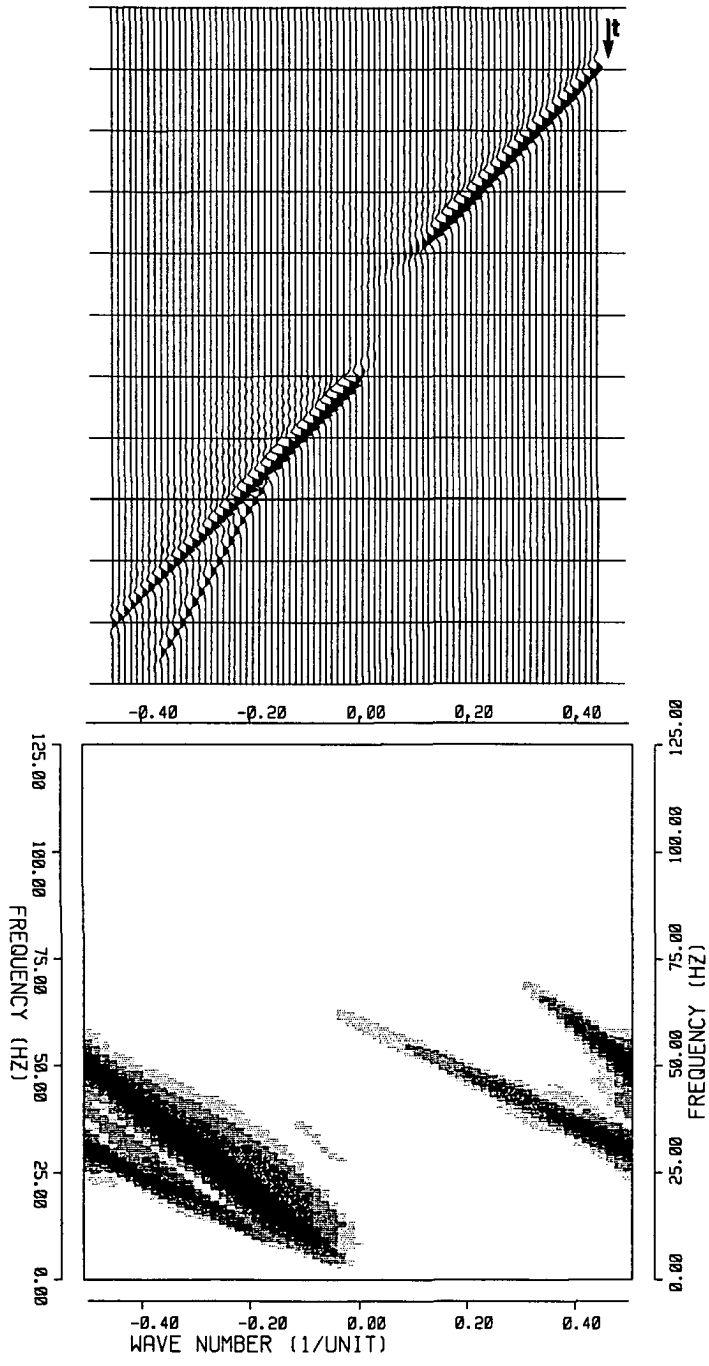


Figure III.10i Top: CRP stack without anti-alias protection of the operator. Bottom: corresponding KF-spectrum.

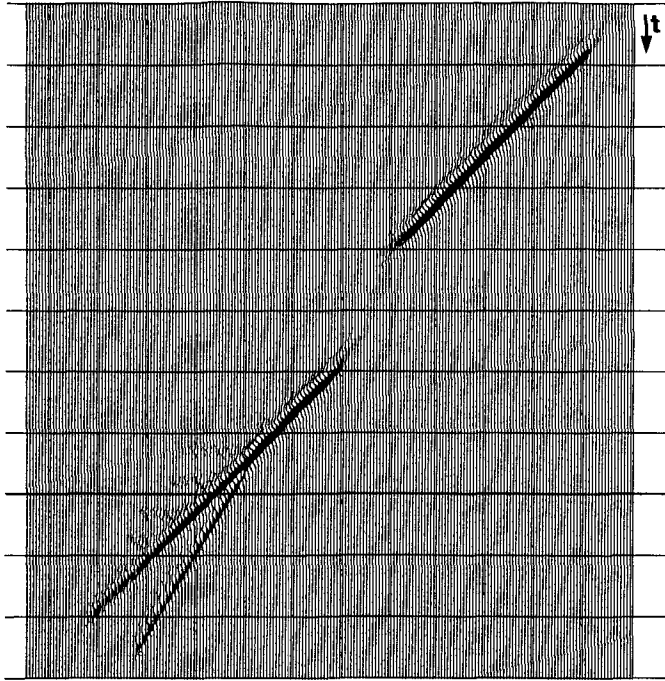


Figure III.10j CRP stack with a finer output grid.

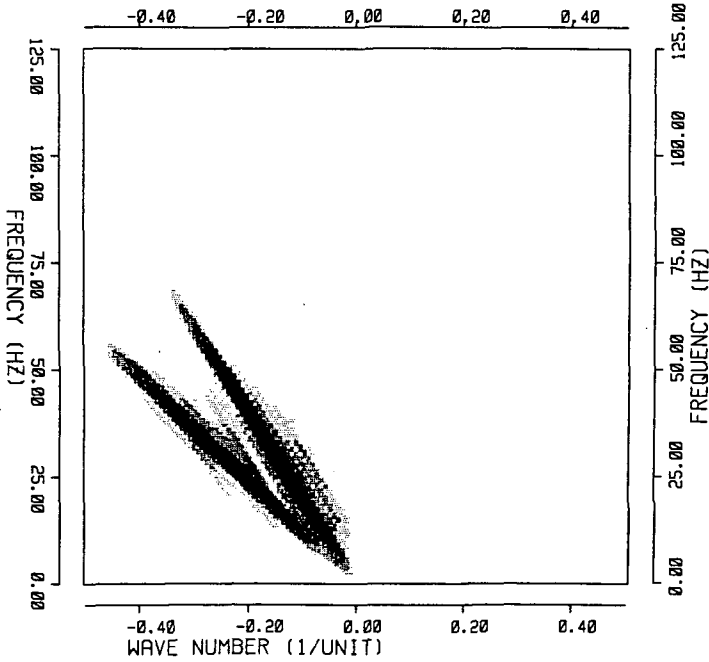


Figure III.10k KF-spectrum of CRP stack with finer output grid.

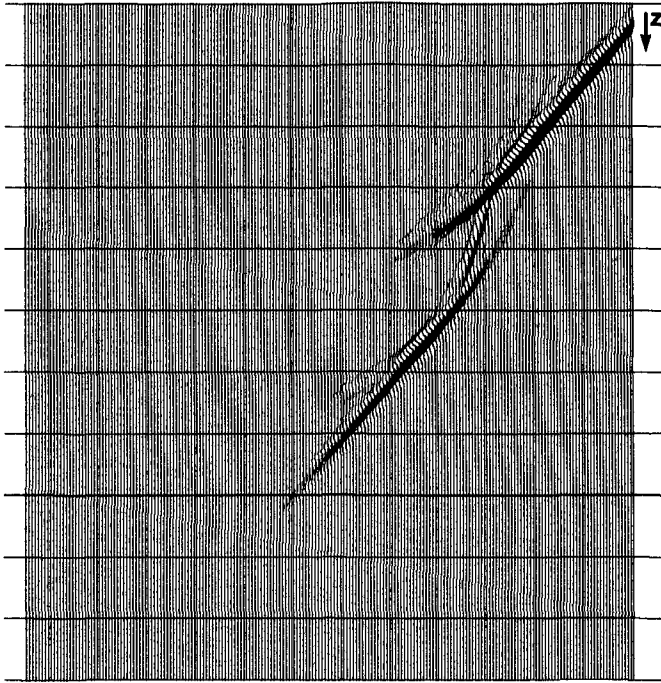


Figure III.10l CRP prestack migrated section; finer output grid.

An example of CRP processing including mapping to a finer grid than the input CMP grid is shown in figure III.10j. Figure III.10k shows the corresponding KF-spectrum and figure III.10l shows the CRP prestack migration result.

Note, that both the CRP prestack migration and the CRP stack have a higher resolution than the corresponding CMP processes!

We conclude that CRP processing uses the multi-offset data:

1. to enhance the signal to noise ratio of the resulting stack (not shown here, but very important for real data);
2. to take full advantage of the dense subsurface sampling of the different offset recordings by repositioning individual traces to their actual surface location or, in other words, to go to a finer grid of stacked traces.

III.6 SUMMARY AND CONCLUSIONS

So far we have presented two DMO schemes for constant velocity media, or homogeneous macro models. The conventional DMO scheme presented in chapter II and the CRP stacking scheme developed in this chapter should yield identical results when applied in homogeneous macro models. The approach of both schemes is, however, entirely different.

In the conventional DMO operator, the dip angle is varied for a chosen offset, see figure III.11a, leading to an elliptical shaped impulse response.

In the CRP stacking scheme, the offset is varied for a chosen dip angle, leading to a V-pattern shaped impulse response, see figure III.11b.

The conventional DMO process is based on a typical time (migration) approach.

The CRP stacking process is on the contrary based on a typical depth oriented approach.

The emphasize in this approach is put on a macro model in which the reflection point smearing needs to be removed. This leads to a description of CRP processing as a very natural extension to the conventional CMP process.

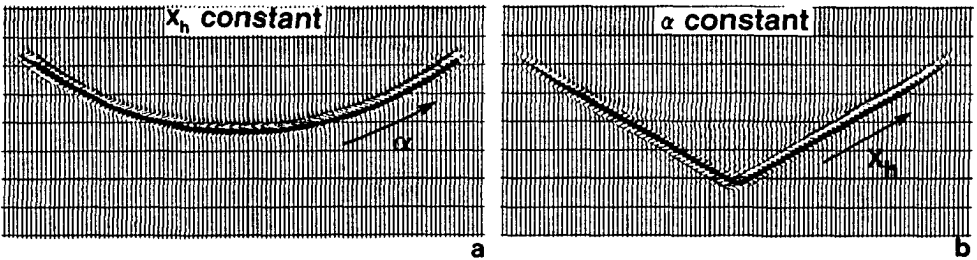


Figure III.11 Two alternative DMO processing schemes:

- a. DMO impulse response for varying dip angle α and fixed offset $2x_h$.
- b. DMO impulse response (or, better: CRP impulse response) for varying offset and fixed dip angle $\pm \alpha$.

We will show in the next chapter that the CRP stacking process — unlike conventional DMO processing — can be extended very easily to inhomogeneous macro models.

Before we start with a generalization of the theory presented so far, we once more show the differences between CMP, CRP and CDP processing on basis of figure III.12. In this figure a single dipping reflector with a constant velocity overburden is shown.

The column at the left side shows the conventional CMP processing. Multi-offset data is sorted according to a common midpoint.

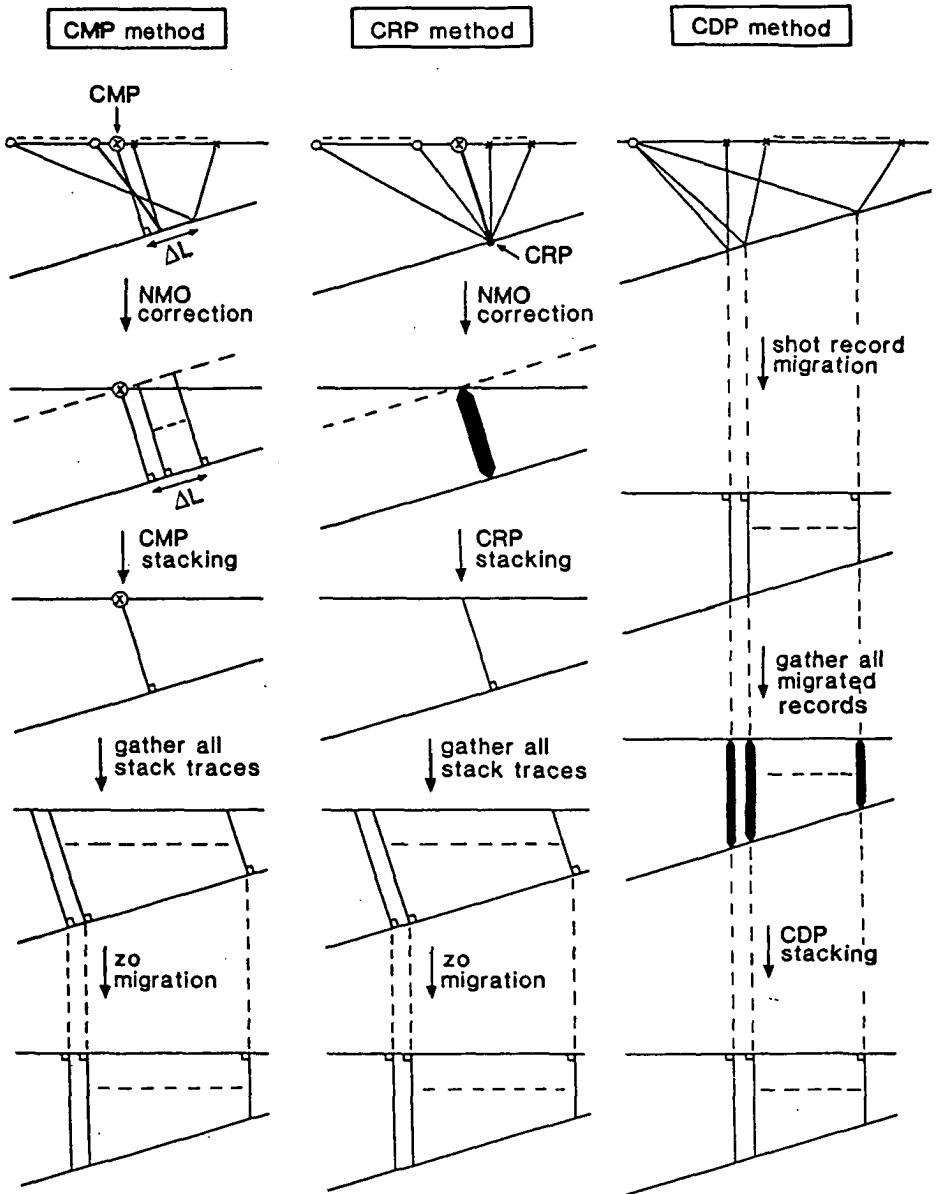


Figure III.12 Simple subsurface geometry showing the principal differences in the CMP, CRP and CDP methods.

Consequently, the reflection points corresponding to the different offsets are smeared. The sorting is followed by a normal moveout correction according to the normal incidence ray from the surface midpoint. Next stacking is performed. Note, that although for one single dip the events from the different offsets stack in phase, the reflection point smear is not compensated. Finally the CMP stack is migrated poststack using an exploding reflector migration algorithm.

In CRP processing (see the middle column of figure III.12) data from a certain shot-receiver pair is corrected according to the normal incidence ray from the specific reflection point to the surface. If we repeat this procedure for each shot-receiver pair and all apparent dip angles in combination with dip filtering we get a final CRP stack in which all dips have been stacked properly without any reflection point smear. Hence diffraction energy is also stacked properly. This is especially important with respect to optimum poststack migration results. Note, that the second picture in the middle column shows that the input for the stacking consists of traces having the same traveltimes, midpoint and reflection point.

A logical consequence of the CRP method is that it is a multi-trace process. Data from one CMP gather is mapped to other CMP gathers.

In fact the reflection point smear in CMP processing is transformed to a surface midpoint "smear" in CRP processing.

In CDP processing the full acoustic wave equation — for constant velocity media the DSR equation — is applied directly to the prestack data. The preferred domain — probably the only practical domain for 3-D applications — is the shot-receiver domain.

The extrapolation can be carried out per shot record (figure III.12, column at the right).

The CDP method is the only applicable method when media becomes arbitrary complicated and the hyperbolic moveout assumption does not hold anymore.

Going from left to right in figure III.12 we conclude that the methods use less assumptions and/or approximations and become more sophisticated. The price we have to pay for that is that the methods also become less robust, more complicated and computationally more intensive.

IV

CRP STACKING IN INHOMOGENEOUS MEDIA

IV.1 INTRODUCTION

This chapter deals with the generalization of CRP stacking to inhomogeneous media. The DMO and CRP algorithms discussed in the previous chapters are all based on the assumption that the medium velocity is constant.

For real data this is quite a crude assumption. On the other hand if the subsurface constitution is not too complex, the NMO correction for zero-dip will make the input to DMO approximately velocity-independent. This explains the relative success of conventional DMO in areas of moderate complexity, that is without distinct lateral and vertical velocity variations.

However, statements like "applying constant velocity DMO is probably better than applying no DMO at all" (Hale, 1983) are too optimistic. There is a growing awareness that application of constant velocity DMO can lead to results that are worse than the results of conventional CMP processing. This will be shown in section 2 of this chapter.

Several attempts have been made to adapt the constant velocity DMO concept to more complicated media, e.g. a stratified earth model. Some start with the formulation of constant velocity DMO, others entirely reformulate the problem of DMO. In section 3 an overview is given of some typical generalizations. It is remarkable that there is a strong

parallel with the way thinking about migration evolved. In the 70's people tried to adapt time-migration algorithms to inhomogeneous media. This route proved to be unsuccessful and it was concluded that the whole migration concept needed to be reformulated in terms of depth technology.

We will therefore present an alternative strategy in section 4, which is fully based on depth technology concepts. The nucleus of the concept is:

Use the apparent dip angle at the surface as a parameter and compute for variable offsets the lateral and temporal shift needed to compensate for the reflection point smear. The computation of the shifts is based on a given macro model. The choice of the apparent dip angle as principal variable is essential.

In section 5 CRP stacking for inhomogeneous media will be evaluated and compared with results of CMP stacking and constant velocity CRP stacking, using synthetic data examples.

A real data example will be shown in the next chapter.

In this chapter the name DMO will refer to CRP stacking for constant velocity media.

IV.2 THE NEED FOR GENERALIZATION OF CRP STACKING

The need for generalization of the CRP stacking concept can be clearly demonstrated with a synthetic data example. CMP stacking and conventional DMO processing will be evaluated in a typical, simple situation.

Consider a dipping reflector with a time dip corresponding to a dip angle α and an inhomogeneous overburden, see figure IV.1. A normal incidence ray to the reflector has a dip ψ_0 at the surface. The NMO velocity along this raypath and the zero-offset traveltime are c_{stack} and t_0 respectively.

We now consider the data from one CMP gather at $x_m = x_0$ and apply both CMP processing and DMO processing.

CMP processing would involve application of NMO correction according to

$$t_h^2 = t_0^2 + \frac{4x_h^2}{c_{stack}^2 (\psi_0)} \quad , \quad (IV.1)$$

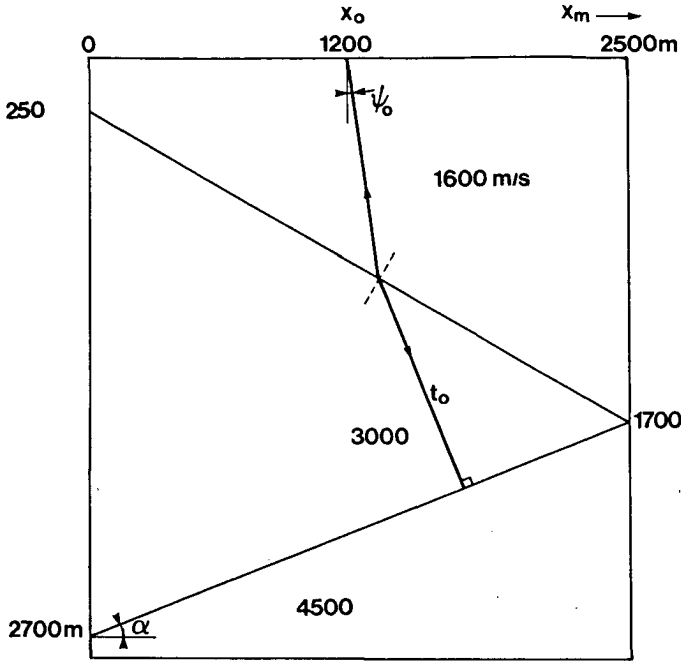


Figure IV.1 Inhomogeneous macro model with normal incidence ray.

followed by stacking over all offsets. The argument ψ_0 for the stacking velocity c_{stack} denotes that the stacking velocity is optimal for this apparent dip angle.

Conventional DMO processing would involve two sequential steps:

1. Application of an NMO correction according to

$$t_h^2 = t_{NMO}^2 - \frac{4x_h^2}{c_{stack}^2(0)}, \quad (IV.2)$$

where $c_{stack}(0)$ denotes the zero-dip stacking velocity.

2. Application of DMO correction according to

$$t_{crp}(x_m) = t_{NMO} \sqrt{1 - \frac{(x_m - x_0)^2}{x_h^2}}. \quad (IV.3)$$

In other words, conventional DMO processing assumes that the process can be split into a velocity-dependent part (correction with velocity $c_{stack}(0)$) and a velocity-independent part (correction for all dips ψ_i).

For a dipping event in a constant velocity medium there will be no discrepancy between the two methods, since there is a relation between the stacking velocities for the different (apparent) dip angles.

This relation reads

$$c_{\text{stack}}(0) = c \quad (\text{IV.4a})$$

$$c_{\text{stack}}(\psi_0) = c_{\text{stack}}(0) / \cos \psi_0 \quad (\text{IV.4b})$$

$$= c / \cos \psi_0 \quad (\text{IV.4c})$$

and is visualized in figure IV.2a.

In an inhomogeneous medium these stacking velocities are in general related to raypaths going through an entirely different part of the subsurface macro model, where relations (IV.4) do not hold at all.

This can be illustrated with the following example. Consider the surface location $x_0 = 1200$ m in figure IV.1. The zero-dip stacking velocity at this location for the second reflector is defined by the stacking velocity along the image ray. The image ray hits the reflector at zero-offset time equal to approximately 2 seconds. This stacking velocity is approximately equal to 5000 m/s. Conventional DMO processing would therefore imply an NMO correction with velocity 5000 m/s followed by DMO to account for the dip-dependency. The stacking velocity versus dip angle curve, related to figure IV.2a is shown in figure IV.2b. Application of DMO implies that this curve is assumed to be true!

Now we compute the actual stacking velocity versus dip angle curve using the stacking velocity formula of Shah (see section IV.4.1), still for $x_0 = 1200$ m and $t_0 = 2$ s, as suggested by figure IV.2c. The curve is shown in figure IV.2d. Figure IV.2e shows the same data, but now each stacking velocity has been multiplied by the cosine of the corresponding apparent dip angle.

Note, that this curve in figure IV.2d bears no relation at all to the idealized curve in figure IV.2b! The left abrupt boundary in figures d and e is a result of rays reaching the left boundary of the model. At small positive start angles, the rays reach the critical angle. The right most part of the figure corresponds to rays that always stay at times smaller than 2 seconds in the first layer and do not reach the interface. (This can be understood by looking at the cosine-normalized stacking velocities for that same range of dip angles, given in figure IV.2e; the stacking velocities then become equal to the interval velocity of the first layer.

The conclusion is therefore, that even for a single dipping reflector in an inhomogeneous medium DMO will lead to erroneous results. This will be illustrated later in section IV.5 in

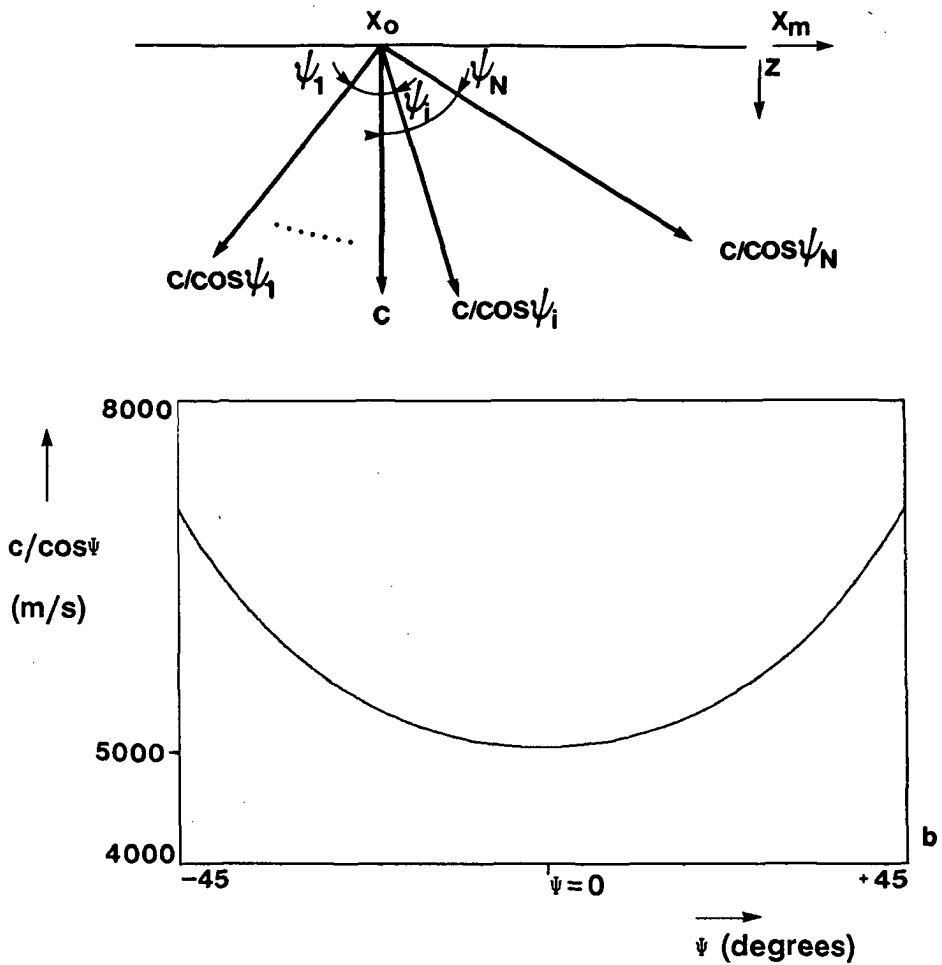


Figure IV.2a,b

- a. Raypaths and corresponding expressions for the stacking velocities. The medium is considered to have a constant velocity.
- b. Stacking velocity versus dip angle curve.

a complete study of the processing of data acquired from the geometry in figure IV:1. The CMP stacking on the other hand, is dip-selective, but this means that in any case at least one dip is properly stacked (provided that the hyperbolic moveout assumption is still valid), as will also be shown in section IV.5.

Even for a horizontally layered earth, DMO may deteriorate a seismic section, when diffraction energy is involved. A well known example (see e.g. Bolondi, 1984) is given by the flanks of diffraction patterns, e.g. from salt domes. Due to the increasing apparent dip

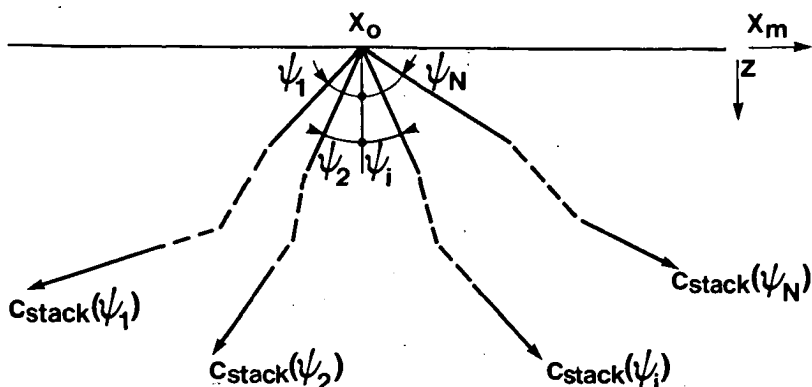


Figure IV.2c Stacking velocities along different rays in an inhomogeneous medium.

for increasing arrival time, the appropriate stacking velocity for a diffraction increases with arrival time. In conventional CMP processing this may coincide with increasing RMS velocity with increasing travel time. Since conventional DMO processing does not take the velocity gradient in depth into account, an extra correction for dipping reflectors is applied. This may just attenuate the diffraction energy from a shallow diffractor. An example is given in figure IV.3. Figure IV.3a shows a conventional CMP stack containing a shallow diffraction which crosses a flat reflection event. The horizontally layered velocity model is depicted at the right. The geometry has been designed such that the diffraction and reflection have exactly the same stacking velocity at the time that they cross. Conventional DMO will aim to add an extra correction to the dipping events, which is incorrect. As can be seen in figure IV.3b, the DMO stack is inferior to the CMP stack. Figure IV.3c anticipates the CRP scheme for inhomogeneous media that will be developed in this chapter and shows the result of its application on these data. We see that the crossing energy is again enhanced.

We may conclude that it is necessary to generalize DMO processing to a CRP algorithm which is able to process data from inhomogeneous media correctly.

IV.3 PREVIOUS ATTEMPTS TO GENERALIZE CRP PROCESSING TO INHOMOGENEOUS MEDIA

Several proposals to generalize CRP stacking to inhomogeneous media have been reported in the literature.

In this section we give a general overview using a rough classification of the different approaches.

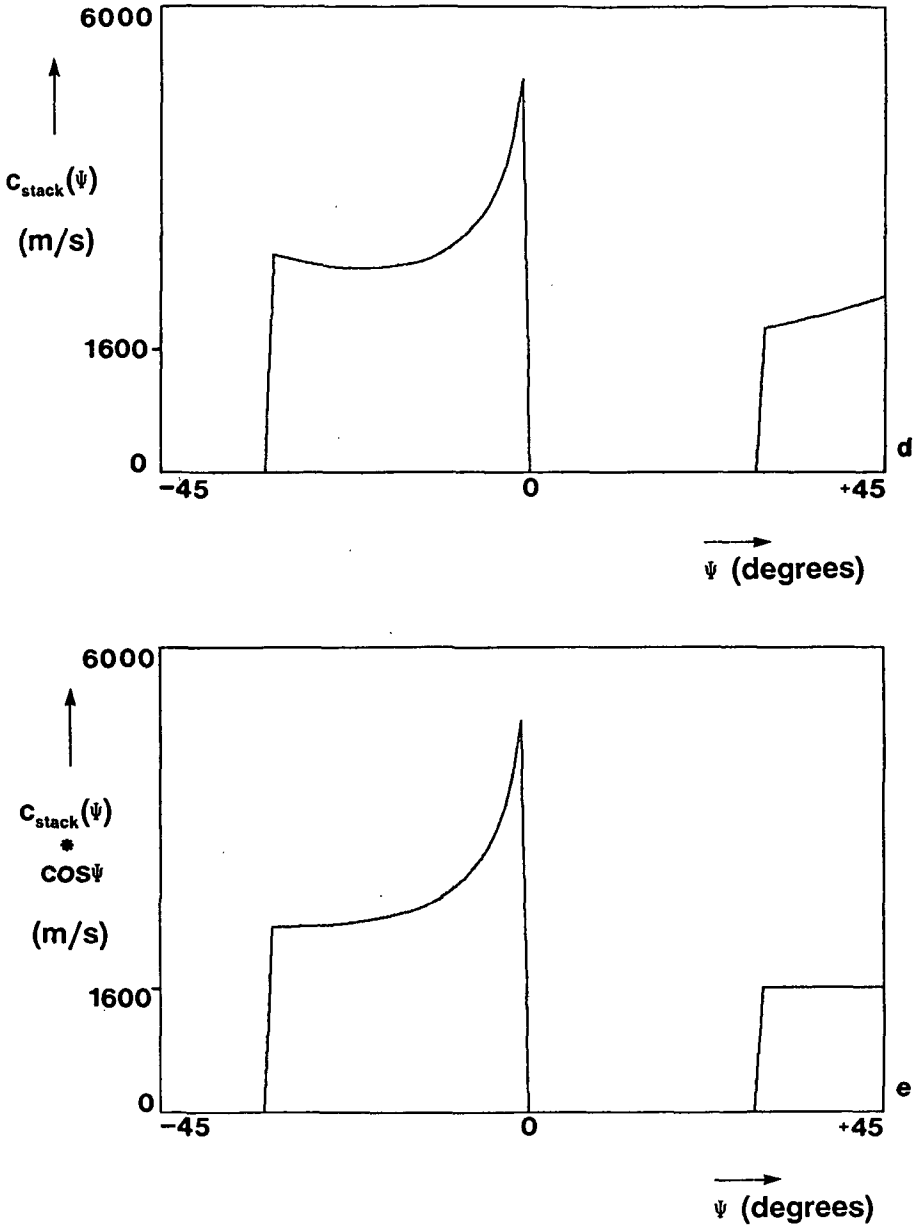


Figure IV.2d,e Stacking velocities in the medium depicted in figure IV.1.

d. Stacking velocity, $x_0 = 1200$ m, $t_0 \approx 2$ seconds, as a function of dip angle.

e. Stacking velocities multiplied by the cosine of the apparent dip (giving "RMS" velocities) as a function of dip. Note that for a constant velocity medium this stacking velocity curve should be constant, equal to the medium velocity.

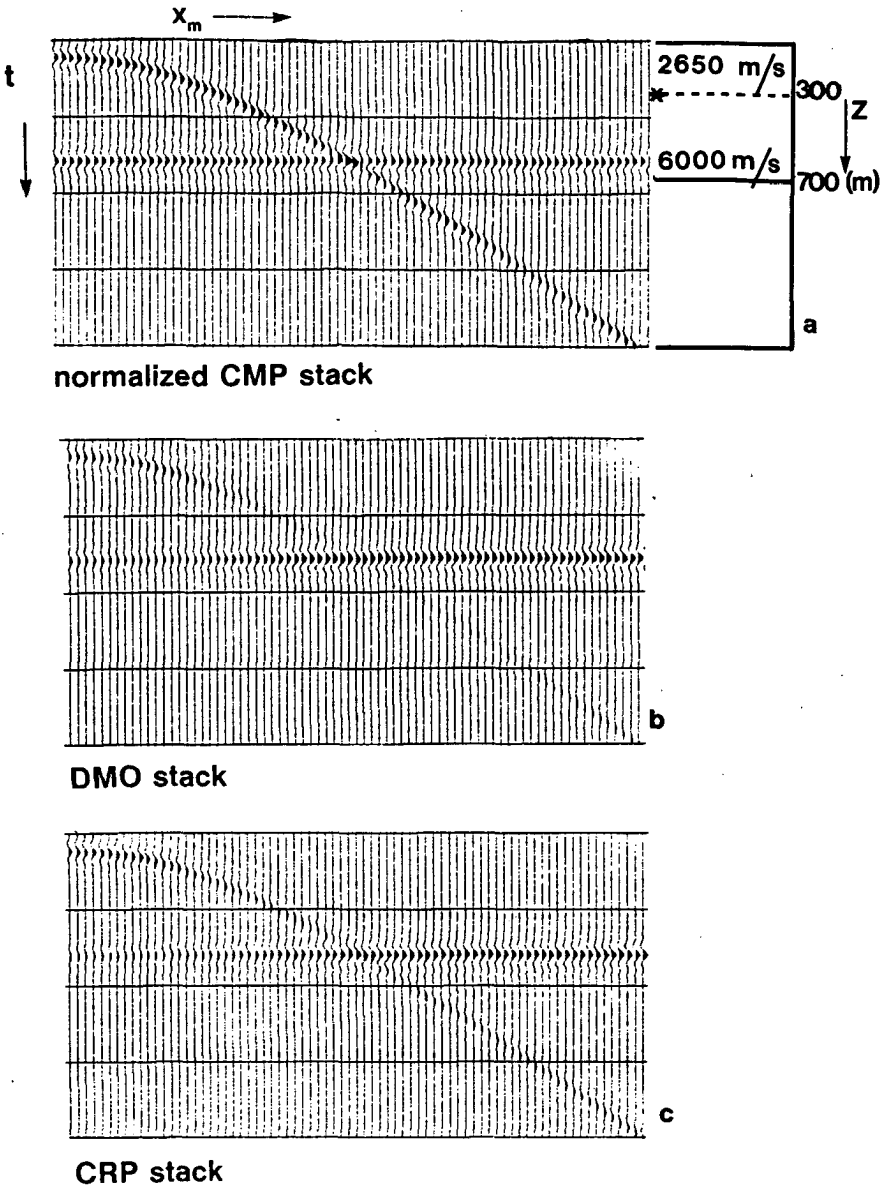


Figure IV.3 A flank of a diffraction crossing a horizontal reflector. The velocity model is depicted at the right side of figure a.

- a. normalized stack (CMP).
- b. conventional constant velocity DMO stack.
- c. CRP stack. The CRP scheme — to be derived yet — enhances again the crossing energy. Note that since the CRP stack has not been normalized, amplitudes are different from those in the CMP stack.

IV.3.1 CRP processing in depth-variable media

For all the schemes presented in chapter II attempts have been made to generalize them to inhomogeneous media.

Although these generalizations apply to depth-variable velocities as well as distinct shot and geophone velocities, most attention has been paid to problems regarding only depth variable velocities. The comparison with the way the thinking about time and depth migration evolved suggests itself again. Incorporating lateral velocity variations in time migration and constant velocity DMO necessarily implies crude approximations, whereas depth-variable velocities can be incorporated more easily.

Since no results have been reported in the literature regarding DMO for lateral velocity variation we will concentrate on DMO for depth variable velocities only.

The most complete treatment on CRP for depth-variable velocity profiles has been given by Hale (1983). Hale suggests the replacement of the constant velocity by the RMS velocity. The dip-dependency in the stacking velocity, that is in constant velocity media the cosine of the dip angle is now accounted for by the difference between the RMS velocity and the NMO velocity for a certain dip angle. The expression for the NMO velocity is given by Shah (1973) — see further on in this chapter — and is based on a wavefront curvature approximation.

Hale (1983) confirms by synthetic experiments that a depth-variable velocity DMO leads to significant better results than the constant velocity DMO algorithm. According to Hale, however, the correction for depth-variable velocity is likely to be small in practice, compared with the total DMO correction.

This statement illustrates once more that in practice a really significant improvement over the conventional CMP stack may only be realized by a rigorous generalization of DMO to inhomogeneous media that include lateral and vertical velocity variations.

IV.3.2 CRP stacking in the midpoint-time-velocity space

Fowler (1984) proposes a procedure which unifies velocity analysis and (full or partial) reflector imaging of the data in a velocity parameterized space. In his approach a sufficient number of constant velocity stacks is formed, filling a 3-D data cube in midpoint-time-velocity, see figure IV.4.

This cube is transformed to the midpoint wavenumber-frequency domain. Next DMO is applied by regridding the data along the velocity axis according to $c_{\text{stack}} = c/\cos \psi_0$ or

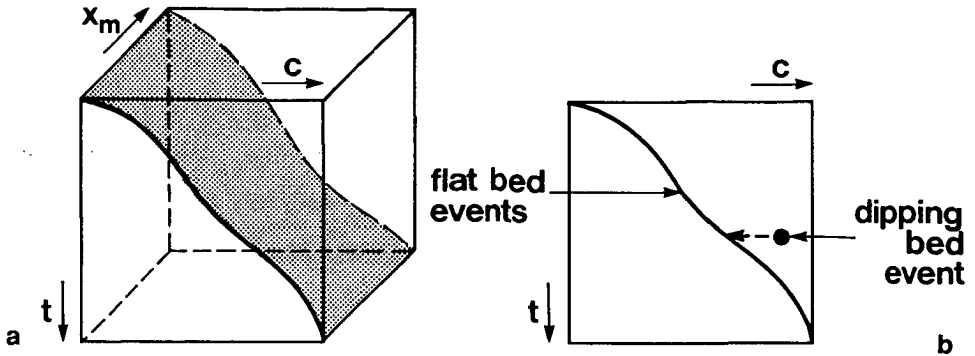


Figure IV.4

- a. Midpoint – time – velocity cube according to Fowler.
 b. DMO moves a dipping bed event towards the zero-dip stacking velocity function.

$$c_{\text{stack}} = \frac{c}{\sqrt{1 - \frac{c^2 k_m^2}{4\omega^2}}}, \quad (\text{IV.5})$$

k_m being the midpoint wavenumber, and c the interval velocity.

Before inverse transformation a Stolt migration can be applied.

Finally in the midpoint-(DMO)velocity-time domain a zero-offset migrated section can be selected by interpolation between the constant velocity migrated sections. The migration step is optional.

By applying the mapping described by (IV.5) to each velocity stack (that is more c -values) the method can be extended to depth-variable velocity media.

Apart from the optional Stolt migration the method offers the same possibilities as the depth-variable DMO algorithm of Hale.

The principal limitation of the method is unfortunately its inaccuracy in the presence of lateral velocity variations.

IV.3.3 CRP stacking according to French

French's method is a serious attempt to apply NMO and DMO in one CRP processing step for inhomogeneous media. Since his method may easily be confused with our CRP technique, which we will develop in the next section, we will present it here in some detail.

As we will see, the CRP stacking proposed by French only implies a proper CRP stacking to a number of selected events.

The method is fully applicable to 3-D data. We will, however, in this section assume the azimuth angle to be zero.

The basis of the method is Levin's formula (III.1) which we give here once more:

$$l = \frac{x_h^2}{(c/2) t_0} \sin \alpha \cos \alpha \quad , \quad (IV.6)$$

with α the reflector dip, c the medium velocity, t_0 the normal incidence two-way time, x_h the half offset and l the reflection point smear on the reflector.

For a homogeneous macro model, proper CRP processing would imply

1. determination of α ,
2. application of a NMO correction using the velocity c and the dip angle α ,
3. application of a DMO lateral and temporal shift, according to (IV.6).

For an unknown inhomogeneous medium, French suggests the modification of relation (IV.6) as follows:

1. replace α by the apparent dip angle ψ_0 at the surface,
2. replace the medium velocity c by the RMS velocity along the normal incidence ray to the reflector. In fact the name RMS is not correct. It is the NMO stacking velocity of the reflector, multiplied by the cosine of the apparent dip angle ψ_0 in order to eliminate the dependency of ψ_0 .

As a result, Levin's formula is generalized, yielding

$$l = \frac{x_h^2}{\left(\frac{c_{stack}(\psi_0) \cos \psi_0}{2} \right) t_0} \sin \psi_0 \cos \psi_0 \quad . \quad (IV.7)$$

The method of French goes as follows. First a surface location and surrounding CMP-gathers are selected. Next NMO and DMO corrections are applied, according to (IV.6), for a whole set of dip angles and velocities. The velocities vary with time and should be chosen "within reasonable geological limits". Next the semblance or coherence of all corrected traces is computed for each combination of dip angle and velocity. The calculation is done over a small time window for each two-way reflection time in the manner of Taner and Koehler (1969). The coherence or semblance maxima are projected on to two coordinate planes, contoured and interpreted. In other words, in a 2-D situation, we get semblance contours of the dip angle versus the zero-offset travel time on one hand and the velocity versus the zero-offset travel time on the other.

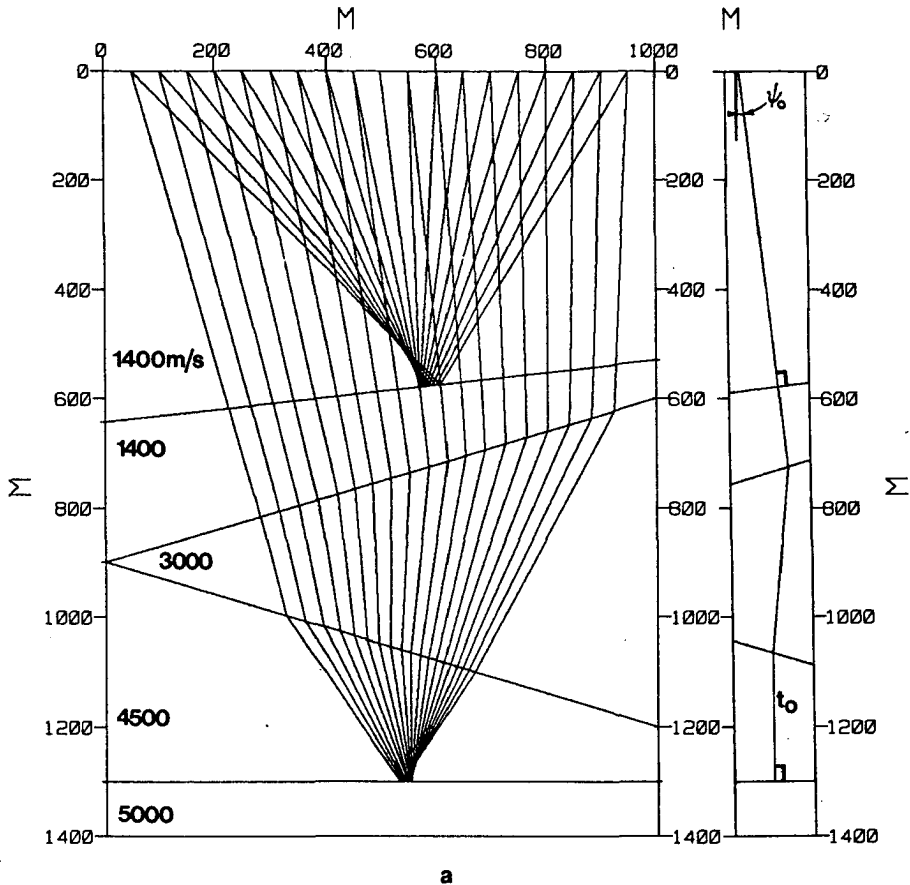


Figure IV.5 Application of Levin's formula to inhomogeneous macro models.

a. offset raytracing and (at the right side) a normal incidence ray to the 1° as well as the 4° interface. Note that the reflection point (RP) smearing (Δx_m) is in opposite directions.

Interpretation of these results implies that for each zero-offset time an optimum combination of velocity and dip angle is chosen. Optimum implies that corresponding reflection points have been properly processed.

The essential difference with the constant velocity DMO is that the DMO correction is now included together with the NMO correction in the velocity analysis, and subsequently applied in one step.

A major drawback of French's method is that in case of conflicting dips, we should select more than one velocity-dip angle pair for the same zero-offset traveltime. In fact the method only properly CRP processes events which have been explicitly defined by the user.

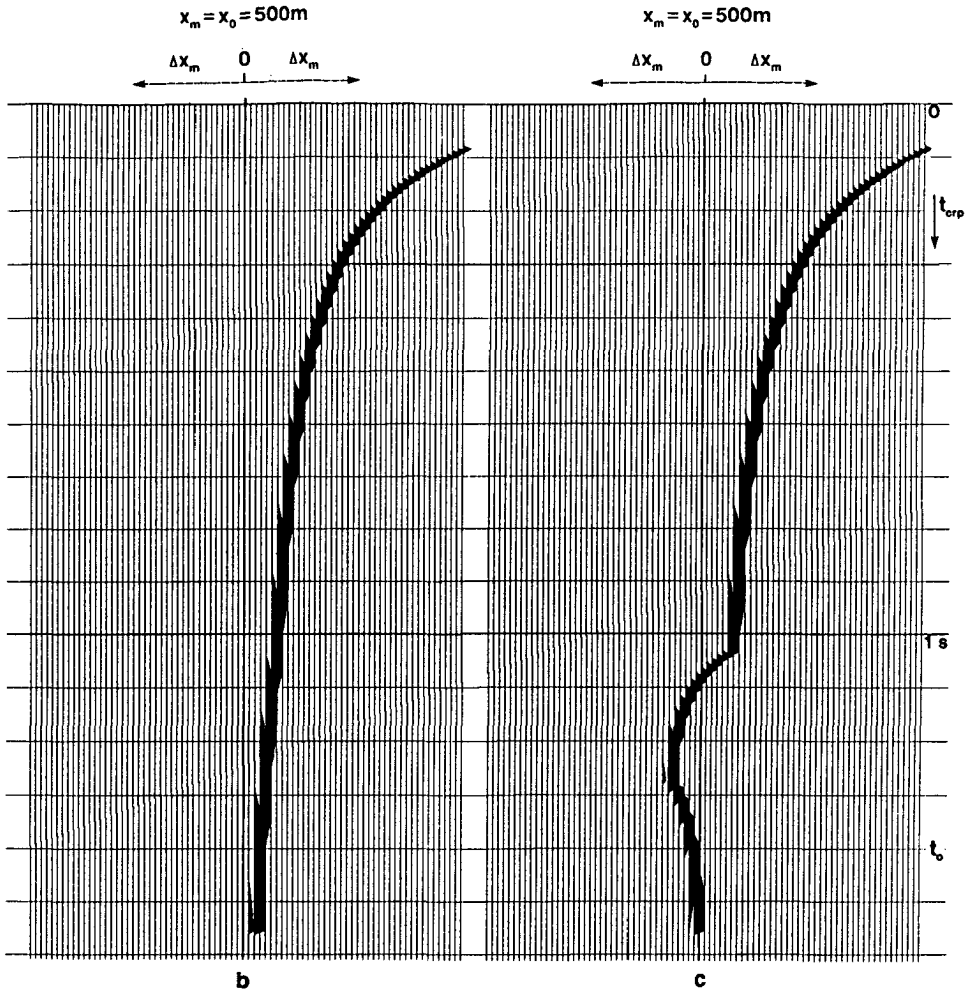


Figure IV.5 (continued)

- b. application of Levin according to formula (IV.7) does not acknowledge the change in sign of Δx_m .
- c. application of a correct CRP processing.

Note: the input trace has a constant amplitude equal to one. The offset is 1000 m.

The method may therefore become impractical for use as a DMO scheme (that is multi-dip scheme) for inhomogeneous media.

Maybe it is even more important to note that the method may fail even in the absence of conflicting dips. The problem lies in the use of Levin's formula for an inhomogeneous

earth. The medium velocity cannot simply be replaced by a kind of RMS velocity, since in an inhomogeneous earth the reflection point smear is also greatly influenced by refraction according to Snell. This statement is illustrated by the following example. Consider the geometry depicted in figure IV.5a. At a certain surface midpoint a normal incidence ray to the first reflector is traced. The geometry has been designed such that the same ray coincides with the normal incidence ray to the fourth reflector. The normal incidence ray has an apparent dip angle ψ_0 at the surface. Along the ray the NMO velocity will increase with time. Application of NMO correction followed by DMO correction according to relation (IV.7) would, apart from a travelttime correction, also imply a lateral shift. This shift will not be identical for both reflectors. They will, however, have the same sign, according to relation (IV.7), since the apparent dip angles are identical. Let's now apply an offset ray tracing to the first and fourth reflector, around the same midpoint. We immediately (figure IV.5a) see that the reflection point smearing for the two reflectors are in opposite directions. In order to visualize the compensation for reflection point smear expressed in terms of a lateral shift at the surface location, a trace at the midpoint location, with a constant amplitude equal to one, and having an offset of 1000 m, is processed both according to French's method and the correct CRP method, to be presented in this chapter. We see that for the first layer French's method is correct, but for deeper layers the method deviates considerably from the correct compensation. We therefore conclude that French's method cannot cope with this situation. French admits this possibility implicitly but plays it down wrongly by saying that "model tests indicate, however, that the reflection point divergence discussed by Levin persists in a predictable manner for realistic subsurface models".

IV.4 A CRP STACKING SCHEME FOR INHOMOGENEOUS MEDIA

In this section we present our CRP method. This method is macro model based and takes lateral as well as vertical velocity variations into account. Also the necessary approximations underlying the method are presented. We start with a CRP stacking scheme that maps multi-offset data to zero-offset. Next a CRP prestack migration scheme is presented.

IV.4.1 Mapping to zero-offset by CRP stacking

The aim of CRP stacking in inhomogeneous media can be summarized as follows.

"CRP processing is a procedure which aims to stack events which are related to a common reflection point. In CMP sorted data the reflection point is smeared in general. Therefore lateral and temporal shifts are applied to the data, together with normal moveout correction. These shifts may be determined by (zero-offset) ray tracing in a macro model".

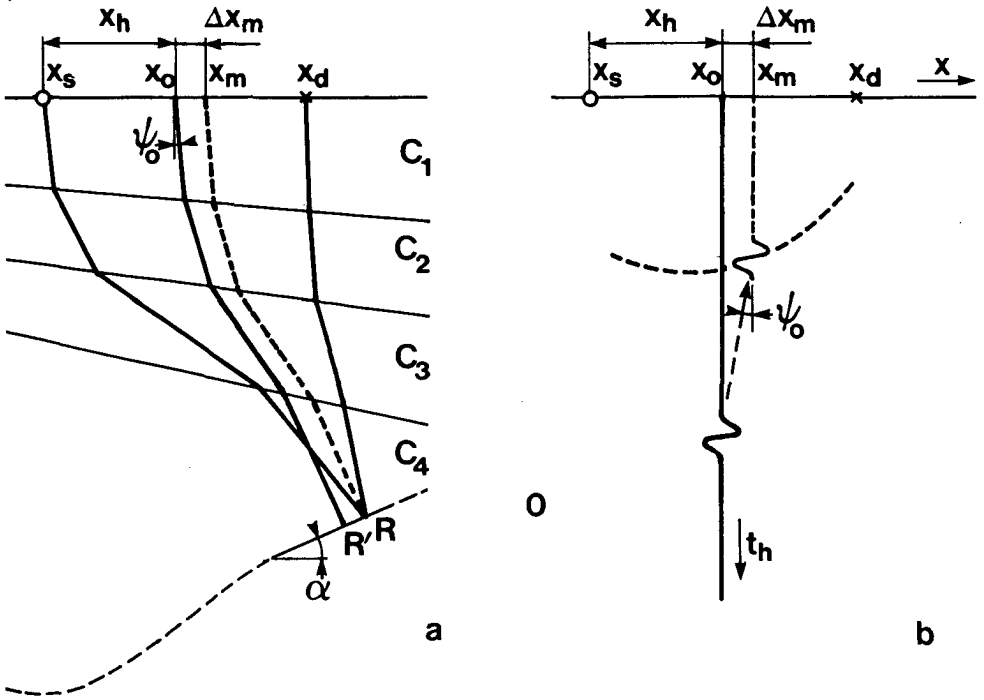


Figure IV.6

- a. Inhomogeneous macro subsurface model.
- b. CRP stacking should map an event in a CMP gather at $x = x_o$ with offset $2x_h$ and traveltme t_h to a position in the zero-offset domain at x_m and t_{crp} . Repeating this mapping for all apparent dip angles ψ_0 gives for this single event the CRP impulse response, denoted by the dashed line.

This can be clarified using the subsurface model depicted in figure IV.6a.

Let us assume that the reflection point R is part of a (small) reflector with (local) dip angle α . If we have a source at x_s and a geophone at x_d — and consequently a midpoint at $x_o = (x_d + x_s)/2$ — then the travel path of the energy reflected by point R is the continuous line $x_s R x_d$. The zero-offset (ZO) ray $x_o R'$ is also shown.

In conventional CMP processing the offset ray $x_s R x_d$ is transformed into the ZO ray $x_o R'$ by application of NMO.

However, offset ray $x_s R x_d$ should ideally be transformed into the ZO ray $x_m R$.

Therefore, the reflection event from subsurface point R should be shifted both in time and in space. This operation is shown in figure IV.6b for one dip ψ_0 of the ZO ray. For the geometry of figure IV.6a the multi-dip result would produce a type of modified dip

moveout operator (see the dashed line in figure IV.6b). Ideally, the computations required for the transformation of the offset ray into the ZO ray $x_m R$ would involve an offset ray tracing followed by a ZO ray tracing $x_m R$ from R to the surface. The difference of the surface coordinates x_0 and x_m and the difference of the traveltimes along path $x_0 R'$ and travel path $x_m R$ indicate the lateral and temporal shift, respectively. Undoubtedly this would be a very time consuming procedure, because the ray tracing has to be done for each angle ψ_0 of interest to produce only one (modified) DMO operator. Because (modified) DMO operators are required for all ZO traveltimes, all offsets and all midpoints of interest, this procedure is not recommended for practical use.

Deregowski (1985) also proposed this method, aiming to process specific target reflectors correctly.

We would like to adapt the process such that it becomes a practically applicable technique for processing every subsurface reflection point, regardless of whether there is a reflector or not.

The main problem with respect to computer requirements of the method described earlier is the offset ray tracing for all offsets and all possible apparent dip angles.

There is a way to avoid the offset ray tracing if we give up some generality. Let us therefore assume the following.

1. In a CMP gather the traveltime versus offset trajectory is approximately hyperbolic. More precisely, we assume that the wavefront curvature approximation to the stacking velocity as proposed by Shah (1973) can be used. This implies that we assume that the medium locally consists of homogeneous layers, separated by plane, dipping interfaces.
2. We assume that the offset is small compared to the depth of the reflection point. This assumption is already implied by Shah's stacking velocity formula.

The model depicted in figure IV.6a is a typical example of a macro model for which Shah's stacking velocity formula holds.

The wavefront curvature approximation of Shah is also known as the normal incidence point (NIP) wavefront curvature approximation (Hubral and Krey, 1980).

For small values of the half offset x_h , the traveltime along the reflected offset ray between source x_s and geophone x_d is well-approximated by the sum of times from x_s to the NIP R' and from R' to x_d . This approximation leads directly to the traveltime relation

$$t_{h,N}^2 = t_{0,N}^2 + \frac{4x_h^2 \cos^2 \psi_0}{C_N^2}, \quad (\text{IV.8a})$$

with

$$C_N^2 = \frac{1}{t_{0,N} \cos^2 \psi_0} \sum_{n=1}^N \prod_{k=0}^{n-1} \left(\frac{\cos^2 \psi_k'}{\cos^2 \psi_k} \right) c_n^2 \Delta t_n, \tag{IV.8b}$$

where

- C_N = NMO velocity for reflection N ,
- $t_{0,N}$ = total two-way zero-offset (ZO) traveltime between the surface and reflector N ,
- c_n = interval velocity in layer n ,
- Δt_n = two-way interval ZO traveltime in layer n ,
- ψ_0 = emergence angle of ZO raypath at surface,
- ψ_0' = ψ_0 ,
- ψ_k = refraction angle of ZO raypath at the k th interface,
- ψ_k' = incidence angle of ZO raypath at the k th interface.

Given expression (IV.8a,b) we are able to apply a traveltime correction from the traveltime $t_{h,N}$ along $x_s R x_d$, to the traveltime t_0 along $x_0 R'$. As explained above, the aim of CRP processing is to apply an additional correction in time and in space, which we shall call Δt_{CRP} and x_m . The additional time correction amounts to the traveltime difference between rays $x_0 R'$ and $x_m R$. The lateral correction amounts to a lateral shift from x_0 to x_m . It turns out that it is possible to derive closed recursive expressions for these lateral and temporal shifts. They are based on the definition of a macro model and on the expression for the NMO velocity along the zero-offset ray C_N . The derivation is quite involved and therefore given in appendix D.

The general form of the expressions describing these shift reads

$$\Delta x_m \sim Q x_h^2 \tag{IV.9a}$$

and

$$\begin{aligned} \Delta t_{crp} &= t_0 - t_{crp}(x_m), \\ &= 2 \Delta x_m \sin \psi_0 / c_1. \end{aligned} \tag{IV.9b}$$

where c_1 is the interval velocity of the first layer. Q is a rather complicated parameter which must be determined by zero-offset raytracing.

Note that the following statements prove to be valid.

1. The lateral shift is approximately proportional to the square of the half offset via a parameter Q . So, no offset raytracing is involved and for one apparent dip angle the zero-offset ray tracing and evaluation of expression (IV.9) lead to the compensation for reflection point smear of all offsets in one CMP gather.

2. For a constant velocity medium, expressions (IV.8) and (IV.9) reduce to the wellknown hyperbolic moveout relation and Levin's expression for a constant velocity medium respectively. Our CRP algorithm is therefore consistent with conventional constant velocity DMO algorithms in constant velocity media.

IV.4.2 CRP prestack migration

Just as in the constant velocity case, it is possible to exploit the CRP concept for direct mapping of multi-offset data to the correct position laterally and in depth. The key formula which describes the reflection point smearing at the reflector surface is given by (D-23a,b) in appendix D.

The method is entirely parallel to the one in the constant velocity case. Given a surface location, an apparent dip angle, a corresponding normal incidence ray to a reflector and the traveltimes along the ray, the reflector smear is computed and since the end point of the normal incidence ray is fully determined by the given parameters the corresponding reflection event for an offset can be mapped directly into the depth domain. Note, that the procedures for CRP stacking and CRP prestack depth migration are quite similar. Even the recursive expressions to be evaluated are the same. The only difference is that in CRP prestack migration we stay at the reflector and do not compute the surface midpoint "smearing". It is therefore not a surprise that CRP prestack migration is as fast as CRP stacking.

This is a very important and interesting statement, since the benefits of CRP stacking really start to pay off after migration.

Examples of the CRP method will be shown in section IV.5.

IV.4.3 Summary of methods and description of the computational flow diagram

The CRP processing method can thus be described as follows, see figure IV.7.

1. Determine a macro model of the subsurface. Although the CRP method assumes the macro model to consist of plane dipping interfaces, locally within the shot-receiver range of a CMP gather, the complete macro model may be far more complex.
2. Select a surface midpoint and read the CMP gathered data related to that midpoint.
3. Perform zero-offset raytracing for a particular apparent dip angle ψ_0 . Compute Q and the stacking velocity for all traveltimes.
4. Compute for all offsets and all zero-offset time values t_0 the complete traveltimes correction (including mapping from offset time t_h to zero-offset time t_0 and an additional CRP traveltimes correction from zero-offset time t_0 to CRP zero-offset time t_{crp}).

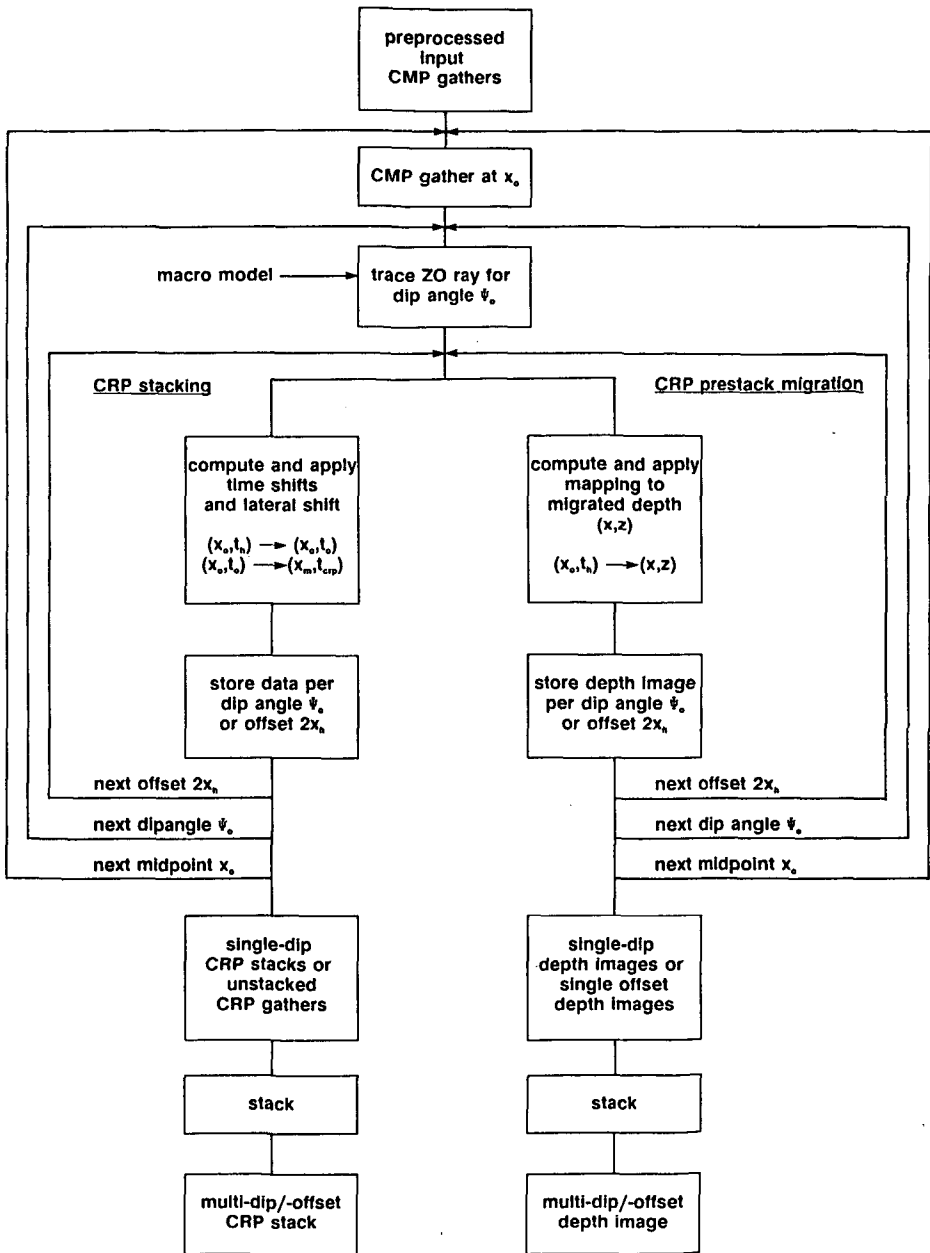


Figure IV.7 Computational flow diagram of CRP processing inhomogeneous macro models.

Compute also for each zero-offset time value t_0 the reflection point smear at the surface of a hypothetical reflector perpendicular to the zero-offset ray at time t_0 , as well as the resulting midpoint “smearing” at the acquisition surface.

- 5 a. Perform CRP correction and stacking,
or, alternatively,
- b. Perform CRP prestack migration by direct mapping into the depth domain.
6. Repeat from step 3 for all other dip angles ψ_0 .
7. Repeat from step 2 for all surface midpoints.
8. Stack the different “dip stacks” or “dip images”.
9. The result is either a CRP zero-offset section or a CRP prestack depth migrated image of the subsurface.

IV.5 A SYNTHETIC DATA EXAMPLE OF CRP STACKING IN AN INHOMOGENEOUS MEDIUM

In this section the CRP stacking scheme is evaluated on data acquired from the model depicted in figure IV.1. We will consider reflections from both interfaces and compare the performance of conventional DMO processing to CRP processing.

Figure IV.8a shows a zero-offset section, which will be used as a reference for the quality of the processing results. In figure IV.8b the result of CRP processing is shown. The CRP prestack migration result is shown in figure IV.8c. We see that the data set has been correctly processed. The amplitude variation along the reflector is a result of the decreasing fold towards the edges of the model. Partly due to the decreasing fold and partly due to rounding effects on the output grid, some noise remains at the right side of the model. Note, that in the region of full fold the wavelet is zero-phase (conforming to the phase of the input wavelet).

Just below the first reflector, on the left-hand side some low frequency noise remains. In order to investigate this specific problem in particular and the result in general we CRP stacked (figure IV.8d) a sparse set of CMP gathers. We also studied the CRP stacking impulse response (figure IV.8e) and CRP prestack migration impulse response (figure IV.8g) for an offset of 1940 m. We notice the following phenomena.

For the first reflector we detect low frequency events just below the left branch of the V-patterns, which are not present in the V-pattern results of conventional DMO processing (see figure III.4b). If we look at the impulse response of the CRP stacking operator for one offset it becomes clear what happens for large negative dip angles (that is rays pointing towards left in the macro model). The normal incidence ray reaches the second layer and

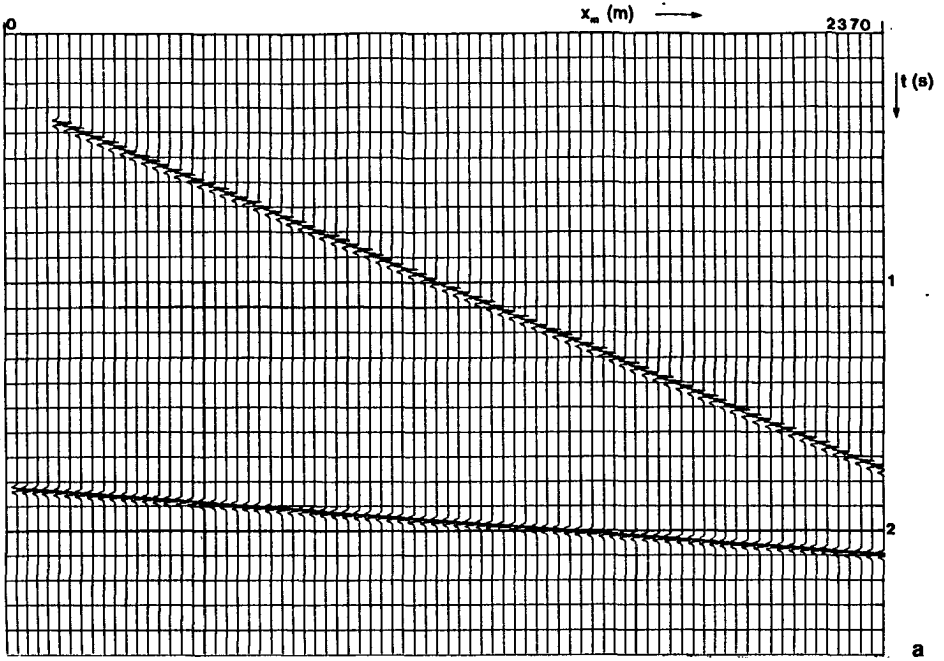


Figure IV.8a Zero-offset section corresponding to the macro model depicted in figure IV.1.

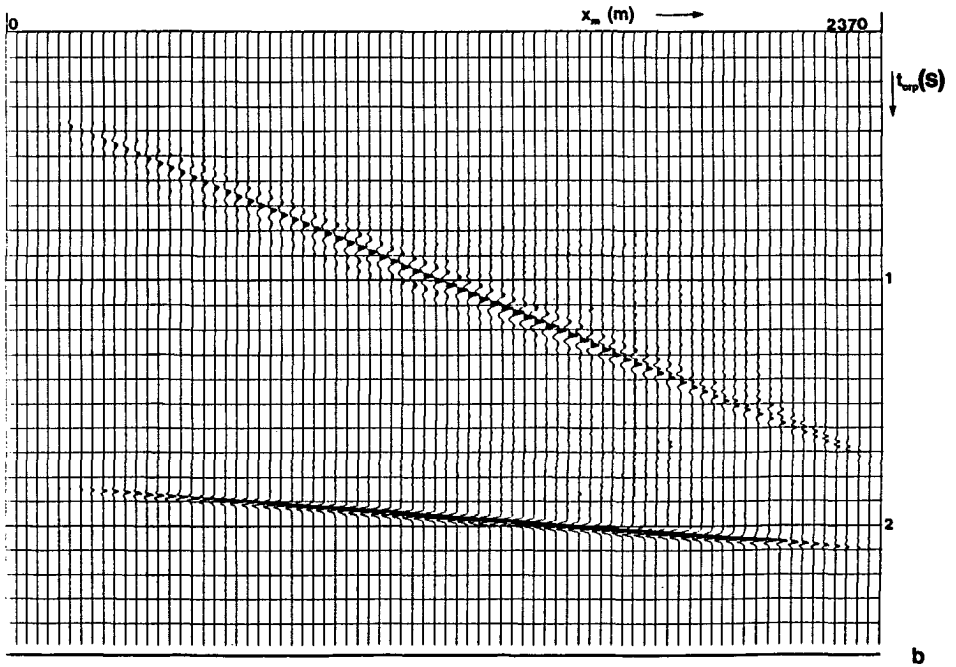


Figure IV.8b CRP stack of data derived from the macro model depicted in figure IV.1.

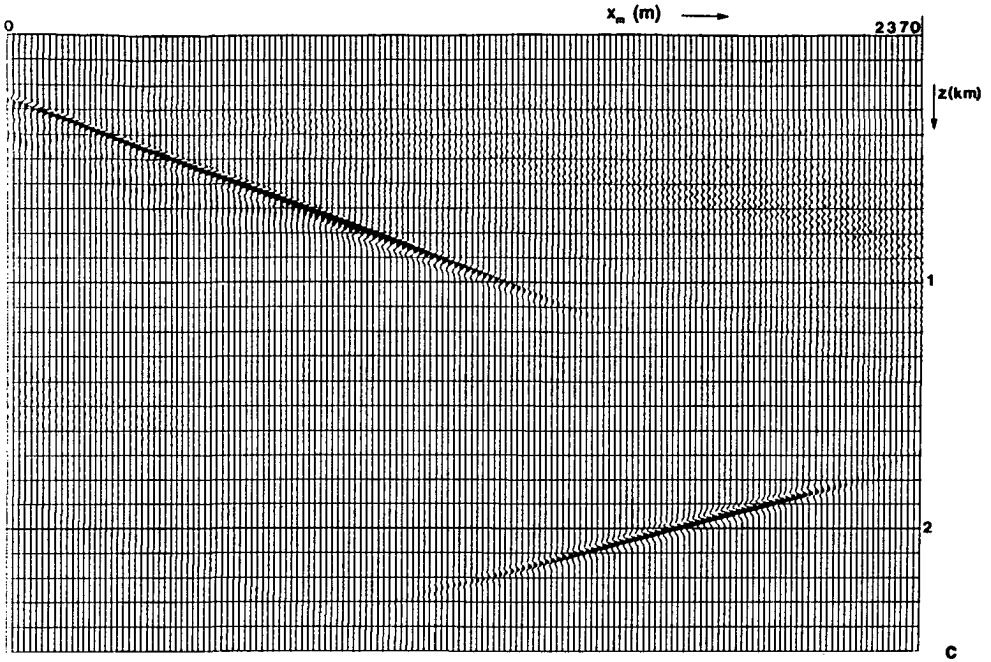


Figure IV.8c Result of CRP prestack migration.

finds another t_0 value which corresponds via the stacking velocity of that time to the offset time t_h . In fact we face the situation for one offset where we find crossing hyperbolic traveltim trajectories (see e.g. figure II.13b). In other words, one event with traveltim t_h on an input trace may correspond via formulae (IV.8) to different zero-offset traveltimes t_0 . These different t_0 -values will lead to different corrections for Δx_m and Δt_{crp} . The CRP operator therefore has to become "multi-valued". Due to the large velocity contrast between the first and second layers, the low frequency events are probably caused by stretching of the data. These events have to be considered as artifacts.

Those (multi-valued) parts of the CRP operator that do not correspond to an existing event have to cancel. That is what we indeed see happen. Although not all energy is cancelled in the CRP stack (probably due to decreasing coverage) most of it is.

Looking at the CRP stacking operator response for the second reflector we see that this operator consists of different parts.

The event on the right-hand side, between 1.5 and 1.6 seconds arises from a zero-offset raytracing that stays entirely in the first layer. Due to the subsurface geometry, this can only be accomplished in the down dip direction of the layer. Figure IV.8h confirms this by

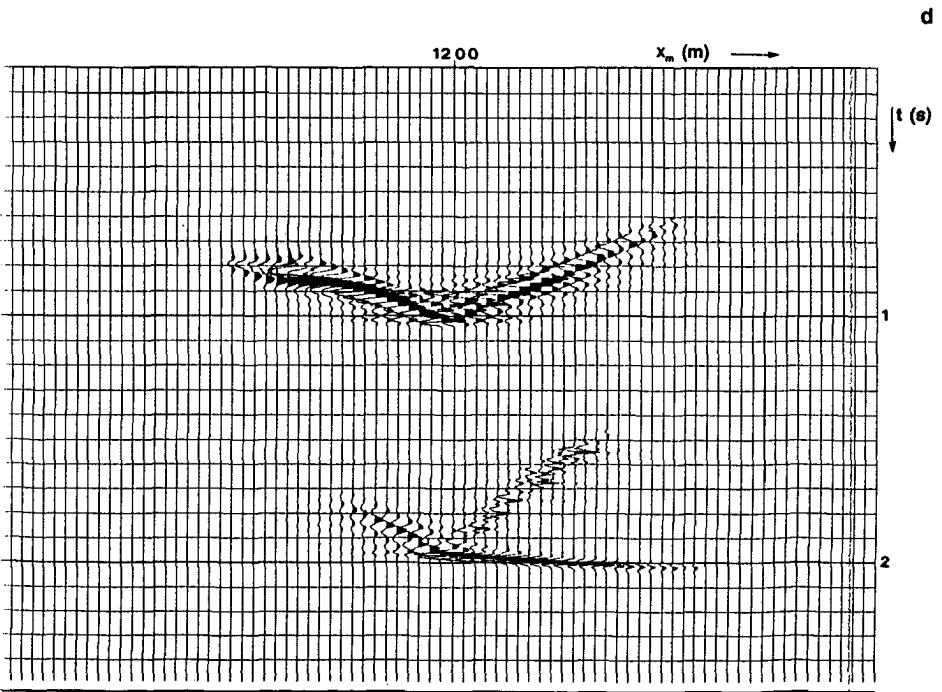
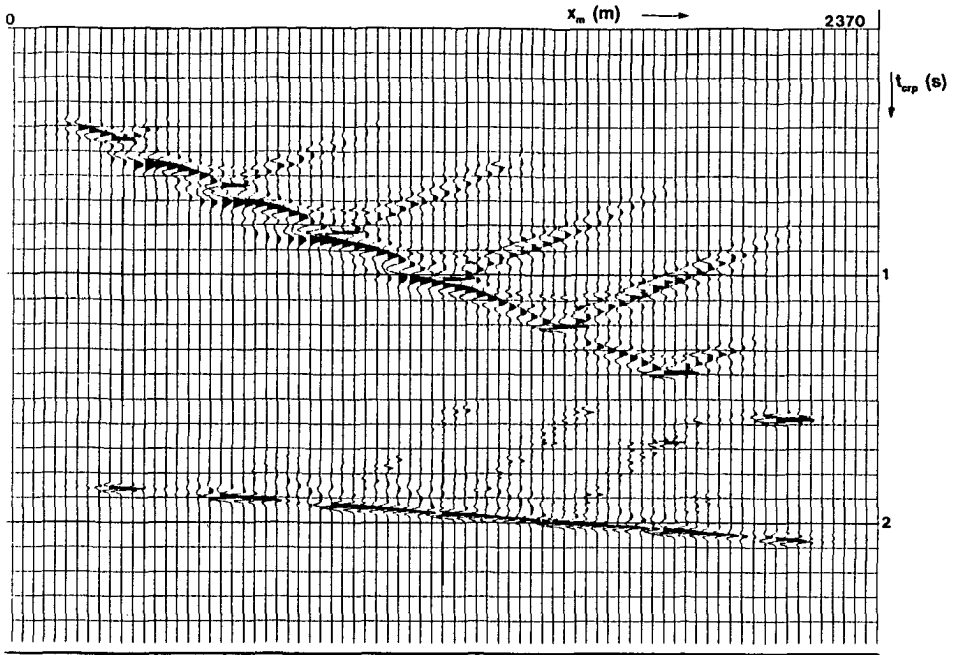


Figure IV.8d CRP stack of a sparse set of CMP gathers, and one single CMP gather (bottom) respectively.

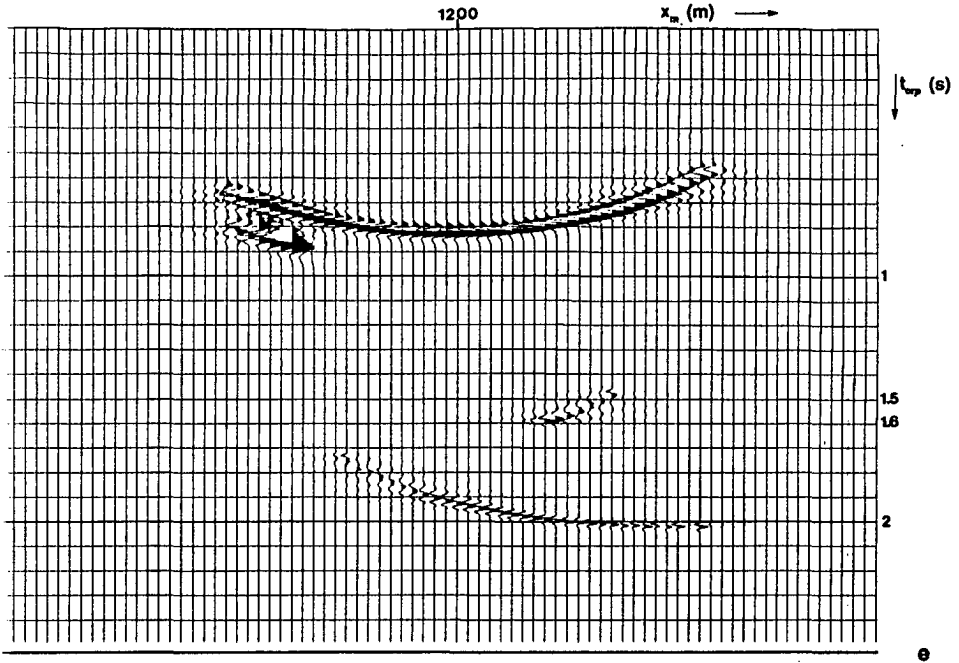


Figure IV.8e CRP stacking impulse response; input: trace at $x_0 = 1200$ m, offset $2x_h = 1940$ m.

showing the impulse response for the same data, where the entire medium is assumed to have a constant velocity, equal to that of the first layer.

The third branch — in the middle — of the V-patterns of the second reflector, see figure (IV.8d) is also explained by exactly the same argument, but now for a summation over all offset operators.

As has been pointed out already, the evaluation of the CRP stacking scheme is done by comparing the CRP mapping to zero-offset — for all offsets — with the modelled zero-offset section. It can be seen very clearly in figure IV.8a that all offsets align very well after CRP processing, thus building constructively the zero-offset reflection event.

One could, on the other hand, also compare a specific CRP stacking operator for one time and offset with the operator based on full offset ray tracing. This is illustrated in figure IV.8h. The figure shows once more the CRP impulse response for the second reflector, depicted in figure IV.8e, and the corresponding offset CRP operator.

Note that in the modelling of the offset operator, no attention was paid to amplitude and phase characteristics. The following phenomena are observed:

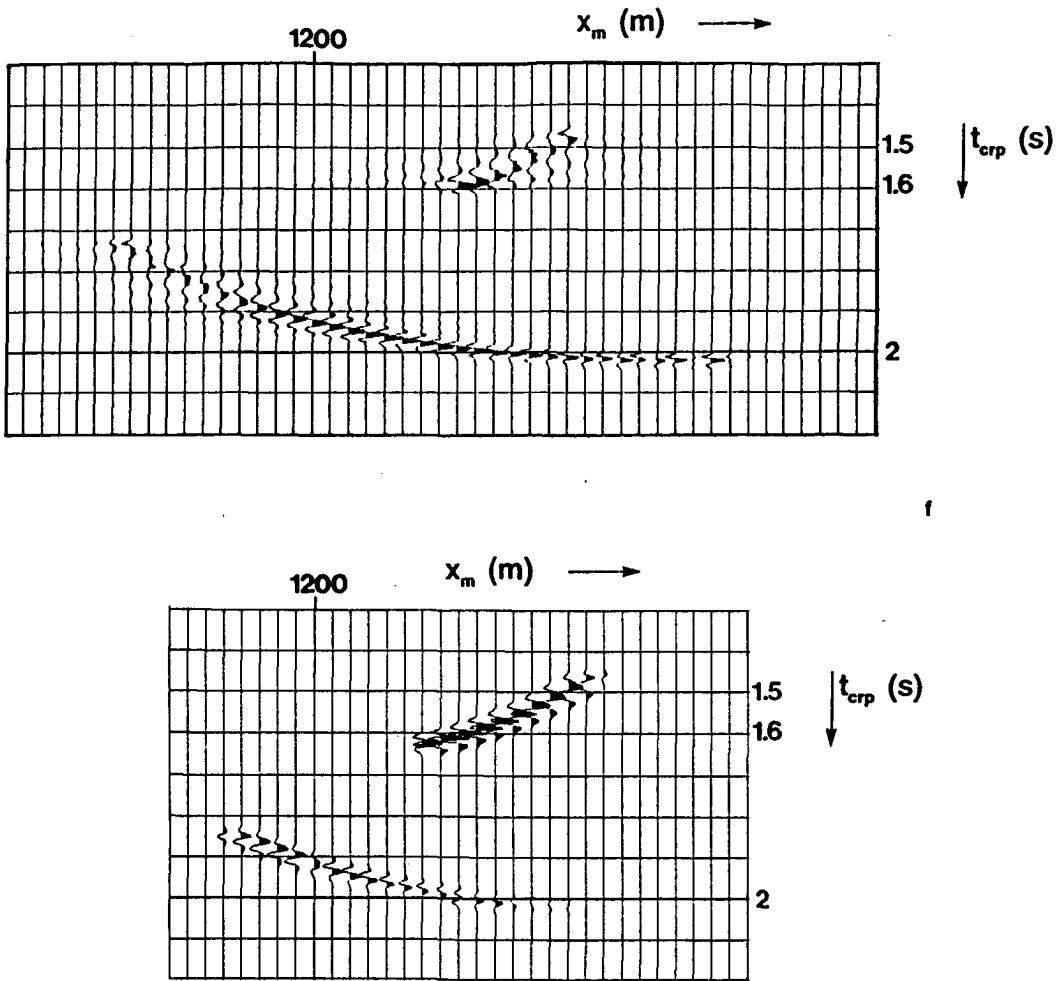


Figure IV.8f CRP operator impulse responses for the second reflector; $x_0 = 1200$ and $2x_h = 1940$ m.
 Top: CRP operator based on zero-offset ray tracing (identical to figure e).
 Bottom: CRP operator based on full offset ray tracing.

The shape of both CRP operators — including the double event — is identical. The zero-offset ray tracing based CRP operator (“ZO CRP”), therefore proves to be adequate in this situation.

The ZO CRP operator is more extended than the offset CRP operator. This can be explained by realizing that the offset rays will reach a critical angle sooner than the zero-offset ray. Although the larger width of the ZO CRP operator has no physical meaning, it will probably not harm us, because it allows the operator to go smoothly to zero, thus avoiding truncation effects.

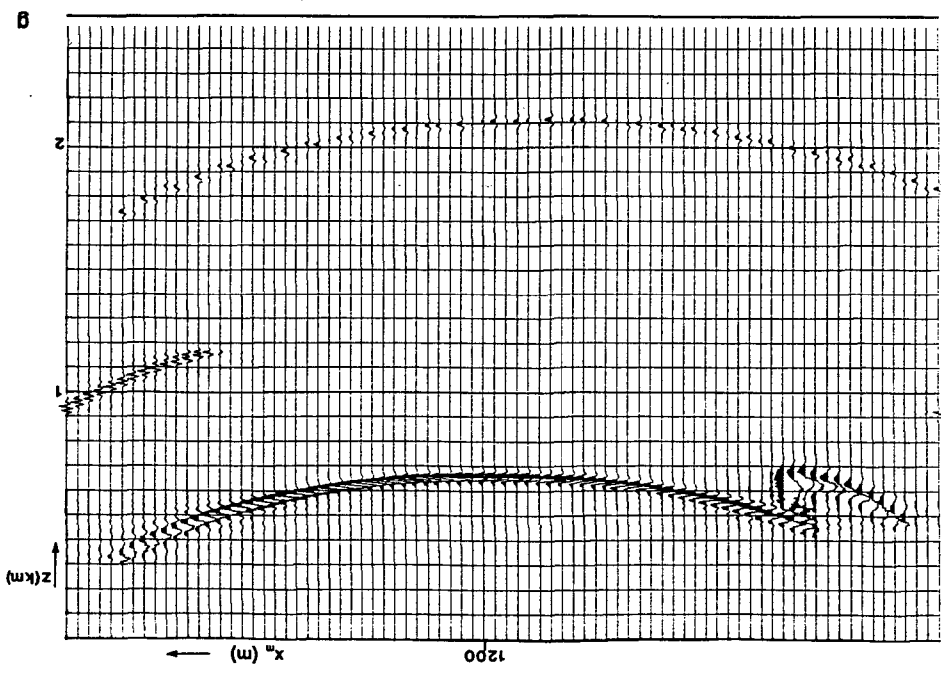


Figure IV.8g CRP prestack migration impulse response; input as in e.

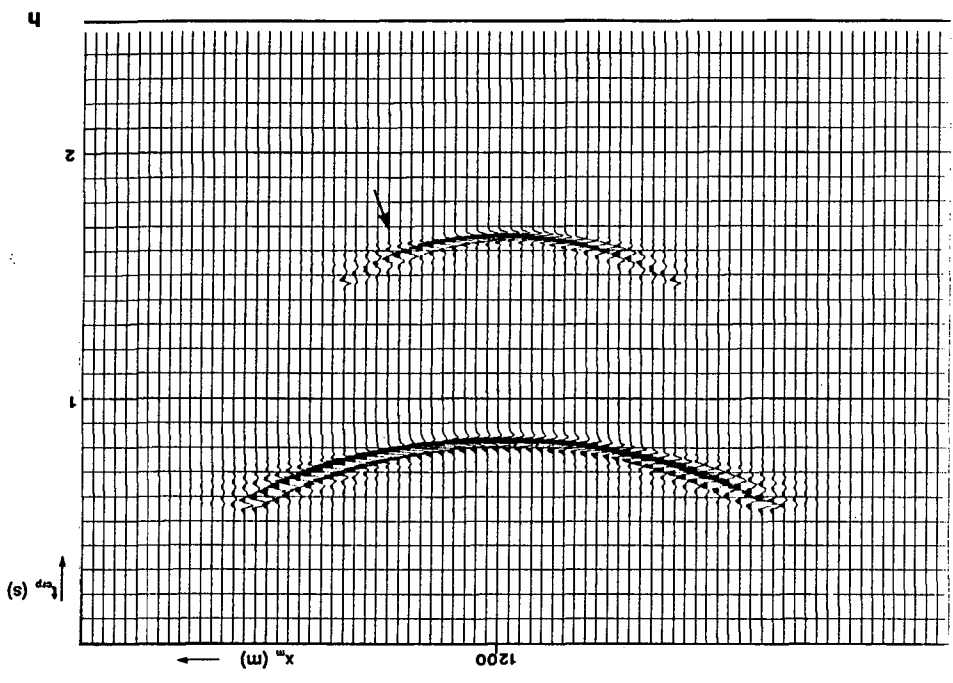


Figure IV.8h Impulse response of CRP stacking operator when the macro model has a constant velocity of 1600 m/s (compare with figure IV.8e, the input data is the same as in e).

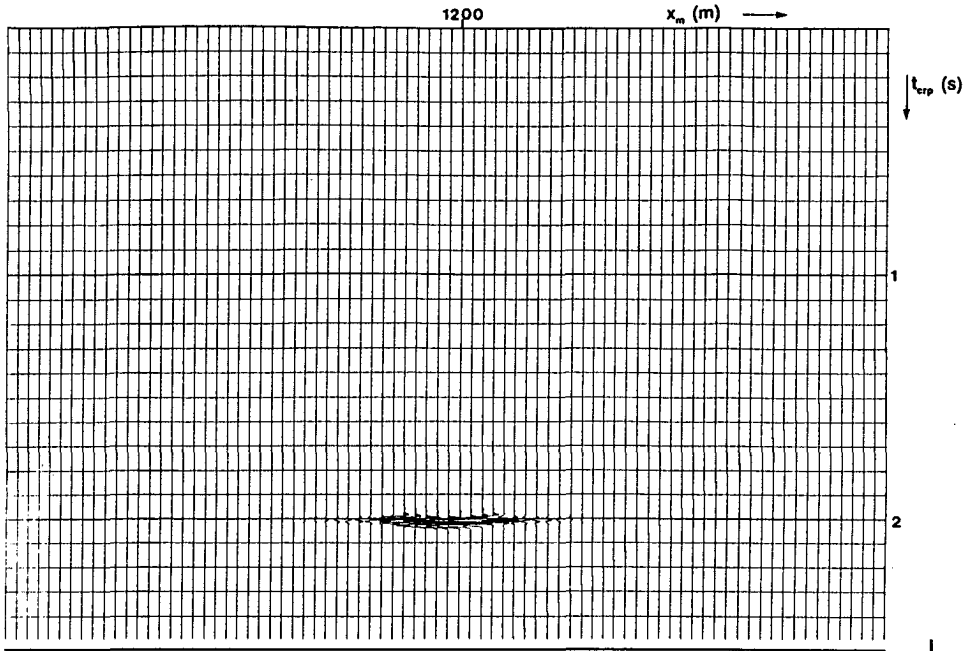


Figure IV.8i DMO impulse response for the second layer only. The velocity has been chosen constant and equal to the zero-dip stacking velocity. Compare with the correct operator depicted in figure e.

On the other hand, the second event between 1.5 and 1.6 s is more extended in the offset CRP operator.

In other words, no general conclusions can be drawn with respect to the width of the operators. The shapes, however, match very well.

Let us now investigate how conventional DMO would work out for the second reflector. According to what has been said in section IV.2, the constant velocity DMO operator is applied after zero-dip NMO correction. We compute the zero-dip stacking velocity at the location 1200 m for the appropriate zero-offset time and compute the constant velocity DMO impulse for an offset equal to 1940 m, after the zero-dip NMO correction. The result shows a very flat but symmetrical DMO operator (see figure IV.8i). Although the zero-dip stacking velocity varies laterally we kept this velocity constant. The DMO stack, shown in figure IV.8j, has been scaled according to the energy level of the same reflector in the CRP stack. We see that especially in the middle, where we have full coverage — and where the velocity is correct —, that the reflection event is highly dispersed. The different offsets do not add constructively, resulting in a low amplitude level. This can be seen even better by

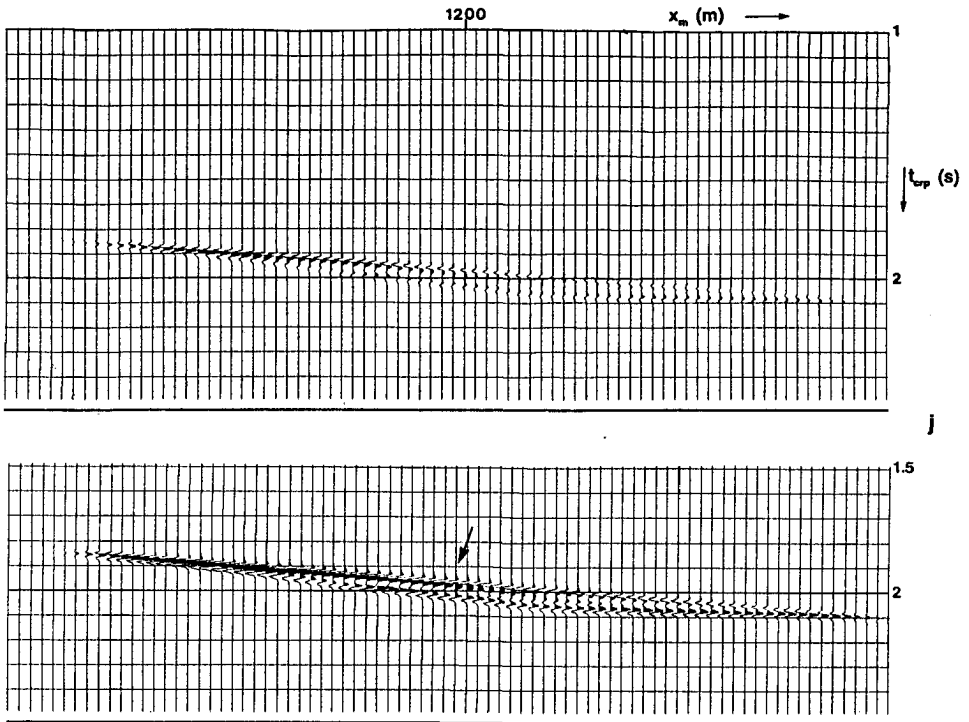


Figure IV.8j DMO stack, scaled to the CRP stack in figure IV.8b (top) and normalized to its own maximum energy (bottom). The arrow indicates the location where the zero-dip stacking velocity has been determined. Note the significant difference between DMO and CRP (figure IV.8b) processing.

processing only the largest offset, see figure IV.8k. This reflection is completely mispositioned. We may conclude that application of constant velocity DMO will not enhance the signal to noise ratio expected by the stacking process, nor will correctly position events for offsets not equal to zero.

Finally, the CMP stack of the second reflector is shown in figure IV.8l. The stacking velocity has been chosen constant, and equal to the stacking velocity at location 1200 m. We see that the CMP stack is far superior to the DMO. This is fully in agreement with the explanation given in section IV.2.

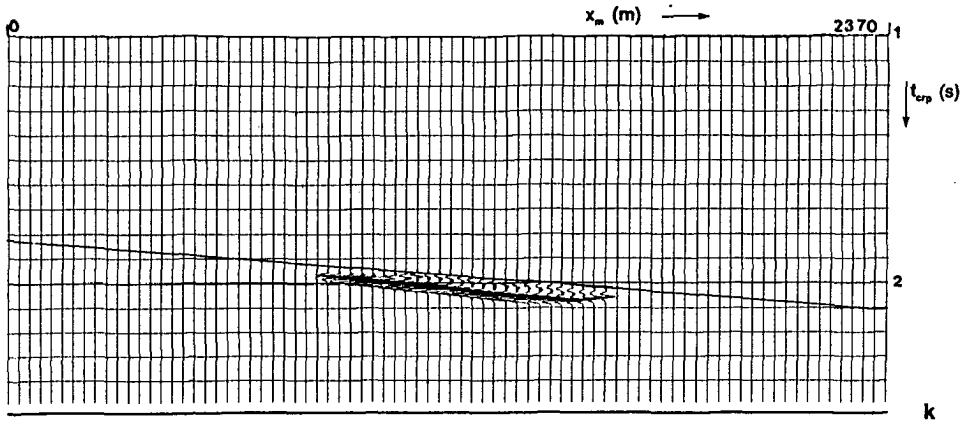


Figure IV.8k DMO stack, only one offset, $2x_h = 1940$ m, has been used. The continuous line indicates the true zero-offset reflection. Hence for inhomogeneous macro models DMO processing produces mis-aligned offsets.

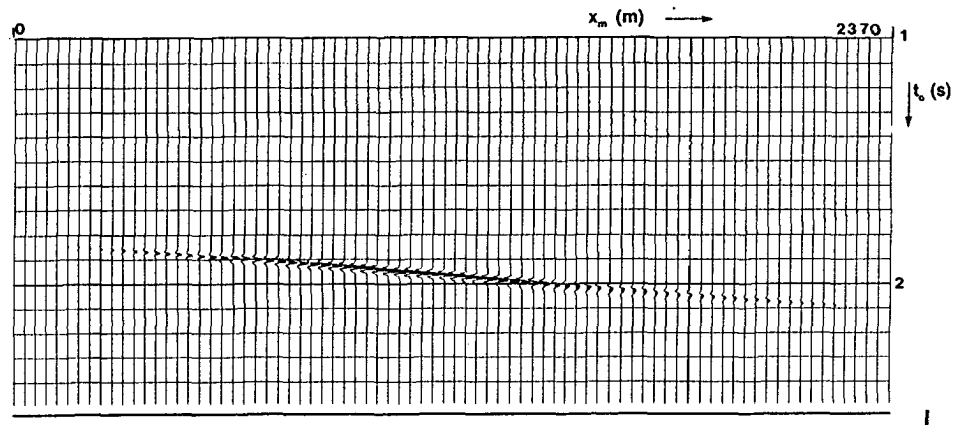


Figure IV.8l CMP stack of second reflector. The stacking velocity has been kept constant and equal to the correct stacking velocity at 1200 m.

CONCLUSIONS

The synthetic data example discussed in this section clearly shows that application of CRP stacking (and prestack migration) — in comparison with CMP and DMO stacking — leads to superior results. All offset information is correctly positioned — contrary to constant velocity DMO — and contributes constructively to a final stack.

REAL DATA EXAMPLE OF CMP, CRP AND CDP PROCESSING

V.1 INTRODUCTION

In this chapter a real data example is discussed (see also Van der Schoot et al. (1989)). The data were kindly provided by NAM, Assen.

The purpose of this chapter is to show the differences in processing results due to application of the different processing schemes.

The term prestack migration is used for wave-equation based migration by shot record inversion.

Where CRP prestack migration is meant, it will be stated explicitly.

V.2 REAL DATA EXAMPLE

Figures V.1 and V.2 show an unmigrated CMP stacked section and the corresponding time-migrated CMP section, respectively. The geological structure is severely affected by salt tectonics. The top salt is the interface between respectively the layers with velocity 3650 and 4465 m/s, see figure V.3.

Notice the large fault, which causes strong lateral velocity variations and makes proper imaging of the base salt reflector — at about 2.3 s — a problem, especially on the right side of the section. Time migration was applied using 90% of stacking velocities.

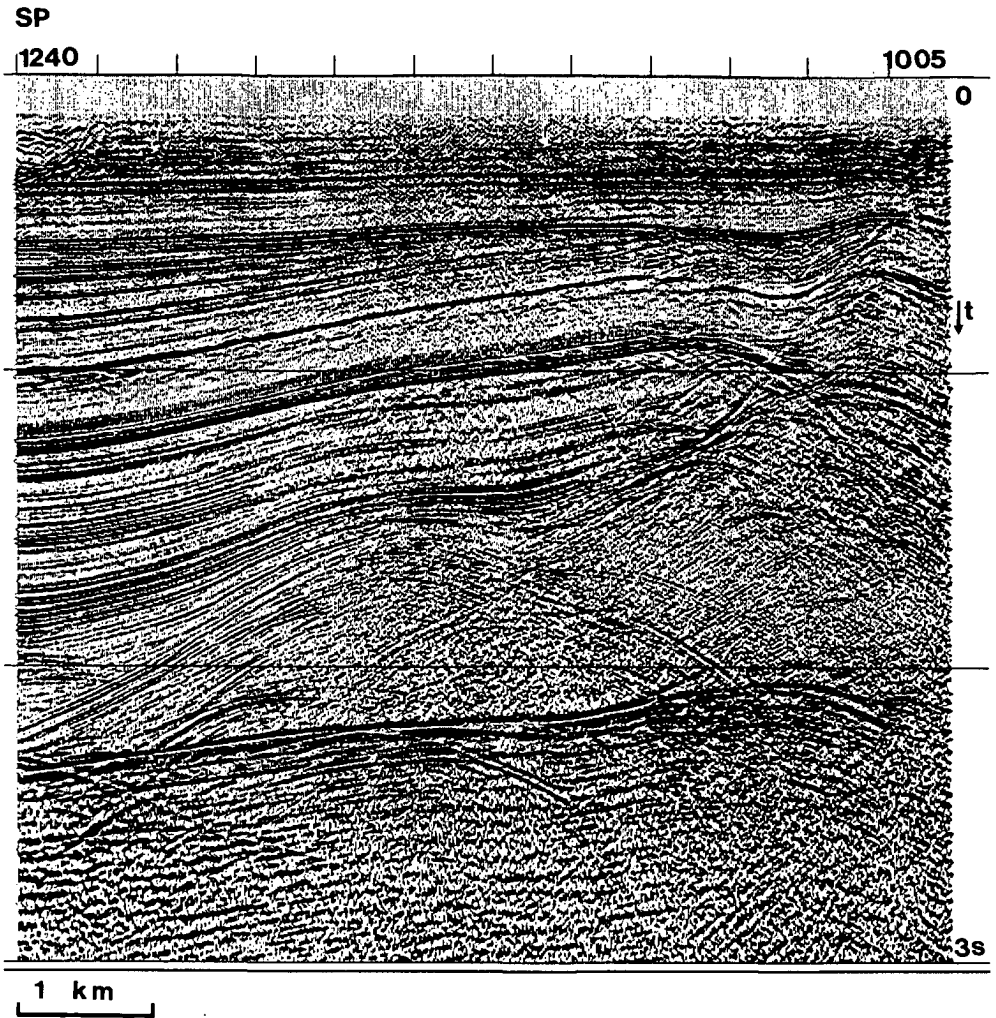


Figure V.1 Unmigrated CMP stack.

Next we digitized the main interpreted horizons and used these time picks together with the stacking velocities to build a macro model by an algorithm which inverts for traveltimes. Having derived a macro model we performed a poststack depth migration. We then found a small mismatch in the position of the fault. An update of the macro model led to a perfect match with the new CMP poststack migration result.

The macro model is shown in figure V.3. The model shows the main geological boundaries and a velocity for each layer (the velocities are indicated without gradients).

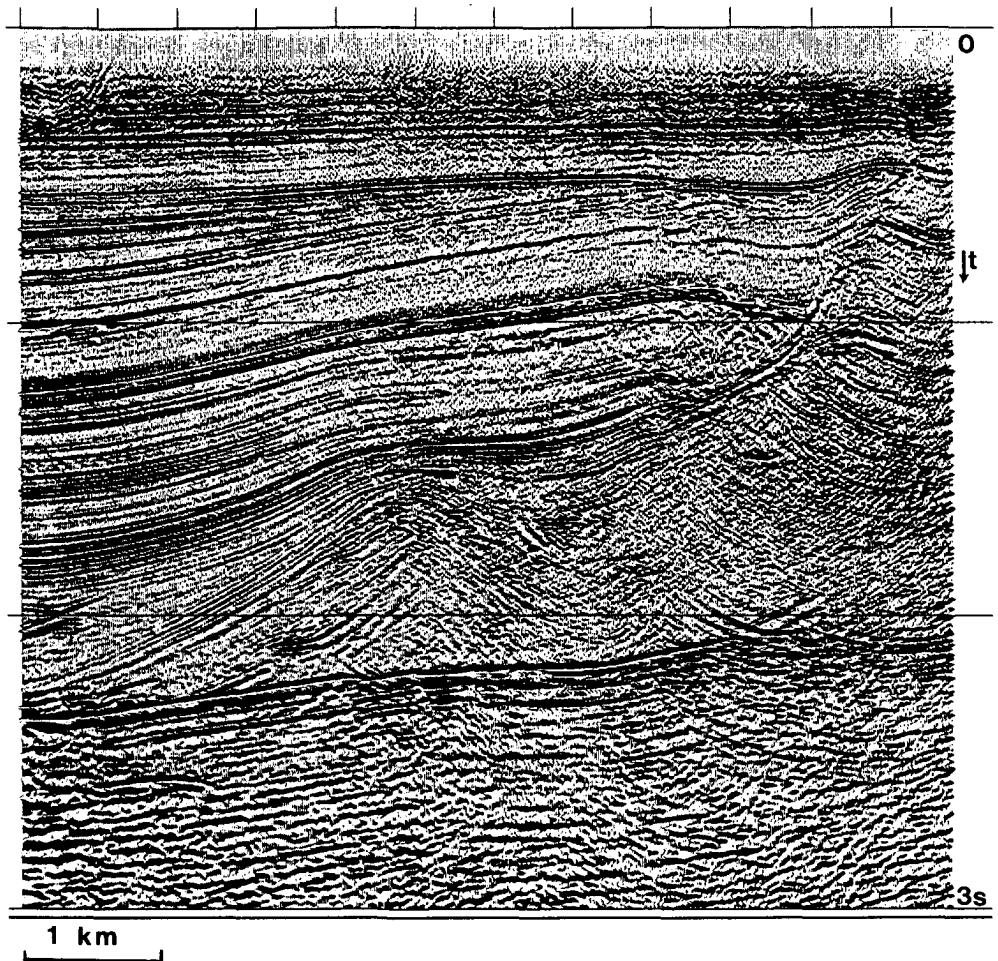


Figure V.2 Poststack time migrated CMP stack.

Figure V.4 shows the result of the corresponding poststack depth migration. The section is plotted in depth, as are all the depth-migrated sections which follow. We can see that there is indeed a very good match between the macro model and the poststack depth migration. In addition, the result of the poststack depth migration is superior to the time migration result.

Note, for instance, that the fault definition for the base salt reflector at 3300 m is far better on the depth-migrated section.

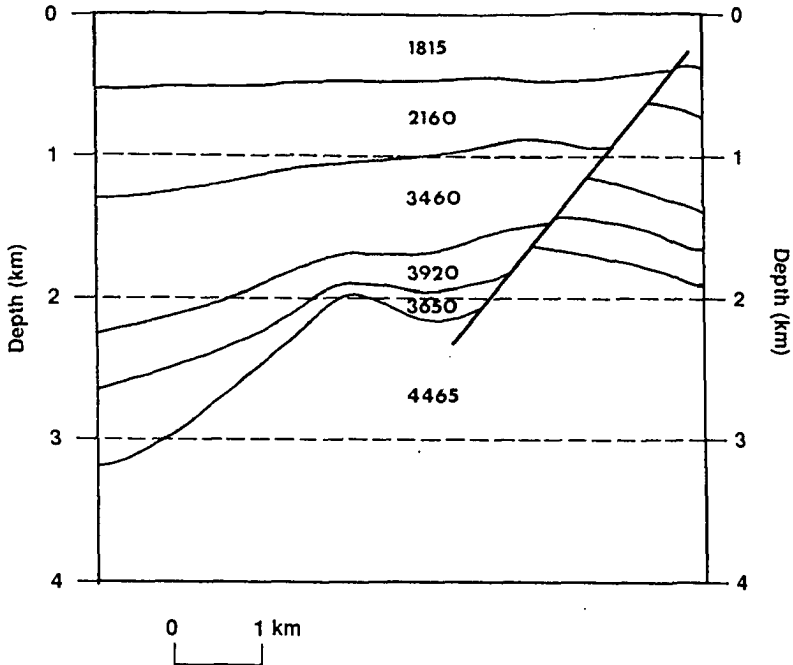


Figure V.3 Macro subsurface model. Velocity variations within a layer are not indicated.

Next we used the macro model to migrate all shot records individually and stacked them to build a prestack depth-migrated section.

Figure V.5a shows three successive shot records from the left end of the line. Migration of one such shot record should give us a single fold prestack migrated image of part of the subsurface, that part being determined by the geometry of the raypaths from the source to the receivers. The migrated shot records are shown in figure V.5b. We see that detailed subsurface information is available from only one migrated shot record.

Having stacked all migrated shot records, the resulting prestack migrated section is shown in figure V.6.

We see that, although the poststack depth-migrated section is good, the prestack depth-migrated section is clearly superior. For instance, we see that the fault definition is much better. On the right side of the poststack depth-migrated section an anhydride reflection (at 3200 m) could easily be misinterpreted as a high block of the base salt, although strange smiles indicate out-of-plane effects. However, on the prestack depth-migrated section the base salt seems to continue to the right as a low block.

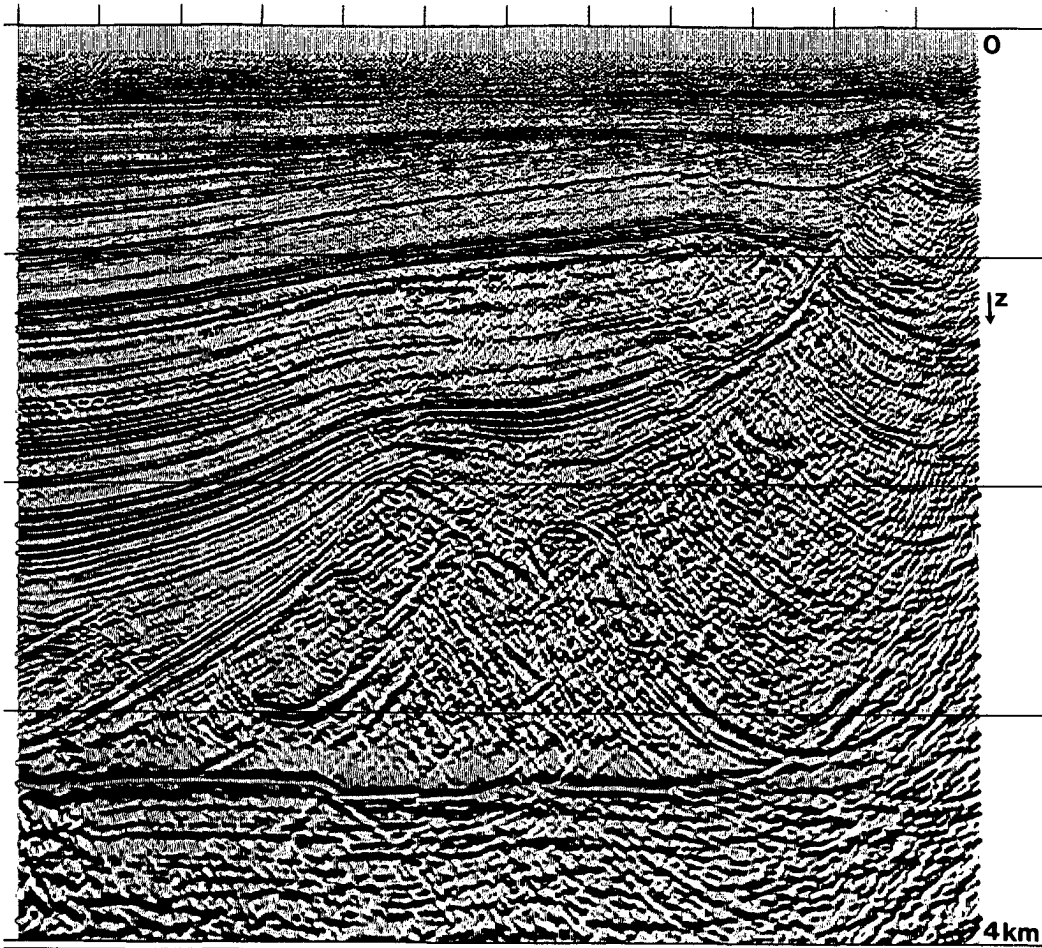


Figure V.4 Poststack depth migrated section.

To appreciate the prestack depth migration, figure V.7 shows some close-ups taken from the poststack and prestack depth-migrated sections. Figure V.7a is a close-up of the upper part of the section. Of course, this is not an important target zone for which we would need to apply a prestack migration. Nevertheless, we can see that the prestack migration result shows far better lateral resolution. The small faults are very precisely defined. Figure V.7b is a close-up of the top salt horizon.

The prestack migration shows good definition of the top salt (between 2.0 and 2.2 km), whereas one has to guess where it is on the poststack depth migration.

Another close-up, shown in figure V.7c is rather self-explanatory. Notice the very sharp fault definition in the base salt reflector.

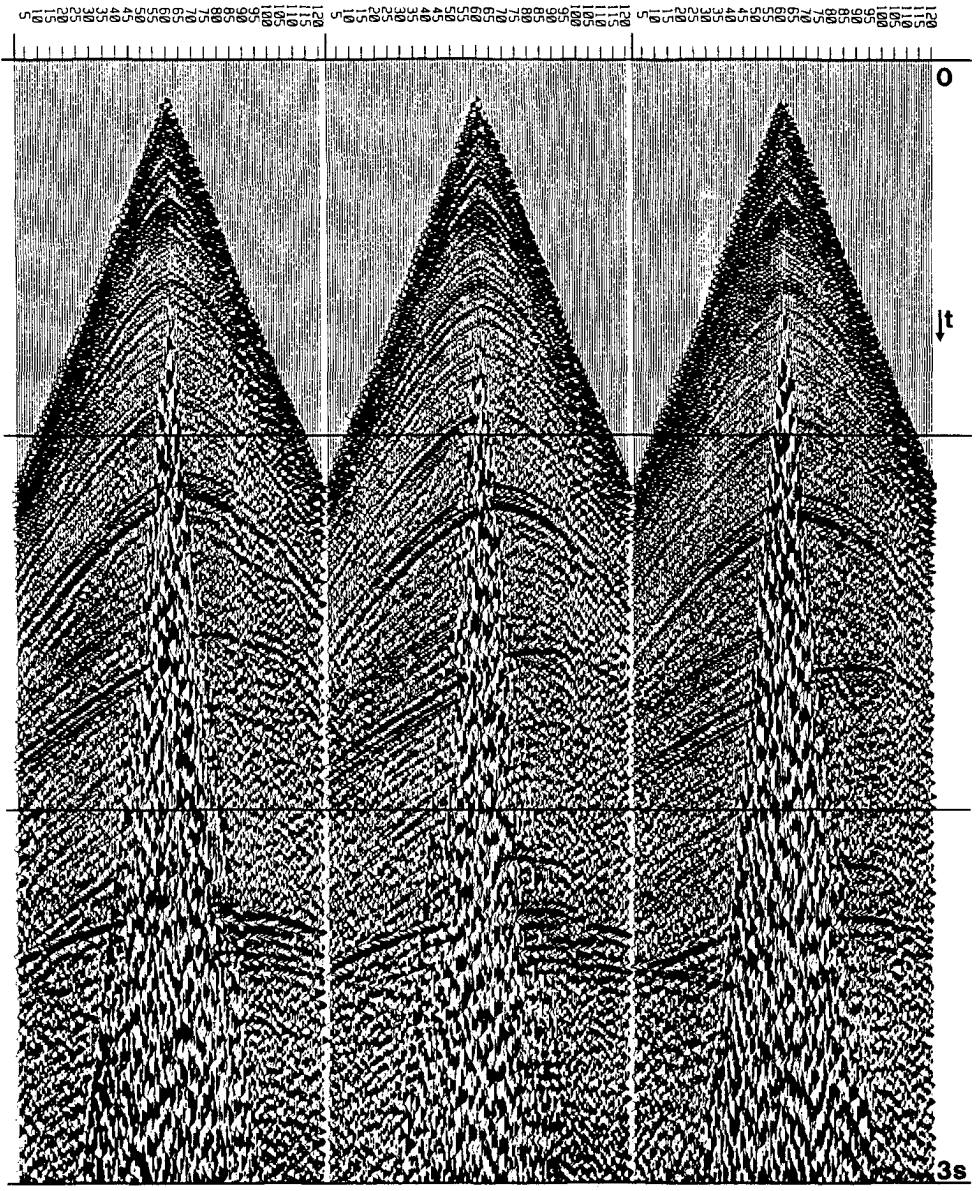


Figure V.5a Unmigrated shot records.

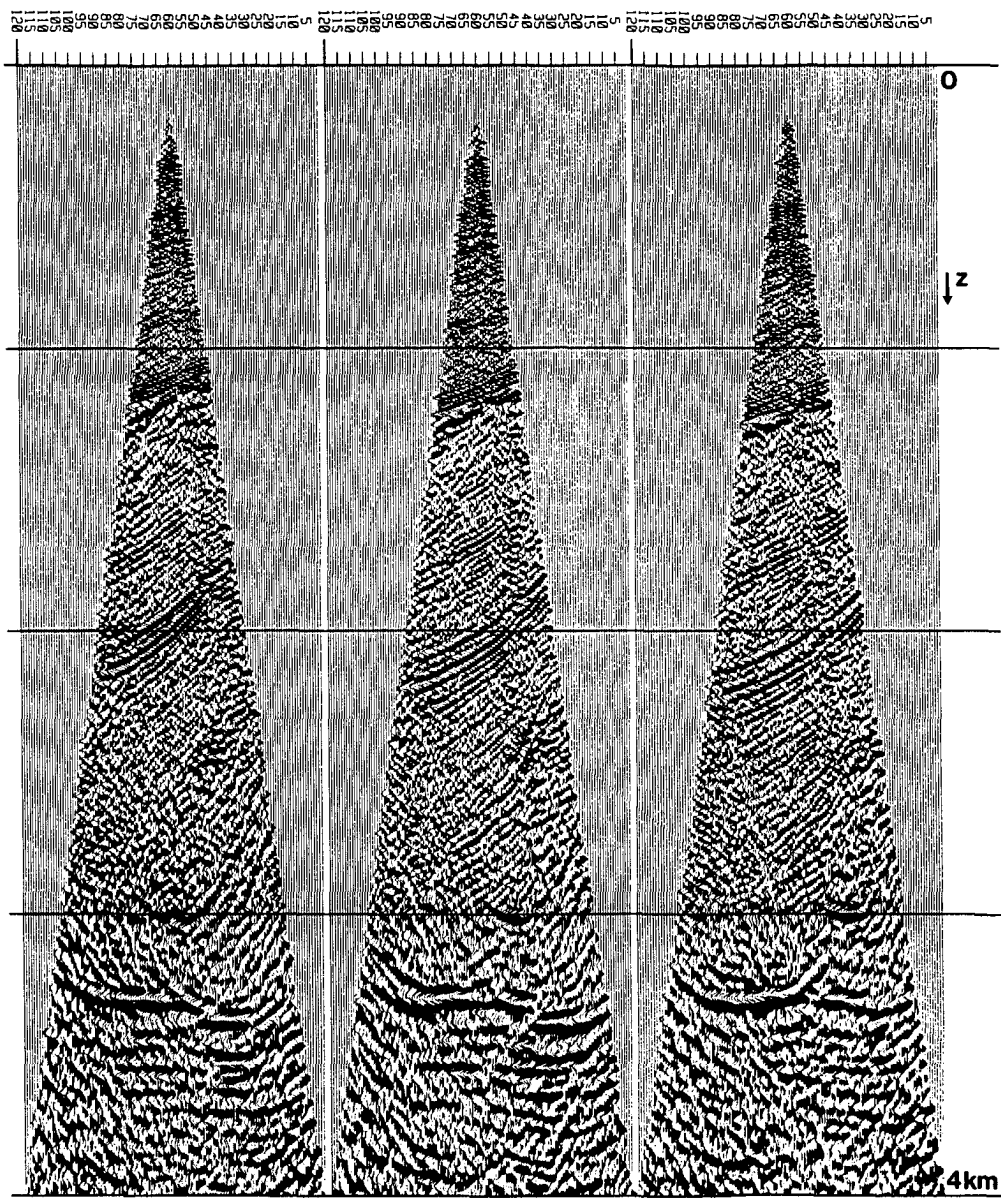


Figure V.5b Migrated shot records.

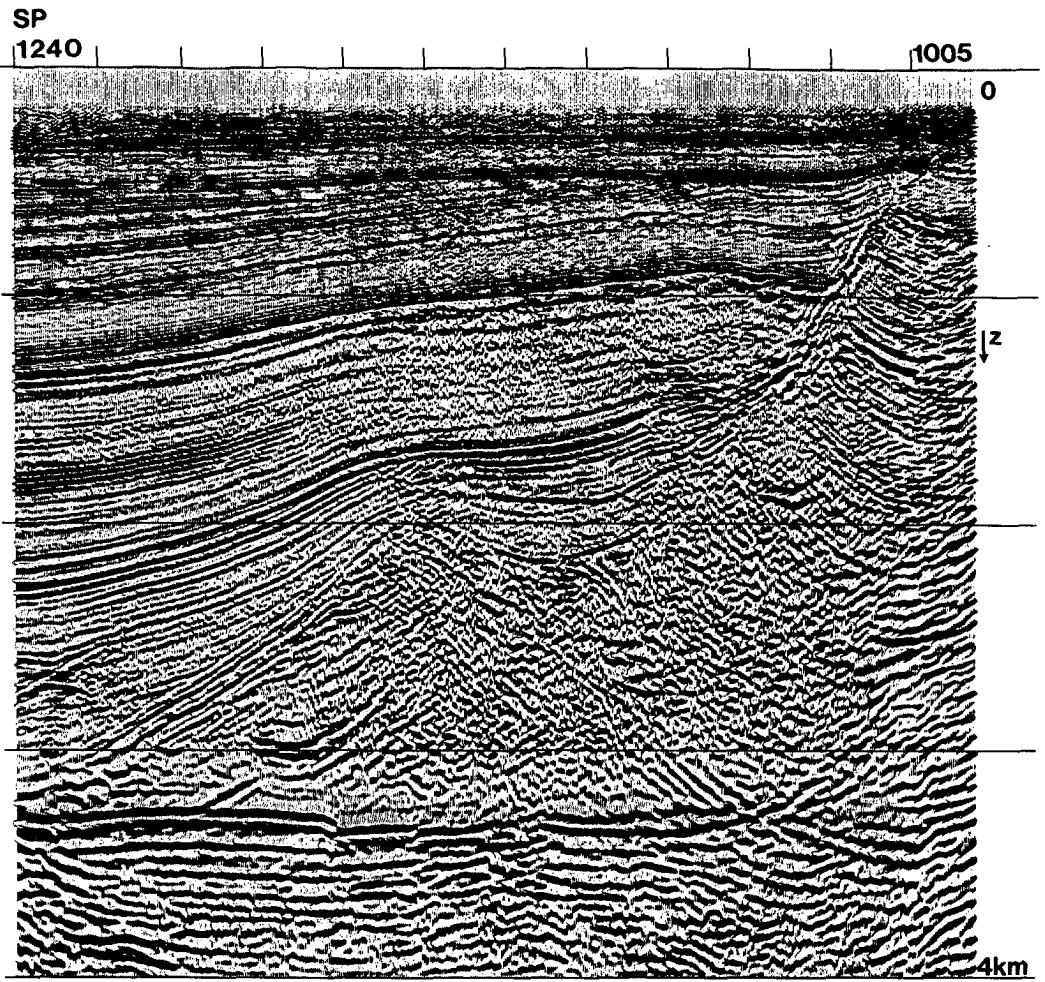


Figure V.6 Prestack migrated section.

We now selected a portion of the complete data set and applied CRP stacking (figure V.8a), CMP stacking (figure V.8b) and conventional constant velocity DMO stacking (figure V.8c).

A comparison leads to the following remarks.

The top salt reflection appears to be continuous on the CMP stack, whereas in the CRP stack this reflection is a little broken. The DMO stack shows a result in between. In this area it is known — from interpretation of 3-D surveys — that a continuous top salt reflector is the most plausible interpretation.

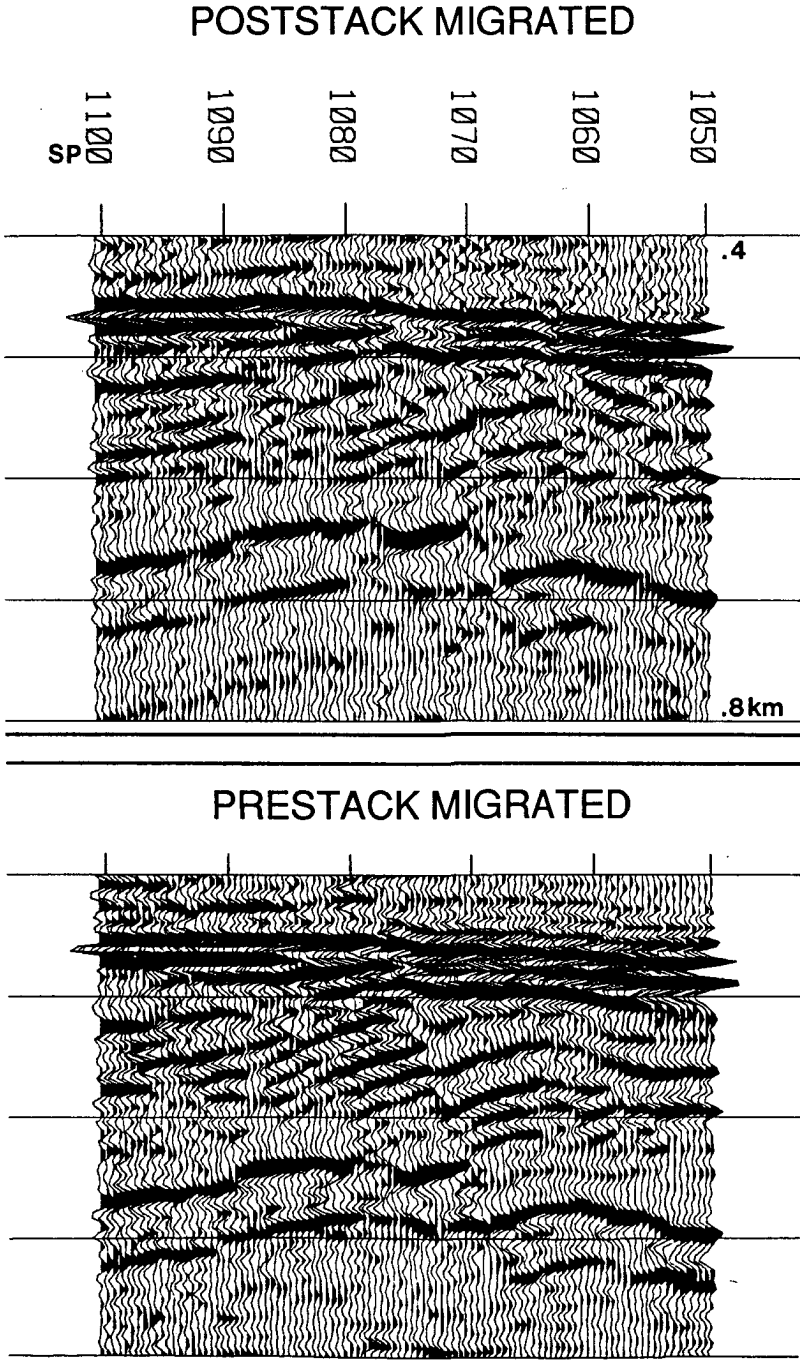


Figure V.7a Comparison between portions of the poststack and prestack depth migrated sections.

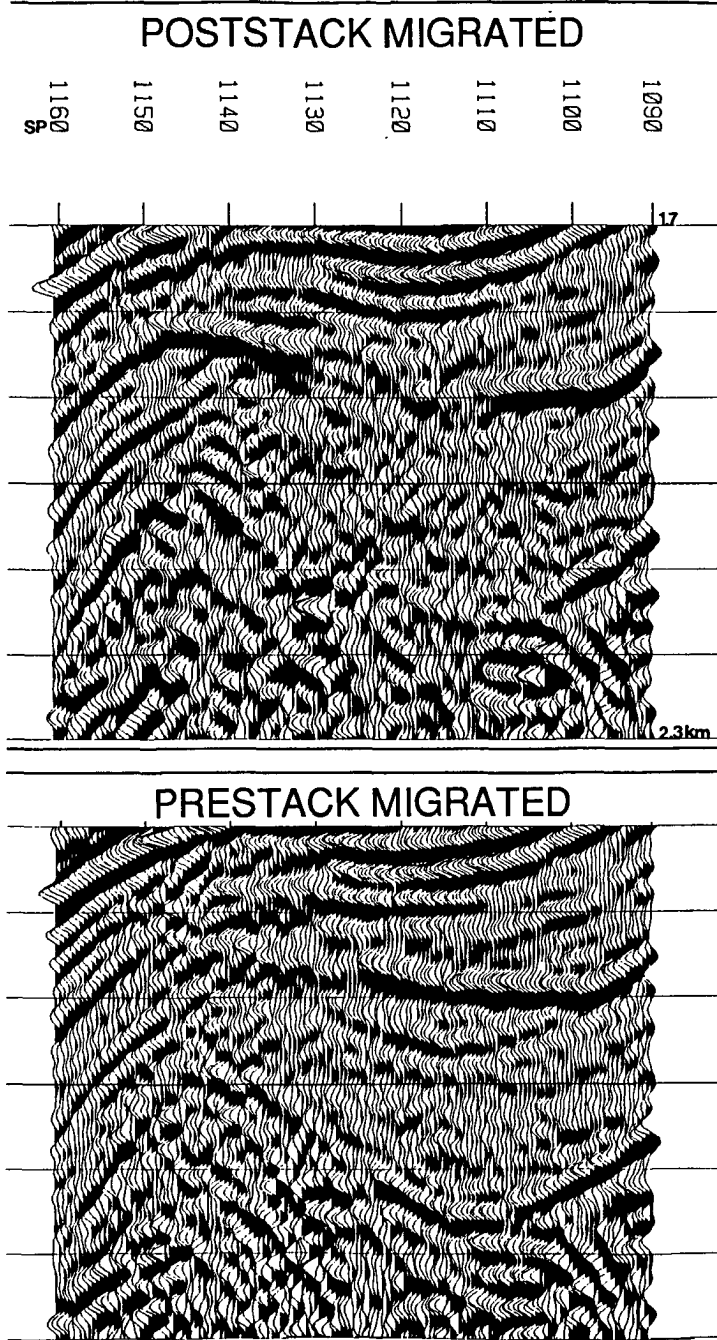


Figure V.7b as in a.

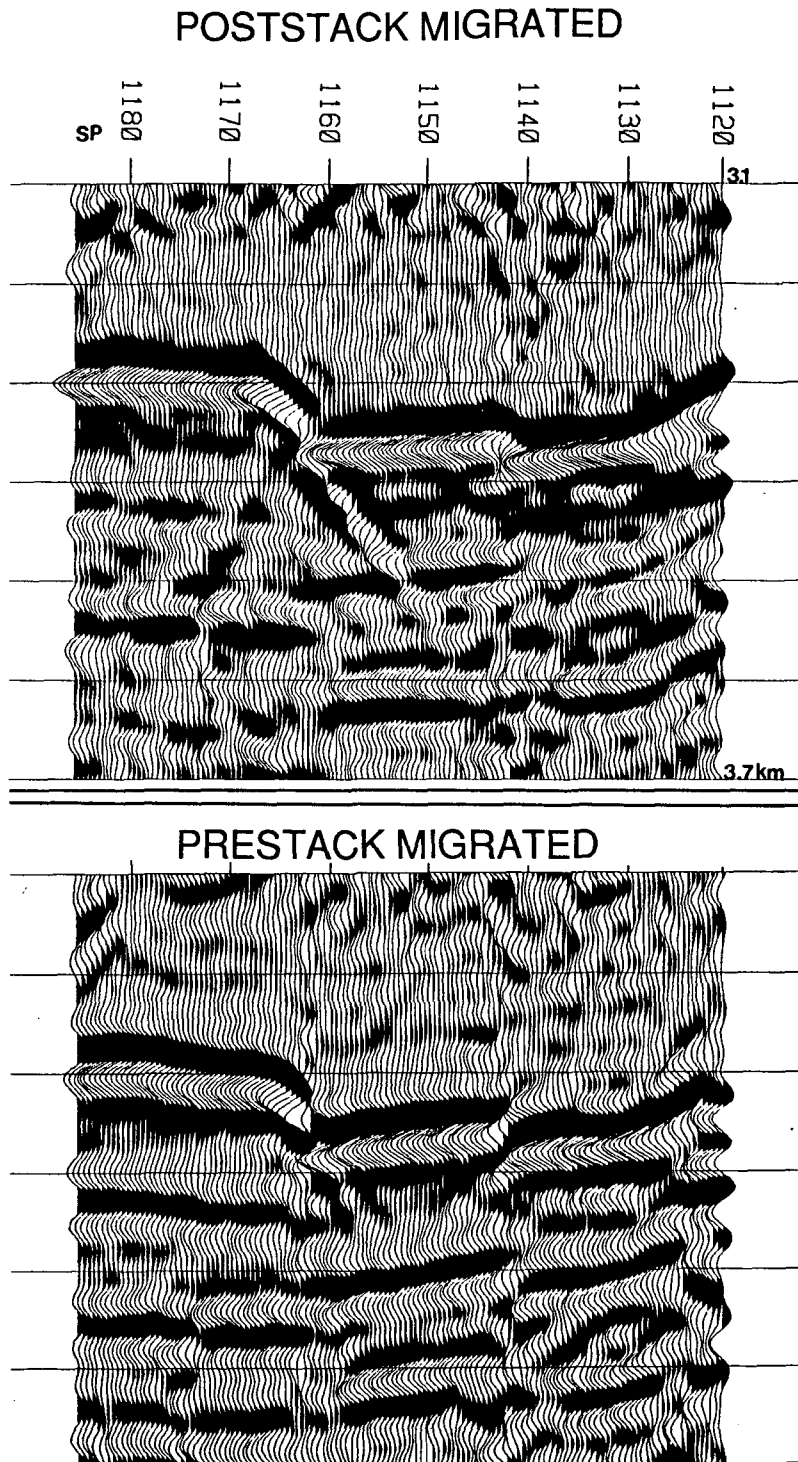


Figure V.7c as in a.

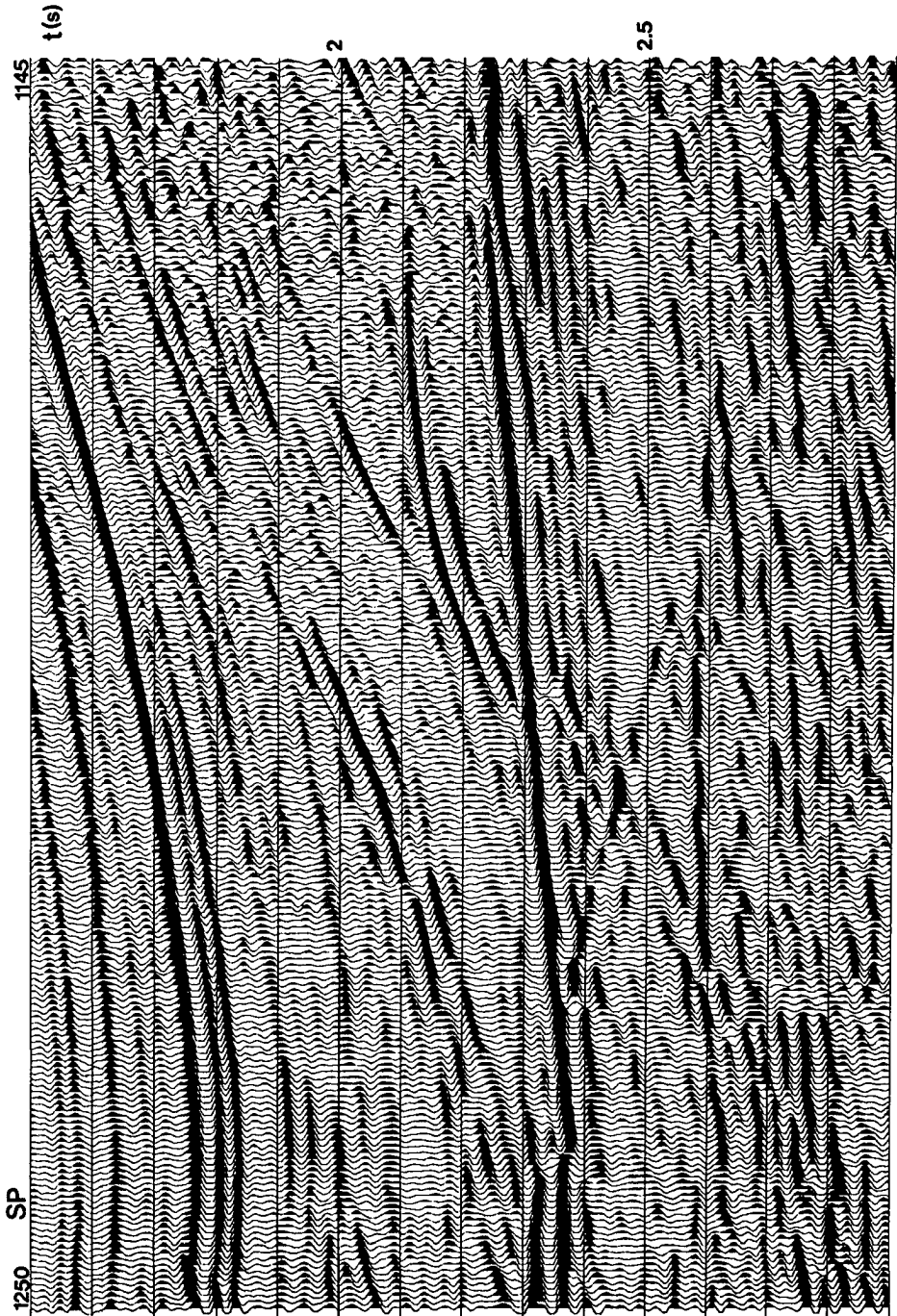


Figure V.8a CRP stack; the CRP scheme is based on the flow diagram depicted in figure IV.7. The macro model used in the CRP processing is depicted in figure V.3.

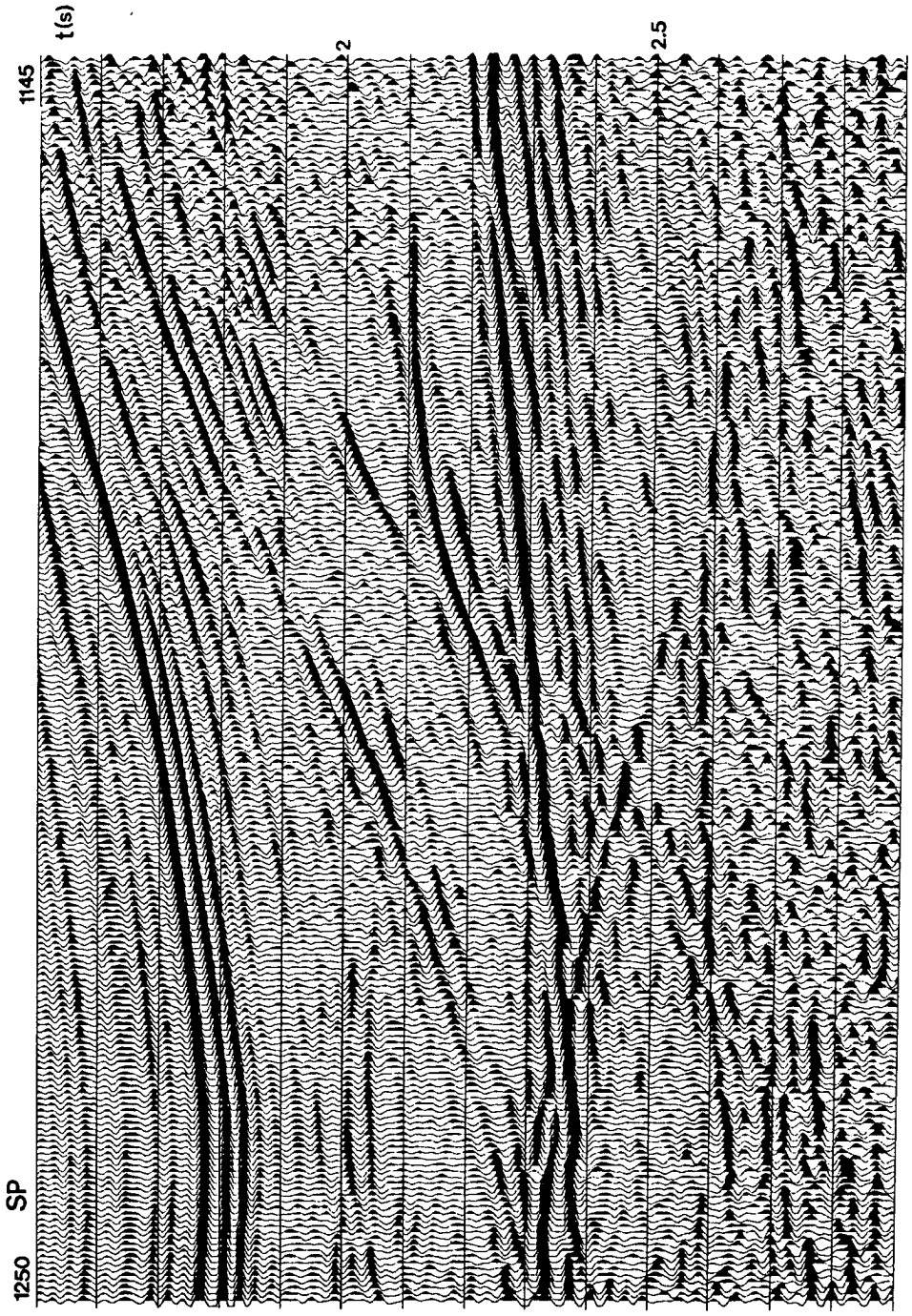


Figure V.8b CMP stack, based on NMO correction and stacking, using stacking velocities derived from conventional velocity analyses.

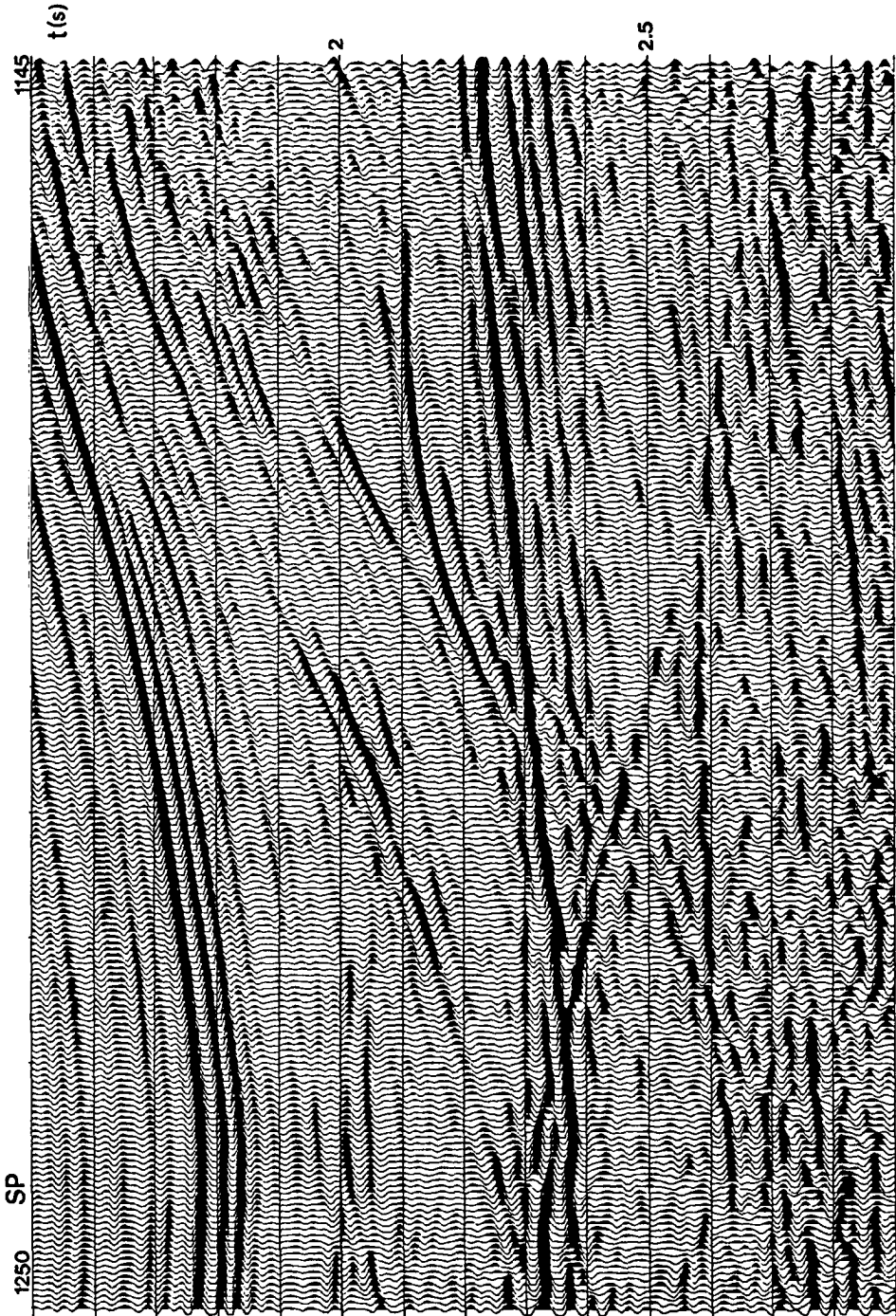


Figure V.8c Conventional (constant velocity) DMO stack. The data is zero-dip NMO corrected before application of ("velocity-independent") DMO.

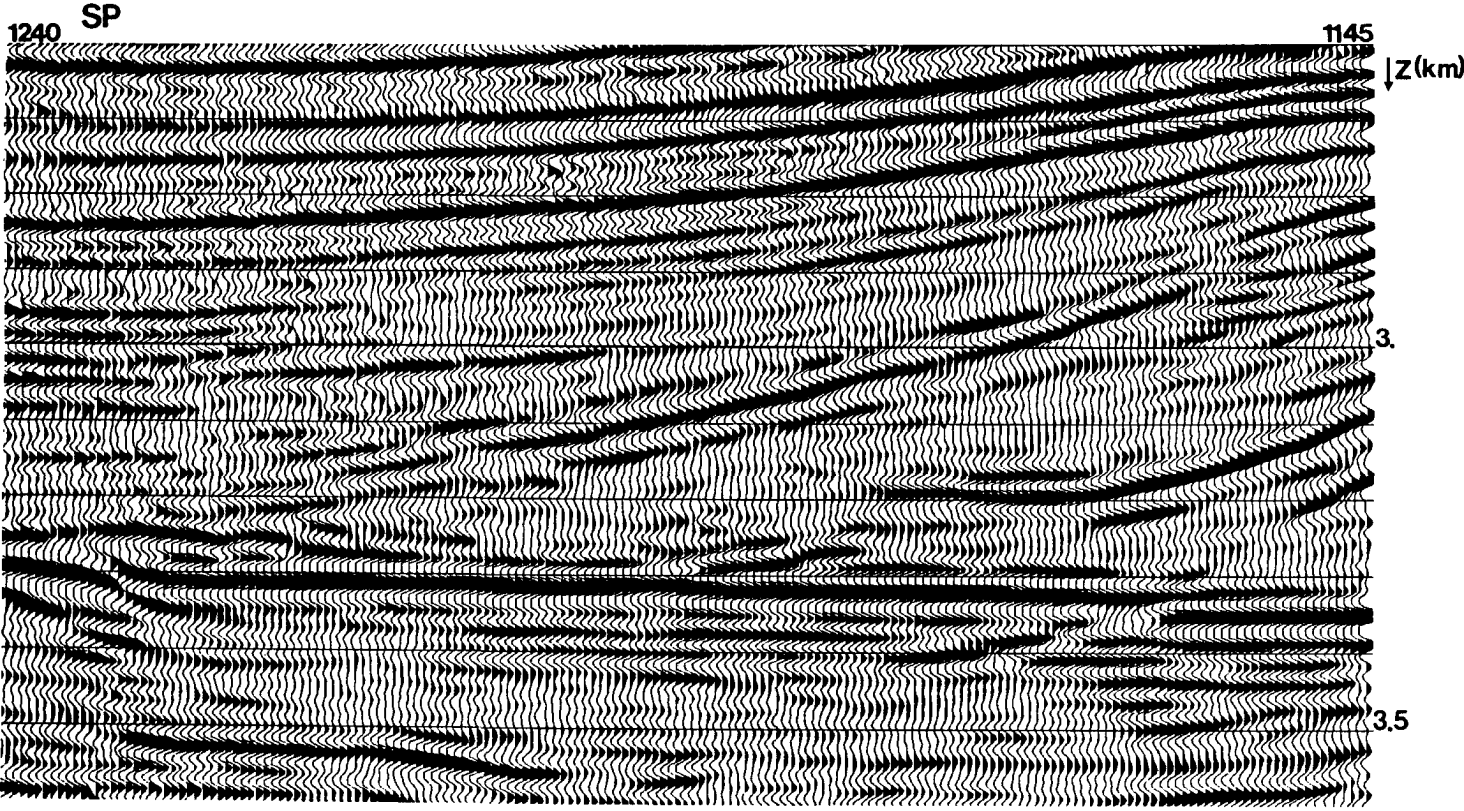


Figure V.8d CRP prestack migrated section based on the flow diagram depicted in figure IV.7.

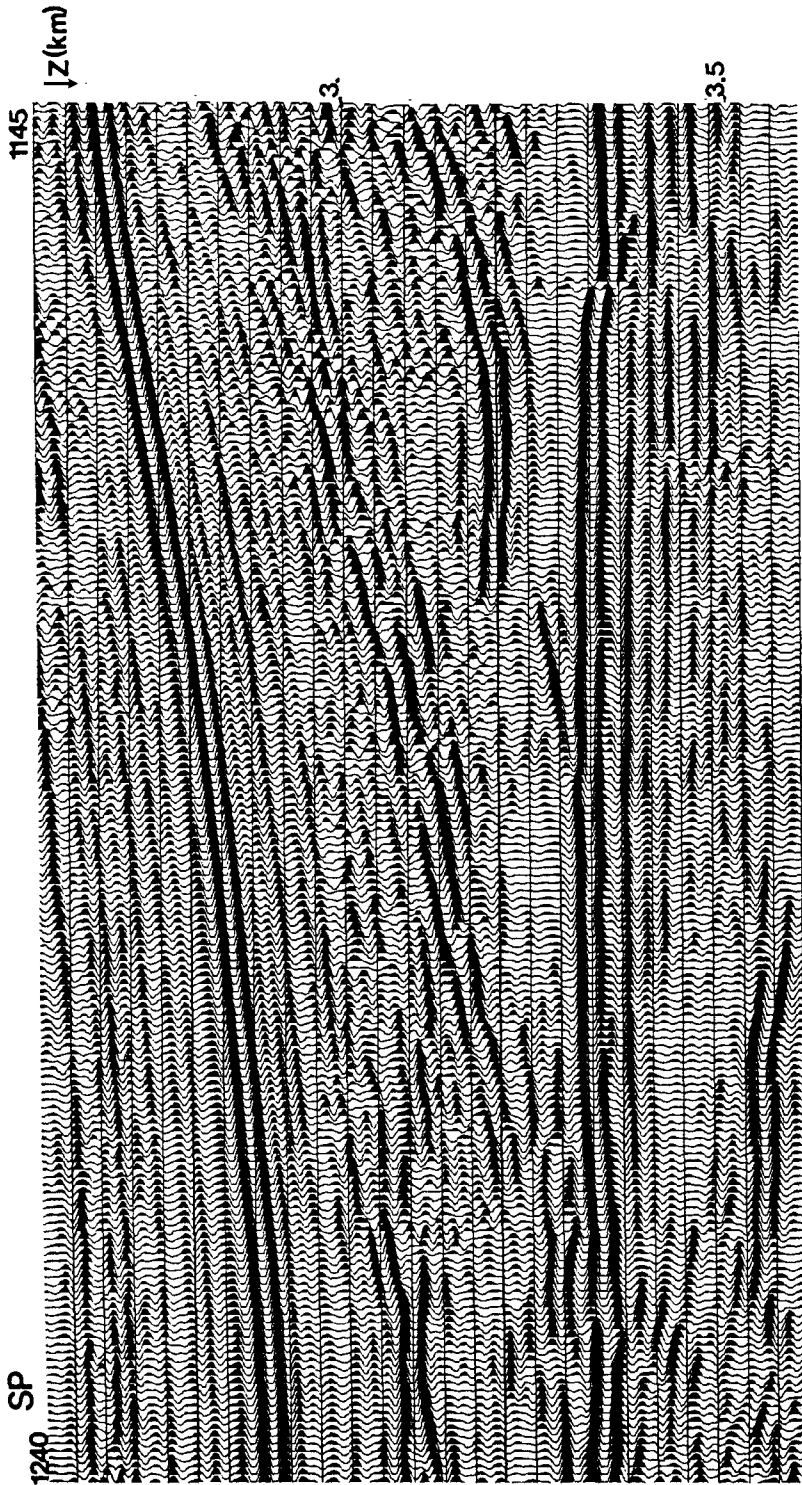


Figure V.8e. Wave equation based prestack migrated section.

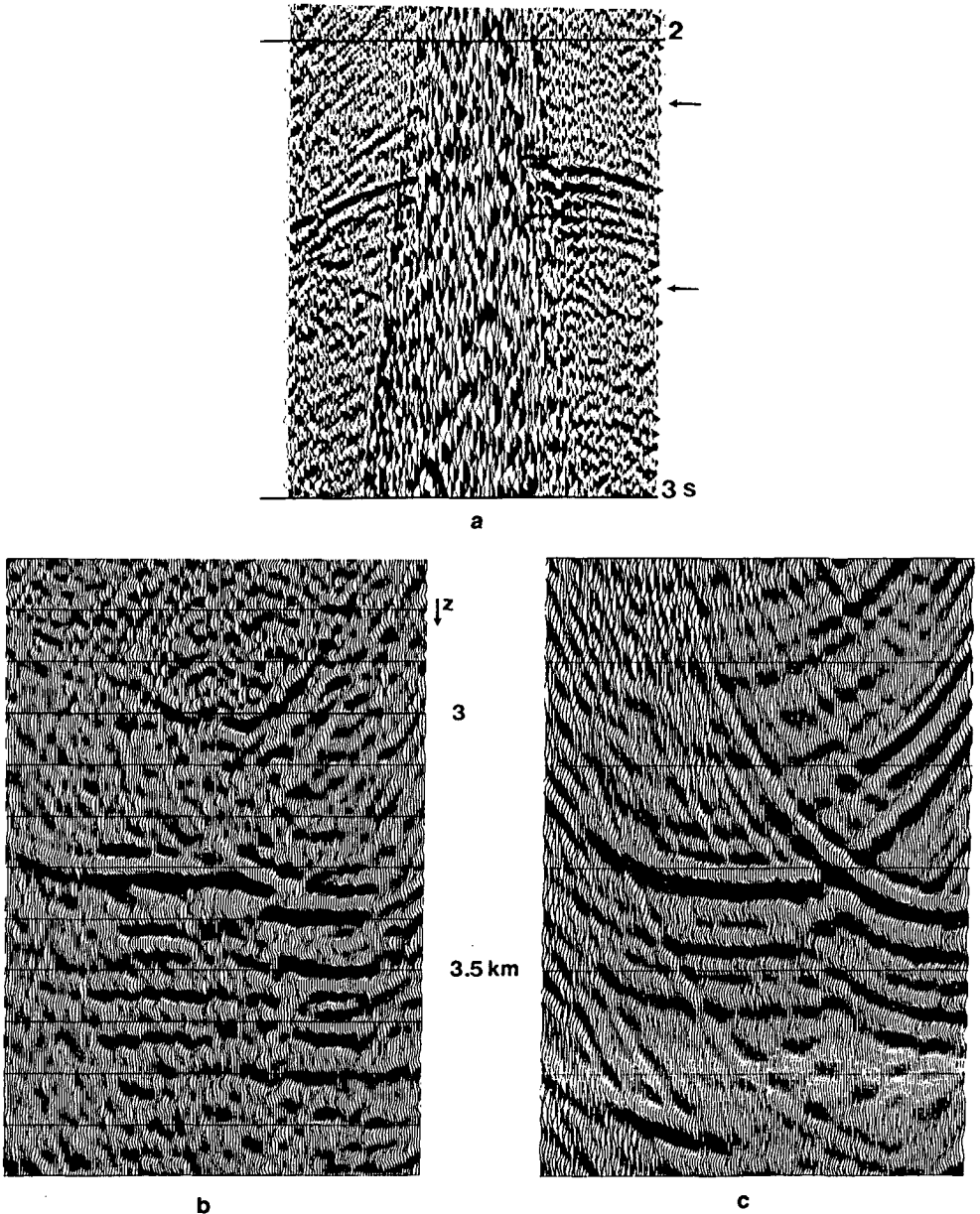


Figure V.9

- a. Unmigrated shot record. A split-spread configuration with a gap of 330 m in the middle has been used. For prestack shot record migration this gap should be filled with zero-traces. The window indicates the data to be migrated.
- b. Wave equation based prestack migration of a portion of the shot record depicted in figure a. Part of the faults shown in figure V.7c can also be seen on this result.
- c. CRP prestack migrated part of shot record. Note that the strong smiling partly has to do with the zero-traces in the middle of the shot record.

At about 2 s in the left part of the CRP section an onlap reflection lines up very well, whereas this reflection is hardly visible on the other sections.

In general the results of CMP, DMO and CRP processing are comparable.

Next we applied a CRP prestack migration on the same portion of data. The result is shown in figure V.8d. A close up of the wave equation based prestack migration (figure V.6) is given in figure V.8e. The following comments can be made.

The wave equation prestack migration shows a better fault definition in the base Zechstein reflector (at about 3.3 km). On the other hand, the preservation of character in the base Zechstein reflector on the CRP migration result and the overall appearance of the CRP migration are good.

Finally, CRP prestack migration can also be used to migrate single shot records. The scheme will then be less efficient, since it is based — see figure IV.7 — on ZO raytracing at one CMP location for CRP processing of all offsets.

An example of a shot record before (a detail of the shot record at the left side in figure V.5a) and — part of it — after CRP prestack migration is shown in figure V.9. The same part is also compared with wave equation prestack migration. It can be seen very clearly that the finite-difference wave equation migration result is dip limited. Furthermore the results are comparable.

V.3 CONCLUSIONS

As we expected, the best results are obtained by application of CDP processing. The poststack time migrated CMP stack gives a poor definition of the target zone, that is the base Zechstein reflector. The poststack depth migrated CMP stack gives a better result, although this result is still inferior to the CDP prestack depth migrated image.

CRP processing gives good results. More experience still has to be gained in the choice of different processing parameters, such as the dip sampling.

The conclusion can be drawn that CRP processing — stacking as well as prestack migration — can be a valuable and cost-effective tool. The CRP prestack migration is an interesting option, since the method is fast and accurate.

VI

CRP STACKING IN 3-D MEDIA**VI.1 INTRODUCTION**

The main emphasize during the course of this research has been laid on understanding and exploiting the concepts of CRP stacking in 2-D media.

However, it is worthwhile to indicate the possibilities of CRP stacking in three dimensions.

VI.2 CRP STACKING IN 3-D MEDIA

If we consider the generalization of the CRP concept we will restrict ourselves to 3-D media locally consisting of constant velocity layers separated by plane arbitrarily dipping interfaces around the normal incidence ray path of each shot-receiver midpoint.

A macro model corresponding to such a medium is shown in figure VI.1.

We now use this model to investigate the characteristics of reflection point smear in 3-D media by raytracing. Although some theoretical studies have been carried out on this subject (see e.g. Krey, 1976) we will restrict ourselves to this raytracing experiment.

Figure VI.1 also shows a CMP location with a number of shot-receiver configurations.

Figure VI.2a shows the reflecting raypaths to the first interface. Since the shot-receiver configuration is in the dip direction of this plane, the situation is a 2-D one and the reflection points clearly lay on a straight line in the vertical plane, see figure VI.2b.

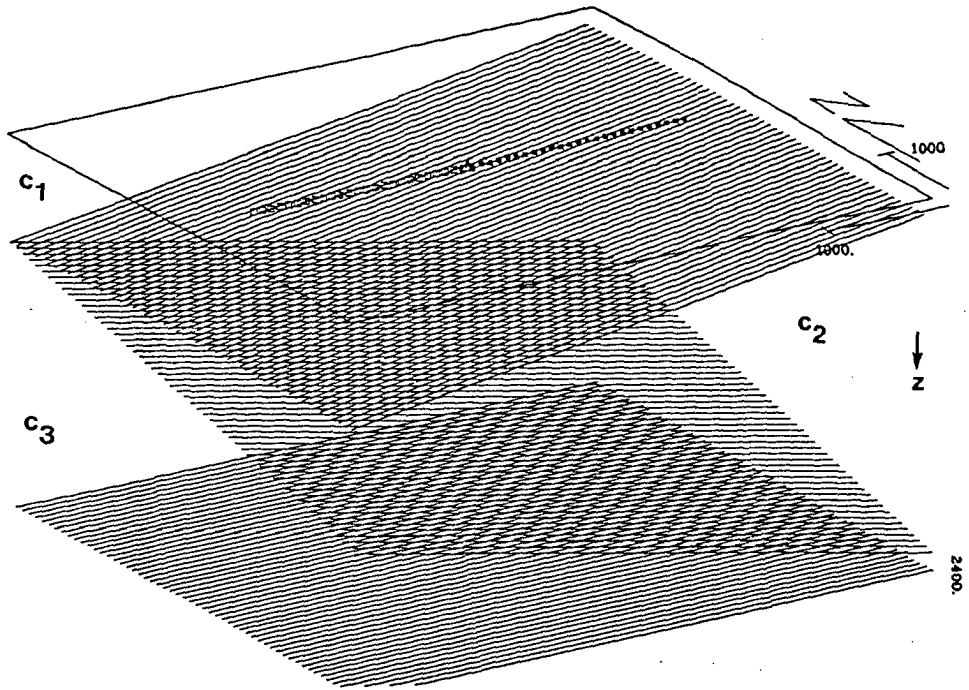
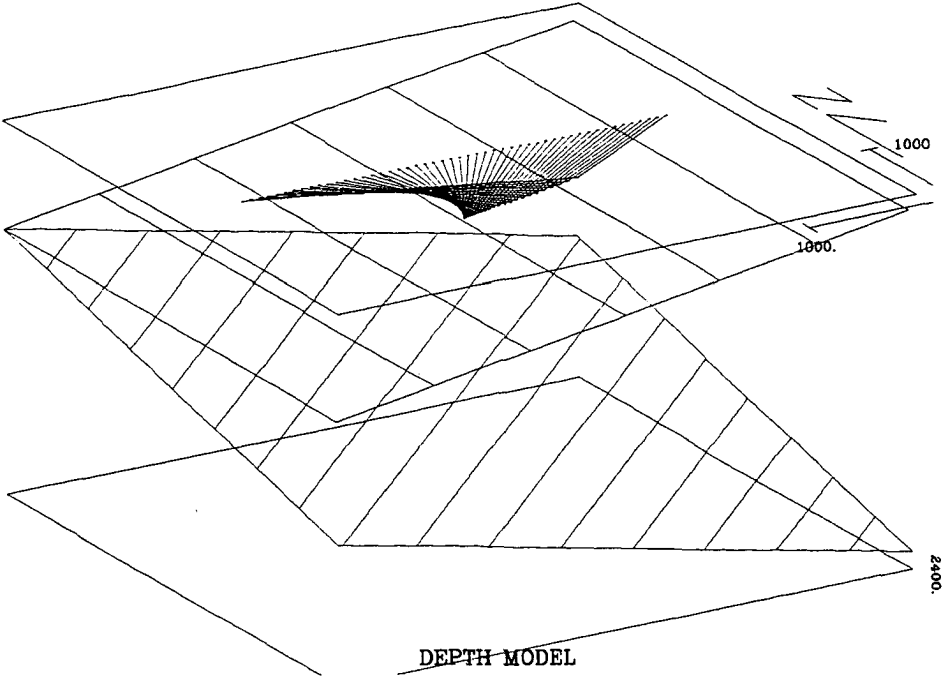


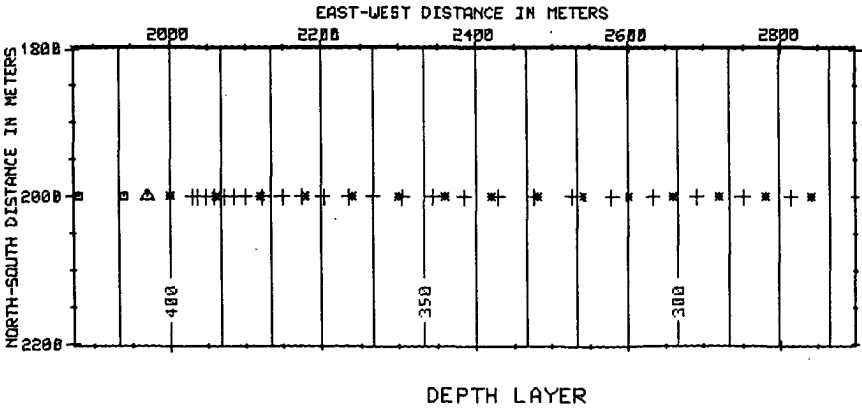
Figure VI.1 3-D macro model. A CMP location with a number of shot-receiver pairs is shown. (Δ = CMP location, \square = receiver, $*$ = shot). The velocities are: $c_1 = 1500$ m/s, $c_2 = 2200$ m/s, $c_3 = 2500$ m/s; the minimum offset is 60 m, maximum offset 2940 m, multiplicity = 25.

Next in figures VI.3a,b and VI.4a,b the raypaths and the corresponding reflection points to the second and third interface are shown. We see that the reflection point smearing still lies on one line, albeit that this line does not lie any more in the vertical plane defined by the shot-receiver positions.

We may conclude therefore that it should be possible to generalize the CRP lateral and temporal shifting formula to 3-D media. Only an azimuth angle has to be added in the derivation to allow a rotation of the line of CMP reflection points outside the vertical plane. The generalization itself should be rather straightforward.



a



b

Figure VI.2 Line of CMP reflection points on the first interface (a). A view from the model surface into (vertical) depth shows that shot-receiver pairs at the surface and reflection points at the first interface lie in the same vertical plane (b). (+ = reflection point).

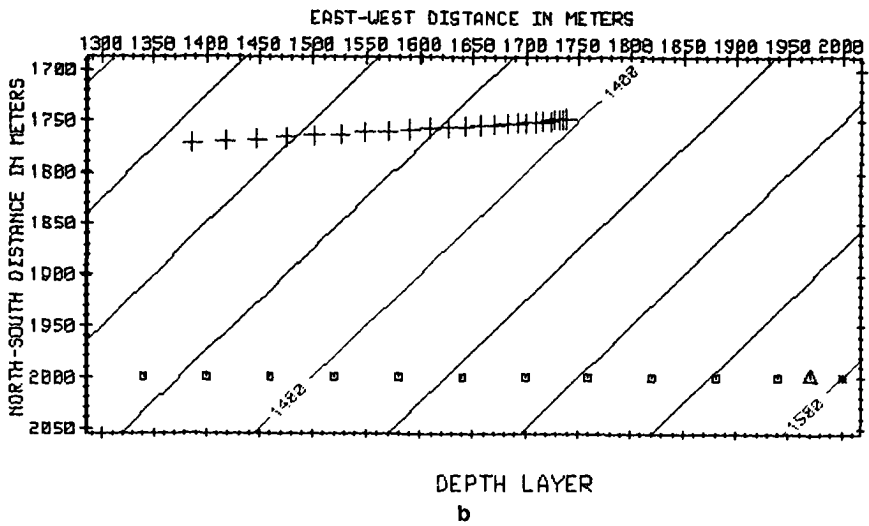
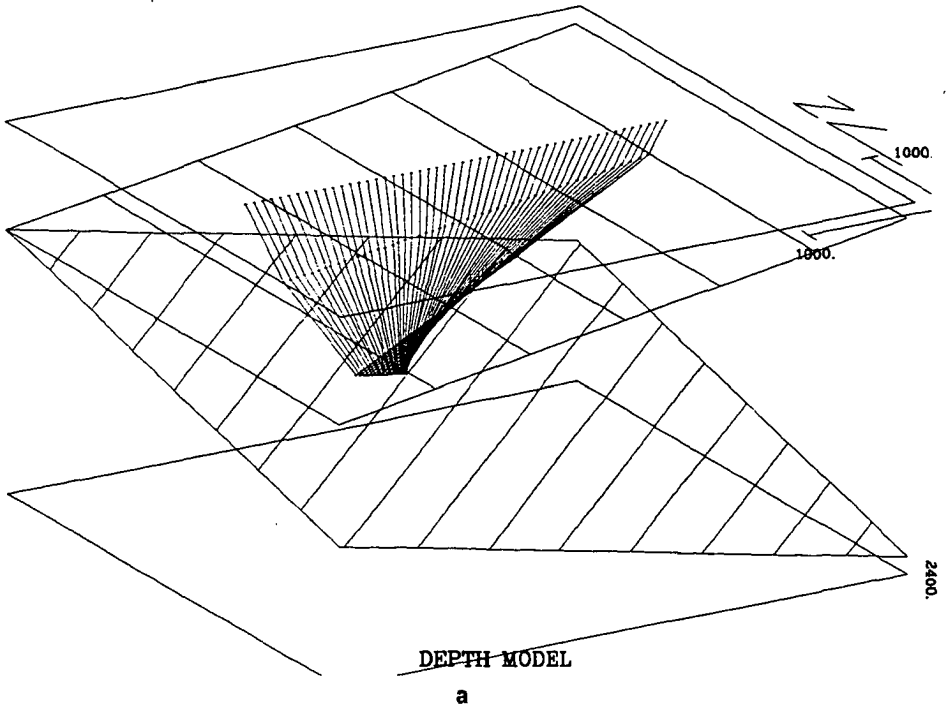
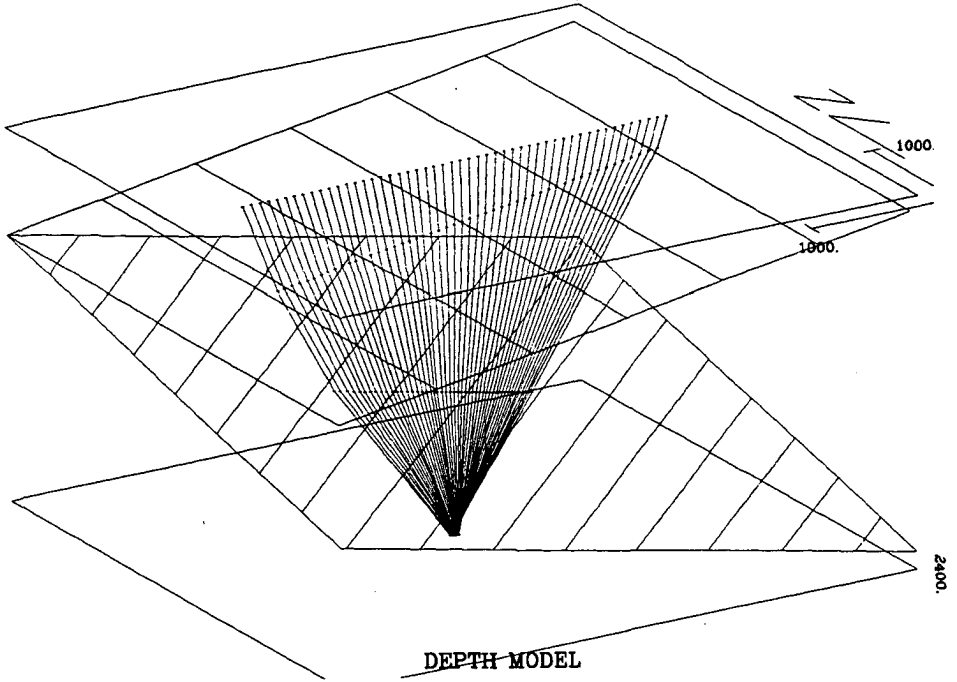
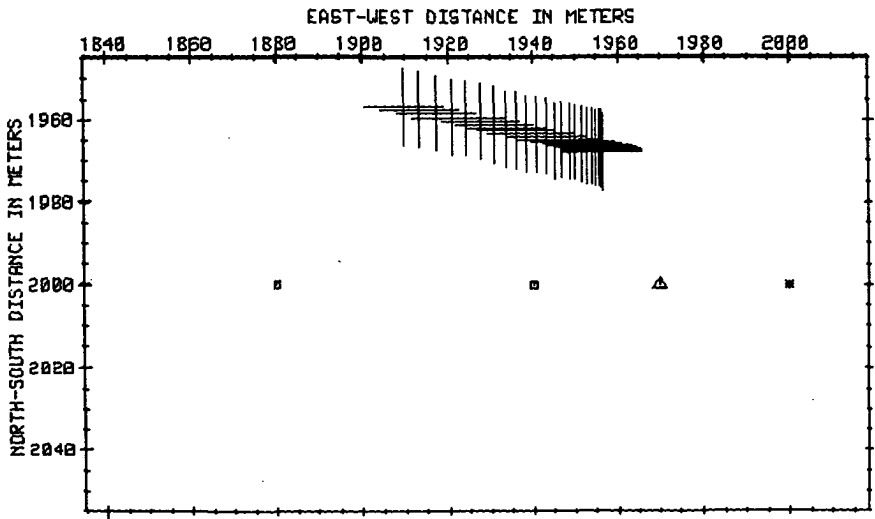


Figure VI.3 As figure VI.2, but now for the second interface. The reflection points on the second interface still lie on one straight line, although not any more in the vertical plane of the surface shot and receiver locations. Note that the squares and triangle indicate part of the receivers and the midpoint of the CMP gather at the surface (compare with figure VI.1).



a



DEPTH LAYER

b

Figure VI.4 As figure VI.2, but now for the third interface.

A serious problem maybe, is that of course not only a zero-offset ray tracing has to be carried out for all dip angles but also for all azimuth angles. Even for zero-offset ray tracing this may become a cumbersome exercise. The dip sampling needed will have to be considered carefully, since computation time may be saved by using a rational choice.

The good news, however, is that we get a CRP prestack migration result for the price of a CRP stack.

APPENDIX A

 THE HALF DIFFERENTIAL FILTER
 IN DMO OPERATORS

Wave-theory dictates that in a DMO operator a time-reversed half-differential filter should be applied to compensate for a phase change due to the integration along the operator.

The Fourier representation of a forward half-differential filter reads

$$\sqrt{j\omega} \quad (A.1)$$

A time-domain representation is given by

$$D_{1/2}(t) = \frac{1}{\sqrt{\pi}} \left(\frac{\delta(t)}{\sqrt{t}} - \frac{1}{2} \frac{H(t)}{t^{3/2}} \right), \quad (A.2)$$

where $H(t)$ is defined as the Heaviside function. In discrete form this expression reads

$$D_{1/2}(n) = \begin{cases} 0 & , n < 0 \\ 1 & , n = 0 \\ - \left[\frac{1}{\sqrt{2n-1}} - \frac{1}{\sqrt{2n+1}} \right] & , n > 0 \end{cases} \quad (A.3)$$

To arrive at a time-reversed version of the filter, the filter coefficients should simply be applied in the decreasing time direction. The resulting filter characteristic is shown in figure A.1. Now the problem is that for zero offset, DMO should do nothing to the data. In other words if the offset of an input trace of the DMO process goes to zero the half-differential filter should not alter the phase of the data. This could be accomplished by applying a tapering to the data (after Deregowski, 1985), such that the filter becomes a unit spike for offset zero. This taper is visualized in figure A.2a-e. The taper can be described by

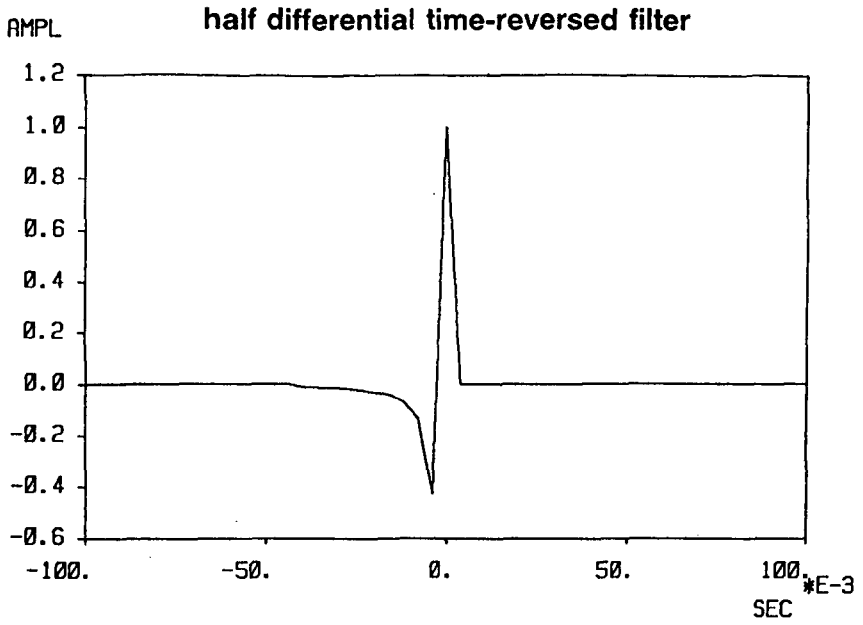


Figure A.1 Half-differential time-reversed filter.

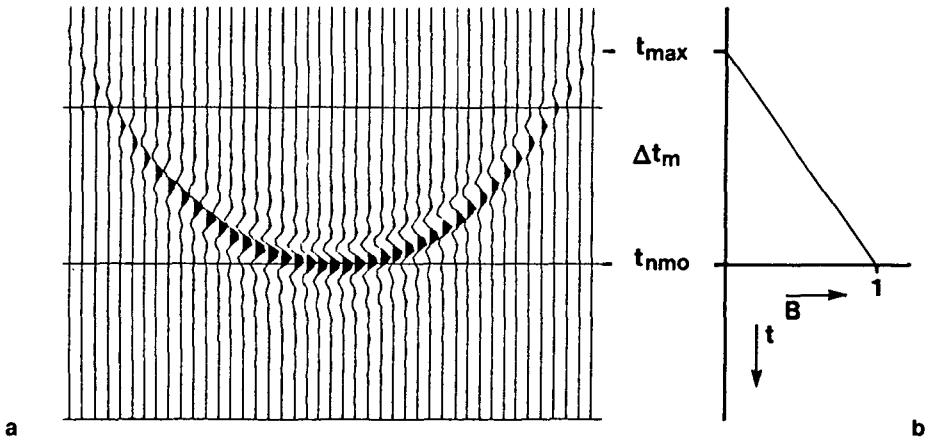


Figure A.2 Visualization of taper, applied to half-differential filter.
 a. DMO impulse response, indicating the meaning of t_{NMO} and Δt_m .
 b. taper B.

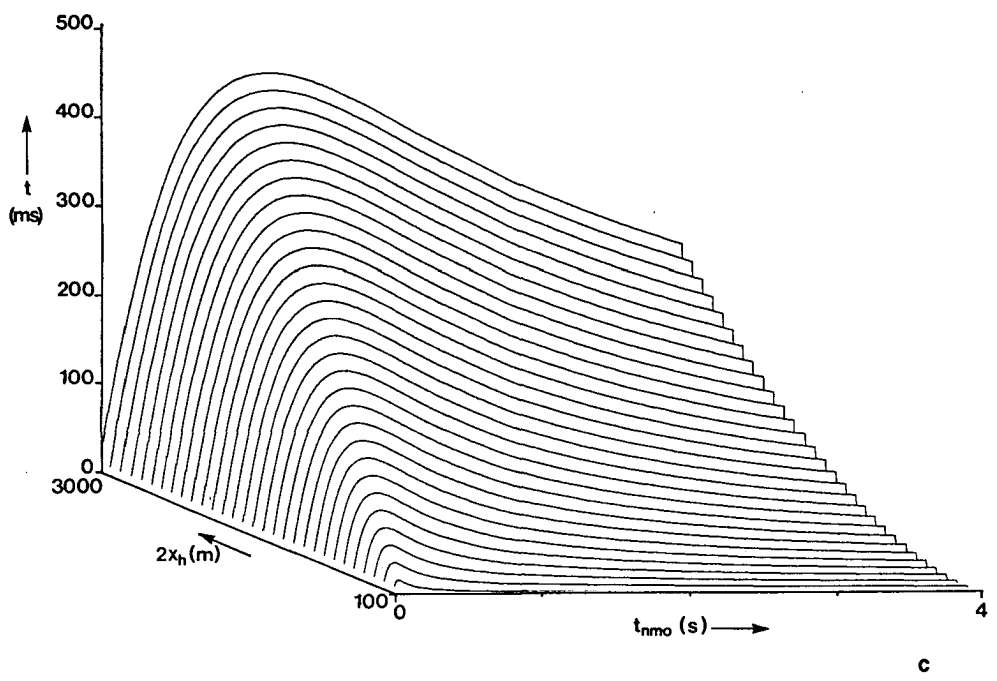


Figure A.2c shape of the taper as a function of offset $2x_h$ and NMO time t_{NMO} . The velocity used is 2000 m/s.

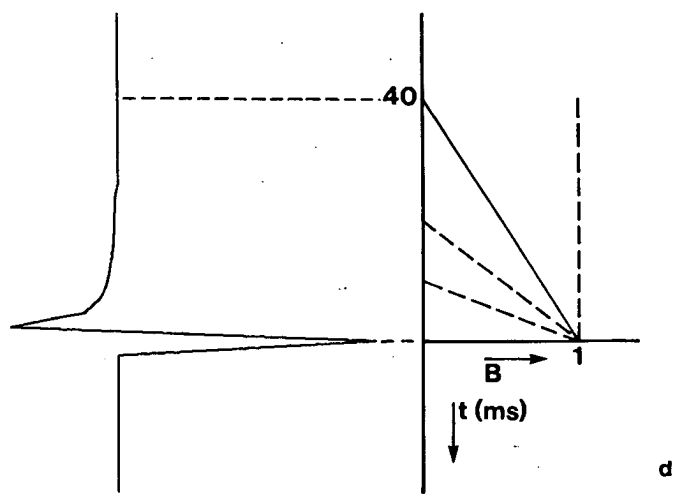


Figure A.2d if Δt_m becomes large compared to the significant length of the filter the taper B can be chosen constant, equal to 1.

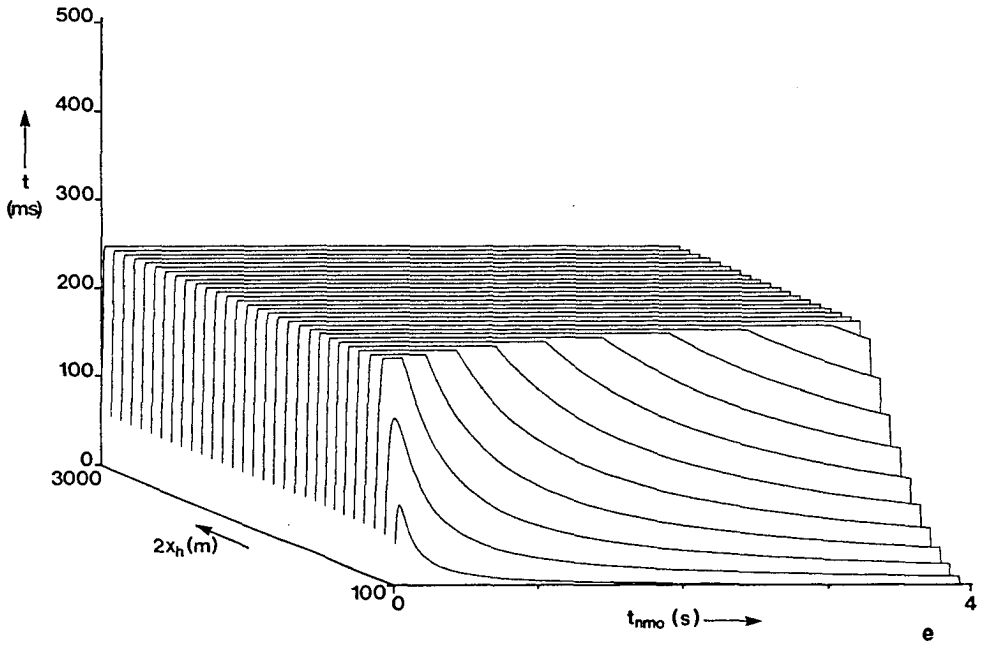


Figure A.2e in this figure Δt_m is truncated to 40 ms, indicating the part where the taper B can be chosen equal to one.

$$B = \begin{cases} 1 - \frac{(t_{NMO} - t_{crp})}{\Delta t_m} & , \text{ for } t_{NMO} - \Delta t_m \leq t_{crp} \leq t_{NMO} \\ 0 & , \text{ otherwise} \end{cases} \quad (A.4)$$

Note, that Δt_m is dependent on the shape of the DMO operator and therefore the offset and zero-offset travel time t_{NMO} .

To give an idea how the filter changes with offset and NMO time, a number of filters are shown in figure A.3.

Finally a synthetic example of a DMO stack, containing one flat event is used to visualize the difference between using and not using a half-differential filter, see figure A.4.

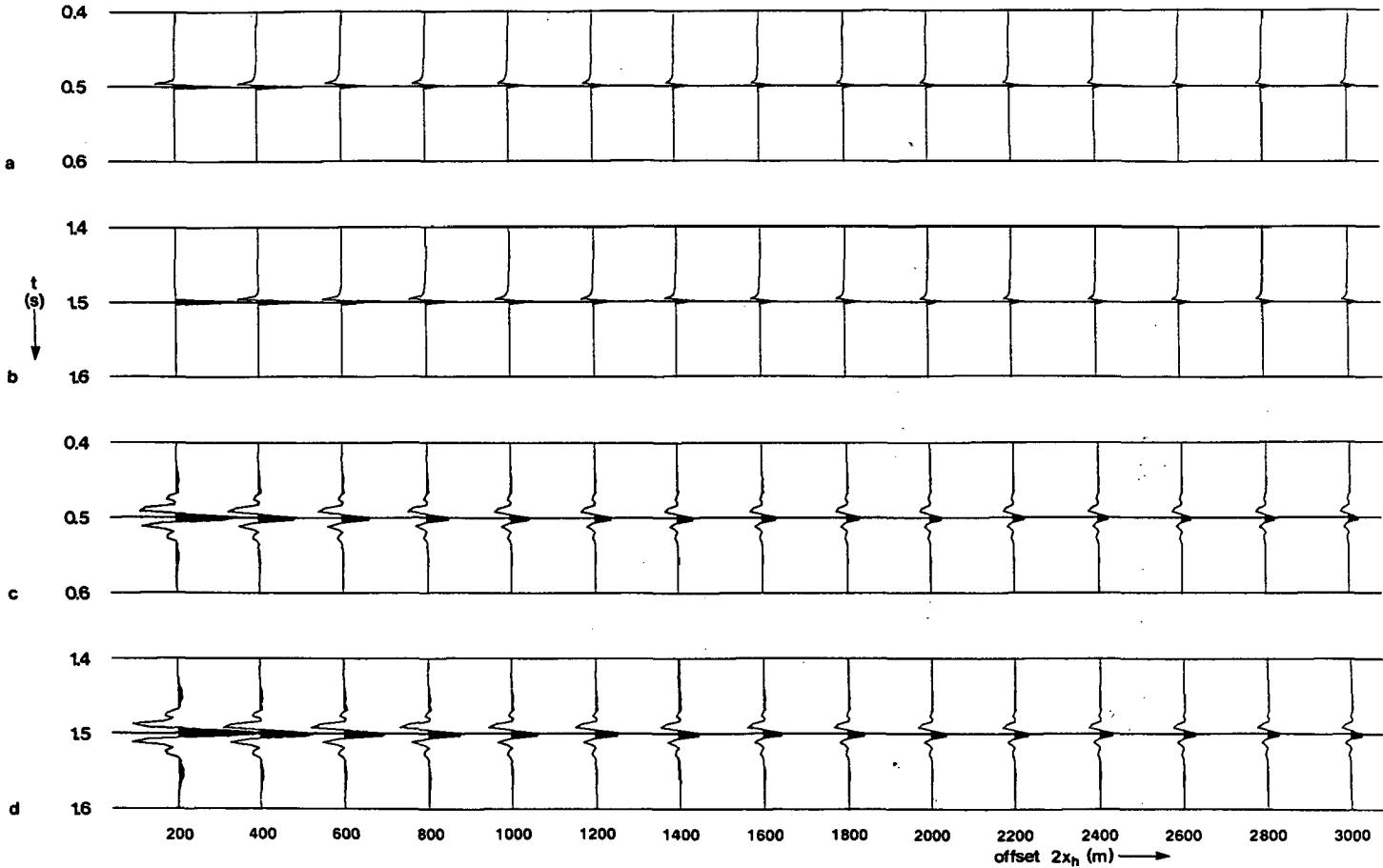
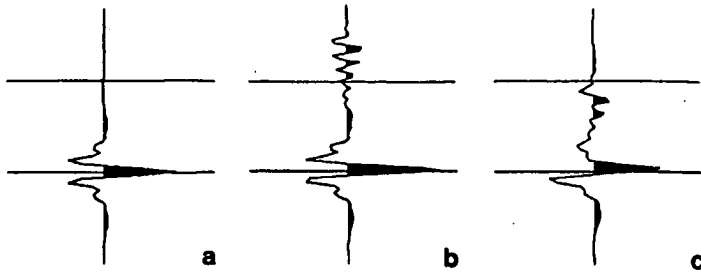


Figure A.3 Application of the half-differential time-reversed filter. The phase change from zero at zero-offset to -45° at maximum offset is clearly visible.
 a,b: input is a spike; c,d: input is a bandlimited zero-phase wavelet.



- a. input wavelet, $t_{\text{NMO}} = 1$ s, offset $2x_h = 1200$ m
- b. one DMO stacked trace, half-differential filter applied
- c. one DMO stacked trace, half-differential filter not applied

Figure A.4a,b,c

- a. In this figure the response of a flat reflector is computed and displayed for one offset of 1200 m. Because all CMP gathers are equal, only one gather is shown.
- b. shows the DMO processed and stacked section, including the half-differential filter. Apart from a noise tail, which has not been cancelled — partly because only one offset is used — the phase has not changed. The wavelet is still zero-phase.
- c. shows the DMO stack which would result if we did not implement the time-reversed half-differential filter. The wavelet has apparently changed in phase by -45° .

APPENDIX B

DERIVATION OF DMO FORMULA

In this appendix the integral formulation for constant velocity DMO will be derived.

Given:

$$x_m - x_0 = \frac{x_h^2}{\frac{c}{2} t_0} \sin \alpha \quad . \quad (\text{III.2}) \quad (\text{B.1})$$

$$t_{\text{crp}}(x_m) = t_0 - \frac{\sin \alpha}{\frac{c}{2}} (x_m - x_0) \quad . \quad (\text{III.4}) \quad (\text{B.2})$$

$$t_{\text{NMO}}^2 = t_0^2 - \frac{4x_h^2}{c^2} \sin^2 \alpha \quad . \quad (\text{III.7}) \quad (\text{B.3})$$

To be derived:

$$t_{\text{crp}}(x_m) = t_{\text{NMO}} \sqrt{1 - \frac{(x_m - x_0)^2}{x_h^2}} \quad . \quad (\text{B.4})$$

Prove:

Substitution of (B.1) into (B.3) yields

$$t_{\text{NMO}}^2 = t_0^2 \left(1 - \frac{(x_m - x_0)^2}{x_h^2} \right) \quad . \quad (\text{B.5})$$

Expression (B.5) can be written as

$$t_0 = t_{\text{NMO}} \left(1 - \frac{(x_m - x_0)^2}{x_h^2} \right)^{-1/2} \quad (\text{B.6})$$

Rewrite (B.1) as

$$\frac{\sin \alpha}{c/2} = \frac{(x_m - x_0)}{x_h^2} t_0 \quad (\text{B.7})$$

This can be rewritten, using (B.6), into

$$\frac{\sin \alpha}{c/2} = \left(\frac{x_m - x_0}{x_h^2} \right) t_{\text{NMO}} \left(1 - \frac{(x_m - x_0)^2}{x_h^2} \right)^{-1/2} \quad (\text{B.8})$$

Substitution of (B.6) and (B.8) into (C-2) yields

$$\begin{aligned} t_{\text{crp}}(x_m) &= t_{\text{NMO}} \left(1 - \frac{(x_m - x_0)^2}{x_h^2} \right)^{-1/2} \left(1 - \frac{(x_m - x_0)^2}{x_h^2} \right) \\ &= t_{\text{NMO}} \sqrt{1 - \frac{(x_m - x_0)^2}{x_h^2}} \end{aligned} \quad (\text{B.9})$$

q. e. d.

Furthermore we can determine the maximum value of $(x_m - x_0)$ as follows. $(x_m - x_0)$ is maximal in (B.1) when α equals $\frac{\pi}{2}$. So

$$x_{\text{max}} = |x_m - x_0|_{\text{max}} = \frac{x_h^2}{\frac{c}{2} t_0} \quad \alpha = \frac{\pi}{2} \quad (\text{B.10})$$

If α equals $\frac{\pi}{2}$, the offset traveltime t_h will be equal to t_0 , as can be witnessed by substitution of $\alpha = \frac{\pi}{2}$ into expression (III.3). This means that (B.10) also can be written as

$$x_{\text{max}} = \frac{x_h^2}{(c/2) t_h} \quad (\text{B.11})$$

APPENDIX C

 THE RELATION BETWEEN SPATIAL
AND DIP ANGLE SAMPLING

This appendix addresses the relation between the spatial Δx_m sampling of a DMO operator and dip angle α sampling.

The question is, for how many dip angles and for what angle distribution does the DMO operator need to be sampled to arrive at an equivalent constant spatial Δx_m sampling along the operator. Therefore we start with formula (III.2), set x_0 for convenience to zero and rewrite it as

$$x_m = \frac{2x_h^2 \sin \alpha}{\sqrt{c^2 t_{NMO}^2 + 4x_h^2 \sin^2 \alpha}} \quad (C.1)$$

Derivation of the derivative yields

$$\frac{\partial x_m}{\partial \alpha} = \frac{2x_h^2 c^2 t_{NMO}^2 \cos \alpha}{\left(c^2 t_{NMO}^2 + 4x_h^2 \sin^2 \alpha\right)^{3/2}} \quad (C.2)$$

so, $\Delta x_m = \frac{\partial x_m}{\partial \alpha} \Delta \alpha$ can be computed and evaluated numerically.

Figures C.1a,b,c show the relation between Δx_m and $\Delta \alpha$ for a constant $\Delta \alpha$ increment of one degree. The different figures correspond to different zero-dip zero-offset times t_{NMO} .

We see especially that Δx_m becomes large for shallow times, large offsets and flat events.

An angle increment of one degree may then result in a too sparsely sampled operator, not with respect to aliasing but with respect to continuity of events. On the other hand, most of data space for large offsets and shallow times will normally be muted in practice.

In figure C.1b we can see that for a zero-offset time of 2 s the angle increment of one degree would be sufficient for the whole offset range to map at least one sample of the operator on each output DMO stack trace, if we choose Δx_m smaller or equal to 20 m.

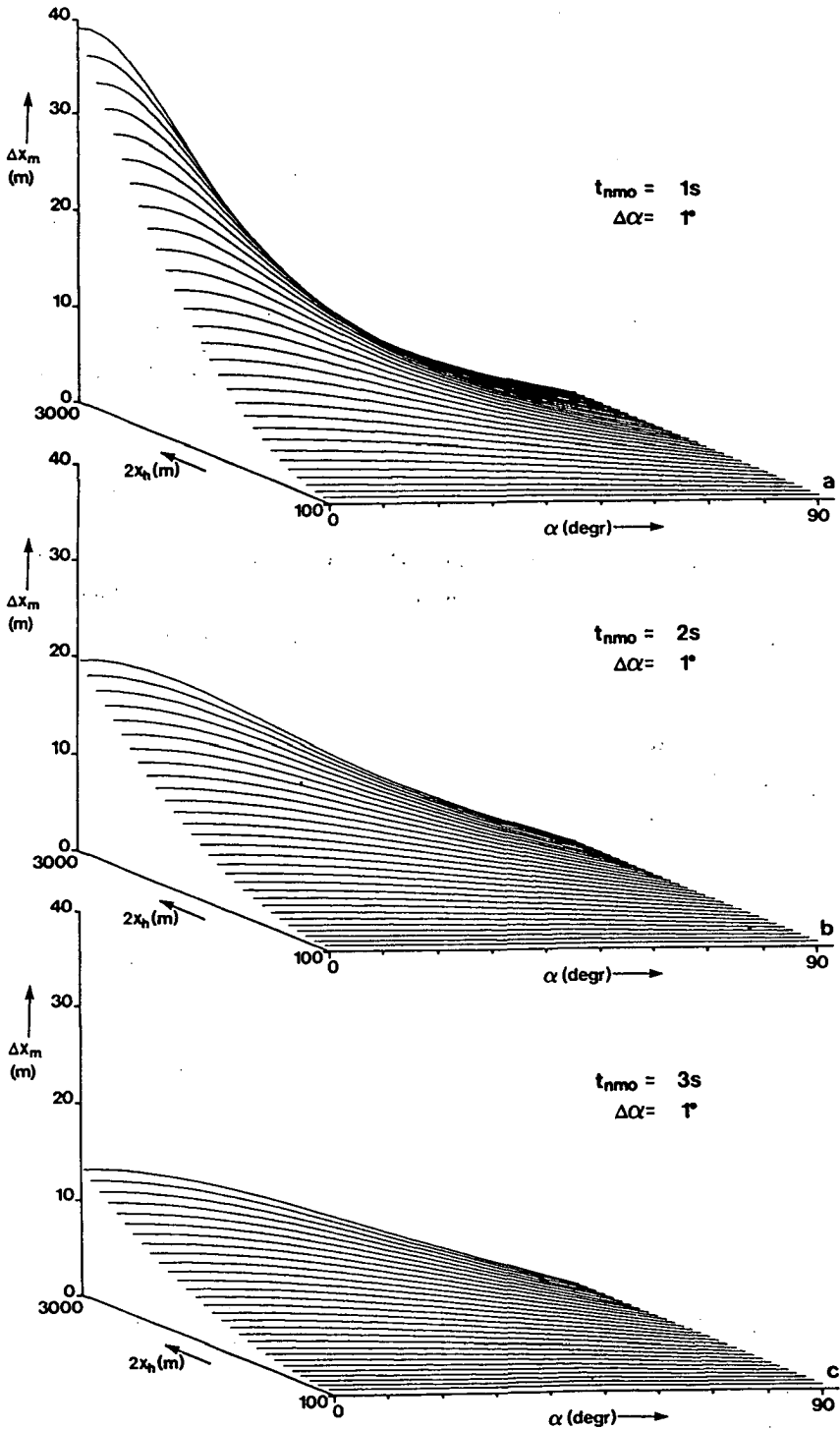


Figure C.1 The relation between the dip angle sampling $\Delta\alpha$ and the spatial sampling Δx_m , for three zero-offset times, as a function of offset and dip angle.

APPENDIX D

DEPTH POINT SMEAR IN INHOMOGENEOUS MEDIA

In this appendix (after C.P.A. Wapenaar) we analyze the depthpoint smear of common midpoint (CMP) rays in a 2-D inhomogeneous medium. We assume that locally the medium consists of homogeneous layers, separated by plane, dipping interfaces, see figure D.1. In the following we consider reflections from the N'th interface. The zero offset (ZO) ray has an emergence angle ψ_0 at the surface and satisfies Snell's law at the interfaces, hence

$$\frac{\sin \psi_{n-1}}{c_n} = \frac{\sin \psi'_{n-1}}{c_{n-1}}, \quad (\text{D.1})$$

where ψ'_{n-1} and ψ_{n-1} are the incidence and refraction angles, respectively, at interface n-1; c_{n-1} and c_n are the propagation velocities above and below interface n-1. The length l_n of the ZO ray in the n'th layer equals $c_n \Delta t_n / 2$, where Δt_n is the two-way ZO traveltime in that layer. The ZO ray is perpendicular to reflecting interface N, hence, $\psi_N = 0$. Consider a CMP ray, with half offset ' x_h ' and depthpoint smear D_N . In the n'th layer the angles of the downgoing and upgoing CMP rays relative to the ZO rays are θ_n^+ and θ_n^- , respectively. In the following we assume that these angles are small for all n. Snell's law, applied to the CMP rays at interface n-1, yields

$$\frac{\sin(\psi_{n-1} \pm \theta_n^\pm)}{c_n} = \frac{\sin(\psi'_{n-1} \pm \theta_{n-1}^\pm)}{c_{n-1}}, \quad (\text{D.2a})$$

or, since θ_n^\pm is small for all n,

$$\frac{\sin \psi_{n-1} \pm \theta_n^\pm \cos \psi_{n-1}}{c_n} \approx \frac{\sin \psi'_{n-1} \pm \theta_{n-1}^\pm \cos \psi'_{n-1}}{c_{n-1}}, \quad (\text{D.2b})$$

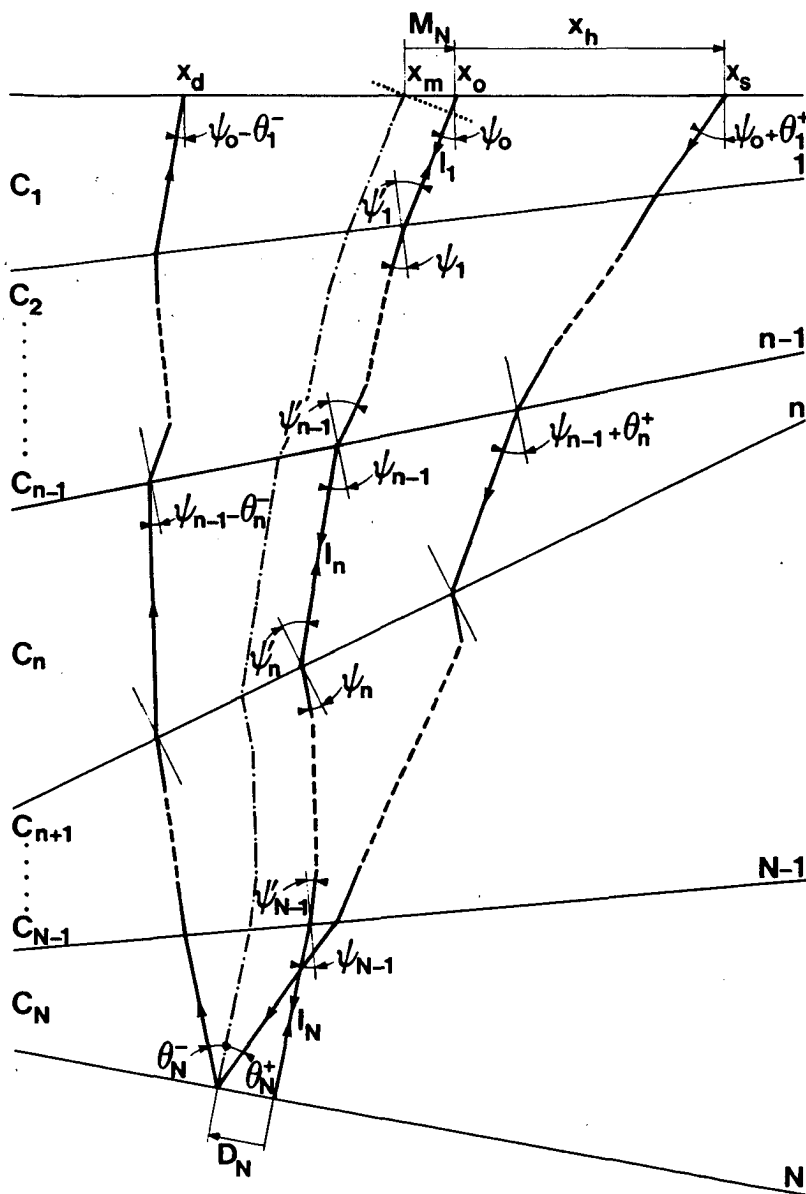


Figure D.1 The reflection point dispersal in the CMP configuration is approximately described by the simple relationship $D_N(h) \approx 4K_N h^2$, with K_N defined by (D.23b).

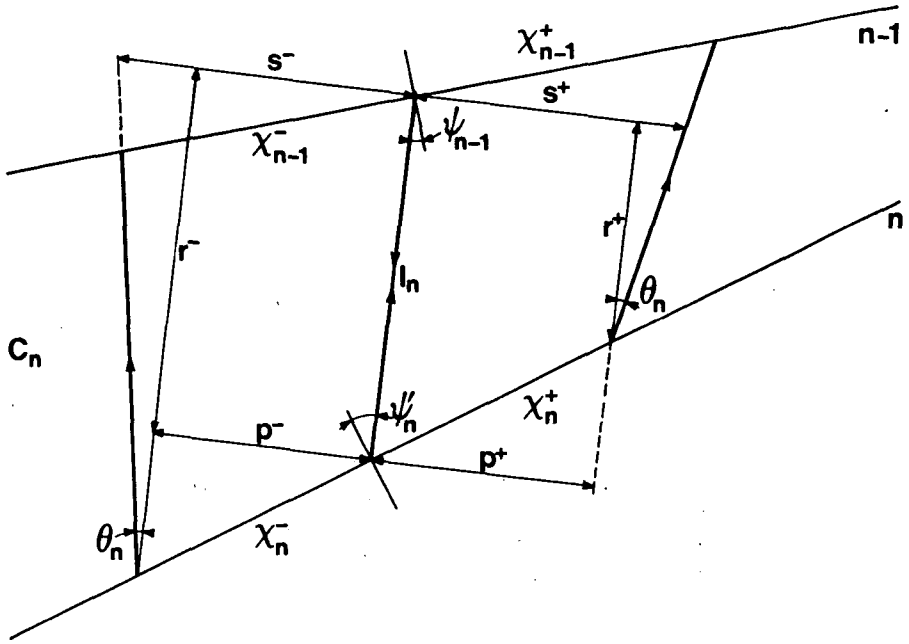


Figure D.2 Close-up of layer n.

or, with relation (D.1),

$$\theta_n^\pm \approx \frac{c_n}{c_{n-1}} \frac{\cos \psi_{n-1}}{\cos \psi_n} \theta_{n-1}^\pm \quad (D.3a)$$

At the reflecting interface N the incidence angle θ_N^+ equals the reflection angle θ_N^- . By applying (D.3a) recursively we may conclude that θ_n^+ equals θ_n^- for all n. We define

$$\theta_n = \theta_n^+ = \theta_n^- \quad (D.3b)$$

Figure D.2 shows a close-up of the n'th layer. At interface n-1, the offsets of the downgoing and upgoing CMP rays relative to the ZO rays are χ_{n-1}^+ and χ_{n-1}^- , respectively.

They can be expressed in terms of χ_n^+ and χ_n^- as follows. Define p^\pm , r^\pm and s^\pm (see figure D.2) according to

$$p^\pm = \chi_n^\pm \cos \psi_n' \quad (D.4a)$$

$$r^\pm = l_n \mp \chi_n^\pm \sin \psi_n' \quad (D.4b)$$

$$s^\pm \approx p^\pm + r^\pm \theta_n \quad (D.4c)$$

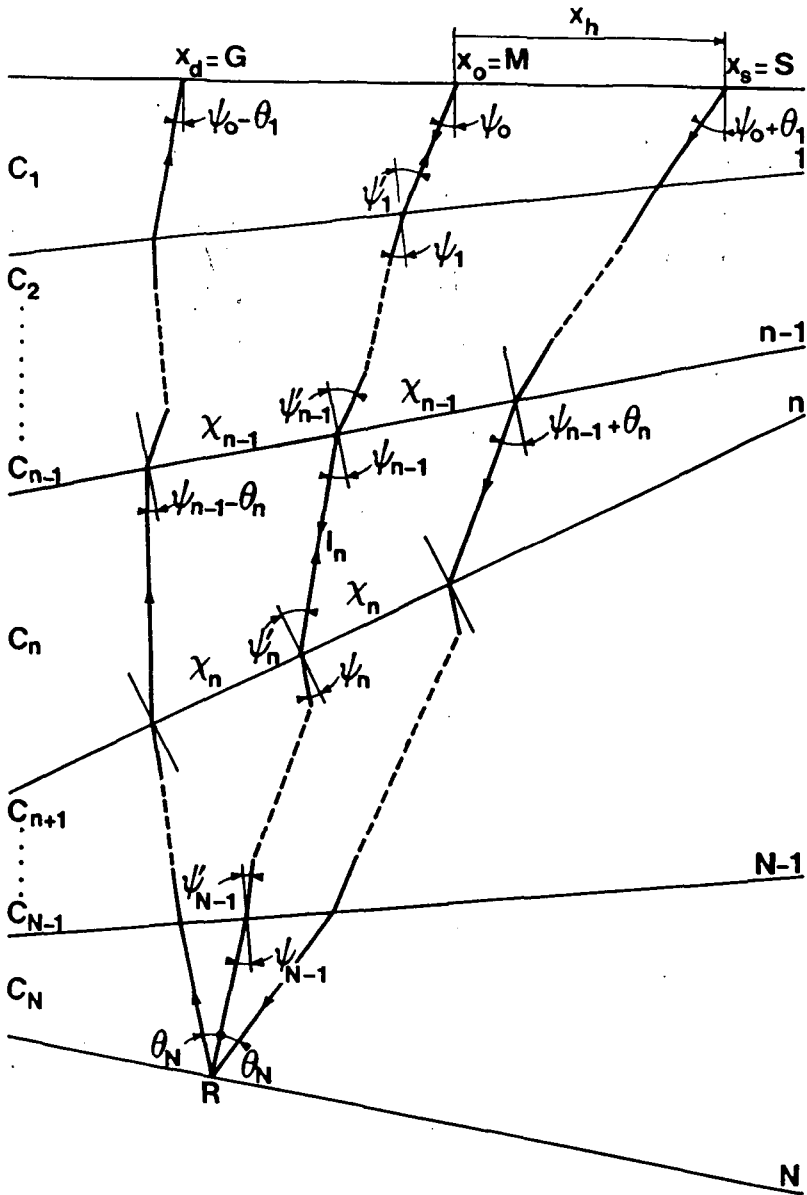


Figure D.3 In the recursive computation of x_{n-1} the midpoint displacement is neglected in all layers. Subsequently the errors are traced back to the N 'th reflector (see also Figure D.5), thus yielding an estimate of the depth point smear.

Then,

$$\frac{\chi_{n-1}^{\pm}}{\sin(\pi/2 \pm \theta_n)} = \frac{s^{\pm}}{\sin(\pi/2 - \psi_{n-1} \mp \theta_n)} \quad (D.5a)$$

or, for small θ_n

$$\chi_{n-1}^{\pm} \approx \frac{s^{\pm}}{\cos \psi_{n-1}} \left[1 \pm \theta_n \tan \psi_{n-1} \right] \quad (D.5b)$$

or, with relation (D.4)

$$\chi_{n-1}^{\pm} \approx \frac{1}{\cos \psi_{n-1}} \left[\left\{ \chi_n^{\pm} \cos \psi_n' + \theta_n \left(\varrho_n \mp \chi_n^{\pm} \sin \psi_n' \right) \right\} \times \left\{ 1 \pm \theta_n \tan \psi_{n-1} \right\} \right] \quad (D.5c)$$

These recursive expressions relate the half offset $x_h (= \chi_0^+ = \chi_0^-)$ to the depth point smear $D_N (= \chi_N^+ = -\chi_N^-)$. However, expressions (D.5c) contain three unknowns χ_n^{\pm} and θ_n , and therefore we follow a different procedure to relate the half offset to the depth point smear.

We define

$$\chi_{n-1} \triangleq \frac{\chi_{n-1}^+ + \chi_{n-1}^-}{2} \quad (D.6a)$$

and

$$\Delta \chi_{n-1} \triangleq \frac{\chi_{n-1}^+ - \chi_{n-1}^-}{2} \quad (D.6b)$$

Here χ_{n-1} represents half the offset between the downgoing and upgoing CMP rays at interface $n-1$; the correction term $\Delta \chi_{n-1}$ represents the midpoint displacement relative to the ZO ray. We now make the following approximation. In the recursive computation of $x_h (= \chi_0^+ = \chi_0^-)$ we start at interface N , assuming zero depthpoint smear $D_N (= \chi_N = 0)$, and neglect the midpoint displacement in all layers, see figure D.3. Next we trace the errors $\Delta \chi_{n-1}$ down to the N 'th reflector and sum all contributions, thus yielding an estimate of the depth point smear D_N . Of course this approximation is only valid when $\Delta \chi_{n-1} \ll \chi_{n-1}$ for all n .

Substitution of (D.5c) into (D.6a) and (D.6b), assuming $\chi_n^+ = \chi_n^- = \chi_n$, yields

$$\chi_{n-1} \approx \frac{1}{\cos \psi_{n-1}} \left[\chi_n \cos \psi_n' + \theta_n \varrho_n \right] \quad (D.7a)$$

and

$$\Delta\chi_{n-1} \approx \frac{\theta_n}{\cos \psi_{n-1}} \left[\chi_n \left(\cos \psi'_n \tan \psi_{n-1} - \sin \psi'_n \right) + \theta_n \varrho_n \tan \psi_{n-1} \right],$$

or

$$\Delta\chi_{n-1} \approx \frac{\theta_n}{\cos^2 \psi_{n-1}} \left[\chi_n \sin \left(\psi_{n-1} - \psi'_n \right) + \theta_n \varrho_n \sin \psi_{n-1} \right]. \quad (\text{D.7b})$$

Note that $\Delta\chi_{n-1}$ is indeed one order smaller than χ_{n-1} . Recursive application of (D.7a) yields

$$\chi_{N-1} \approx \frac{1}{\cos \psi_{N-1}} \theta_N \varrho_N, \quad (\text{D.8a})$$

$$\chi_{N-2} \approx \frac{1}{\cos \psi_{N-2}} \left[\frac{\cos \psi'_{N-1}}{\cos \psi_{N-1}} \theta_N \varrho_N + \theta_{N-1} \varrho_{N-1} \right], \quad (\text{D.8b})$$

or, with relation (D.3),

$$\chi_{N-2} \approx \frac{\theta_{N-1}}{c_{N-1} \cos \psi_{N-2}} \left[\left(\frac{\cos \psi'_{N-1}}{\cos \psi_{N-1}} \right)^2 c_N \varrho_N + c_{N-1} \varrho_{N-1} \right], \quad (\text{D.8c})$$

etc. This result can be generalized to

$$\chi_q \approx \frac{\theta_{q+1}}{c_{q+1} \cos \psi_q} \sum_{n=q+1}^N \left[\left(\prod_{k=q+1}^{n-1} \frac{\cos \psi'_k}{\cos \psi_k} \right)^2 c_n \varrho_n \right], \quad (\text{D.9a})$$

where

$$\sum_{N+1}^N (\dots) \triangleq 0; \quad \prod_{q+1}^q (\dots) \triangleq 1, \quad (\text{D.9b})$$

and

$$\varrho_n = c_n \Delta t_n / 2. \quad (\text{D.9c})$$

For $q=0$ we obtain

$$2\chi_h = 2\chi_0 \approx \frac{\theta_1}{c_1 \cos \psi_0} \sum_{n=1}^N \left(c'_n \right)^2 \Delta t_n, \quad (\text{D.10a})$$

where

$$c'_n = \left(\prod_{k=0}^{n-1} \frac{\cos \psi'_k}{\cos \psi_k} \right) c_n \tag{D.10b}$$

and

$$\psi'_0 \hat{=} \psi_0 \tag{D.10c}$$

Before we analyze the depthpoint smear, we compute the traveltimes along the ZO ray and the CMP ray. The total traveltime along the ZO ray is given by the sum of the two-way interval ZO traveltimes Δt_n , hence

$$t_{0,N} = \sum_{n=1}^N \Delta t_n \tag{D.11}$$

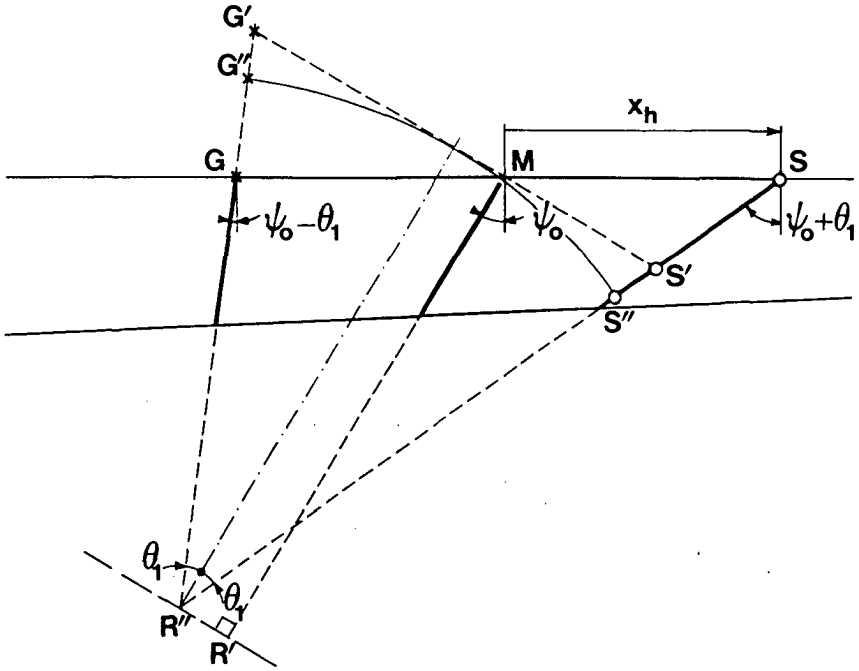


Figure D.4 The total traveltime along a CMP ray is most easily derived from a replacement model in which a secondary source in the subsurface radiates a spherical wavefront to the surface.

The traveltime along the CMP ray SRG (see figure D.3) is equal to the sum of the traveltimes along the rays RS and RG. For convenience we place a secondary source in R and assume that the wavefront which arrives at the surface is spherical. Figure D.4 shows the first layer with the spherical wavefront. From this figure we may conclude that the traveltime along the CMP ray is given by

$$t_{h,N} = t_{0,N} + \frac{\overline{SS''} - \overline{GG''}}{c_1} , \quad (\text{D.12a})$$

where

$$\overline{SS''} = \overline{SS'} + \overline{S'S''} \quad (\text{D.12b})$$

and

$$\overline{GG''} = \overline{GG'} - \overline{G'G''} \quad (\text{D.12c})$$

Since

$$\overline{SS'} = \overline{GG'} \quad (\text{D.12d})$$

and

$$\overline{S'S''} = \overline{G'G''} \quad (\text{D.12e})$$

we may write (D.12a) as

$$t_{h,N} = t_{0,N} + \frac{2 \overline{S'S''}}{c_1} , \quad (\text{D.13a})$$

or

$$t_{h,N}^2 \approx t_{0,N}^2 + \frac{4 t_{0,N} \overline{S'S''}}{c_1} . \quad (\text{D.13b})$$

In order to compute $\overline{S'S''}$ we construct a virtual source R'' at the center of the spherical wavefront. Referring to figure D.4, we obtain

$$\cos \theta_1 = \overline{MR'} / \overline{S'R''} = \overline{MR'} / (\overline{MR'} + \overline{S'S''}) \quad (\text{D.14a})$$

and

$$\tan \theta_1 = \frac{1}{2} \overline{G'S'} / \overline{MR'} . \quad (\text{D.14b})$$

Assuming θ_1 is small yields

$$\overline{S'S''} \approx \frac{1}{4} \overline{G'S'} \theta_1 , \quad (\text{D.15a})$$

where

$$\overline{G'S'} = \overline{MS'} + \overline{MG'} \quad , \quad (D.15b)$$

or

$$\overline{G'S'} \approx \left[\sin \left(\pi / 2 - \psi_0 - \theta_1 \right) + \sin \left(\pi / 2 - \psi_0 + \theta_1 \right) \right] x_h \quad , \quad (D.15c)$$

or

$$\overline{G'S'} \approx 2x_h \cos \psi_0 \quad , \quad (D.15d)$$

hence

$$\overline{S'S''} \approx \frac{1}{2} x_h \theta_1 \cos \psi_0 \quad . \quad (D.15e)$$

Substitution of (D.15e) into (D.13b), using (D.10a) yields

$$t_{h,N}^2 \approx t_{0,N}^2 + \frac{(2x_h)^2}{C_N^2} \quad , \quad (D.16a)$$

where

$$C_N^2 = \frac{1}{t_{0,N} \cos^2 \psi_0} \sum_{n=1}^N (c'_n)^2 \Delta t_n \quad (D.16b)$$

with c'_n defined by (D.10b). Relation (D.16) represents a hyperbolic relationship between the offset and the traveltime along a CMP ray. The asymptotes are determined by the reciprocal of the effective velocity C_N . Now we derive the relationship between the offset and the depthpoint smear. In the recursive computation of χ_{q-1} we neglected the midpoint displacement $\Delta\chi_{q-1}$ in each layer. For layer q this involves a lateral shift (in the opposite direction) of the normal incidence ray over a distance $-\Delta\chi_{q-1} \cos \psi_{q-1}$, see also figure D.5. If we trace this distance down to the N 'th reflector we obtain the partial depthpoint smear d_q (related to layer q only), according to

$$d_q = -\Delta\chi_{q-1} \cos \psi_{q-1} \prod_{j=q}^N \frac{\cos \psi_j}{\cos \psi'_j} \quad , \quad (D.17a)$$

with

$$\psi_N \hat{=} \psi'_N \hat{=} 0 \quad . \quad (D.17b)$$

For the total depthpoint smear we write

$$D_N \approx \sum_{q=1}^N d_q \quad . \quad (D.18)$$

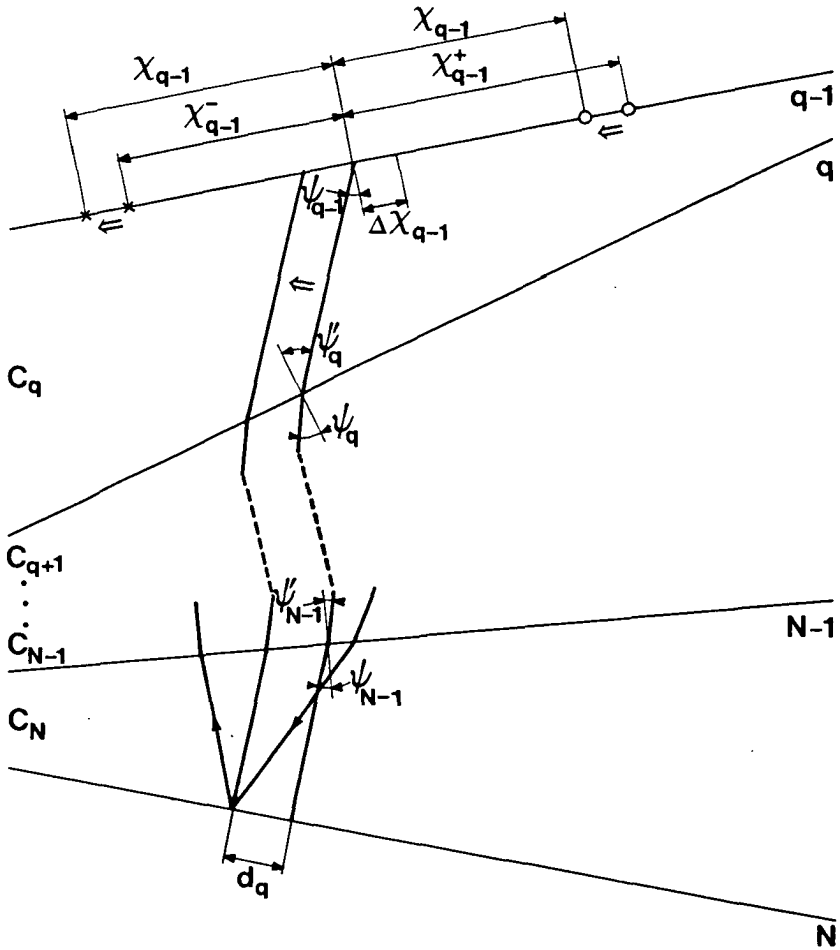


Figure D.5 The partial depthpoint smear d_q (related to layer q only) is found by tracing the error $\Delta\chi_{q-1}$ back to the N' th reflector.

According to relations (D.3), (D.7b) and (D.9) we may write for the midpoint displacement in layer q

$$\Delta\chi_{q-1} \approx A_q \theta_1^2, \tag{D.19a}$$

where

$$A_q = \frac{c_q}{2c_1^2 \cos^2 \psi_{q-1}} \left[\frac{\sin(\psi_{q-1} - \psi'_q)}{\cos \psi'_q} \sum_{n=q+1}^N (c'_n)^2 \Delta t_n + \sin \psi_{q-1} (c'_q)^2 \Delta t_q \right], \quad (D.19b)$$

with

$$\sum_{N+1}^N (\dots) \hat{=} 0 \quad (D.19c)$$

and c'_n defined by (D.10b). Substitution of this result into (D.17) and (D.18) yields

$$D_N \approx \theta_1^2 \sum_{q=1}^N \left[F_q \sum_{n=q+1}^N (c'_n)^2 \Delta t_n + G_q (c'_q)^2 \Delta t_q \right], \quad (D.20a)$$

where

$$F_q = E_q \frac{\sin(\psi_{q-1} - \psi'_q)}{\cos \psi'_q}, \quad (D.20b)$$

$$G_q = E_q \sin \psi_{q-1}, \quad (D.20c)$$

with

$$E_q = -\frac{c_q}{2c_1^2 \cos \psi_{q-1}} \prod_{j=q}^N \frac{\cos \psi_j}{\cos \psi'_j}. \quad (D.20d)$$

This can be rewritten as

$$D_N \approx \theta_1^2 \sum_{n=1}^N \left[(c'_n)^2 \Delta t_n \sum_{q=1}^{n-1} F_q + G_n (c'_n)^2 \Delta t_n \right], \quad (D.21a)$$

or

$$D_N \approx \theta_1^2 \sum_{n=1}^N (H_n + G_n) (c'_n)^2 \Delta t_n, \quad (D.21b)$$

where

$$H_n = \sum_{q=1}^{n-1} F_q, \quad (D.21c)$$

with

$$H_1 \hat{=} 0. \quad (D.21d)$$

From relations (D.10a) and (D.16b) we may derive

$$\theta_1 \approx \frac{2x_h c_1}{t_{0,N} \cos \psi_0 C_N^2} . \quad (\text{D.22})$$

Substitution in (D.21b) yields

$$D_N(x_h) \approx 4K_N x_h^2 , \quad (\text{D.23a})$$

where

$$K_N = \frac{c_1^2}{t_{0,N}^2 \cos^2 \psi_0 C_N^4} \sum_{n=1}^N (H_n + G_n) (c_n')^2 \Delta t_n . \quad (\text{D.23b})$$

Note that for a single layer configuration this expression reduces to

$$D_1(x_h) = -\frac{2 \sin \psi_0 \cos \psi_0}{c_1 t_{0,1}} x_h^2 \quad (\text{D.24})$$

which is exact.

Note that the total midpoint displacement $x_m - x_0$ at the surface reads

$$M_N(x_h) = \frac{-D_N(x_h)}{\cos \psi_0} \prod_{n=1}^N \frac{\cos \psi_n'}{\cos \psi_n} \quad (\text{D.25})$$

see also figure D.1. Finally, note that the two-way traveltime $t_{0,N}'$ along the dashed ZO raypath is given by

$$t_{0,N}' = t_{0,N} - \frac{2 M_N(x_h) \sin \psi_0}{c_1} , \quad (\text{D.26})$$

with $t_{0,N}$ given by (D.11).

Improvements in accuracy may be expected when (D.2a) is expanded up to the second order. The first order approximation (D.3) is valid when terms like $\theta_n^2 - \theta_{n-1}^2$ are small compared to θ_n^2 .

REFERENCES

- Beasley, C.J. and Mobley, E., 1988, Amplitude and anti-aliasing treatment in (x,t) domain DMO, 58th Ann. Intern. Mtg., Soc. Explor. Geophys., Expanded Abstracts, 1113-1116.
- Berg, L.E., 1984, Prestack partial migration, method overview and presentation of processed data, presented at the 54th Ann. Intern. Mtg., Soc. of Explor. Geoph., Atlanta, (GECO brochure).
- Berkhout, A.J., 1984, Seismic migration, imaging of acoustic energy by wave field extrapolation, A. theoretical aspects, Developments in Solid Earth Physics 14A, Elsevier, Amsterdam.
- Berkhout, A.J., 1985, Seismic migration, imaging of acoustic energy by wave field extrapolation, B. practical aspects, Developments in Solid Earth Physics 14B, Elsevier, Amsterdam.
- Bolondi, G., Loinger, E. and Rocca, F., 1982, Offset continuation of seismic sections, Geophysical Prospecting **30**, 813-828.
- Bolondi, G., Loinger, E. and Rocca, F., 1984, Offset continuation in theory and practice, Geophysical Prospecting **32**, 1045-1073.
- Delphi Research proposal, 1988, Delft University of Technology, Delft, The Netherlands.
- Deregowski, S.M. and Rocca, F., 1981, Geometrical optics and wave theory of constant offset sections in layered media, Geophysical Prospecting **29**, 374-406.

- Deregowski, S.M., 1982, Dip-moveout and reflector point dispersal, *Geophysical Prospecting* **30**, 318–322.
- Deregowski, S.M., and Brown, S.M., 1983, A theory of acoustic diffractors applied to 2-D models, *Geophysical Prospecting* **31**, 293–333.
- Deregowski, S.M., 1985, An integral implementation of Dip Moveout, presented at the 47th Ann. Mtg. of the EAEG, Budapest.
- Deregowski, S.M., 1986, What is DMO?, *First Break* **4**, July 1986, 7–24.
- Duijndam, A.J.W., 1987, Detailed Bayesian inversion of seismic data, PhD thesis, Delft University of Technology, Delft, The Netherlands.
- Fowler, P., 1984, Velocity independent imaging of seismic reflectors, 54th Ann. Internat. Mtg., Soc. Explor. Geophys., Expanded Abstracts, 383–385.
- French, S.F., Perkins, W.T. and Zoll, R.M., 1984, Partial migration via true CRP stacking, 54th Ann. Intern. Mtg., Soc. Explor. Geophys., Expanded Abstracts, 799–802.
- French, S.F., Perkins, W.T. and Zoll, R.M., 1985, Partial migration of true 3-D seismic reflection surveys via common reflection-point stacking, presented at the 17th Ann. OTC, Houston.
- Guion, D.J. and Pearson, W.C., 1982, Gravity exploration for petroleum in Railroad Valley, Nevada – search for the subtle trap, *The deliberate search for the subtle trap*, M.T. Halbouty (ed.), AAPG Memoir 32. Tulsa, Oklahoma.
- Hale, I.D., 1983, Dip-moveout by Fourier transform, PhD thesis, Stanford University.
- Hale, I.D., 1984, Dip-moveout by Fourier transform, *Geophysics* **49**, 741-757.
- Hubral, P. and Krey, Th., 1980, Interval velocities from seismic reflection time measurements, SEG monograph, Larner (ed.), Tulsa, Oklahoma.

- Jakubowicz, H., 1985, A simple efficient method of pre-stack partial migration, presented at the 46th Ann. Mtg. of the EAEG, London.
- Kinneging, N.A., 1989, Three-dimensional redatuming of seismic shot records. PhD thesis, Delft University of Technology, Delft, The Netherlands.
- Krey, Th., 1975, Computation of interval velocities from common reflection point moveout times for n layers with arbitrary dips and curvatures in three dimensions when assuming small shot-geophone distances, *Geophysical Prospecting* **24**, 91–111.
- Levin, F.K., 1971, Apparent velocity from dipping interface reflections, *Geophysics* **36**, 510–516.
- Liner, C., 1988, General theory and comparative anatomy of dip moveout, Center for wave phenomena, Colorado school of mines, Golden, Colorado.
- Ottolini, R. and Claerbout, J.F., 1984, The migration of common midpoint slant stacks, *Geophysics* **49**, 237–249.
- Ristow, D. 1988, Dip-moveout, 8. Mintrop Seminar, May 3–8 1988, Kassel.
- Salvador, L. and Savelli, S., 1982, Offset continuation for seismic stacking, *Geophysical Prospecting* **30**, 829–849.
- Shah, P.M., 1973, Use of wavefront curvature to relate seismic data with subsurface parameters, *Geophysics* **38**, 812–825.
- Taner, M.T. and Koehler, F., 1969, Velocity spectra-digital computer derivation and applications of velocity functions, *Geophysics*, **34**, 859–881.
- Tarantola, A., 1986, A strategy for nonlinear elastic inversion of seismic data, *Geophysics*, **51**, 1983–1903.
- Telford, W.M., Geldart, L.P., Sheriff, R.E., and Keys, D.A., 1976, *Applied geophysics*, Cambridge University Press.

Triton Research proposal, 1985, Delft University of Technology, Delft, The Netherlands.

Van der Schoot, A., Romijn, R., Larson, D.E., and Berkhout A.J., 1989, Prestack migration by shot record inversion and common depth point stacking: a case study, *First Break* 7, 293–304.

Wapenaar, C.P.A. and Berkhout, A.J., 1985, Velocity determination in layered systems with arbitrary curved interfaces by means of wave field extrapolation of CMP data, *Geophysics* 50, 63–76.

Yilmaz, O., 1979, Pre-stack partial migration, PhD thesis, Stanford University.

Yilmaz, O., and Claerbout, J.F., 1980, Prestack partial migration, *Geophysics* 45, 1753–1779.

SUMMARY

Dip moveout or DMO is known to be a valuable tool in today's processing schemes. DMO can be seen as an extension to the conventional processing sequence of NMO correction, CMP stacking and poststack migration. Processing with DMO approximates the result of (time) migration before stack. DMO is generally based on the assumption that the medium velocity is constant, although approximate generalizations of DMO in the presence of depth-variable velocities have been proposed. All the efforts put into the development of the DMO algorithm are based on the concept of the "time-domain technology". We could, however, start with the concept of "depth-technology" (compare e.g. time migration versus depth migration).

In this thesis a depth-oriented approach to DMO, which we call "common reflection point (CRP) stacking" is presented. In this approach, the CRP operator design is based on a macro model of the subsurface, in which ray tracing is performed. Lateral as well as vertical velocity variations are therefore allowed. To obtain an exact (with respect to travel-times) CRP operator for the inhomogeneous media, offset ray tracing for all offsets should be done. It is shown in this thesis that the multi-offset ray tracing can be approximated by efficient zero-offset ray tracing, in combination with a simple mathematical relation.

The derivation of CRP stacking also reveals another very important property of the depth-oriented DMO approach not shared by the time-oriented approach. Namely, that it contains all the ingredients necessary to carry out a direct mapping of multi-offset data to their correct lateral and vertical position in depth. In other words, an approximated prestack depth migration can be accomplished by CRP processing, which is as efficient as CRP stacking itself.

This thesis starts with a general introduction to CMP, CRP and CDP processing schemes. Next the CRP scheme is compared with conventional DMO schemes. Ample attention is paid to the evaluation of CRP stacking and prestack migration on synthetic and real data. Although the theory presented in this thesis is developed for 2-D media, indications are given of how the CRP concept can be extended to 3-D media.

SAMENVATTING

Dip moveout (DMO) wordt algemeen gezien als een waardevolle processing stap, die optioneel in seismische data processing toegepast kan worden. DMO vormt dan een uitbreiding van de conventionele processing, die o.m. bestaat uit NMO correctie, CMP stacking en poststack migratie. Een processing sequentie waarin DMO is inbegrepen, benadert het resultaat van (tijd)migratie voor stack. In het algemeen zijn DMO schema's gebaseerd op de veronderstelling dat de snelheid van het medium constant is. Generalisaties van DMO voor diepte afhankelijke snelheidsverdelingen zijn ook wel voorgesteld. Alle inspanningen om dergelijke DMO schema's te ontwikkelen zijn gebaseerd op tijd-domein concepten. Het is echter beter om DMO opnieuw te formuleren op basis van diepte-technologie concepten (vergelijk bijvoorbeeld tijd- en diepte-migratie). In deze dissertatie wordt een diepte-georiënteerde benadering van DMO gepresenteerd, die we "common reflection point (CRP) stacking" noemen. In deze benadering is het ontwerp van de CRP operator gebaseerd op ray tracing in een macro (d.i. diepte-interval snelheids) model.

Zowel laterale als verticale snelheidsvariaties zijn in dit macro model toegestaan. Om een — wat betreft looptijden — exacte CRP operator voor inhomogene media te bepalen, zou een offset ray tracing voor alle offsets moeten worden uitgevoerd. In deze dissertatie wordt beschreven hoe de multi-offset ray tracing benaderd kan worden door een combinatie van efficiënte zero-offset ray tracing en een simpele mathematische relatie.

De afleiding van het CRP stacking concept brengt een belangrijke eigenschap van de diepte-georiënteerde benadering aan het licht, die niet gedeeld wordt door de tijd-domein georiënteerde benadering. In de diepte-georiënteerde benadering zijn nl. alle ingrediënten aanwezig om een directe mapping van multi-offset data naar hun correcte positie, lateraal en in diepte, uit te voeren. Met andere woorden, met behulp van het CRP processing schema

kan een — zij het benaderde — prestack migratie uitgevoerd worden, die net zo efficiënt is als CRP stacking zelf.

Deze dissertatie begint met een algemene introductie tot CMP, CRP en CDP processing. Vervolgens wordt het CRP schema vergeleken met conventionele DMO schema's. Uitgebreide aandacht wordt besteed aan de evaluatie van CRP stacking en prestack migratie op synthetische en echte data.

Hoewel de theorie in deze dissertatie ontwikkeld wordt voor 2-D media, worden er ook indicaties gegeven hoe het CRP concept uitgebreid kan worden tot 3-D media.

CURRICULUM VITAE

Name: van der Schoot, Adriaan
 Born: November 4, 1956
 Nationality: Dutch

Education

1969 – 1975 secondary school (Atheneum B)
 1975 – 1982 Delft University of Technology
 (Applied Physics)
 1981: B.Sc.
 medical ultrasound
 thesis: The construction of an acoustic
 measurement system for making
 ultrasound measurements
 1982: M.Sc.
 medical ultrasound
 thesis: The influence of quantization on synthetic
 focussing by means of inverse wave field
 extrapolation

Employment

1979 – 1982 Research assistant with the group of experimental cardiology,
 Erasmus University Rotterdam
 1982 – 1985 TNO Institute of Applied Geoscience
 processing geophysicist
 1985 – present Delft Geophysical b.v.
 1985 – 1988: research geophysicist / manager R & D
 1988 – present: manager geophysical data processing

TU Delft 17 oktober 1989

STELLINGEN

behorende bij het proefschrift

“Common reflection point stacking, a macro model driven approach to dip moveout”

1. Verschillende “common-offset” secties bevatten structureel gezien naast compatibele ook complementaire informatie. De secties dienen daarom — voor of na migratie — niet zonder meer opgeteld (“stacked”) te worden, maar gecombineerd te worden tot een fijner (lateraal) bemonsterde eind sectie. Eén en ander zal tot een significante economische verbetering in 3-D technieken leiden.
2. De suggestie van Hale dat het toepassen van “constant velocity” DMO altijd beter is dan het niet toepassen ervan is door de praktijk achterhaald (Hale, 1983, Dip-moveout by Fourier transform, Stanford University).
3. Het is beter om van multi-offset data te spreken dan van prestack data.
4. Interactieve processing is voornamelijk zinvol met het oog op het bepalen van snelheidsmodellen. Voor andere toepassingen biedt interactieve processing geen wezenlijke voordelen.
5. Het testen van parameters in seismische data processing wordt onvoldoende ondersteund door geldige beoordelingscriteria. Parameter keuzes worden dan ook dikwijls meer bepaald door de mate waarin numerieke artefacten worden gereduceerd dan door de geofysische kwaliteit van het resultaat.
6. Lawaai is een wezenlijk kenmerk van dit technologisch tijdperk.
7. Kennis maakt de mens vrij, technologie daarentegen bindt hem.
8. Ascese en vrijheid hebben alles met elkaar te maken.
9. Volledig nihilisme is principieel onvereenigbaar met het leven (naar H. Küng, “Existiert Gott?”).
10. Het christelijk geloof is niet onredelijk, maar boven-redelijk, consistent en zeer de moeite waard.